Flow Control for Bubble Management in a Membrane-free Alkaline Water Electrolyser

Bo Yang

School of Electrical and Mechanical Engineering
The University of Adelaide
South Australia, 5005
Australia

A thesis submitted in fulfilment of the requirements
for the degree of Ph.D. in Mechanical Engineering
12 March 2024

Thesis summary

The global challenge of rapid population growth and environmental degradation has spurred the search for sustainable, clean, and low-carbon energy solutions. Hydrogen has been widely used as a feedstock for chemical processes and is recognised as a clean alternative to traditional fuels. Currently, a significant portion of H_2 production relies on fossil fuel-based processes, contributing to global warming and toxic gas emissions. Consequently, there is an increasing interest in investigating different approaches for H_2 production from non-fossil sources. Among these, water electrolysis has emerged as a leading method for generating clean H_2.

The membrane-free water electrolyser (MFE) is a novel cell design that eliminates the membrane in a conventional water electrolyser. This innovative approach not only reduces both capital and maintenance costs but also facilitates the increase of operating temperature and pressure, resulting in improved cell efficiency. Moreover, it reduces the overall cost of H_2 considering the pressurisation or liquefaction of H_2 for transportation. However, the membrane-free design faces challenges related to gas crossover and scalability, and these factors are closely related to bubble behaviour in the electrolyser channel. The research in this thesis is motivated by the need to address these challenges.

The research aims to minimise the gas crossover in MFEs by developing the technique to better control bubble distribution in the electrolyser channel. The thesis first demonstrates the feasibility of using MFEs for industrial-scale liquid H_2 (LH_2) production. While MFE offers lower ohmic resistance compared to conventional ones, they face challenges in producing high-purity H_2 due to the lack of a physical barrier to separate H_2 and O_2. To address this issue, a cryogenic cooling system is employed to purify H_2 gas by removing O_2. The specific energy consumption for LH_2 production using MFEs and conventional alkaline water electrolysers under different operating conditions has been calculated. Findings indicate that MFEs could potentially provide more cost-effective operations in the production of LH_2, since the electric power saved from their higher efficiency outweighs the cost of oxygen removal. Furthermore, improving the product H_2 purity further reduces cooling load requirements, leading to reduced operating costs. This emphasises the significance of effectively managing bubble distribution in an MFE.

To facilitate the investigation of bubble behaviour in MFEs, it is necessary to develop a technique that can generate bubbles in an electrolyser channel with controllable size and frequency. Consequently, the research focuses on the study of H_2 bubble formation and departure from a microelectrode in an MFE. Systematic studies were carried out to examine the impact of applied current and the geometry of microelectrodes on the size and frequency of bubbles. Additionally, the process of single and continuous bubble formation is investigated. Building upon these findings, an electrolytic microbubble generator is developed, capable of producing single bubbles with diameters ranging from 0.3 mm to 1.4 mm, which encompasses the control target – the large bubbles with diameters greater than 0.3 mm, formed through coalescence in MFEs.

Employing the technique of generating single microbubbles, this research includes an experimental study focused on the rising trajectories of H_2 bubbles in an electrolyser channel. The lift and drag forces on bubbles are assessed based on their rising trajectories, and a new correlation is proposed for estimating the shear-induced lift forces on bubbles with diameters ranging from 0.3 mm to 1.0 mm. The study highlights the critical role of the electrolyte's velocity field in governing bubble distribution within an MFE. It is shown that maintaining a parabolic velocity profile in the electrolyte allows H_2 and O_2 bubbles to rise close to the electrode where they evolve. However, as the void fraction increases, bubbles near the electrode induce a high local velocity, disrupting the velocity field and leading to gas crossover. This highlights that depending solely on applying a parabolic electrolyte flow at the inlet of the electrolyser channel may not be effective in eliminating gas crossover in MFE.

The final part of the research introduces a novel technique to suppress the crossover of H_2 and O_2 within the MFE channel. The approach involves the implementation of flow controllers to manipulate the velocity field in the electrolyser channel, generating a lift force that prevents H_2 and O_2 bubbles from mixing. This significantly alleviates gas crossover within the electrolyser. While this technique does not completely prevent gas crossover, it provides valuable insights into the potential of active flow control methods for enhancing the performance of MFE.

The thesis makes significant contributions by developing a new understanding of bubble behaviour in an MFE, along with the development of techniques to control bubble distribution within such systems. The research demonstrates the viability of MFEs for LH_2 production, positioning this technology as an appealing option for clean H_2 generation. The creation of the microbubble generator introduces a straightforward yet highly effective tool for conducting fundamental studies on bubble behaviour. Additionally, the study on forces acting on rising bubbles highlights the critical role of the velocity field of the electrolyte in governing bubble distribution, a key factor for managing gas crossover. Moreover, the innovative flow controllers effectively address gas crossover issues and enable the scaling-up of MFEs. These findings provide valuable insights into the MFE technology, propelling the prospects of efficient and sustainable H_2 production. The research outcomes contribute significantly to the clean energy sector, fostering the implementation of membrane-free water electrolysers as a promising pathway towards a greener future.

Declaration

I certify that this work contains no material which has been accepted for the award of any other degree or diploma in my name, in any university or other tertiary institution and, to the best of my knowledge and belief, contains no material previously published or written by another person, except where due reference has been made in the text. In addition, I certify that no part of this work will, in the future, be used in a submission in my name, for any other degree or diploma in any university or other tertiary institution without the prior approval of the University of Adelaide and where applicable, any partner institution responsible for the joint award of this degree.

The author acknowledges that copyright of published works contained within the thesis resides with the copyright holder(s) of those works.

I give permission for the digital version of my thesis to be made available on the web, via the University's digital research repository, the Library Search and also through web search engines, unless permission has been granted by the University to restrict access for a period of time.

I acknowledge the support I have received for my research through the provision of an Australian Government Research Training Program Scholarship.

Bo Yang

Acknowledgements

I want to start by expressing my heartfelt gratitude to Prof Maziar Arjomandi, my principal supervisor, whose unwavering kindness and patience have been instrumental in my academic journey. I am deeply indebted to him for shaping the direction of my research, setting clear goals, and guiding me through challenges throughout these years. My sincere appreciation also goes to my co-supervisors, Dr Mehdi Jafarian and Dr Navid Freidoonimehr, for their invaluable support, encouragement, and guidance.

I extend my sincere gratitude to Prof Graham Nathan, Prof Paul Medwell, Dr Mohsen Sarafraz, Dr Zhiwei Sun for their valuable advice. I am thankful for the support and assistance from Mr Phil Schmidt, Mr Scott Letton, Mr Robert Dempster and Mr Jason Peak from the Mechanical and Electrical workshops.

I want to thank my family, especially my amazing wife who provided unwavering support, love, and understanding throughout this journey. I am truly grateful for their patience and sacrifices, especially during those times when my research took precedence, and I couldn't spend as much time with them as I would have liked.

I also want to express my gratitude to all my friends for their companionship and support during this academic pursuit. The time we spent together has made this journey even more memorable.

Finally, I want to acknowledge the Australian Government Research Training Program Scholarship for the financial support for my research.

Acronyms

AWE	Alkaline water electrolysis
LH_2	Liquid hydrogen
MFE	Membrane-free water electrolyser
PEM	Proton exchange membrane electrolysis
SOE	Solid oxide electrolysis

List of Figures

List of Tables

Contents

Chapter 1

Introduction

1.1 Background

Hydrogen has emerged as a versatile energy carrier for humanity to address the critical challenge of pursuing sustainable, clean, and low-carbon energy solutions. Hydrogen is one of the cleanest energy sources, with benefits such as non-toxic emissions and high heat of combustion (HHV = 142 MJ/kg and LHV = 121MJ/kg) (Zohuri 2019). In addition to its conventional applications in food industry, hydrocarbon synthesis and metallurgical processes, H_2 has recently been used as fuel in aerospace engineering and fuel cell technology. While its adoption in the transportation sector is currently limited to a few applications, research and development efforts are ongoing (Dawood *et al.* 2020). At present, more than 90% of H_2 produced worldwide are from reforming or gasification of hydrocarbons such as methane (CH_4), naphthalene and coal (Barelli *et al.* 2008), which contribute to global warming and toxic gas emissions. Production of H_2 from non-fossil fuel sources like biomass and municipal waste has been investigated in lab-scale (Soo *et al.* 2015, Zhang *et al.* 2019). However, these approaches encounter additional challenges, such as NOx and heavy metal emissions due to feedstock contamination, the complexities of managing toxic by-products, and relatively low overall efficiency levels (Moreno and Dufour 2013, Ochoa *et al.* 2020). Nonetheless, H_2 production from non-fossil fuels is regarded as a promising solution in mitigating global warming and reducing pollutant emissions (Abanades and Flamant 2006, Cardoso *et al.* 2015).

Water splitting is considered the cleanest method for H_2 production since it only produces H_2 and O_2 (Chatenet *et al.* 2022). Although there are various water splitting technologies including direct thermal (Luo *et al.* 2018), thermochemical (Abanades and Flamant 2006) and photocatalysis (Chung *et al.* 2018), water electrolysis stands as one of the most advanced methods, with technologies such as alkaline water electrolyser (AWE) and proton exchange membrane electrolyser (PEM) being available on commercial scale (Shiva Kumar and Himabindu 2019, Brauns and Turek 2020). Several factors play a role in determining the efficiency of water electrolysis cells, such as the cell configuration (Wilberforce *et al.* 2017, Phillips and Dunnill 2019), the surface characteristics of the electrode material (Zhou *et al.* 2020, Hodges *et al.* 2022), type of catalyst (Lu and Ammon 1982, Li *et al.* 2011), electrolyte property (Xu *et al.* 2009, Peraud *et al.* 2017), electrical conductivity of separator (for AE cell) or membrane (for PEM cell) (Shiva Kumar and Himabindu 2019, Fortin *et al.* 2020, Hua *et al.* 2022), and operating conditions including temperature, pressure and applied voltage (Kuleshov *et al.* 2020, Lamy and Millet 2020, Salehmin *et al.* 2022). Furthermore, mitigating the bubble effect is crucial to enhance the efficiency of water electrolysers. Gas bubbles within the electrolyser elevate cell resistance and reduce the effective electrode area, thereby degrading cell performance (Sides and Tobias 1980, Sillen *et al.* 1982). It is also found that gas bubbles contribute to about 30% of the total energy loss in water electrolysers (Zeng and Zhang 2010). Therefore, a deeper understanding of bubble behaviour is necessary for enhancing the overall efficiency of water electrolysers.

In modern alkaline electrolyser cells, a membrane is installed between the cathode and anode to isolate H_2 and O_2 gases (Paidar *et al.* 2016, Hua *et al.* 2022). Although the membrane plays a crucial role in gas separation, it still introduces resistance, subsequently reducing the cell efficiency. Additionally, the membrane is prone to degradation, particularly under elevated temperatures and pressures, leading to considerable maintenance costs and restricting the implementation of high-pressure and high-temperature electrolysers (Fortin *et al.* 2020, Salehmin *et al.* 2022, Swiegers *et al.* 2022). Furthermore, it is estimated that membranes contribute to about 9% of the capital cost for an industrial electrolyser (Esposito 2017). Consequently, there is a rising interest in the development of membrane-free water electrolyser (MFE) technology, which eliminates the need for a membrane to reduce both capital and maintenance costs (O'Neil *et al.* 2016, Manzotti *et al.* 2022).

Moreover, MFE technology can effectively narrow the gap between the anode and cathode, thereby reducing ohmic losses while achieving a reasonable purity of H_2. In recent years, various MFE configurations have been developed, primarily relying on the electrolyte flow field to manage the distribution of H_2 and O_2 bubbles in the electrolyser channels. Notable designs include the flow-through (Gillespie *et al.* 2015, Rajaei *et al.* 2021) and flow-by (O'Neil *et al.* 2016, Hashemi *et al.* 2019) MFEs. This research focuses on the flow-by configuration, with a specific focus on understanding the interaction between the electrolyte and bubbles. Such understanding is crucial for minimising gas crossover, as highlighted in prior studies (Amini, Lee *et al.* 2014, Zhang, Li *et al.* 2017).

In general, the flow-by MFEs offer several advantages over their conventional counterparts, including enhanced durability, simplified cell design, improved efficiency, and reduced capital and maintenance costs (Esposito 2017). Despite the advantages, this emerging technology still requires extensive research and development. The primary challenges it faces include issues with gas crossover, low current density, and difficulties in scaling up (Esposito 2017, Manzotti *et al.* 2022).

In an MFE, due to the lack of a physical barrier that restricts the crossover of H_2 and O_2 in the electrolyser channel, the separation of the two gases relies solely on the electrolyte flow field. Most of the flow-by MFEs can only operate at a laminar flow regime and low current densities. For such operating conditions, the shear-induced lift force on bubbles propels them towards the electrode where they evolve (O'Neil *et al.* 2016, Aoyama *et al.* 2017, Gavrilov *et al.* 2018). Nonetheless, the magnitude of the lift force is usually at least an order of magnitude smaller than that of the drag force. Therefore, local turbulence in the electrolyte can sometimes dominate the trajectories of bubbles and lead to their mixing. At high current densities, bubble generation becomes highly random and chaotic (Mandin *et al.* 2008, Zhang and Zeng 2012), leading to a more pronounced gas crossover (Swiegers *et al.* 2022).

Additionally, the literature scarcely addresses the size limitations inherent to a flow-by MFE. As the electrolyser channel length increases, the gas hold-up within the channel also rises. Consequently, a greater number of bubbles tend to accumulate downstream in the electrolyser channel, causing a pronounced gas crossover. This limitation poses a significant obstacle to the scalability of flow-by MFEs, hindering their ability to achieve industrial scales without encountering the issues mentioned above.

The primary motivation behind this research is to enhance the performance of the flow-by MFE by controlling bubble distribution in the cell. To attain this goal, this study focuses on investigating the behaviour of bubbles rising in a bounded channel with a fully developed laminar flow. Moreover, a novel technique is proposed to create the desired velocity profile in the electrolyser channel, thereby effectively controlling bubble distribution and mitigating gas crossover. The outcomes of this research hold the potential to significantly advance our understanding of bubble-liquid two-phase flow and have valuable implications for the MFE industry.

1.2 Aims and objectives

The research aims to develop a new understanding of bubble behaviour in membrane-free water electrolysers (MFEs) and the techniques to alleviate bubble mixing in the electrolyser channel. Four objectives are defined as follows:

The first objective is to explore the viability of utilising MFEs for commercial-scale liquid H_2 (LH_2) production through the implementation of cryogenic cooling. In this approach, the raw H_2 produced from MFEs is purified by liquefying and separating O_2. Through a series of sensitivity studies, the influence of crucial parameters on the specific energy consumption of LH_2 production is analysed. These parameters include the operating temperature and pressure of the cell stack and the purity level of the H_2 gas.

The second research objective involves the development of a technique to generate single microbubbles within an electrolyser channel, thus facilitating the subsequent investigation of bubble behaviour in such a medium. To accomplish this objective, a novel concept of a single microbubble generator is developed to produce micro-electrolytic bubbles in the electrolyte. The systematic investigation explores the influence of the bubble generator's geometrical features and the applied current on the sizes and frequencies of the bubbles.

The third research objective is to develop an understanding of bubble rising behaviour in an electrolyser channel. Utilising the microbubble generator developed in the previous study, H_2 bubbles with various diameters are injected into an electrolyser channel. The impact of electrolyte flow and bubble diameters on the trajectories of the bubbles are systematically studied, and the shear-induced lift force and drag force on the bubbles are subsequently investigated.

The fourth research objective aims to control bubble distribution in an MFE by manipulating the electrolyte flow field. To this end, a flow controller has been developed, capable of maintaining an optimal velocity field in the MFE. This design ensures that the shear-induced lift force consistently directs the H_2 and O_2 bubbles towards the electrodes where they evolve. Employing this technique could significantly reduce gas crossover in MFEs, enhancing their viability for industrial applications.

1.3 Thesis outline

The thesis comprises seven chapters. Chapter 1 provides an overview of the thesis and introduces the background and objectives of the research.

Chapter 2 offers a comprehensive review of recent publications in the research field, identifying gaps in existing knowledge. The literature review begins by introducing the current status of global H_2 demand, production, purification, transportation, and liquefaction. Subsequently, it introduces the fundamentals of H_2 production from water electrolysis, including the origins of overpotentials, ionic species transport, and the influence of bubbles on the electrolyser performance. Detailed attention is given to the research and development of membrane-free water electrolysers (MFE), encompassing aspects such as cell design, H_2/O_2 separation techniques, as well as the advantages and disadvantages associated with MFE technology. The chapter then shifts focus to recent work on bubble behaviour in MFEs, including the formation of electrolytic bubbles, their rising behaviour in bounded flows, and bubble visualisation techniques. Numerical studies on modelling bubble rising in a liquid and bubble distribution in a water electrolyser are also included.

Chapters 3 to 6 present the key findings of this research, consisting of four manuscripts published or currently under review in peer-reviewed journals. In Chapter 3, the feasibility of using membrane-free water electrolysers for industrial-scale liquid hydrogen (LH_2) production is presented. A mathematical model for H_2 generation via both alkaline and membrane-free water electrolysers is developed. The raw H_2 output from these electrolysers serves as the feedstock for subsequent purification and liquefaction processes. Using Aspen HYSYS® software, this study systematically investigates the influence of electrolyser operating conditions and raw H_2 purity on the total power consumption for LH_2 production. The findings reveal that membrane-free water electrolysers offer an energy-efficient alternative to alkaline water electrolysers, potentially reducing power consumption by up to 10%. Importantly, this study also revealed that improving the product H_2 purity can reduce the cooling load required for O_2 separation, consequently leading to reduced operating costs.

The following chapters focus on developing knowledge about bubble behaviour in an MFE and techniques to minimise gas crossover by controlling bubble distribution in an electrolyser channel. Specifically, chapter 4 presents the study of the growth and departure of H_2 bubbles from a microelectrode. The effect of applied current and geometries of the microelectrode on the diameters and frequencies of bubbles are systematically investigated. The mechanism for single and continuous bubble formation from a microelectrode is also discussed. Based on the findings, an electrolytic microbubble generator is developed, which can produce bubbles with diameters ranging from 0.3 mm to 1.4mm at an interval of approximately 1s. This novel bubble-producing technique lays the groundwork for further examination of bubble rising behaviour in the electrolyser channel.

Chapter 5 presents the experimental study on electrolytic H_2 bubbles rising in an electrolyser channel with fully developed laminar flow. The lift and drag forces on bubbles are assessed based on their rising trajectories. A new correlation is proposed for estimating the shear-induced lift forces on bubbles with diameters of 0.3 mm-1.0 mm. This study highlights the critical role of the electrolyte flow field in governing the distribution of bubbles within an MFE. When the electrolyte maintains a parabolic velocity profile, H_2 and O_2 bubbles will rise close to the electrode due to the shear-induced lift force. However, this can only happen when the void fraction is relatively low so that the bubble-induced velocity is negligible. As the void fraction increases, bubbles near the electrode induce a high local velocity, disrupting the velocity field in the electrolyte. This high velocity near the electrode generates a lift force that propels bubbles towards the channel centre, leading to gas crossover. Consequently, it is shown that relying solely on electrolyte flow cannot guarantee the effective separation of O_2 and H_2 bubbles in an MFE.

Chapter 6 presents a novel technique to enhance the separation of H_2 and O_2 bubbles within an MFE. A series of flow controllers are installed in the electrolyser channel of an MFE. The geometric parameters of the flow controlling device on the bubble distribution in the electrolyser channel are subsequently investigated. It is found that the flow controllers can effectively maintain the optimal velocity field in the electrolyser channel. This ensures that the shear-induced lift force on the H_2 and O_2 bubbles always pushes them towards the electrode where they evolve. As a result, the gas crossover is significantly alleviated. While this technique does not entirely eliminate the gas crossover issue in MFEs, it provides valuable insights into the effectiveness of flow control strategies in enhancing the performance of these systems.

Finally, Chapter 7 offers a comprehensive summary of the key findings derived from this research. Recommendations for future work are also provided.

1.4 Publication arising from the thesis

1.4.1 Published journal papers

Yang, B., M. Jafarian, N. Freidoonimehr, and M. Arjomandi, Trajectory of a spherical bubble rising in a fully developed laminar flow. International Journal of Multiphase Flow, 2022. 157. DOI: 10.1016/j.ijmultiphaseflow.2022.104250.

Yang, B., M. Jafarian, N. Freidoonimehr, and M. Arjomandi, Controlled bubble formation from a microelectrode single bubble generator. Journal of Fluids Engineering, 2023. 145(11). DOI: 10.1115/1.4062962.

Yang, B., Jafarian, M., Freidoonimehr, N., & Arjomandi, M. (2024). Flow control for bubble management in a membrane-free electrolyser. International Journal of Multiphase Flow, 174, 104770.

1.4.2 Manuscript under review

Yang, B., M. Jafarian, N. Freidoonimehr, and M. Arjomandi, Membrane-free water electrolyser for liquid hydrogen production. Submitted to International Journal of Hydrogen Energy.

1.4.3 Conference presentation

Yang, B., M. Jafarian, N. Freidoonimehr, and M. Arjomandi, A method for production of single microbubbles for the study of shear-induced lift force on microbubbles, AFMC 2022: The 23rd Australasian Fluid Mechanics Conference [AFMC2022-113] Australasian Fluid Mechanics Society.

1.5 Thesis format

This thesis is submitted in the format of a collection of publications, adhering to the University of Adelaide's formatting guidelines. The printed and online versions of this thesis are identical, with the electronic version being available in PDF format.

References

Abanades, S. and G. Flamant (2006). "Thermochemical hydrogen production from a two-step solar-driven water-splitting cycle based on cerium oxides." Solar Energy **80**(12): 1611-1623.

Amini, H., W. Lee and D. Di Carlo (2014). "Inertial microfluidic physics." Lab Chip **14**(15): 2739-2761.

Aoyama, S., K. Hayashi, S. Hosokawa, D. Lucas and A. Tomiyama (2017). "Lift force acting on single bubbles in linear shear flows." International Journal of Multiphase Flow **96**: 113-122.

Barelli, L., G. Bidini, F. Gallorini and S. Servili (2008). "Hydrogen production through sorption-enhanced steam methane reforming and membrane technology: A review." Energy **33**(4): 554-570.

Brauns, J. and T. Turek (2020). "Alkaline water electrolysis powered by renewable energy: a review." Processes **8**(2): 248.

Cardoso, D. S. P., L. Amaral, D. M. F. Santos, B. Šljukić, C. A. C. Sequeira, D. Macciò and A. Saccone (2015). "Enhancement of hydrogen evolution in alkaline water electrolysis by using nickel-rare earth alloys." International Journal of Hydrogen Energy **40**(12): 4295-4302.

Chatenet, M., B. G. Pollet, D. R. Dekel, F. Dionigi, J. Deseure, P. Millet, R. D. Braatz, M. Z. Bazant, M. Eikerling, I. Staffell, P. Balcombe, Y. Shao-Horn and H. Schafer (2022). "Water electrolysis: from textbook knowledge to the latest scientific strategies and industrial developments." Chem Soc Rev **51**: 4583-4762.

Chung, K.-H., S. Jeong, B.-J. Kim, K.-H. An, Y.-K. Park and S.-C. Jung (2018). "Enhancement of photocatalytic hydrogen production by liquid phase plasma irradiation on metal-loaded TiO_2/carbon nanofiber photocatalysts." International Journal of Hydrogen Energy **43**(24): 11422-11429.

Dawood, F., M. Anda and G. M. Shafiullah (2020). "Hydrogen production for energy: An overview." International Journal of Hydrogen Energy **45**(7): 3847-3869.

Esposito, D. V. (2017). "Membraneless electrolyzers for low-cost hydrogen production in a renewable energy future." Joule **1**(4): 651-658.

Fortin, P., T. Khoza, X. Cao, S. Y. Martinsen, A. Oyarce Barnett and S. Holdcroft (2020). "High-performance alkaline water electrolysis using Aemion™ anion exchange membranes." Journal of Power Sources **451**: 227814.

Gavrilov, A. A., K. A. Finnikov, Y. S. Ignatenko, O. B. Bocharov and R. May (2018). "Drag and lift forces acting on a sphere in shear flow of power-law fluid." Journal of Engineering Thermophysics **27**(4): 474-488.

Gillespie, M. I., F. van der Merwe and R. J. Kriek (2015). "Performance evaluation of a membraneless divergent electrode-flow-through (DEFT) alkaline electrolyser based on optimisation of electrolytic flow and electrode gap." Journal of Power Sources **293**: 228-235.

H. Hashemi, S. M., P. Karnakov, P. Hadikhani, E. Chinello, S. Litvinov, C. Moser, P. Koumoutsakos and D. Psaltis (2019). "A versatile and membrane-less electrochemical reactor for the electrolysis of water and brine." Energy & Environmental Science **12**(5): 1592-1604.

Hodges, A., A. L. Hoang, G. Tsekouras, K. Wagner, C. Y. Lee, G. F. Swiegers and G. G. Wallace (2022). "A high-performance capillary-fed electrolysis cell promises more cost-competitive renewable hydrogen." Nature Communications **13**(1): 1304.

Hua, D., J. Huang, E. Fabbri, M. Rafique and B. Song (2022). "Development of anion exchange membrane water electrolysis and the associated challenges: a review." ChemElectroChem **10**(1): e202200999.

Kuleshov, V. N., S. V. Kurochkin, N. V. Kuleshov and E. Y. Udris (2020). "High-pressure alkaline water electrolyser of coaxial configuration." Journal of Physics: Conference Series **1683**(5): 052039.

Lamy, C. and P. Millet (2020). "A critical review on the definitions used to calculate the energy efficiency coefficients of water electrolysis cells working under near ambient temperature conditions." Journal of Power Sources **447**: 227350.

Li, X., F. C. Walsh and D. Pletcher (2011). "Nickel based electrocatalysts for oxygen evolution in high current density, alkaline water electrolysers." Phys Chem Chem Phys **13**(3): 1162-1167.

Lu, P. W. T. and R. L. Ammon (1982). "Sulfur dioxide depolarized electrolysis for hydrogen production: Development status." International Journal of Hydrogen Energy **7**(7): 563-575.

Luo, M., Y. Yi, S. Wang, Z. Wang, M. Du, J. Pan and Q. Wang (2018). "Review of hydrogen production using chemical-looping technology." Renewable and Sustainable Energy Reviews **81**: 3186-3214.

Mandin, P., A. A. Aissa, H. Roustan, J. Hamburger and G. Picard (2008). "Two-phase electrolysis process: From the bubble to the electrochemical cell properties." Chemical Engineering and Processing: Process Intensification **47**(11): 1926-1932.

Manzotti, A., E. Quattrocchi, A. Curcio, S. C. T. Kwok, M. Santarelli and F. Ciucci (2022). "Membraneless electrolyzers for the production of low-cost, high-purity green hydrogen: A techno-economic analysis." Energy Conversion and Management **254**: 115156.

Moreno, J. and J. Dufour (2013). "Life cycle assessment of hydrogen production from biomass gasification. Evaluation of different Spanish feedstocks." International Journal of Hydrogen Energy **38**(18): 7616-7622.

O'Neil, G. D., C. D. Christian, D. E. Brown and D. V. Esposito (2016). "Hydrogen production with a simple and scalable membraneless electrolyzer." Journal of The Electrochemical Society **163**(11): F3012-F3019.

Ochoa, A., J. Bilbao, A. G. Gayubo and P. Castaño (2020). "Coke formation and deactivation during catalytic reforming of biomass and waste pyrolysis products: A review." Renewable and Sustainable Energy Reviews **119**: 109600.

Paidar, M., V. Fateev and K. Bouzek (2016). "Membrane electrolysis—History, current status and perspective." Electrochimica Acta **209**: 737-756.

Peraud, J. P., A. J. Nonaka, J. B. Bell, A. Donev and A. L. Garcia (2017). "Fluctuation-enhanced electric conductivity in electrolyte solutions." Proceedings of the National Academy of Sciences of the United States of America **114**(41): 10829-10833.

Phillips, R. and C. Dunnill (2019). Zero gap cell design for alkaline electrolysis. A PhD Thesis, Energy Safety Research Institute, Swansea University Prifysgol Abertawe.

Rajaei, H., A. Rajora and J. W. Haverkort (2021). "Design of membraneless gas-evolving flow-through porous electrodes." Journal of Power Sources **491**: 229364.

Salehmin, M. N. I., T. Husaini, J. Goh and A. B. Sulong (2022). "High-pressure PEM water electrolyser: A review on challenges and mitigation strategies towards green and low-cost hydrogen production." Energy Conversion and Management **268**: 115985.

Shiva Kumar, S. and V. Himabindu (2019). "Hydrogen production by PEM water electrolysis – A review." Materials Science for Energy Technologies **2**(3): 442-454.

Sides, P. J. and C. W. Tobias (1980). "Primary potential and current distribution around a bubble on an electrode." Journal of the Electrochemical Society **127**(2): 288-291.

Sillen, C. W. M. P., E. Barendrecht, L. J. J. Janssen and S. J. D. van Stralen (1982). "Gas bubble behaviour during water electrolysis." International Journal of Hydrogen Energy **7**(7): 577-587.

Soo, C. S., W. S. Yap, W. M. Hon and L. Y. Phang (2015). "Mini review: hydrogen and ethanol co-production from waste materials via microbial fermentation." World Journal of Microbiology and Biotechnology **31**(10): 1475-1488.

Swiegers, G. F., A. L. Hoang, A. Hodges, G. Tsekouras, C.-Y. Lee, K. Wagner and G. Wallace (2022). "Current status of membraneless water electrolysis cells." Current Opinion in Electrochemistry **32**: 100881.

Wilberforce, T., Z. El-Hassan, F. N. Khatib, A. Al Makky, J. Mooney, A. Barouaji, J. G. Carton and A.-G. Olabi (2017). "Development of Bi-polar plate design of PEM fuel cell using CFD techniques." International Journal of Hydrogen Energy **42**(40): 25663-25685.

Xu, Q., M. Nakajima, S. Ichikawa, N. Nakamura, P. Roy, H. Okadome and T. Shiina (2009). "Effects of surfactant and electrolyte concentrations on bubble formation and stabilization." Journal of Colloid and Interface Science **332**(1): 208-214.

Zeng, K. and D. Zhang (2010). "Recent progress in alkaline water electrolysis for hydrogen production and applications." Progress in Energy and Combustion Science **36**(3): 307-326.

Zhang, D. and K. Zeng (2012). "Evaluating the behavior of electrolytic gas bubbles and their effect on the cell voltage in alkaline water electrolysis." Industrial & Engineering Chemistry Research **51**(42): 13825-13832.

Zhang, J., W. Li and G. Alici (2017). Inertial microfluidics: mechanisms and applications. Advanced Mechatronics and MEMS Devices II**:** 563-593.

Zhang, Y., P. Xu, S. Liang, B. Liu, Y. Shuai and B. Li (2019). "Exergy analysis of hydrogen production from steam gasification of biomass: A review." International Journal of Hydrogen Energy **44**(28): 14290-14302.

Zhou, D., P. Li, W. Xu, S. Jawaid, J. Mohammed‐Ibrahim, W. Liu, Y. Kuang and X. Sun (2020). Recent advances in non‐precious metal‐based electrodes for alkaline water electrolysis. ChemNanoMat **6**(3): 336-355.

Zohuri, B. a. (2019). Hydrogen energy challenges and solutions for a cleaner future, Springer International Publishing: Imprint: Springer.

Chapter 2

Literature review

2.1 Hydrogen as clean energy carrier

2.1.1 Hydrogen demand

In 2021, the worldwide demand for hydrogen surpassed 94 million tonnes (Mt), marking a 50% increase since 2000 and a 5% rise from the preceding year (International Energy Agency 2022). As shown in Figure 2-1a, the chemical industry and refining sector are the two major consumers of H_2, contributing to 53 Mt and 40 Mt of H_2 consumption, respectively. Although there is a rapid development in new H_2 applications such as heavy industry, power generation and transport sectors, they only contribute to about 0.04% of global H_2 demand. China, the United States, the Middle East, Europe and India are the largest H_2 consumers in the world (Figure 2-1b) (International Energy Agency 2022, Hydrogen Council 2023).

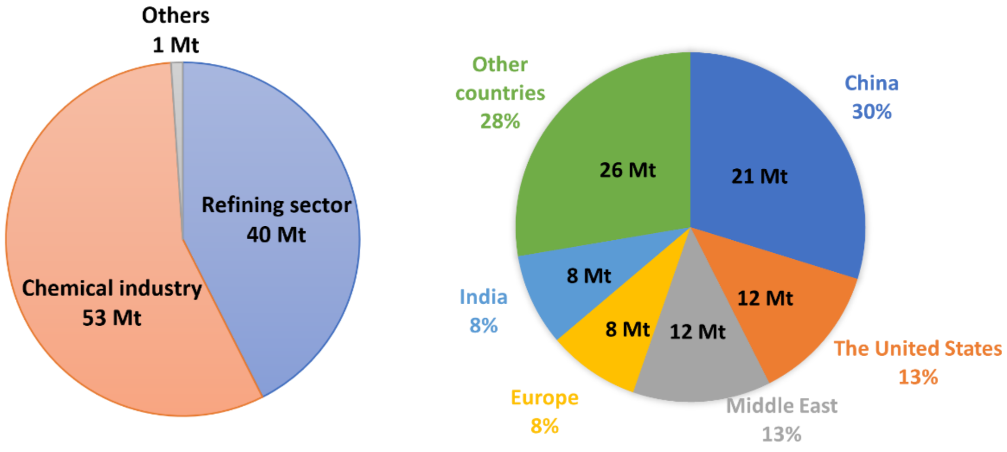

(a) (b)

Figure 2-1. Global hydrogen demand (a) by sectors and (b) by regions in 2011 (International Energy Agency 2022, Hydrogen Council 2023).

Chemical industries mainly use H_2 for the production of ammonia (34 Mt), methanol (15 Mt) and direct reduction of iron (5 Mt). Ammonia serves as the fundamental element for all mineral nitrogen fertilisers, constituting approximately 70% of the total global ammonia demand. The remaining 30% of ammonia usage is attributed to other industrial applications, including explosives, pharmaceuticals and synthesis of fibres and other chemical products (International Energy Agency 2022). Methanol is an essential raw material for chemical synthesis and pharmaceuticals and can be used as a clean-burning fuel (Hydrogen Council 2023, Liu *et al.* 2023). On the other hand, refineries primarily rely on H_2 to eliminate impurities like sulphur and to convert heavy oil fractions into lighter and more valuable products (Moradpoor *et al.* 2023).

Figure 2-2 presents the cost of H_2 from different pathways. Until 2021, nearly 80% of H_2 worldwide was derived from natural gas, with an average cost of about USD 1.0-2.5/kg H_2 (Sá *et al.* 2010, Bac *et al.* 2019, International Energy Agency 2022). Almost the rest of the H_2 was produced from coal gasification at about USD 1.0-2.0/kg H_2 (Shi *et al.* 2022, Hydrogen Council 2023). However, H_2 produced from fossil fuels can result in the emission of greenhouse gases. With the rising awareness of climate change in recent years, the production of H_2 through water electrolysis has gained increasing attention. Although only 0.04 Mt H_2 was produced via water electrolysis in 2021, it experienced a nearly 20% increase compared to 2020 (International Energy Agency 2022). By 2030, H_2 production from water electrolysis is projected to reach 0.3 Mt (International Energy Agency 2022). At the current stage, the main drawback of this technology is its higher H_2 cost (USD 4.0-9.0/kg H_2) compared with conventional pathways (Esposito 2017). Fortunately, with the continuous cost reductions of renewable technologies and efficiency improvement of water electrolysers in recent years, it is projected that the cost of H_2 will decrease to USD 1.5-3.0 kg H_2 by 2030 (Li 2017, International Energy Agency 2022).

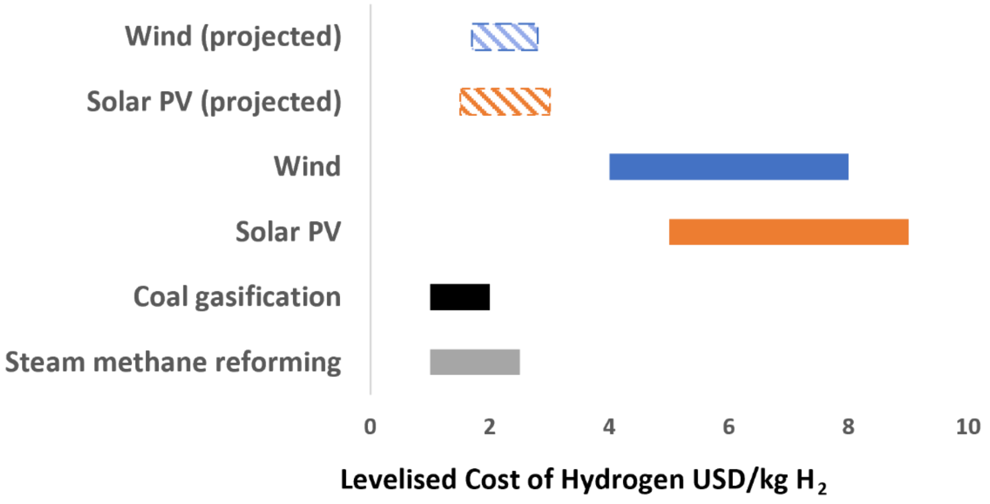

Figure 2-2. Levelised cost of hydrogen from different pathways (Sá *et al.* 2010, Bac *et al.* 2019, International Energy Agency 2022).

To conclude, the global H_2 market has grown significantly, predominantly driven by demand in the chemical and refining sectors, with major consumers including China, the United States and Europe. While hydrogen production at present mainly relies on fossil fuel reforming, the economic viability of H_2 production from water electrolysis is expected to improve with advancements in renewable energy technologies.

2.1.2 Hydrogen production from water-splitting

Water splitting involves breaking down water molecules into H_2 and O_2:

$$H_2O(l) \rightarrow H_2(g) + 0.5O_2(g),\ \Delta H^0 = 285.85\ \text{kJ/mol, 298 K.} \qquad (2\text{-}1)$$

Several water-splitting technologies are available, including direct thermal water splitting, thermochemical water splitting, photocatalysis and electrolysis (Wentorf Jr and Hanneman 1974, Goldstein *et al.* 2005, Barbarossa *et al.* 2006, Ni *et al.* 2007, Maeda and Domen 2010, Ping *et al.* 2018). Water thermolysis refers to the breakdown of water molecules by the action of heat (Wentorf Jr and Hanneman 1974). Noring *et al.* (1981) conducted a series of experimental studies of direct water thermolysis in a solar furnace for H_2 production. Water was injected into a solar furnace at a temperature of 2500K, and the composition of product gas was analysed. They showed that only about 4% of water was successfully converted into H_2 and O_2. In fact, the Gibbs free energy theory shows that water decomposition reaction will only become spontaneous at extremely high temperatures (>4500K) (Wentorf Jr and Hanneman 1974).

Notably, the reaction temperature of water decomposition can be remarkably reduced by introducing chemical energy. Since the pioneering work of Funk *et al.* (1966), various thermochemical water-splitting cycles have been identified and tested. Nakamura *et al.* (1977) investigated a two-step cycle using Fe_3O_4 for H_2 production from water splitting. Their proposed cycle was thermodynamically feasible despite its high temperature (2500K) requirement. Subsequently, lab-scale research on sulphur-iodine, hybrid sulphur, copper-chlorine and magnesium-chlorine cycles was reported in the literature (Struck *et al.* 1980, Lu and Ammon 1982, Sim *et al.* 1993, Simpson *et al.* 2006, Allen *et al.* 2014, Özcan and Dincer 2016, Gorensek *et al.* 2017, Özcan and Dincer 2018). Among these cycles, the sulphur-iodine cycle water-splitting system was by far the most efficient water-splitting method (Goldstein *et al.* 2005, Barbarossa *et al.* 2006, Ping *et al.* 2018). Nevertheless, achieving reasonable efficiency in thermochemical water splitting still requires high temperatures, typically exceeding 500 °C.

The photocatalytic water splitting method uses photons to decompose water molecules (Ni *et al.* 2007, Maeda and Domen 2010), and this technology has been intensively investigated in recent years (Ni *et al.* 2007, Shamim, Dincer *et al.* 2014, Mohamed *et al.* 2015, Bicer *et al.* 2017, Li 2017, Chung *et al.* 2018). The main challenges for this technique are its relatively low efficiency (about 2%) and the high cost of noble metal catalysts (Maeda and Domen 2010). The requirement for a high level of solar irradiance has also limited the industrial scale-up of this technology.

Electrolysis is a well-established technology for water splitting (Leroy 1980). The water electrolysis technique for H_2 production was first discovered in the 19th century and was soon developed for industrial scales due to the high demand for ammonia in the early 1900s (El-Emam and Özcan 2019). (Fundamentals about water electrolysis are discussed in Section 2.2 of the thesis.) Three main technologies for water electrolysis are currently available, including alkaline water electrolysis (AWE), proton exchange membrane electrolysis (PEM), and solid oxide electrolysis (SOE) (Dubey *et al.* 2010, Esposito *et al.* 2012, Fiegenbaum *et al.* 2013, Yilmaz and Kanoglu 2014, Cardoso *et al.* 2015, Lamy 2016). The working principles for the electrolysers are shown in Figure 2-3.

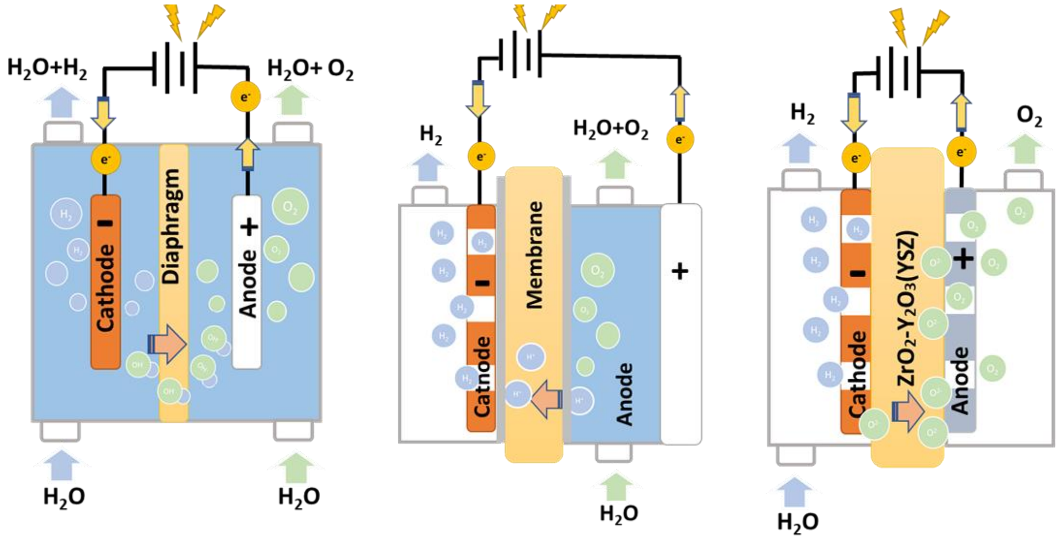

(a) (b) (c)

Figure 2-3. Working principles of (a) AWE, (b) PEM and (c) SOE.

Each technology has its benefits and drawbacks. Conventional AWE is a mature technology that utilises inexpensive materials with high durability. However, the current density of industrial AWE is limited to 0.2-0.4 A/cm^2 to achieve a reasonable efficiency (about 65%). At higher current densities, the efficiency of the AWE drops dramatically due to the bubble effect: gas bubbles cover the electrode surface and reduce its effective area, and the high gas holdup in the electrolyte significantly increases the ohmic resistance (Vogt 2012, Vogt 2017). Higher current densities can also lead to increased gas crossover, adversely affecting H_2 purity and operating safety (Marini *et al.* 2012, David *et al.* 2019). Compared to conventional AWE, the PEM can operate at higher pressures and offers a higher efficiency and power density. However, it has higher maintenance and capital costs owing to the use of noble metal and short membrane lifetime (3-5 years) (Carmo *et al.* 2013). The SOE is an emerging technology with potential for the highest efficiency among these technologies;

however, it requires a high operating temperature (>700 °C), posing challenges to the material's durability (Lo Faro *et al.* 2019). A comparison of AWE, PEM and SOE systems is provided in Table 2-1.

Presently, PEM and AWE technologies contribute to approximately 30% and 60% of the deployed capacity, respectively (Hydrogen Council 2023). The global water electrolyser capacity is projected to increase from 700 MW in 2022 to 230 GW by 2030 (Hydrogen Council 2023). This significant growth in capacity reflects the rising global demand for H_2 as an essential feedstock and a clean and sustainable energy carrier. As countries strive to meet their decarbonisation targets and reduce greenhouse gas emissions, H_2 production via water electrolysis, powered by renewable energy sources, is emerging as a promising solution.

Table 2-1. A comparison of AWE, PEM and SOE systems (Marini *et al.* 2012, Godula-Jopek *et al.* 2015, Schmidt *et al.* 2017).

	AWE	**PEM**	**SOE**
Cathode material	Ni, Ni-Mo alloys	Pt, Pt-Pd	Ni/YSZ
Anode material	Ni, Ni-Co alloys	RuO_2, IrO_2	LSM/YSZ
Current density (Acm^{-2})	0.2-0.4	0.6-2.0	0.3-2.0
Efficiency (%)	About 70%	About 75%	75-85%
Temperature (°C)	60-80	50-70	700-1000
Pressure (bar)	<30	<70	<25
H_2 purity (%)	99	99.99	99.9
Stack Lifetime (h)	90 000	20 000	10 000
Maturity	Mature	Commercial	R&D
Capital Cost (Euro/kW)	1000-1200	1860-2320	2000 (estimated)
Advantages	Low capital cost and high durability	Compact, high pressure and high efficiency	Very high efficiency
Challenges	Corrosive electrolyte and low current density	High material and maintenance cost	Material durability

2.1.3 Hydrogen purification

The composition and concentration of impurities within H_2 vary based on the method by which H_2 is produced. In the case of steam methane reforming, H_2

purity typically ranges from 75% to 80%. The primary impurities include CO_2, CH_4, CO and N_2 (Barelli *et al.* 2008, Dawood *et al.* 2020). In contrast, coal gasification can yield a higher H_2 purity level (85%-95%), with impurities such as CO_2, CO, N_2 and H_2S persisting (Barelli *et al.* 2008, Loutzenhiser and Muroyama 2017). In contrast, H_2 produced from water electrolysers can have exceptional purity levels (>99%), and the only impurities typically present in the H_2 gas are O_2 and water vapour (Diogo *et al.* 2013).

H_2 purity requirements are dependent on the endpoint applications. Generally, H_2 with relatively low purity (about 98%) is well suited for applications such as combustion engines and direct reduction of iron (Yip *et al.* 2019, Wang *et al.* 2021). In contrast, fuel cell technology, chemical synthesis, and spaceship engines necessitate elevated purity grades (>99.95%) (Du *et al.* 2021, Luberti and Ahn 2022). Ultra-high purity of H_2 (>99.999%) is often required for semiconductor applications (Dawood, Anda *et al.* 2020). In addition, the presence of particular impurities is of significant concern. For example, in PEM fuel cells, even trace contaminates such as H_2S (0.004 ppm), CO (0.2 ppm) and CO_2 (2 ppm) can lead to catalyst poisoning and significantly undermine their overall performance (Murugan and Brown 2015).

Hydrogen purification system aims to separate H_2 from other gases. Pre-treatment of crude H_2 often involves employing chemical absorption-based processes or cryogenic distillation to achieve >95% purity (Luberti and Ahn 2022). Following pre-treatment, the enriched H_2 gas can be further purified using more advanced technologies, including pressure swing adsorption (PSA), metal hydrides, selective membrane, catalytic oxidation and cryogenic separation (Yue *et al.* 2021, Amin *et al.* 2023).

- **Pressure swing adsorption**

PSA system employs porous absorbents such as activated carbon, zeolite molecular sieve and hydroxyl aluminium silicate clay (HAS-Clay) to extract impurities from H_2 gas (Luberti and Ahn 2022). In the PSA process, the H_2 feed gas is introduced in an absorbent vessel at ambient pressure. As the pressure of the vessel increases, impurity gases with a higher affinity for the absorbent materials than H_2 become entrapped within the adsorbent matrix. This selective capture process results in the purification of H_2 gas. Once the adsorbent reaches its maximum capacity, the purified H_2 is collected from the adsorbent vessel, and the impurities in the adsorbent material are released by depressurising the vessel.

For PSA technology, the selection of absorbent materials is critical, as they have different adsorption affinities for distinct gases. For instance, activated carbon is an excellent absorbent for removing hydrocarbons. However, it is notably less efficient in removing impurities such as H_2O and N_2. Zeolites show efficient adsorption of hydrocarbons; however, CH_4 stands as an exception (Du *et al.* 2021). Furthermore, optimising process design and developing novel high-performance adsorbents are recognised as the pathways for enhancing PSA performance process (Xiao *et al.* 2018, Zhang *et al.* 2021).

- **Metal hydride**

Metal hydride technology employs specific metals and alloys to achieve H_2 purification. The use of $LaNi_5$, ZrCo and TiFe, as well as rare earth metals like yttrium (Y), palladium (Pd) and neodymium (Nd) for H_2 purification are currently under research and development (Bellosta *et al.* 2019, Amin *et al.* 2023). For H_2 purification, the H_2-rich gas is introduced into a metal hydride reactor under elevated pressures. Here, the metal selectively reacts with H_2 to form metal hydride compounds, while the impurities remain unbound and are subsequently vented off. The purified H_2 is retrieved by depressurising and heating the reactor. The current research on metal hydride focuses on improving H_2 recovery rate and discovering new materials. Notably, metal hydride technology is also a promising pathway for H_2 storage (Blinov *et al.* 2021).

- **Permeable membrane**

Membrane technology has become a prominent method for the separation and purification of H_2. This process utilises selectively permeable membranes as the separation medium, which are typically based on Pd, V, Y, Zr, or Ni alloys. When in contact with these membranes, H_2 molecules can dissociate into protons and electrons. These charged particles pass through the film and subsequently recombine on the other side to form H_2 (Pacheco *et al.* 2020). Larger molecules, including impurities like CO_2, N_2, O_2, and CH_4, are effectively blocked due to their size. Non-metallic materials, such as polymers and graphene, are also under investigation for H_2 purification applications (Amin *et al.* 2023). However, significant pressure drops, high costs, and limited membrane lifespans have hindered the broader industrial adoption of this technology.

- **Catalytic oxidation**

Catalytic oxidation is a newly emerged technology for the purification of H_2 produced from water electrolysers. This technique can effectively remove O_2 by recombining it with H_2 to form water. This reaction is promoted by a catalyst such as Pd- and Pt-based alloys (Kim *et al.* 2022). These catalysts have a strong affinity to H_2 and O_2, which can remarkably reduce the reaction's activation energy. The prominent benefit of catalytic oxidation is that it does not consume external energy compared with other H_2 purification techniques. This has made the catalytic oxidation receive considerable research attention (Ge *et al.* 2012). However, the drawbacks of such technology are prominent. The excessive formation of water can block the catalyst layer and degrade reactor effectiveness (Kim *et al.* 2020). Also, the reaction of water formation is highly exothermic, which can create hot spots on the surface of catalyst, causing ignition and embrittlement of catalyst particles (Chen *et al.* 2013).

- **Cryogenic cooling**

The cryogenic cooling technique separates gases according to their different boiling points (as shown in Table 2-2) (Don and Robert 2008). This concept has been widely used in refineries to separate H_2 from other gases (Aasadnia *et al.* 2021). To purify H_2 produced from fossil fuels, it is essential to remove CO_2, CH_4 and H_2O from the H_2-rich gas by pre-cooling system, as they will solidify and clog the equipment at low temperatures (<90K) (Aasadnia *et al.* 2021). After decreasing the temperature to about 75K, the majority of the impurities in the H_2 gas will become a liquid, and the H_2 gas is consequently separated. However, there is still a portion of impurities that remain as saturated vapour in the H_2. Further decreasing the cooling temperature can achieve a higher purity of H_2, but it will result in higher energy consumption.

In conclusion, the pathway of H_2 purification greatly depends on the method of production and the composition of raw H_2 gas. Techniques such as pressure swing adsorption, metal hydrides, permeable membranes, catalytic oxidation, and cryogenic cooling offer unique advantages and challenges in achieving the desired purity levels for specific applications.

Table 2-2. Boiling and melting points for H_2 and impurities at 1 atm (Don and Robert 2008).

Compound	Boiling point (K)	Melting point (K)
Water (H_2O)	373	273
Propane (C_3H_8)	231	86
Carbon dioxide (CO_2)	195	-
Ethane (C_2H_6)	185	101
Methane (CH_4)	112	90
Oxygen (O_2)	90	55
Argon (Ar)	87	84
Carbon monoxide (CO)	82	68
Nitrogen (N_2)	77	63
Hydrogen (H_2)	20	13
Helium (He)	4	-

2.1.4 Hydrogen transportation

Currently, the majority of H_2-producing infrastructures are constructed close to the consumer. With the increasing demand, H_2 trading has vigorously grown in recent years, necessitating its mass transportation. Gaseous H_2 at atmospheric temperature and pressure has a very low volumetric energy density (11 kJ/L), making it economically unfeasible for transportation unless it is pressurised or liquified, as shown in Figure 2-4. In other cases, H_2 needs to be transformed into other chemicals (such as liquid organic H_2 carriers or ammonia) before being shipped economically (Modisha *et al.* 2019, Lucentini *et al.* 2021, Wan *et al.* 2021).

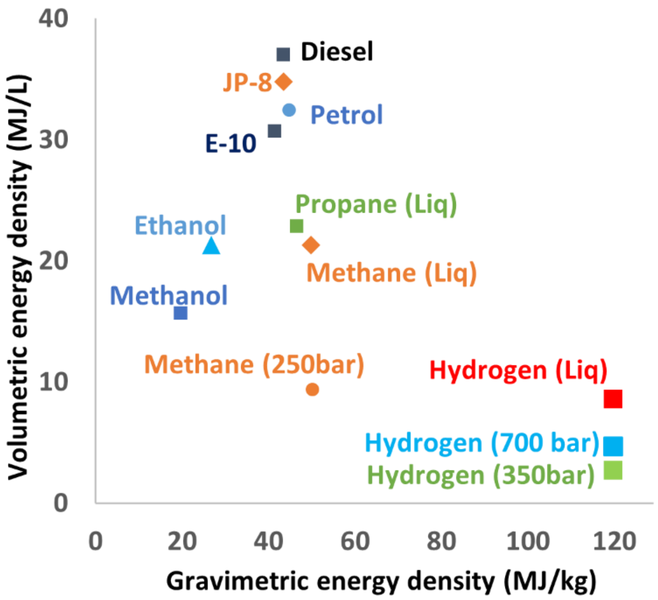

Figure 2-4. Energy densities for various fuels based on their lower heating values (Hydrogen and Fuel Cell Technologies Office, Pistidda 2021).

The scale of the H_2 demand is the primary consideration for the type of transport. For consumers with relatively small H_2 demands, delivering gaseous H_2 in pressurised cylinders with container trailers is a viable option (Gim *et al.* 2012, Zohuri 2019). This approach offers flexibility and can cater to various locations, making it suitable for dispersed or remote consumers. However, it may not be as cost-effective for larger-scale demands due to the limitations of truck capacity and the associated transportation costs. Notably, gaseous H_2 can also be delivered through pipelines to consumers with large demand (Sun and Frank Cheng 2022, Erdener *et al.* 2023).

Liquid H_2 (LH_2) offers a high volumetric energy density, making it well-suited for consumers with medium-sized H_2 requirements. Currently, most of LH_2 is transported by thermo-insulated cryogenic vessel trailers. Furthermore, transporting LH_2 by large cargo ship is applicable but still a challenging task (Johnston *et al.* 2022). However, producing LH_2 is an energy-intensive process: it must be cooled to cryogenic temperatures (20K) at about 9 bar before being filled into the trailer. The specific energy consumption associated with liquid hydrogen production is substantial, accounting for at least 35% of its lower heating value (Al Ghafri *et al.* 2022). Additionally, the transportation of LH_2 presents further challenges, as a significant portion of H_2 is lost due to boil-off, which substantially escalates transportation costs (Zohuri 2019, Al Ghafri *et al.* 2022). Therefore, converting H_2 into ammonia or other carrier fluids could be a more efficient method for long-distance transportation (Modisha *et al.* 2019, Wan *et al.* 2021).

2.1.5 Hydrogen liquefaction

Hydrogen liquefaction is the conversion of gaseous H_2 into its liquid state. In an industrial H_2 liquefaction plant, liquid hydrogen (LH_2) is achieved by cooling H_2 to approximately 20K under a pressure of 10 bar. The Claude cycle is one of the conventional techniques for H_2 liquefaction (Barron 1966). The main process of a simple Claude cycle for LH_2 production includes the compression and pre-cooling, Ortho-to-Para conversion and H_2 liquefaction, as illustrated in Figure 2-5 (Al Ghafri *et al.* 2022).

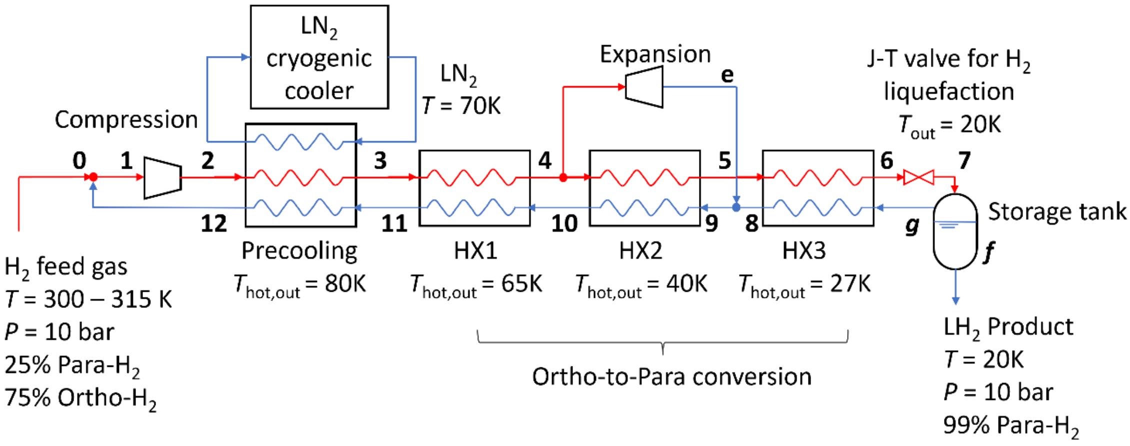

Figure 2-5. Schematic flow diagram of a simple Claude cycle for H_2 liquefaction (Yang *et al.* 2023).

The temperature-entropy (T-S) diagram of the ideal simple Claude cycle is provided in Figure 2-6. H_2 feed gas is firstly compressed before being pre-cooled to approximately 80K by an external cooling system, typically a liquid N_2 (LN_2) cryogenic cooler. Then, the pre-cooled H_2 is further cooled down via a series of heat exchangers (HX1, HX2 and HX3).

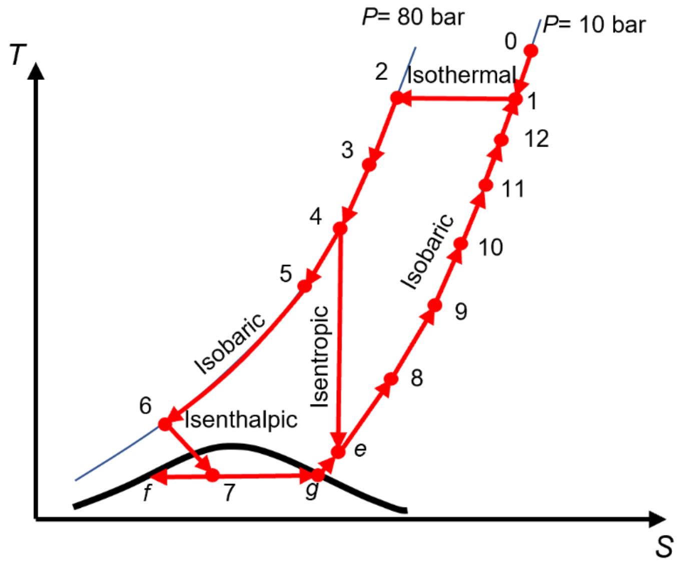

Figure 2-6. T-S diagram of a simple Claude cycle for hydrogen liquefaction.

The liquefaction of H_2 occurs at the Joule-Thomson valve (J-T valve), where the pressure of H_2 drops significantly, and the temperature is consequently cooled to 20K. Intermediate extraction is employed to improve system efficiency, where a stream of H_2 is directed through a turbine and subsequently combined with the vapour emanating from the LH_2 storage tank. This vapour, in a feedback loop, is channelled back through the heat exchangers, cooling the incoming gaseous H_2. The exhaust vapour H_2 then merges with the incoming feed gas at the inlet of the cooling cycle.

Theoretically, to produce LH_2 from a simple Claude cycle, the minimum specific energy consumption is about 22 kWh/kg_{H2} (Al Ghafri *et al.* 2022). In recent years, a few variations have been developed to enhance system efficiency. The modern state-of-the-art system, incorporating dual compression, optimised heat exchangers, helium refrigeration cycle and dedicated intermediate extraction systems, has been shown to achieve a specific energy consumption of about 13-18 kWh/kg_{H2} (Krasae-in *et al.* 2010, Yin and Ju 2020).

2.2 Alkaline water electrolysis

2.2.1 Alkaline water electrolysis principle

Figure 2-7 presents the basic components of an alkaline water electrolyser (AWE), which consists of a power supply, an electrolyte, an anode, a cathode, and a diaphragm (commonly a membrane for modern systems) (Cossar *et al.* 2022, Hua *et al.* 2022). A direct current (DC) power source is utilised to facilitate the movement of electrons from the anode to the cathode, where they interact with hydrogen ions to produce H_2 gas. Simultaneously, hydroxide ions migrate through the separator towards the anode.

The electrochemical reactions on the cathode and anode sides are:

Cathode: $\mathrm{H_2O + 2e \rightarrow H_2 + 2OH^-}$, (2-2)

Anode: $\mathrm{2OH^- \rightarrow 0.5O_2 + H_2O + 2e}$. (2-3)

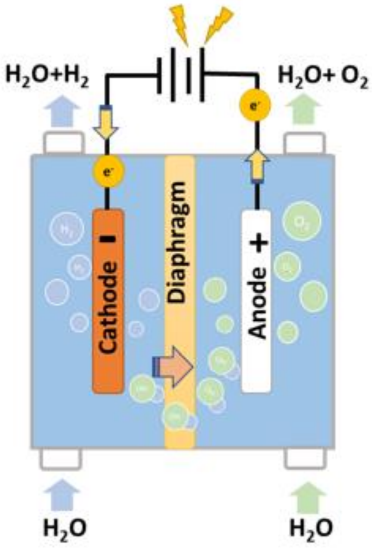

Figure 2-7. Schematic diagram of water electrolysis system (Zeng and Zhang 2010).

The resistances in the electrolyser circuit are caused by the electrochemical reactions, activation energies and the electrical resistance in the circuit, electrode, and electrolyte, as shown in Figure 2-8.

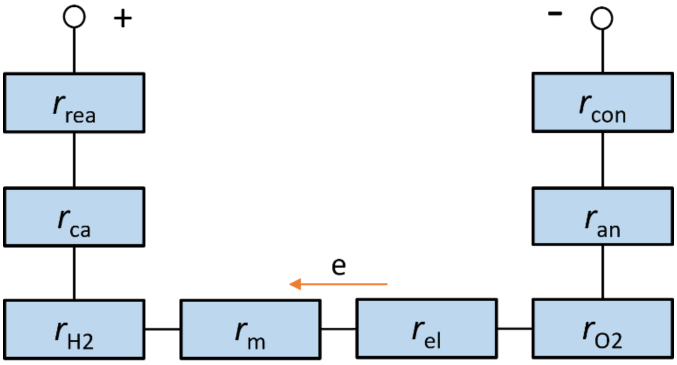

Figure 2-8. Electrical circuit analogue of a water electrolysis system (Aikens 1983).

The total resistance can be expressed as (Zeng and Zhang 2010):

$$r_{\mathrm{Total}} = r_{\mathrm{rea}} + r_{\mathrm{ca}} + r_{\mathrm{H_2}} + r_{\mathrm{m}} + r_{\mathrm{el}} + r_{\mathrm{O_2}} + r_{\mathrm{an}} + r_{\mathrm{con}}\,. \qquad (2\text{-}4)$$

In this equation, r_{rea} is the resistance for water splitting reaction, r_{ca} and r_{an} are caused by the activation energy of H_2 and O_2 formation, respectively. The $r_{\mathrm{H_2}}$ and $r_{\mathrm{O_2}}$ are the resistances due to the gas bubbles. The r_{m} and r_{el} are the resistances from electrolyte and membrane, respectively. The r_{con} is the resistance due to the concentration gradient of ions near the electrode (Diogo *et al.* 2013, Godula-Jopek 2015). Using Ohm's Law, the cell voltage (V_{cell}) can be written as the sum of the reaction potential (V_{rea}), ohmic overpotential (V_{ohmic}), activation overpotential (V_{act}), and concentration overpotential (V_{con}):

$$V_{\mathrm{cell}} = V_{\mathrm{rea}} + \underbrace{(V_{\mathrm{ca}} + V_{\mathrm{an}})}_{V_{act}} + \underbrace{(V_{\mathrm{m}} + V_{\mathrm{el}} + V_{\mathrm{H_2}} + V_{\mathrm{O_2}})}_{V_{ohmic}} + V_{\mathrm{con}}\,, \qquad (2\text{-}5)$$

The reaction potential accounts for the energy that drives the splitting reaction:

$$V_{\mathrm{rea}} = {-\Delta G}/{nF} \, , \tag{2-6}$$

where ΔG is the Gibbs free energy (kJ/mol), F is the Faraday constant (96485 c/mol), and n is the number of moles of electrons (n=2 mol for water electrolysis) (Aikens 1983). The reaction potential can be calculated according to the Nernst equation (Abdin *et al.* 2017):

$$V_{\mathrm{rea}} = V^0 + (T - T^0) \times \frac{\Delta S^0}{nF} + \frac{RT}{2F}\left[\ln\left(\frac{p_{\mathrm{H_2}}\sqrt{p_{\mathrm{O_2}}}}{a_{\mathrm{H_2O}}}\right)\right] . \tag{2-7}$$

In this equation, V^0, T^0 and $\frac{\Delta S^0}{nF}$ stands for the reaction potential, temperature and standard state entropy change (-0.9×10^{-3} J/(mol·K)$^{-1}$) at 298K and 1 atm. R is the gas constant, 8.314 J/(mol·K). $p_{\mathrm{H_2}}$ and $p_{\mathrm{O_2}}$ are the partial pressure of H_2 and O_2, respectively and $a_{\mathrm{H_2O}}$ is the water activity.

The activation overpotentials can be calculated according to the Butler-Volmer equation (Bessarabov and Millet 2018):

$$V_{\mathrm{ca}} = \frac{RT}{\alpha_{\mathrm{ca}}F}\ln\left(\frac{j}{j_{\mathrm{ca}}(1-\theta)}\right) , \tag{2-8}$$

$$V_{\mathrm{an}} = \frac{RT}{\alpha_{\mathrm{an}}F}\ln\left(\frac{j}{j_{\mathrm{an}}(1-\theta)}\right) , \tag{2-9}$$

where α_{ca} and α_{an} stand for the charge transfer coefficient for the cathode and anode, respectively. j is the current density (A/m^2), and j_{ca}, j_{an} are the effective exchange current densities for cathode and anode (A/m^2), respectively (Bessarabov and Millet 2018). The term $(1-\theta)$ accounts for the bubble coverage (θ) over the electrode, which is empirically solved as (Vogt 2012):

$$\theta = \left[-97.25 + 182\frac{T}{T_0} - 84\left(\frac{T}{T_0}\right)^2\right] \times \left(\frac{j}{j_{\mathrm{lim}}}\right)^{0.3} \times \frac{P}{P - P_{\mathrm{H_2O}}^{\mathrm{SAT}}} , \tag{2-10}$$

Where j_{lim} is the limiting current density (300kA/m^2). P is the pressure (Pa), and $P_{\mathrm{H_2O}}^{\mathrm{SAT}}$ is the saturation pressure of water (Pa).

For AWE, it is normally assumed the ohmic overpotential is proportional to the current in the circuit (I):

$$V_{ohmic} = I\left(r_{\mathrm{H_2}} + r_{\mathrm{m}} + r_{\mathrm{el}} + r_{\mathrm{O_2}}\right) , \qquad (2\text{-}11)$$

The resistance of the membrane r_{m} is calculated as:

$$r_{\mathrm{m}} = \frac{\delta_{\mathrm{m}}}{k_{\mathrm{m}} A}, \qquad (2\text{-}12)$$

where δ_{m} , k_{m} and A are the thickness, the electrical conductivity, and area of the membrane, respectively. Consider the H_2 and O_2 bubbles, the sum of the electrolyte resistance (r_{el}) and the bubble resistance ($r_{\mathrm{H_2}} + r_{\mathrm{O_2}}$) can be calculated using Bruggeman's equation (Rue and Tobias 1959, Tjaden *et al.* 2016):

$$r_{\mathrm{el}} + r_{\mathrm{H_2}} + r_{\mathrm{O_2}} = \frac{\delta_{\mathrm{el}}}{(1-\varphi)^{1.5} k_{\mathrm{el}} A} , \qquad (2\text{-}13)$$

where φ is the void fraction of electrolyte. δ_{el} is the thickness of the electrolyte, defined as the spacing of the electrodes minus δ_{m} , and k_{el} is electrolyte conductivity.

The concentration overpotential is often expressed as (Abdin *et al.* 2017):

$$V_{\mathrm{con}} = \frac{RT}{4F}\left(2\ln C'_{\mathrm{ca}} + \ln C'_{\mathrm{an}}\right) , \qquad (2\text{-}14)$$

where C'_{ca} and C'_{an} are the concentration gradient of OH$^-$ at the vicinity of electrode. However, under normal operating conditions (0.2-0.4 A/cm2), the concentration overpotential is typically negligible when compared to other overpotentials. The cell voltage under different current densities for an AWE is shown in Figure 2-9.

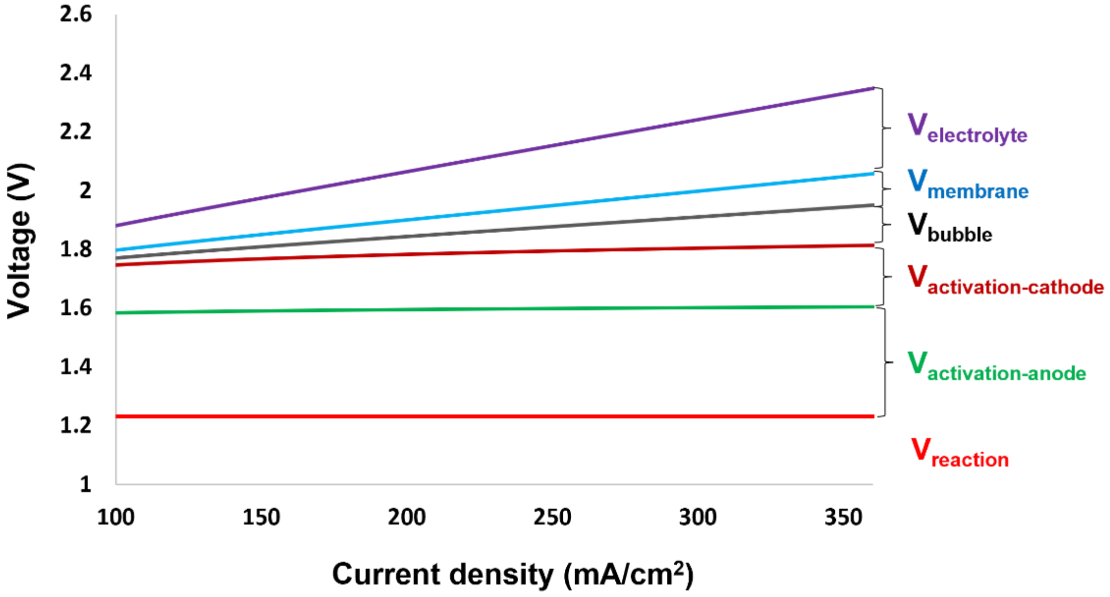

Figure 2-9. The polarisation curve of an alkaline water electrolyser at different current densities. Contributions of reaction potential and other overpotentials are shown. The parameters of the electrolyser are referenced from Abdin *et al.* (2017).

The Faradic efficiency of the cell is expressed as (Abdin *et al.* 2017):

$$\eta = V_{\mathrm{rea}}/V_{\mathrm{cell}}. \tag{2-15}$$

As can be seen, the key to increasing water electrolyser efficiency is to minimise the cell voltage. Intensive studies have been conducted to enhance water electrolyser efficiency by minimising activation and ohmic overpotentials. The incorporation of catalysts (Wang *et al.* 2021, Xu *et al.* 2021) and porous electrodes (Rajaei *et al.* 2021, Hodges *et al.* 2022) have been demonstrated to substantially reduce activation overpotentials. Although these aspects are vigorously investigated, they fall outside the scope of the current research.

To minimise the ohmic overpotential from the electrolyte, industrial AWE cell utilises a 30 wt% KOH aqueous solution as the preferred electrolyte, offering numerous advantages over alternatives including NaOH and acidic solutions. These include exceptional electrical conductivity, optimal chemical stability, commercial availability and excellent electrode compatibility (David *et al.* 2019, Brauns and Turek 2020). On the other hand, the recent advancements in anion exchange membrane technology have resulted in rapid development, offering membranes with high electrical conductivity (0.04-0.13 S/cm) and reduced thickness (25-100μm) (Cossar *et al.* 2022, Hua *et al.* 2022) to further decrease ohmic overpotential.

Optimising the cell design of AWE has become a subject of growing interest in research. For instance, some works focus on optimising the spacing between the anode and cathode in a conventional AWE setup. Early studies have involved analytical modelling to analyse the distribution of void fraction along the electrode (Nagy 1976, Vogt 1983). These investigations aim to enhance the overall performance and efficiency of AWE systems through a better understanding and optimisation of their cell design. Following these studies, Nagai and other researchers conducted experimental investigations and revealed that the optimal electrode spacing for AWE typically ranges between 2-5 mm (Nagai *et al.* 2003, Nagai *et al.* 2003, Nagai *et al.* 2006). The specific spacing is influenced by current density, electrode height, electrode surface wettability, and electrode inclination.

Recently, novel cell designs, including the zero-gap electrolyser (Kraglund *et al.* 2016, Haverkort and Rajaei 2021), membrane-free electrolyser (Hashemi *et al.* 2015, Holmes-Gentle *et al.* 2017) and bubble-free electrolyser (Tiwari *et al.* 2019, Tsekouras *et al.* 2021) have been proposed. These innovative designs show great promise for operating at high-efficiency levels, primarily due to their ability to substantially reduce the ohmic overpotential and effectively manage bubble coverage over the electrodes. Recent advances in membrane-free electrolysers are detailed in Chapter 2.3 of this thesis.

Another noteworthy strategy is to raise the operating pressure and temperature of the electrolyser. Increasing operating temperature can lead to a reduction in activation energy and higher electrical conductivity of the electrolyte, resulting in reduced activation and ohmic overpotentials, ultimately enhancing cell efficiency. However, it is essential to consider that operating the electrolyser at temperatures above 80 °C may pose a challenge as it could render the membrane vulnerable. On the other hand, elevating the operating pressure offers advantages such as facilitating the pressurisation or liquefaction of H_2 gas for transportation. Additionally, according to Henry's law, both H_2 and O_2 gas solubility increase with rising pressure. Consequently, high-pressure AWE systems can potentially exhibit a lower ohmic overpotential due to reduced void fraction in the electrolyte. However, it's crucial to consider the trade-offs, as higher pressure may also lead to increased gas crossover, potentially affecting H_2 purity and causing membrane degradation issues (Salehmin *et al.* 2022, Solovey *et al.* 2022).

2.2.2 Ionic species transport

The ionic species transport in a water electrolysis cell occurs through the following three mechanisms: migration, diffusion and convection (Aikens 1983). Migration refers to the movement of ions within the electrolyte under an electrical field. The velocity of the ions subjected to an electric field is known as the migration velocity (Haring 1936):

$$v_m = -zu\mathrm{F}\nabla\Phi. \tag{2-16}$$

Here, z is the number of electronic charges on the ion. F is the Faraday constant (96485 c/mol). Φ is the electric potential (V), and u is the mobility of ion ($m^2s^{-1}V^{-1}$). The mobility of ions is described by Einstein's relation (Haring 1936):

$$u = \frac{D}{\mathrm{k_B}T}. \tag{2-17}$$

In this equation, $\mathrm{k_B}$ is Boltzmann's constant (1.38×10^{-23}J/K), T is the absolute temperature (K), and D is the diffusion coefficient (m^2/s). The migration flux density ($kg/m^2\cdot s$) is given by (Aikens 1983):

$$J_m = cv_m = \frac{-zcD\mathrm{F}\nabla\Phi}{\mathrm{k_B}T}. \tag{2-18}$$

Diffusion is the movement of a species from the regions of high concentration to the regions of low concentration. In a water electrolyser, the mass transfer due to diffusion dominates at the gas diffusion layer near the electrode. The diffusive flux is given by Fick's first law (Aikens 1983):

$$J_d = -D\nabla c\,. \tag{2-19}$$

Convection is the movement of a species due to fluid dynamic forces. Industrial water electrolysers are commonly equipped with an electrolyte circulation system, where forced convective mass transfer is present, making convection the predominant mode of mass transport in the electrolyser channels (Jang and Gan 2018). The equations describing fluid convection are governed by continuity and Naiver-Stokes equations:

$$\frac{\partial\rho}{\partial t} + \nabla(\rho\vec{v}) = 0 \tag{2-20}$$

$$\rho\left(\frac{\partial\vec{v}}{\partial t} + \vec{v}\nabla\vec{v}\right) = -\nabla p + \mu\nabla^2\vec{v} + f, \tag{2-21}$$

where $\vec{v}$ is the velocity of the fluid (m/s), ρ is the density of the fluid (kg/m^3), p is the pressure (Pa), and μ is the fluid viscosity (Pa·s). The convective flux density (J_c) (kg/m^2·s) of a species is given by (Nikonenko *et al.* 2009):

$$J_c = c\vec{v}\,. \tag{2-22}$$

The net flux (kg/m^2·s) of one ion species in an electrolyte given by the Nernst-Planck equation, where migration, diffusion and convection terms are combined (Kodým *et al.* 2016):

$$J = J_m + J_d + J_c = \frac{-zcD\mathrm{F}\nabla\Phi}{\mathrm{k_B}T} - D\nabla c + c\vec{v}\,. \tag{2-23}$$

Due to the neutrality of electrolyte, the convective term for mass transfer in the electrolyte bulk is often omitted (Kodým *et al.* 2016). The forced convection of the electrolyte flow will not change the distribution of electric field, and it has no contribution to the migration mass transfer either. Convection can influence the concentration gradient of ions in the vicinity of electrode and the thickness of diffusion layer. It can also cause mixing of the electrolyte, which can affect the concentration gradient and serve as an effective means to bring reactants to the electrode surface.

Different empirical equations for the Sherwood number (Sh) in an electrolyser were presented in the literature (Aikens 1983, Vogt 1983, Riegel *et al.* 1998) in the form of:

$$Sh = \frac{h}{D/L} = aRe^{b}Sc^{c}k_{\varphi}\,, \tag{2-24}$$

where h, D and L are the convective mass transfer coefficient (m/s), mass diffusivity (m^2/s), and characteristic length (m), respectively. The parameters a, b and c depend on the flow regimes and electrolyser structure, and they range from 0.02-0.04, 0.7-1.2, 0.3-0.5, respectively (Aikens 1983, Vogt 1983, Riegel *et al.* 1998). Some recent studies suggest the use of additional factor k_{φ} to correlate Sh for the existence of gas bubbles (Vogt 2016); however, no widely accepted model has been reported in the literature yet.

2.2.3 Void fraction and current density distribution

Industrial alkaline water electrolysers commonly employ a vertical displacement configuration, where bubbles generated at the electrode surfaces ascend within the electrolyser channel. As gas accumulation occurs, the void fraction increases along the length of the channel (Figure 2-10). Consequently, this uneven distribution of void fraction leads to a nonuniform current density distribution along the electrode. The distribution of void fraction and current density is critical to the performance of water electrolysers (Eigeldinger and Vogt 2000, Nagai *et al.* 2003).

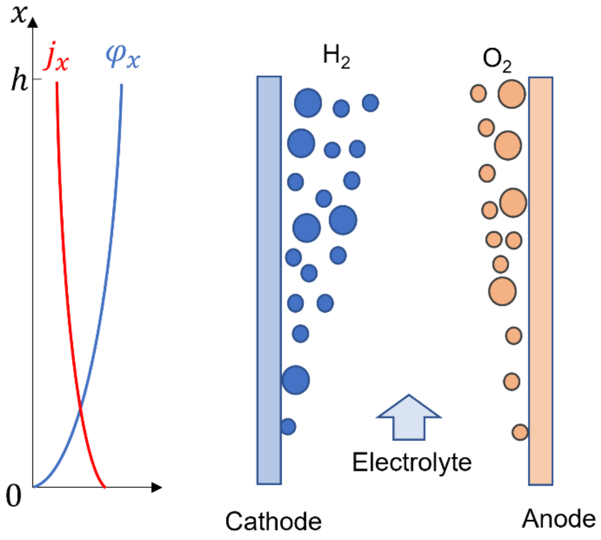

Figure 2-10. The distribution of current density (j_x) and void fraction (φ_x) in an AWE. The separator is not shown for clarity (Eigeldinger and Vogt 2000, Nagai *et al.* 2003).

Tobias (Tobias 1959) conducted a theoretical study into the current density and void fraction distribution of a vertical water electrolysis cell. Based on a one-dimensional mathematical model, Tobias quantitatively evaluated the impact of gas evolution on current density distribution and cell voltage in an electrolyser without electrolyte circulation. Later, Nagy *et al.* (1976) investigated the current density distribution of an electrolyser with a stagnant electrolyte. Drawing from Tobias' model (Tobias 1959), they studied the effect of electrode geometry, gas bubble rise velocity, polarisation resistance, and electrolyte conductivity on the current density distribution.

Vogt (Vogt 1983) took a step forward by refining the previously proposed analytical models in order to predict the current density distribution in a water electrolyser with a circulating electrolyte. In his work, the bubble rising velocity (v_g) is calculated using the average rising velocity of the bubble swam (v_r), and the flow velocity of the liquid entraining the swam is correlated by void fraction:

$$v_g = v_r(1-\varphi_x)^4 + \frac{V_L}{\delta w(1-\varphi_x)}, \tag{2-25}$$

where φ is the void fraction, V_L is the volumetric flow rate of electrolyte (m/s), δ is the space between electrodes (m), and w is the width of electrode (m). If the total height of the electrode is h, the current density at x of the electrode ($0 < x < h$) is:

$$j_x = \nabla\Phi k_{\mathrm{el}}\delta\left(1 + C_1\frac{x}{h}\right)^{-3}, \tag{2-26}$$

where $\nabla\Phi$ is the voltage over the electrodes (V), and k_{el} is the conductivity of electrolyte (S/m)). The distribution of the void fraction is:

$$\varphi_x = 1 - \left(1 + C_2\frac{x}{h}\right)^{-2}. \tag{2-27}$$

The dimensionless parameters C_1 and C_2 are:

$$C_2 = \frac{\nabla\Phi k_{\mathrm{el}}h}{2v_g\delta^2}C_1, \tag{2-28}$$

$$C_1 = \frac{\mathrm{R}T\varepsilon}{p\mathrm{F}n}, \tag{2-29}$$

where p is the operating pressure (Pa), and T is the temperature (K). R represents the gas constant (8.3145 J/mol·K). F is the Faraday constant (96485 c/mol). ε/n is the number of charges per mole of gas (c/mol).

2.3 Membrane-free water electrolyser

Recent studies have focused on developing electrolysers without membranes, with the goal of improving cell efficiency and lowering both capital and maintenance costs. Also, by eliminating the membrane, a membrane-free water electrolyser (MFE) has the potential to operate at elevated temperature and pressure, which can improve cell efficiency and facilitate the pressurisation or liquefaction of H_2 for further transportation. In the literature, flow-through and flow-by cell designs are the two of the most investigated concepts of MFE.

2.3.1 Flow-through design

Figure 2-11 shows the cell structure of a flow-through membrane-free water electrolyser (MFE). The key feature of the flow-through electrolyser is that the cathode and anode are porous and installed in separate channels. The electrolyte passes through the porous electrode and carries the evolved bubbles downstream, by which the H_2 and O_2 are separated.

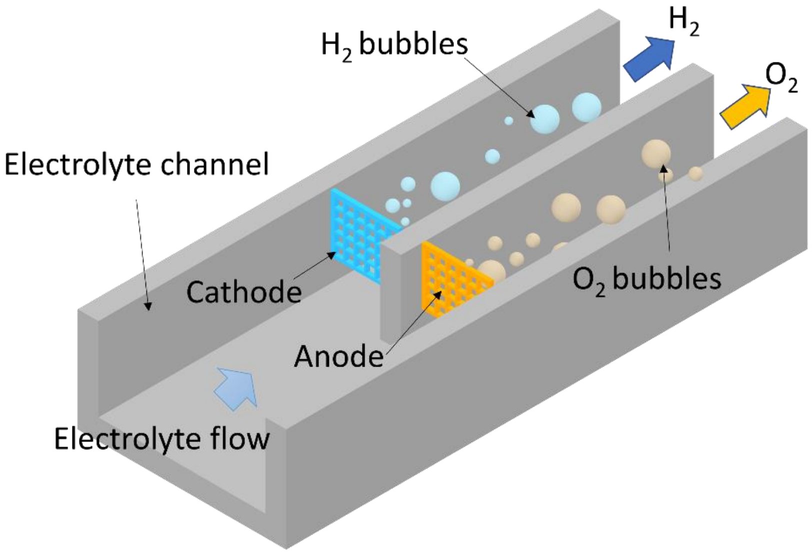

Figure 2-11. The concept of flow-through MFE. The electrolyte flows through the porous electrodes in separate channels.

The concept of a porous flow-through electrode can be traced back to the 1980s, during which nickel foam emerged as an exceptional electrode material characterised by its high ratio of surface area to volume, cost-effectiveness, and catalytic properties (Langlois and Coeuret 1989, Langlois and Coeuret 1989). A number of flow-through MFEs have been developed recently, as shown in Table 2-3.

Table 2-3. A summary of the recent development of flow-through MFE for hydrogen production.

Authors	Electrode position	Maximum current density (mA/cm^2)	H_2 purity	Remarks
O'Neil *et al.* (2016)	Angled	150	-	Simple but suffers from gas crossover
Talabi *et al.* (2017)	Angled	200	-	Same as above
Davis *et al.* 2018)	Angled	40	98%	Separate bubble by buoyancy; high gas crossover >5%
Gillespie *et al.* (2015)	Parallel	4000	98.98%	High H_2 purity but low efficiency due to pumping power
Gillespie and Kriek (2017)	Parallel	2500	90.50%	Same as above
Gillespie and Kriek (2018)	Parallel	4000	99.81%	Same as above
Rajaei *et al.* (2021)	Parallel	-	-	Correlation for optimising DEFT-like cells

In the works of Talabi, O’Neil and others (O'Neil *et al.* 2016, Talabi *et al.* 2017), flow-through MFE using mesh electrodes and parallel H_2 and O_2 channels were presented (Figure 2-12a). Although their design is simple and scalable, gas crossover in their MFE is prominent, particularly at high current densities and low electrolyte velocities. On the other hand, the divergent electrode-flow-through (DEFT^{TM}) alkaline electrolyser proposed by Gillespie and other researchers is one of the popular flow-through designs in the literature, as shown in Figure 2-12b (Gillespie *et al.* 2015, Gillespie and Kriek 2017, Gillespie and Kriek 2018).

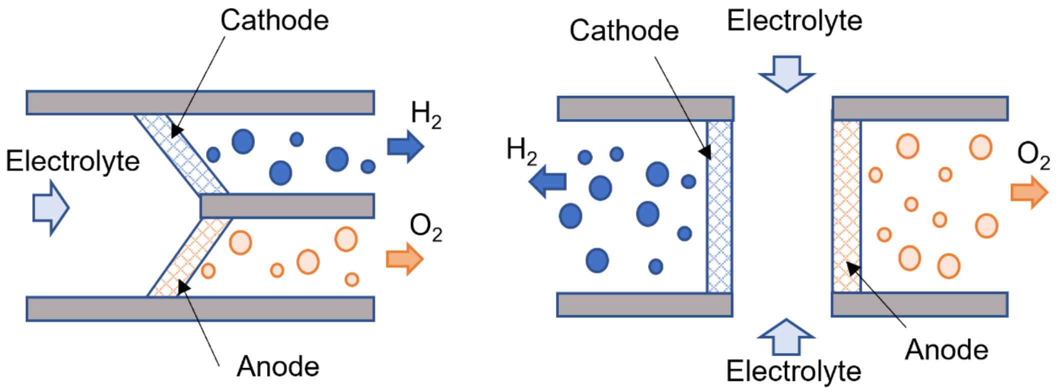

(a) (b)

Figure 2-12. Two variations of flow-through MFE. (a) Flow-through MFE developed by O'Neil *et al.* (2016) and Talabi *et al.* (2017) where the electrode is angled positioned and (b) DEFT^{TM} cell developed by Gillespie *et al.* (2015).

The DEFT^{TM} design incorporates two mesh electrodes positioned opposite and parallel to facilitate the circumferential exit of electrolyte from opposite directions. This setup offers the advantage of closely spacing the cathode and anode, effectively minimising the ohmic overpotential. In one of their studies (Gillespie *et al.* 2015), they utilised mesh electrodes with a 30 mm diameter and a spacing of 2.5 mm. At a current density of approximately 0.3 A/cm^2, the cell efficiency reached 72%, and H_2 purity was around 99.8%. To further enhance efficiency, they reduced the electrode spacing to 0.8 mm, resulting in an increased cell efficiency of 75% without significantly affecting H_2 purity. Later, they demonstrated that the scaled-up DEFT^{TM} cell stack can be operated at a nominal operating current density of 3.5 A/cm^2, a temperature of 60 °C with an H_2 purity of 99.81% and overall plant efficiency of 35% based on the higher heating value of H_2.

The drawback of the DEFT-like system is that when the spacing between the mesh electrodes is reduced, it results in an increase in pumping power. This rise in pumping power can significantly reduce the overall efficiency of the electrolyser cell. To address this, Rajaei *et al.* (2021) investigated the minimum electrolyte velocity required to ensure effective gas separation from the mesh electrode. They examined the H_2 purity from the electrolysers with various mesh sizes and electrode spacing, all operated at different voltages and flow velocities. Through a combination of analytical and experimental studies, they developed a correlation to calculate the optimal design parameters for a DEFT-like cell. This correlation determines the ideal mesh size, electrode spacing and electrolyte velocity under a specified applied voltage, which will optimise the system's performance and ensure efficient gas separation while minimising the pumping power.

2.3.2 Flow-by design

The flow-by membrane-free water electrolyser (MFE) is also a widely adopted cell design. As shown in Figure 2-13, in a flow-by MFE, the cathode and anode are positioned parallel to each other. The electrolyte passes over the electrode surfaces and carries O_2 and H_2 gas bubbles downstream. This type of electrolyser maintains a laminar flow in the electrolyser channel, where the shear-induced lift force (F_L) realise the separation of H_2 and O_2 (Segré and Silberberg 1961, Esposito 2017). The recent developments on flow-by MFE are summarised in Table 2-4.

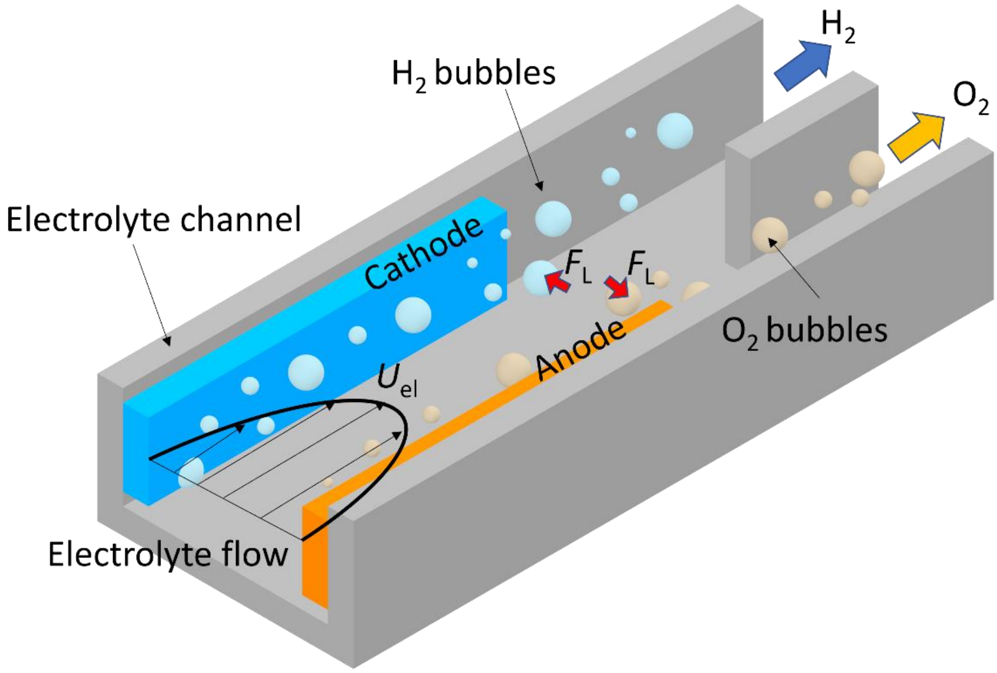

Figure 2-13. The cell structure of a flow-by MFE, where the cathode and anode are placed face-to-face in the electrolyser channel.

Table 2-4. A summary of recently developed flow-by MFE for hydrogen production reported in the literature.

Authors	Electrode position	Maximum current density (mA/cm^2)	H_2 purity	Remarks
De *et al.* (2020)	Coplanar	35	93.14%	Feed acidic catholyte and alkaline anolyte from different inlets; Low current density
De *et al.* (2021)	Coplanar	150	97.72%	High efficiency operated at 150 mA/cm^2; microfluidic device
Hashemi *et al.* (2015)	Facing	300	99.6%	High product purity; microfluidic device
Hashemi *et al.* (2019)	Facing	450	99%	High product purity from a scaled-up device
Rarotra *et al.* (2017)	Facing	-	-	Electrolysis of sea water
Pang *et al.* (2020)	Facing	-	-	Investigated the trade-offs of operating conditions and cell geometrical parameters.

The performance of a microfluidic flow-by MFE has been vigorously investigated (Hashemi *et al.* 2015, Hadikhani *et al.* 2018, Hashemi *et al.* 2019, Hadikhani *et al.* 2020, Hadikhani *et al.* 2021). The prototype microfluidic flow-by MFE consists of two electrodes positioned face-to-face at a spacing of only 105μm, which can remarkably reduce ohmic overpotential (Hashemi *et al.* 2015). In this work, acidic, neutral, and alkaline electrolytes were tested in the electrolyser. The results showed that their device can be operated at 300mA/cm^2 with a 42% power conversion efficiency and an H_2 purity of 99.6%. Subsequently, a scaled-up flow-by MFE was developed, where the electrodes (10mm long, 4mm wide) were installed in a 25 mm-long electrolyser channel with a gap of 1 mm. This device showed promising performance by achieving 99% H_2 purity at a current density of 450 mA/cm^2 and an electrolyte Reynolds number of 300.

The flow-by MFE proposed by De *et al.* (2020), De *et al.* (2021) and Samir *et al.* (2022) also adopts microfluidic design. In their device, two electrodes are coplanar positioned with a spacing of 150μm in a 0.8 mm-wide, 15mm-long electrolyser channel. Electrolytic bubbles are released from the electrode under buoyancy force and then carried downstream following the electrolyte. In one of their work (De *et al.* 2021), their electrolyser reached an H_2 purity of 97.72% when operated at a current density of 150 mA/cm^2 and a voltage of 2.2V. Similar studies on microfluidic flow-by MFE are reported by Rarotra *et al.* (2017) and Rarotra *et al.* (2021).

Pang *et al.* (Pang *et al.* 2020) investigated bubble behaviour in a flow-by MFE with a high-speed camera. This technique enables the evaluation of void fraction and bubble distribution in the electrolyser channel. In their study, the electrodes were arranged face-to-face and in parallel within a vertically oriented electrolyser channel. The study systematically examined the width of H_2 bubble plumes, closely linked to gas crossover, across various Reynolds numbers (Re), channel widths, and current densities. The trade-offs between productivity, H_2 purity, electrode spacing, current density, and cell efficiency are prominently demonstrated in their findings. Specifically, increasing current density enhances H_2 yield but reduces H_2 purity and efficiency. Conversely, decreasing electrode spacing improves cell efficiency while limiting current density due to increased gas crossover.

2.3.3 Benefits and drawbacks of MFE

The membrane-free water electrolyser (MFE) presents numerous potential advantages over its conventional counterparts. To begin with, its distinct design eliminates the need for intricate membranes, setting it apart from conventional proton exchange membrane electrolysis (PEM) and alkaline water electrolysis (AWE) systems. Unlike these systems, an MFE is characterised by its simplicity, comprised solely of a channel, anode, and cathode, without the mandatory requirement of a gas separator. This starkly contrasts with PEM systems, which involve the incorporation of bipolar plates, membranes, gas diffusion layers, gaskets, ionomers, and current collectors (Carmo *et al.* 2013, Abbasi *et al.* 2019). Notably, the decreased number of components leads to lower manufacturing costs. This outcome stems from the diminished requirement for intricate assembly processes, thereby fostering greater cost-efficiency. Moreover, the simplified design affords enhanced flexibility in the selection of construction materials (Bui *et al.* 2020).

Another notable advantage of the MFE lies in its exceptional durability, heightened resistance to impurities, and remarkable ability to withstand even the most challenging operational conditions that often prove detrimental to conventional membrane-based systems (Esposito 2017). In contrast, both AWE and PEM systems are constrained to operating within specific temperature and pressure limits, typically below 80 °C to extend the lifespan of their delicate membranes. However, the MFE exhibits a far more robust performance envelope, allowing for the exploration of higher operating temperatures and pressures (Abbasi *et al.* 2019, Brauns and Turek 2020).

The expanded operational range comes with strategic advantages. Elevating the operating temperature of MFEs contributes to improved cell efficiency while eliminating the need for a cooling system, a requirement inherent to conventional systems. The associated reduction in capital costs makes this approach economically appealing. Furthermore, elevated operating temperatures also improve electrolyte conductivity, subsequently minimising the ohmic overpotential—a key contributor to energy losses in electrolysis processes. Moreover, the adoption of high-pressure operation within the membrane-free aligns with the cost-effective transportation of generated H_2. This is because high-pressure conditions facilitate the pressurisation and liquefaction of H_2, a crucial consideration for efficient and practical H_2 transportation.

The advantages of MFEs also lie in their potential to accommodate a wide variety of electrolytes. Recent studies have highlighted the adaptability of MFE to a wide range of electrolytes, including acidic, alkali, and pH-neutral types (Gillespie *et al.* 2015, O'Neil *et al.* 2016). However, conventional AWE and PEM systems are constrained by the selectivity of their membranes and consequently have limited options for electrolyte solutions.

Despite these advantages, MFE also faces a number of challenges. One of the most crucial factors is the trade-off between current density and cell efficiency, primarily attributed to the occurrence of gas crossover at elevated current densities (O'Neil *et al.* 2016, Bui *et al.* 2020). This phenomenon can significantly hinder electrolyser efficiency. The scaling-up of microfluidic electrolysers is also challenging. Further research is vital to overcome these limitations. Specifically, the development of novel cell designs that minimise gas crossover while maintaining high current densities and efficiency is a prominent pathway for improvement. Moreover, finding effective strategies to control the bubble distribution can help mitigate both the H_2 purity and safety concerns associated with gas crossover.

2.4 Bubble behaviour in membrane-free water electrolyser

2.4.1 Bubble formation and growth

As water electrolysis is initiated, the concentrations of dissolved H_2 and O_2 near the electrodes intensify until the adjacent electrolyte achieves a certain level of supersaturation—often reaching values 20-120 times higher than the saturation concentration (Maciel *et al.* 2009, Pereiro *et al.* 2019). This elevated state of supersaturation initiates the nucleation of bubbles inside the microcavities of the electrode surface (Jones *et al.* 1999). These tiny bubbles progressively assimilate H_2 or O_2 from the neighbouring, extensively supersaturated electrolyte, eventually growing in size (Vogt 2013), as shown in Figure 2-11.

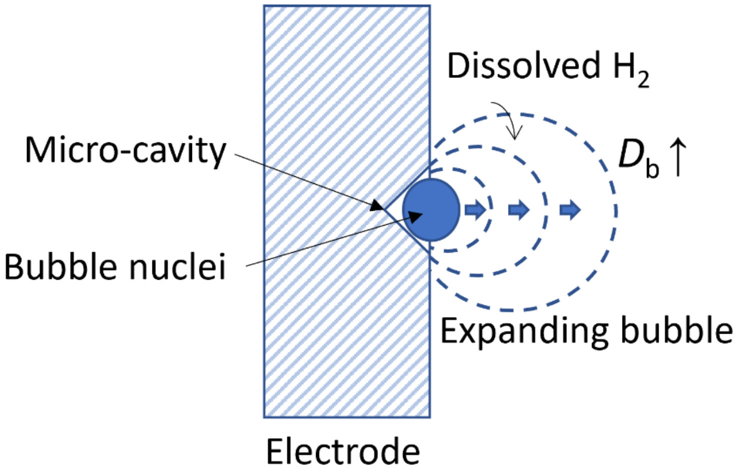

Figure 2-14. Bubble nucleation originating from a cavity within an electrode and its subsequent expansion in size (Vogt 2013).

2.4.2 Bubble departure

The growing gas bubbles on the electrode experience various forces, including buoyancy, drag, lift, surface tension and hydrodynamic pressure forces, which determine their departure diameters (Takemura *et al.* 2002, Lee and Balachandar 2010). Figure 2-15 shows the balance of forces for a bubble growing at the electrode surface:

$$\sum F_x = F_D + F_B - F_{gr,x} - F_{\sigma,x}, \tag{2-30}$$

$$\sum F_y = F_h + F_{gr,y} + F_{\sigma,y} - F_{cp} - F_L, \tag{2-31}$$

Where F_D is the drag force caused by the electrolyte flow, F_B is the buoyancy force, F_{gr} is the bubble growth force, F_σ is the surface tension force, F_h is the hydrodynamic pressure force, F_{cp} is the contact pressure force, and F_L is the lift force. As long as $\sum F_x < 0$ and $\sum F_y < 0$, the bubble is adhered to the electrode surface. With the growth of the bubble, the F_b increases until $\sum F_y > 0$. Then, the bubble slides along the electrode surface and may coalesce with other bubbles. Once $\sum F_x > 0$, the bubble leaves the electrode surface and moves into the bulk of the electrolyte.

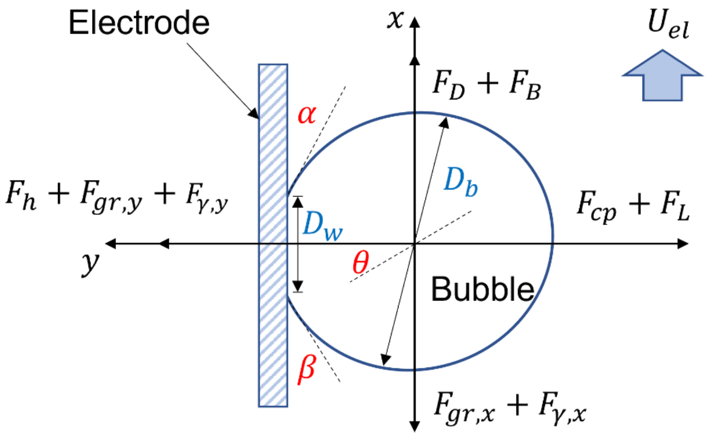

Figure 2-15. Forces on bubbles growing at the surface of an electrode in a water electrolyser.

It is worth noting that the Marangoni effect can potentially influence bubble departure (Meulenbroek *et al.* 2021). A few studies proposed that there exist temperature and concentration gradients near the electrode surface, which introduce Marangoni flow in the wedge between the electrode and bubble (Alhendal *et al.* 2010, Lubetkin 2003). However, due to the uncertainties in estimating the temperature and concentration gradient, it is challenging to evaluate the forces introduced by the Marangoni effect.

- **Surface tension force on a growing bubble**

As the bubble grows on the electrode surface, buoyancy force induces a tilt in its orientation. Consequently, the contact angle varies between the advancing contact angle (α) and the receding contact angle (β). Assuming the contact line is circular, the following equation can be used to calculate the general contact angle $\vartheta(\zeta)$ (Klausner *et al.* 1993):

$$\vartheta(\zeta) = \beta + (\alpha - \beta)\left[3(\frac{\zeta}{\pi})^2 - 2(\frac{\zeta}{\pi})^3\right], 0 \le \varphi \le \pi, \qquad (2\text{-}32)$$

where ζ is the polar angle around the bubble. This equation can be further simplified to:

$$\vartheta(\zeta) = \beta + (\alpha - \beta)\frac{\zeta}{\pi}, 0 \leq \zeta \leq \pi. \quad (2\text{-}33)$$

In x- and y- directions, the surface tension forces are expressed as (Klausner *et al.* 1993):

$$T_{\gamma,x} = -\int_0^{\pi} d_w \gamma_{el} \cos\vartheta \cos\zeta \, d\zeta \ , \quad (2\text{-}34)$$

$$T_{\gamma,y} = -\int_0^{\pi} d_w \gamma_{el} \sin\vartheta \, d\zeta \ , \quad (2\text{-}35)$$

where d_w is the bubble contact diameter (m). Substitution of (2-33) in (2-34) and (2-35) gives (Klausner *et al.* 1993):

$$T_{\gamma,x} = -d_w \gamma_{el} \frac{\pi(\alpha - \beta)}{\pi^2 - (\alpha - \beta)^2} (\sin\alpha + \sin\beta) \quad (2\text{-}36)$$

$$F_{\gamma,y} = -d_w \gamma_{el} \frac{\pi}{\alpha - \beta} (\cos\beta - \cos\alpha). \quad (2\text{-}37)$$

Yun *et al.* (2012) demonstrated that the bubble contact diameter (d_w) as about 1/15 of bubble diameter for subcooled flow boiling system. Nonetheless, there is no well-established model for determining the bubble contact diameter as they grow on the surface of an electrode. Precise measurement of the contact angle of bubbles also presents a notable challenge.

- **Drag force on a growing bubble**

The drag force for a bubble in a liquid is expressed as:

$$F_D = \frac{C_D}{8} \pi {D_b}^2 \rho_{el} {U_{el}}^2. \quad (2\text{-}38)$$

The drag coefficient (C_D) for bubbles in water has been intensively investigated. Multiple correlations have been proposed to estimate drag forces acting on bubbles of different diameters, including those by Schiller and Naumann (1933), Mei *et al.* (1994) and Tomiyama *et al.* (Tomiyama *et al.* 2002). However, there is no widely accepted correlation for drag force for bubbles growing at an electrode surface. One of the widely-used correlations for C_D is (Tomiyama 1998):

$$C_D = max\left[min\left\{\frac{16m}{Re_b}\left(1+0.15{Re_b}^{0.687}\right), \frac{48m}{Re_b}\right\}, \frac{8}{3}\frac{Eo}{Eo+4}\right], \quad 1 \le m \le 1.5\ . \tag{2-39}$$

In Equation 2-39, the parameter m refers to the degree of contamination. The $m = 1$ is for bubbles rising in pure water, whereas $m = 1.5$ is used for fully contaminated bubbles (Tomiyama 1998, Chen *et al.* 2023). This occurs because impurities in the water, when adhering to the bubble's surface, can suppress its internal circulation, thereby significantly increasing the drag (Clift *et al.* 1978).

In Equation 2-39, Re_b is bubble Reynolds number defined as:

$$Re_b = \frac{\rho_{el} U_{el} D_b}{\mu_{el}}, \tag{2-40}$$

where μ_{el} and ρ_{el} are the dynamic viscosity (kg/(m·s)) and density (kg/m^3) of the electrolyte, respectively, and U_{el} and D_b are the bubble rising velocity (m/s) and bubble diameter (m), respectively. The parameter Eo is the Eötvös number, accounting for the impact of bubble shape on drag forces (Clift 1978):

$$Eo = \frac{(\rho_{el} - \rho_g) g {D_\mathrm{b}}^2}{\gamma_{el}}. \tag{2-41}$$

Here, ρ_g is the gas density (kg/m^3), g is the gravitation acceleration (9.8 m/s^2), and γ_{el} is the surface tension of the electrolyte (N/m).

- **Shear-induced lift force on a growing bubble**

For a bubble growing on the electrode surface, the shear-induced lift force acts on it in a direction perpendicular to the electrode surface. This force, generated by the velocity gradient of the fluid, tends to push the bubble away from the electrode surface (Amini *et al.* 2014, Martel and Toner 2014). To calculate shear-induced lift force on a spherical bubble attached to a wall, Mei and Klausner (1994) established the following equations:

$$F_L = -\frac{1}{8}\rho\pi {D_b}^2 {U_{el}}^2 C_L \tag{2-42}$$

$$C_L = 3.87\tau^2({\mathrm{Re}_b}^{-2} + 0.118\tau^2)^{0.25} \tag{2-43}$$

where τ is the dimensionless shear rate, which is defined as:

$$\tau = \left|\frac{dU_{el}}{dy}\right| \frac{D_b}{2U_{el}} \tag{2-44}$$

- **Buoyancy force on a growing bubble**

The buoyancy force experienced by a gas bubble at the electrode surface can be expressed as:

$$F_B = \frac{1}{6}\pi {D_b}^3 (\rho_{el} - \rho_g) g\ . \tag{2-45}$$

- **Contact pressure force on a growing bubble**

The contact pressure force is generated from the pressure difference across the interface and acts in a direction perpendicular to the electrode surface. This force can be determined using the following equation as proposed by Klausner *et al.* (1993):

$$F_{cp} = -\frac{\gamma_{el}\pi {d_w}^2}{2r_0}, \tag{2-46}$$

where γ_{el} is the surface tension (N/m) , and r_0 is the radius of curvature of the bubble (m) at the reference point on the electrolyte surface, assumed to be five times the bubble radius (r_b) (Klausner *et al.* 1993, Mei *et al.* 1994).

- **Hydrodynamic pressure force on a growing bubble**

The hydrodynamic pressure force is expressed as (Klausner *et al.* 1993):

$$F_h = \frac{1}{2}\frac{9}{4}\rho_L {U_{el,r}}^2 \frac{\pi {d_w}^2}{4} \tag{2-47}$$

Where $U_{el,r}$ is the electrolyte velocity at the bubble surface.

- **Bubble growth force**

As the bubble grows, the change in its volume will result in a force applied by the surrounding liquid. Klausner *et al.* (1993) suggested the following equations to calculate bubble growth force:

$$F_{gr,x} = -\rho_L \pi {r_b}^2 \left(r_b \ddot{r_b} + 1.5\dot{r_b}^2\right)\sin\theta, \tag{2-48}$$

$$F_{gr,y} = \rho_L \pi {r_b}^2 \left(r_b \ddot{r_b} + 1.5\dot{r_b}^2\right) cos\theta. \tag{2-49}$$

Here, θ is the tilt angle of the bubble. The bubble diameter follows the growth law:

$$r_b(t) = kt^{0.5}\,, k = (2\,JaD)^2\ , \tag{2-50}$$

where D is the diffusion coefficient. The Jakob number (Ja) is defined as:

$$Ja = \frac{\mathrm{R}T}{p}\Delta c_b, \tag{2-51}$$

where Δc_b is the concentration difference at the bubble/electrolyte interface. Note that:

$$\dot{r(t)} = \frac{k}{2}t^{-0.5} = \frac{k^2}{2r}, \tag{2-52}$$

$$\ddot{r(t)} = -\frac{k}{4}t^{-1.5} = -\frac{k^4}{4r^3}. \tag{2-53}$$

Then, Equation (2-45) and (2-46) can be simplified to:

$$F_{gr,x} = -\frac{\rho_L \pi k^4 sin\theta}{8}\ , \tag{2-54}$$

$$F_{gr,y} = \frac{\rho_L \pi k^4 cos\theta}{8}\ . \tag{2-55}$$

Note that for a bubble with a diameter of 0.01 mm to 1 mm, the value for the bubble growth force (<10^{-13} N) is negligible compared to other forces (i.e. buoyance force: 10^{-12} ~10^{-9} N, surface tension force: 10^{-9} ~10^{-6} N, drag force: 10^{-11} ~10^{-8} N, shear-induced lift force: 10^{-13} ~10^{-9} N, hydrodynamic pressure force: 10^{-9} ~10^{-6} N) (Mei et al. 1994, Klausner *et al.* 1993, and Zhang and Zeng 2012). Hence, the key forces influencing bubble departure diameters are buoyancy, surface tension, drag, shear-induced lift, and hydrodynamic pressure forces. The calculated bubble departure diameter is typically less than 100μm (Kolev 2007, Zhang and Zeng 2012, Taqieddin *et al.* 2017).

2.4.3 Bubble rising in wall-bounded flow

Gas bubbles and the electrolyte form a gas-liquid two-phase flow in a water electrolysis cell. The specific characteristics of this flow regime can exhibit significant variation, influenced by factors such as channel dimensions, surface tension, volumetric fractions, velocities, densities, and viscosities of both gas and liquid phases. This variability can lead to a range of flow patterns, encompassing bubbly flow, slug flow, churn flow, and annular flow (Chen *et al.* 2006). In the context of membrane-free water electrolysers (MFE), the prevalent flow regime typically falls within the regime of bubbly flow (Swiegers *et al.* 2022).

Bubble rising behaviour is governed by a series of factors. These include the shape of the bubble and the forces acting upon it. Clift *et al.* found that Eötvös number (Eo), Morton number (Mo) and bubble Reynolds number (Re_b) can determine the shape of a free-rising bubble (Clift 1978):

$$Eo = \frac{(\rho_{el} - \rho_g) g {D_\mathrm{b}}^2}{\gamma_{el}} \ , \tag{2-41}$$

$$Mo = \frac{(\rho_{el} - \rho_g) g {\mu_{el}}^4}{{\rho_{el}}^2 {\gamma_{el}}^3} , \tag{2-57}$$

$$Re_b = \frac{\rho_{el} U_b D_b}{\mu_{el}} . \tag{2-40}$$

Depending on these parameters, the bubbles can be spherical, ellipsoidal, or skirted (Clift 1978, Fernandez *et al.* 2014, Zhou *et al.* 2020). In the literature, the Weber number is also widely used to estimate the shape of bubbles (Pistorius 2014, Chen *et al.* 2023):

$$We = \frac{\rho_{el} D_b {U_{el}}^2}{\gamma_{el}} \ . \tag{2-58}$$

When $We \ll 1$, the bubble can maintain a spherical shape, whereas the bubble becomes oblate or skirted when $We \gg 1$. The Bubble will become ellipsoidal when We is close to unity. Nevertheless, bubbles rising within water or conventional electrolyte solutions with low viscosities typically exhibit $Re_b < 200$, $Eo < 1$ and $We \ll 1$ (Hreiz *et al.* 2015, Yang *et al.* 2022). These parameters contribute to the predominance of a spherical shape for these bubbles.

Figure 2-16 shows a free rising, spherical bubble in a vertical water electrolyser channel at a distance of s to the wall. The flow is assumed to be fully developed, and any interaction from neighbouring bubbles can be disregarded. Then, the bubble is subjected to drag (F_D), shear-induced lift (F_{LS}), wall-induced lift (F_{LW}), and buoyancy (F_B) forces.

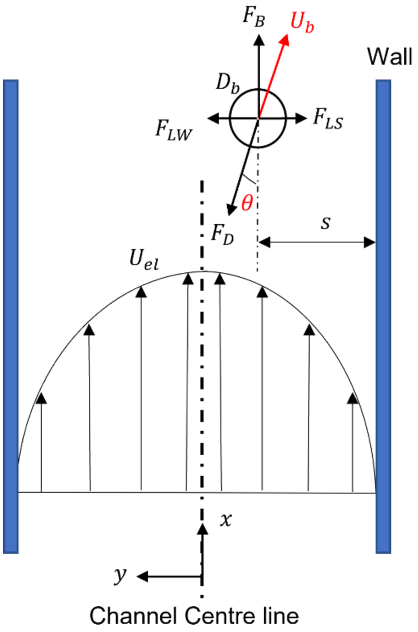

Figure 2-16. Forces acting upon a bubble in a wall-bounded, fully developed laminar flow.

The balance of forces can be written as:

$$(\rho_g + \alpha\rho_{el})V_b \frac{d\overrightarrow{U_b}}{dt} = \overrightarrow{F_B} + \overrightarrow{F_D} + \overrightarrow{F_{LS}} + \overrightarrow{F_{LW}}\,. \tag{2-59}$$

Here, V_b is the bubble volume, and $(\rho_g + \alpha\rho_{el})V_b$ represents the sum of the bubble mass and its virtual mass. The virtual mass coefficient, α, equals 0.5 for spherical bubbles (Kolev 2007).

- Buoyancy force

Since the bubble is spherical, the buoyance force can be calculated using Equation 2-45.

- Drag force

Since an electrolyte is used, bubbles in the water electrolyser can be considered as fully contaminated (Vogt 1983, Yang *et al.* 2022). Consequently, the drag coefficient for solid spheres can be used for determining the drag force for bubble rising in electrolyte bulk ($s/D_b \gg 1$) (Schiller and Naumann 1933, Tomiyama 1998):

$$C_D = \frac{24}{Re_b}\left(1 + 0.15{Re_b}^{0.687}\right) \tag{2-60}$$

It is found that when a bubble rises near the wall ($s/D_b \leq 1$), it experiences a slight increase in drag (Magnaudet *et al.* 2003). Zeng *et al.* (2005) proposed the following correlation for C_D for bubble rising in the near wall region:

$$C_D = \frac{24}{Re_b}(1 + \frac{3}{8Re_b}) + \frac{66.654}{L^*} - 8.364\,, \tag{2-61}$$

and the dimensionless separation (L^*) is defined as:

$$L^* = \frac{s}{D_b}Re_b \tag{2-62}$$

- Lift force for bubble rising outside wall region ($s/D_b > 1$)

Recent research indicates that when bubbles rise in regions where $s/D_b > 1$, their motions are predominantly influenced by F_{LS}, whereas F_{LW} is negligible (Takemura *et al.* 2009, Takemura and Magnaudet 2009, Zeng *et al.* 2009). Since a free rising bubble is leading the flow, a relative velocity is established between the bubble and the surrounding flow. The presence of velocity gradient in the flow will result in different relative velocities at the bubble-liquid interface. The direction of the lift force experienced by the bubble is influenced by this relative velocity between the bubble and the surrounding fluid. Specifically, the lift force tends to be directed towards the region where this relative velocity is the highest (Saffman 1965, McLaughlin 2006, Shi *et al.* 2020). In an electrolyser channel with laminar flow, the fluid velocity is higher in the centre and decreases towards the walls. Therefore, a bubble rising in such a channel will generally experience a F_{LS} that pushes it towards the channel walls, where the relative velocity between the bubble and the fluid is lower compared to the centre of the channel.

Table 2-5 summarises the recent studies on the shear-induced lift force coefficient of a bubble rising in simple shear flow. Some literature suggests that F_{LS} on a contaminated bubble is comparable to the force on a solid particle (Takemura and Magnaudet 2009, Shi and Rzehak 2019).

Table 2-5. Summary of recently proposed correlations for shear-induced lift force coefficient for a bubble rising in a shear flow.

Author	Correlation	Conditions
Tomiyama *et al.* (2002)	$C_{LS} = \begin{cases} min[0.288\tanh(0.121Re), f(Eo)], & Eo < 4 \\ f(Eo), & 4 \le Eo \le 10.7 \end{cases}$ $f(Eo) = 0.00105\,Eo^3 - 0.0159Eo^2 - 0.0204Eo + 0.474$	$-5.5 < \log_{10} Mo < -2.8$, $1.39 < Eo < 5.74$, $0 < w < 8.3$ s^{-1}
Xu *et al.* (2021)	$C_{LS} = \max(-6.3(1 - 2.1\,\varepsilon^{0.2})\tanh(2.8(Eo - 1.3\varepsilon_1), -3.65exp(-0.05\varepsilon^{0.2}Eo - 0.2\varepsilon_1))$ $\varepsilon = (\frac{Sr}{Re})^{0.5}, \varepsilon_1 = (SrRe)^{0.5}$	$\log_{10} Mo = -11$, $1 < Eo < 55$, $0.28 < w < 0.51$ s^{-1}, counterflow
Legendre and Magnaudet (1998)	$C_{LS} = \sqrt{\left(\frac{6}{\pi^2}\frac{2.255}{\sqrt{SrRe}(1 + 0.2Re/Sr)^{1.5}}\right)^2 + \left(\frac{1}{2}\frac{Re + 16}{Re + 29}\right)^2}$	$0.1 < Re_b < 500$, $0 < Sr < 1$
Lee (2020)	$C_{LS} = 0.5 - 2.8\chi^{2.2}Oh$ $\chi = 1 + 0.163Eo^{0.757}$ $Oh = \frac{\mu}{(\rho ud)^{0.5}}$	$\log_{10} Mo = -10.6$ $0.63 < Eo < 54.8$

The F_{LS} on a particle in a simple shear flow has been extensively studied. For a solid spherical particle moving in a simple shear flow, a number of theoretical models have been developed to evaluate F_{LS} (Cox and Hsu 1977, Asmolov 1999, and Yahiaoui and Feuillebois 2010). For spherical bubbles in a low-Reynolds-number shear flow, Legendre and Magnaudet (1997) proposed an analytical expression for C_{LS}.

In addition to theoretical models, direct numerical simulation (DNS) of F_{LS} acting on a solid particle in a simple shear flow has also been conducted. For example, Feng *et al.* (1994) reported that the behaviour of a spherical solid particle in a Poiseuille flow is affected by factors such as particle rotation, shear slip, wall lubrication, and the curvature of the velocity profile. Later, Legendre and Magnaudet (1998) conducted an investigation into the lift force acting on a spherical bubble (0.1<Re_b<500) in a simple shear flow using DNS. Their found the minimum lift force coefficient to be 0.3 at Re_b=5, which then incrementally rose to 0.5 as Re_b increased. In a recent study, Shi *et al.* (2020) demonstrated how various factors such as slip velocity, Re_b, shear rate, and the distance between the bubble and the wall, influence F_{LS} for a spherical bubble. They also proposed new correlations for C_{LS}. Moreover, Mortazavi and Tryggvason (2000) discovered that droplet Reynolds number, deformability, and viscosity ratio were the key factors determining the trajectory of a deformable droplet in a Hagen-Poiseuille flow. In addition, increasing the flow Reynolds number can lead to oscillatory motion of droplets.

Experimental studies on F_{LS} on bubbles mainly focused on large and deformed bubbles ($D_b > 1$ mm). Xu *et al.* (2021) and Li *et al.* (2016) studied the effect of F_D and F_{LS} on the transverse motion of bubbles in a downward water flow. They generated a simple shear flow field using a curved screen. A submerged nozzle was utilised to generate bubbles with diameters ranging from 1 to 20 mm. The $C_D$and C_L were subsequently calculated by recording the trajectories of bubbles. Tomiyama *et al.* (2002) studied F_{LS} on air bubbles with 2.8 mm < D_b < 5.7 mm. In their work, a shear flow was generated using two roller belts at the side of a tank filled with water-glycerol solution. Bubbles were formed through a submerged nozzle placed at the bottom of the tank. The C_L were obtained under 1.39 < Eo <5.74, −5.5 <$\log_{10} Mo < -$ 2.8 and a shear rate up to 8.3 s^{-1}. Based on this work, Aoyama *et al.* (2017) expanded the experimental data to −6.6 < $\log_{10} Mo < -$ 3.2 and 0.022 < Eo < 5.0. However, recent research has indicated that numerous existing models for predicting lift forces on bubbles in viscous fluids might not be appropriate for estimating the lift forces on bubbles in low-viscosity fluids (Ziegenhein *et al.* 2018, Lee and Lee 2020).

- Lift force for bubble rising in wall region ($s/D_b < 1$)

Literature suggests that the influence of F_{LW} should be considered for bubbles rise in the wall region ($s/D_b < 1$). The direction of F_{LW} depends on various factors. For a contaminated bubble, F_{LW} acts to propel it away from the wall (Zeng *et al.* 2005, Amini *et al.* 2014). For small, clean bubbles (Re_b <35), there is also a tendency for them to be repelled by the wall. Conversely, clean bubbles that have a Re_b ≥35 experienced an attraction towards the wall (Takemura and Magnaudet 2003). Notably, as the bubble exits the wall region, F_{LW} decrease significantly (Shi and Rzehak 2020, Shi *et al.* 2020).

The correlation proposed by Zeng *et al.* (2005) can be used to calculate C_L for contaminated spherical bubbles rising in wall region. This correlation considers lift forces induced by both the wall and shear:

$$C_L = \frac{9}{8}(1 - \frac{11}{32}L^{*2}), \tag{2-63}$$

and the dimensionless separation (L^*) can be obtained using Equation 2-62.

2.4.4 Flow visualisation in water electrolysers

Table 2-6 summarises recent studies on bubble visualisation in electrolysers. Particle image velocimetry (PIV) and bubble image velocimetry (BIV) are the two widely used techniques for the visualisation of bubbly flow in an electrolyser. PIV has been widely used as a non-intrusive tool to visualise the instantaneous velocity field of fluid flow (Raffel 2018). To visualise the flow field, small size particles are added to the flow of interest, where they are illuminated by a laser sheet. A camera is used to record the movement of the tracers, and the images are further processed by the cross-correlation technique to obtain the velocity field of the flow (Raffel 2018). However, the PIV technique faces two major challenges for gas-liquid two-phase flow in a water electrolyser:

The first challenge is how to minimise the influence of seeding particles on the behaviour of gas bubbles. The size of seeding particles (5-50μm) is within the range of fine bubbles generated from the electrode surface (10-100μm). The seeding particles will have a strong impact on bubble behaviour compared to other systems such as flow boiling and bubble column (Sillen *et al.* 1982). Also, the seeding particles in the vicinity of the electrode will act as nucleation sites, which changes the characteristics of bubble generation. The second challenge is the separation of the velocity field for both gas and liquid phases from the PIV result (Hreiz *et al.* 2015). Unlike in flow boiling and bubble column systems, where bubble boundaries are readily visible under adequate illumination (Kazakis *et al.* 2008, Chen *et al.* 2012), the fine bubbles in a water electrolyser form a pseudo-continuous layer near the electrodes. This layer obscures individual bubbles, making it challenging to distinguish them and identify the gas/liquid interface in the resulting images.

Table 2-6. A summary of recent studies on bubble visualisation in electrolysers.

Author	Operating conditions	Technique		
		Bubble velocity	Flow velocity	Void fraction
Riegel *et al.*(1998)	Re=7800 J = 500-6250 A/m^2 Electrolyte: 5wt% KOH	BIV (LED light source)	-	Calculated by local resistance
Boissoneau *et al.* (2000)	Re=0 J = 500-2000 A/m^2 Electrolyte: 5wt% KOH	BIV (LED light source)	-	-
Nagai *et al.* (2003)	Re=0 J = 1000-16000 A/m^2 Electrolyte: 8.5-25.5wt% KOH	BIV (LED light source)	-	-
Aldas *et al.* (2008)	Re=500-2000 J = 1000-5000 A/m^2	BIV (LED light source)	-	Calculated by local resistance
Abdelouahed *et al.* (2014)	Re=0 J = 500-2000 A/m^2 Electrolyte: 2wt% NaOH	BIV (LED light source)	CFD (Euler-Lagrange model)	-
Hreiz *et al.* (2015)	Re=0 J = 130 A/m^2 Electrolyte: 2wt% NaOH	BIV (LED light source)	CFD (Euler-Lagrange model)	-
Tanaka *et al.* (2005)	Re=0 J = 400-1200 A/m^2 Electrolyte: 0.1wt% K_2SO_4	BIV (LED light source)	-	-
Chen *et al.* (2018)	Re=0	PIV (YAG laser, 50μm polycrystalline tracer, V3V camera) CFD (Euler-Euler model)		-
Lee *et al.* (2019)	Re=600-1200 J = 400-1200 A/m^2 Electrolyte: 0.8wt% KOH	BIV (LED light source)	-	-

To overcome these challenges, bubble image velocimetry (BIV) has been used for the flow visualisation of bubbly flow in water electrolysers (Hreiz *et al.* 2015). BIV does not use additional tracing particles. Instead, it only obtains the velocity field of bubbles in the flow. BIV also tends to use LED as the light source rather than laser sheet. Nevertheless, the BIV technique can only provide information about the bubbles.

In summary, both PIV and BIV techniques have been used to investigate the flow field in a water electrolyser. PIV is more effective at capturing the velocity field of fluid flow, whereas BIV focuses on the movement of bubbles.

Nonetheless, accurately measuring the flow velocity near the electrode surface is still challenging due to the interference from the dense layer of bubbles.

2.4.5 Single bubble generation for studying bubble behaviour

Generating bubbles with controlled size and frequency is crucial for studying bubble behaviour. This is because uncontrolled bubble formation can result in continuous in-line bubbles or bubble plumes, making it difficult to visualise and track individual bubbles. The inevitable interactions between bubbles also pose challenges to investigating the effect of the flow field on these bubbles.

Conventionally, bubbles are generated by supplying gas through a submerged nozzle (or a needle) (Kumar and Kuloor 1970, Sanada and Abe 2013). Consider a bubble is formed from a submerged nozzle in a quiescent liquid, the bubble detaching radius (r_d) can be estimated at the point where the buoyancy and surface tension forces acting on the bubble reach equilibrium (Kumar and Kuloor 1970, Kolev 2007):

$$r_d = \left(\frac{3\gamma_{el}D_o}{4\rho_{el}g}\right)^{\frac{1}{3}} \tag{2-64}$$

Here γ_{el} and ρ_{el} are the surface tension (N/m) and density (kg/m^3) of the liquid, respectively; D_o is the diameter of the nozzle (m), and g is the gravitational acceleration (m/s^2).

Equation 2-64 indicates that to produce microbubbles (D_b < 1 mm), a very small nozzle (D_o< 50μm) is required. This presents challenges in fabrication nozzles of such diminutive size. Several techniques have been developed to reduce bubble departure diameter, such as employing co-flow liquid over the growing bubble (Evangelio *et al.* 2015, Kim *et al.* 2021) and utilising orifice movement to enhance bubble departure (Vejrazka *et al.* 2008).

However, continuously injecting gas into the nozzle without regulation is likely to result in the formation of a bubble plume, as the nozzle offers limited control over the gas flow rate (Davidson and Schüler 1997, Bari and Robinson 2013).

To control the gas flow supplied to the nozzle, timed gas injection technique has been adopted by various research teams to realise single bubble generation (Najafi *et al.* 2008, Parkinson *et al.* 2008, Kim *et al.* 2021). This technique relies on a group of precision gas valves with precise control, which can feed pulsed gas flow to the nozzle to ensure the bubbles are formed at desired frequencies.

Generally, electrolysis of water tends to produce a dense bubble plume. However, it was found that when the electrode size is reduced to micrometre-scale, it can produce single bubbles under certain conditions (Li *et al.* 2011, Fernandez *et al.* 2014, Yang *et al.* 2015). In an experimental work by Fernández *et al.* (2014), a platinum microelectrode with a diameter of 125μm was fabricated and coated with an optical resin to investigate the formation of H_2 bubbles. In their work, single bubbles with a diameter of 500-800 μm were successfully generated at a frequency of 1.5-3.5 Hz. Yang *et al.* (2015) studied the formation and departure of single H_2 bubbles from a microelectrode. Single H_2 bubbles with a diameter of 100-300 μm were generated using a microelectrode fabricated by embedding a 100μm diameter platinum wire into an epoxy resin. Others have found that the bubble diameter decreases when the size of the electrode is reduced (Fernández *et al.* 2012, Luo and White 2013, Bashkatov *et al.* 2019). The recent works pertaining to the generation of single bubbles are summarised in Table 2-7.

Table 2-7. A summary of techniques used for generating single bubbles in water.

Bubble generation method	Bubble size	Bubble frequency	Control technique/instrument	Author
Gas and water injection through a 4mm nozzle.	0.5-2.5mm	-	Control the actuation time of gas and water supply valves	Ohl (2001)
Gas injection through a 0.5mm diameter	2-4mm	up to 70Hz depending on gas	Precision valves and pressure sensors	Ostmann and

orifice using a piston-cylinder		injection rate.		Schwarze (2018)
Gas injection through a 0.3 mm inner diameter capillary tube using pressurised air	1-3mm	1-18Hz depending on gas injection rate.	Regulating valve sets and pressure gauge	Duhar and Colin (2006)
Gas injection through a 2mm inner diameter capillary tube using pressurised air	>5mm	20-50Hz depending on gas injection rate.	Regulating valve sets with flow meter	Zhang and Shoji (2001)
Gas injection through a slit on an elastic tube with an inner diameter of 5mm and an acoustic pressure wave to generate gas pulse.	about 0.5mm	Controllable, up to 500Hz	Slit opened periodically by acoustic wave generated by a loudspeaker.	Abe and Sanada (2015)
Gas injection through syringe needles with an inner diameter of 0.5-1.2mm	about 3mm	-	Gas injection rate controlled by fine tuning syringe displacement with a cordless drill and a rotary motion sensor.	Lesage and Marois (2013)
Gas injection through nozzles with inner diameter of 0.292-3.025mm	0.9-7.35mm	-	Gas injection controlled by a pressure controller, a flowmeter, and valves.	Bolaños-Jiménez *et al.* (2008)
Gas bubble injection through a nozzle near the outlet of a pressurised chamber to generate external flow	0.05-0.8 mm	0.1-8Hz depending on bubble size.	External flow is controlled by the pressure in a chamber.	Evangelio, *et al.* (2015)

around the needle.				
Gas injection through a micropipette with an inner diameter of less than 1μm.	less than 0.2mm	One bubble per cycle.	Gas controlled by pressure sensors to generate a pressure pulse.	Kim *et al.* (2021)
Gas injection through needles (20-450μm) with rapid movements to accelerate bubble departure.	0.2-2.5mm	40-160Hz depending on needle size.	Specially designed needle.	Vejrazka *et al.* (2008)
Electrolytic bubble generated from a 125μm diameter platinum wire.	0.2-0.8 mm	1-8Hz depending on bubble size.	Bubble diameter controlled by applied voltage.	Fernandez *et al.* (2014)
Electrolytic bubble generated from a 100μm diameter platinum wire.	about 1 mm	60-180Hz depending on bubble size.	Bubble diameter controlled by applied voltage.	Bashkatov *et al.* (2019)
Electrolytic bubble generated from a 100μm diameter platinum wire.	0.05-0.25mm	1-1000Hz depending on bubble size.	-	Yang *et al.* (2015)

In summary, the generation of single bubbles with controllable frequency and size is crucial for studying bubble rising behaviour in liquids. Conventional methods, like gas injection through submerged nozzles, face challenges due to the requirement for extremely small nozzle sizes to produce microbubbles. To address this, some studies have utilised orifice movement and timed gas injection. Although the literature suggests that microelectrodes can generate single microbubbles (Fernandez et al. 2014, Bashkatov *et al.* 2019), systematic studies examining how microelectrode geometric parameters influence bubble size and frequency are notably lacking.

2.4.6 CFD studies on electrolytic bubble behaviour

Computational Fluid Dynamics (CFD) is an effective tool to investigate bubble behaviour in water electrolysers. One commonly used approach is the Volume of Fluid (VOF) model, which is suitable for investigating formation, growth, departure, and rising, as well as the coalescence of bubbles. When it comes to bubble plumes, the Euler-Euler methods are frequently employed (Hreiz *et al.* 2015).

The VOF model is well suitable for capturing the interface between the bubble and the liquid. In this model, the fluid domain is divided into computational cells, each represented by a volume fraction α. This fraction signifies the proportion of the cell occupied by the liquid phase. When modelling a single H_2 bubble in an electrolyte, a cell with α_g = 0 is entirely liquid phase, whereas a cell with α_g = 1 is entirely gas phase. For cells where 0 < α_g < 1, the cell contains the interface between the two phases (Lafmejani *et al.* 2017, Liu and Luo 2018). Tracking this interface is made possible by solving the continuity equation for the volume fraction of the gas phase:

$$\nabla \cdot \left(\alpha_g \boldsymbol{v}_g\right) = S_g + \left(\dot{m}_{gl} - \dot{m}_{lg}\right). \tag{2-65}$$

Here, α_g denotes the volume fraction of the gas phase, and $\boldsymbol{v}_g$ is the velocity vector of the gas phase. S_g represents the mass source added to the cell. $\dot{m}_{gl}$ and $\dot{m}_{lg}$ refer to the mass flux from the gas phase to the liquid phase and from the liquid phase to the gas phase, respectively.

The limitation of VOF model is the generation of spurious currents when modelling microbubbles, which can lead to non-physical results (Zahedi *et al.* 2012). The spurious currents are the high velocities at the bubble-liquid interface, predominantly originating from surface tension modelling. These currents cannot be mitigated by simply refining the mesh or reducing the time step. Nonetheless, they can be alleviated by employing improved surface tension models. Recent advancements in surface tension modelling include Continuum Surface Stress (CSS) (Lafaurie *et al.* 1994), Coupled Level-set VOF (CLSVOF) (Sussman and Puckett 2000), Parabolic Reconstruction of Surface Tension (PROST) (Renardy and Renardy 2002), height function (Struyven *et al.* 2022) and Piecewise Linear Interface Calculation (PLIC) (Cifani *et al.* 2016).

In the Euler-Euler model, each phase in the electrolysers is treated as a separate, interpenetrating continuum. In the Euler-Euler model, the governing mass equation for the i-*th* phase is:

$$\nabla \cdot (\alpha_i \rho_i \boldsymbol{v}_i) = S_i \ . \tag{2-66}$$

where α, ρ and $\boldsymbol{v}$ are the volume fraction, density and velocity vector, respectively. The sum of the volume fractions for all phases equals unity, i.e., $\sum \alpha_i = 1$. The S is the volumetric source term for the mass added into the system, and S_l = 0 is for the liquid phase. In the literature, a common practice is to add H_2 and O_2 at the thin layer near the electrode surface (Rodríguez and Amores 2020, Zarghami, Deen *et al.* 2020). The flow rate (kg/s) of H_2 and O_2 added as the mass source are calculated according to Faraday's Law (Zhou *et al.* 2020):

$$\dot{m}_{\mathrm{H_2}} = M_{\mathrm{H_2}} \dot{n}_{\mathrm{H_2}} = \frac{I M_{\mathrm{H_2}}}{2\mathrm{F}}, \tag{2-67}$$

$$\dot{m}_{\mathrm{O_2}} = M_{\mathrm{O_2}} \dot{n}_{\mathrm{O_2}} = \frac{I M_{\mathrm{O_2}}}{4\mathrm{F}}. \tag{2-68}$$

Here, $M_{\mathrm{H_2}}$ and $M_{\mathrm{O_2}}$ are the molar weight (kg/mol) of H_2 and O_2, respectively. The parameter n is the molar flow rate (mol/s). I is the current (A), and F is the Faraday constant (96485 c/mol).

At steady state, the momentum balance for the i-*th* phase is:

$$\nabla \cdot (\alpha_i \rho_i \boldsymbol{v}_i \boldsymbol{v}_i) = -\alpha_i \nabla p + \nabla \cdot \boldsymbol{\tau}_i + \alpha_i \rho_i \boldsymbol{g} + \sum F_i \ . \tag{2-69}$$

The stress-strain tenor ($\boldsymbol{\tau}$) is defined as:

$$\boldsymbol{\tau}_i = \alpha_i \mu_{m,i} (\nabla \boldsymbol{v}_i + \nabla \boldsymbol{v}_i^T) \ , \tag{2-70}$$

where μ_m is the molecular dynamic viscosity. The external forces $\sum F_i$ considered in the model include drag force, lift force, virtual mass force, and turbulent dispersion force.

The Euler-Euler model is often used to simulate the bubble layers in an electrolyser cell. Obata *et al.* (Obata *et al.* 2021) investigated the void fraction distribution in a membrane-free, solar-powered water electrolyser using two-dimensional CFD simulations. In their study, they applied a fully developed laminar velocity profile at the inlet of the electrolyser channel, where electrodes are positioned on each side of the channel. The formation of H_2 and O_2 was considered as a mass flux added to the cells corresponding to the cathode and anode. The Euler-Euler multiphase model was adopted to calculate the volume fractions and velocity vectors of H_2 and O_2 gases. Their results showed that gas crossover could be reduced by either increasing the inlet flow velocity while maintaining laminar flow or by expanding the channel width. Furthermore, they concluded that the crossover is mainly attributable to gas bubbles rather than to dissolved gases.

In a recent work, Zarghami *et al.* (2020) simulated bubbly flow in a water electrolyser using the Euler-Euler approach. In their work, they developed a 3D model of a vertical membrane-free alkaline water electrolyser with a length of 400 mm and an electrode spacing of 8 mm. H_2 and O_2 were added to the cell adjacent to the electrodes as volumetric source terms. Given that the Reynolds number of the electrolyte was approximately 7600, a turbulent model was adopted. Their results show that the thickness of the bubble layer increases with the increase in applied current density but decreases with the Reynolds number of the electrolyte. They also found that drag, lift, and turbulence dispersion forces are critical for accurately modelling the propagation of the bubble layer along the electrode.

It is worth noting that the Euler-Lagrangian method can also be employed to model bubble behaviour in a water electrolyser channel. This approach treats bubbles as a discrete phase and the electrolyte as a continuous phase. Bubbles are injected into the computational domain at discrete time steps. In the work of Hreiz *et al.* (2015), a 3D model for a vertical, membrane-free water electrolyser was developed. By employing the Euler-Lagrangian method, their model successfully predicted the spread and dispersion of bubbles within the electrolysis cell. The authors concluded that when modelling bubble plumes in water electrolysers, the Euler-Lagrangian approach offers advantages over the Euler-Euler models, in which additional forces and mechanisms are often deemed necessary.

2.5 Summary of identified gaps

The membrane-free water electrolyser (MFE) is an emerging technology for clean H_2 production, with the potential to be operated at elevated temperatures and pressures to achieve improved cell efficiency while reducing capital and maintenance costs. Currently, MFEs remain in the research and development phase due to a series of technical challenges. One of the most critical issues is the low purity of produced H_2, attributed mainly to gas crossover. While some pioneering studies have attempted to address this issue, further research is needed for successful scaling-up of this novel concept. Based on the literature review, the following gaps have been identified:

- MFE for liquid hydrogen production

The current literature lacks discussion on the feasibility of using MFE for liquid hydrogen (LH_2) production. In an MFE cell, gas crossover at industrial scale is inevitable due to the absence of a membrane separating H_2 and O_2. While enhancing H_2 purity can improve the cell's overall performance, achieving purity levels comparable to conventional alkaline water electrolysers (AWE) and proton exchange membrane electrolysers (PEM) may be unrealistic and unnecessary. However, if MFE can attain higher efficiency and use the conserved electrical power for H_2 purification, the technology remains a viable pathway for clean H_2 production. Considering that H_2 liquefaction is a mature technology, utilising MFE for LH_2 production—while separating O_2 during cryogenic cooling—appears promising. Such discussion is noticeably absent in current literature.

- Shear-induced lift force on a microbubble in a parabolic flow

While the bubble behaviour in an MFE cell is directly related to the gas crossover, there is limited knowledge of the shear-induced lift force acting on microbubbles (D_b <1 mm) as they rise through an electrolyser channel with a parabolic velocity profile. Existing correlations for calculating the shear-induced lift force coefficient (C_{LS}) are primarily applicable to large or deformed bubbles within a simple shear flow. Moreover, experimental data of C_{LS} for bubbles with diameters less than 1 mm is unavailable. Numerous studies proposed correlations of C_{LS} in the context of solid spheres moving in a simple shear flow. However, C_{LS} for solid spheres or bubbles moving in a flow with a parabolic velocity profile has not been investigated in detail.

- Generation of single microbubble

Another challenge in studying microbubble behaviour is generating individual microbubbles in an electrolyte with controllable sizes and frequencies. Most existing studies that require single-bubble generation utilise pulsed gas injection via a submerged nozzle. This approach necessitates a dedicated control system to precisely modulate the gas flow, preventing the formation of continuous bubbles. The gas feeding and control systems are complex, and the adjustment of the frequencies and magnitude of the pressure pulses can be time-consuming. On the other hand, generating microbubbles from an electrode offers a seemingly simpler alternative. However, this method typically results in a bubble plume rather than single bubbles. While some studies have explored the generation of single bubbles from a microelectrode, they primarily focused on how the size of the microelectrode affects bubble diameters. There is also a lack of systematic research on how the geometrical parameters of these microelectrodes influence the characteristics of the bubbles produced.

- Flow control for bubble management in MFE

The MFE cell proposed in the literature relies solely on a parabolic flow field in the electrolyser channel to generate a shear-induced lift force that separates H_2 and O_2. These cells are generally limited to low current densities to minimise gas crossover. However, the risk of gas crossover increases along the length of the electrolyser channel for two main reasons. First, the growth of bubble layer along the electrode narrows the gap between the H_2 and O_2 bubbles, increasing the likelihood of crossover. Secondly, the bubbles induce high fluid velocity near the electrode, which dramatically alters the flow field in the electrolyser channel. As a result, the shear-induced lift force tends to push bubbles to the channel centre. Ideally, given the nature of the shear-induced lift force, the velocity profile should be configured in such a way that this lift force consistently directs bubbles toward the channel wall. However, current studies have not sufficiently explored how to establish an optimal velocity field to prevent bubble mixing effectively. Also, the feasibility of employing a flow controller to create a specific flow field that reduces gas crossover has yet to be demonstrated.

References

Aasadnia, M., M. Mehrpooya and B. Ghorbani (2021). A novel integrated structure for hydrogen purification using the cryogenic method. Journal of Cleaner Production **278**: 123872.

Abbasi, R., B. P. Setzler, S. Lin, J. Wang, Y. Zhao, H. Xu, B. Pivovar, B. Tian, X. Chen, G. Wu and Y. Yan (2019). A roadmap to low-cost hydrogen with hydroxide exchange membrane electrolyzers. Adv Mater **31**(31): e1805876.

Abdelouahed, L., R. Hreiz, S. Poncin, G. Valentin and F. Lapicque (2014). Hydrodynamics of gas bubbles in the gap of lantern blade electrodes without forced flow of electrolyte: Experiments and CFD modelling. Chemical Engineering Science **111**: 255-265.

Abdin, Z., C. J. Webb and E. M. Gray (2017). Modelling and simulation of an alkaline electrolyser cell. Energy **138**: 316-331.

Abe, K. and T. Sanada (2015). The mechanism of bubble generation using a slit elastic tube and an acoustic pressure wave in the gas phase. Chemical Engineering Science **128**: 28-35.

Aikens, D. A. (1983). Electrochemical methods, fundamentals and applications. Journal of Chemical Education **60**(1): A25.

Al Ghafri, S. Z. S., S. Munro, U. Cardella, T. Funke, W. Notardonato, J. P. M. Trusler, J. Leachman, R. Span, S. Kamiya, G. Pearce, A. Swanger, E. D. Rodriguez, P. Bajada, F. Jiao, K. Peng, A. Siahvashi, M. L. Johns and E. F. May (2022). Hydrogen liquefaction: a review of the fundamental physics, engineering practice and future opportunities. Energy & Environmental Science **15**(7): 2690-2731.

Aldas, K., N. Pehlivanoglu and M. Mat (2008). Numerical and experimental investigation of two-phase flow in an electrochemical cell. International Journal of Hydrogen Energy **33**(14): 3668-3675.

Alhendal, Y., A. Turan and W. I. A. Aly (2010). VOF simulation of marangoni flow of gas bubbles in 2D-axisymmetric column. Procedia Computer Science **1**(1): 673-680.

Allen, J. A., G. Rowe, J. T. Hinkley and S. W. Donne (2014). Electrochemical aspects of the hybrid sulfur cycle for large scale hydrogen production. International Journal of Hydrogen Energy **39**(22): 11376-11389.

Amin, M., A. S. Butt, J. Ahmad, C. Lee, S. U. Azam, H. A. Mannan, A. B. Naveed, Z. U. R. Farooqi, E. Chung and A. Iqbal (2023). Issues and challenges in hydrogen separation technologies. Energy Reports **9**: 894-911.

Amini, H., W. Lee and D. Di Carlo (2014). Inertial microfluidic physics. Lab Chip **14**(15): 2739-2761.

Aoyama, S., K. Hayashi, S. Hosokawa, D. Lucas and A. Tomiyama (2017). Lift force acting on single bubbles in linear shear flows. International Journal of Multiphase Flow **96**: 113-122.

Asmolov, E. S. (1999). The inertial lift on a spherical particle in a plane Poiseuille flow at large channel Reynolds number. Journal of Fluid Mechanics **381**: 63-87.

Bac, S., S. Keskin and A. K. Avci (2020). Recent advances in materials for high purity H2 production by ethanol and glycerol steam reforming. International Journal of Hydrogen Energy **45**(60): 34888-34917.

Barbarossa, V., S. Brutti, M. Diamanti, S. Sau and G. De Maria (2006). Catalytic thermal decomposition of sulphuric acid in sulphur–iodine cycle for hydrogen production. International Journal of Hydrogen Energy **31**(7): 883-890.

Barelli, L., G. Bidini, F. Gallorini and S. Servili (2008). Hydrogen production through sorption-enhanced steam methane reforming and membrane technology: A review. Energy **33**(4): 554-570.

Bari, S. D. and A. J. Robinson (2013). Experimental study of gas injected bubble growth from submerged orifices. Experimental Thermal and Fluid Science **44**: 124-137.

Barron, R. F. (1966). Cryogenic systems. New York, McGraw-Hill.

Bashkatov, A., S. S. Hossain, X. Yang, G. Mutschke and K. Eckert (2019). Oscillating hydrogen bubbles at Pt microelectrodes. Physical Review Letters **123**(21): 214503.

Bellosta von Colbe, J., J.-R. Ares, J. Barale, M. Baricco, C. Buckley, G. Capurso, N. Gallandat, D. M. Grant, M. N. Guzik, I. Jacob, E. H. Jensen, T. Jensen, J. Jepsen, T. Klassen, M. V. Lototskyy, K. Manickam, A. Montone, J. Puszkiel, S. Sartori, D. A. Sheppard, A. Stuart, G. Walker, C. J. Webb, H. Yang, V. Yartys, A. Züttel and M. Dornheim (2019). Application of hydrides in hydrogen storage and compression: Achievements, outlook and perspectives. International Journal of Hydrogen Energy **44**(15): 7780-7808.

Bessarabov, D. and P. Millet (2018). Fundamentals of Water Electrolysis. PEM Water Electrolysis**:** 43-73.

Bicer, Y., G. Chehade and I. Dincer (2017). Experimental investigation of various copper oxide electrodeposition conditions on photoelectrochemical hydrogen production. International Journal of Hydrogen Energy **42**(10): 6490-6501.

Blinov, D. V., V. I. Borzenko, A. V. Bezdudny and A. N. Kazakov (2021). Metal hydride hydrogen storage and purification technologies. Journal of Physics: Conference Series **2039**(1): 012005.

Boissonneau, P. and P. Byrne (2000). An experimental investigation of bubble-induced free convection in a small electrochemical cell. Journal of Applied Electrochemistry **30**(7): 767-775.

Bolaños-Jiménez, R., A. Sevilla, C. Martínez-Bazán and J. M. Gordillo (2008). Axisymmetric bubble collapse in a quiescent liquid pool. II. Experimental study. Physics of Fluids **20**(11): 112104.

Brauns, J. and T. Turek (2020). Alkaline water electrolysis powered by renewable energy: a review. Processes **8**(2): 248.

Bui, J. C., J. T. Davis and D. V. Esposito (2020). 3D-Printed electrodes for membraneless water electrolysis. Sustainable Energy & Fuels **4**(1): 213-225.

Cardoso, D. S. P., L. Amaral, D. M. F. Santos, B. Šljukić, C. A. C. Sequeira, D. Macciò and A. Saccone (2015). Enhancement of hydrogen evolution in alkaline water electrolysis by using nickel-rare earth alloys. International Journal of Hydrogen Energy **40**(12): 4295-4302.

Carmo, M., D. L. Fritz, J. Mergel and D. Stolten (2013). A comprehensive review on PEM water electrolysis. International Journal of Hydrogen Energy **38**(12): 4901-4934.

Chen, D., L.-m. Pan and S. Ren (2012). Prediction of bubble detachment diameter in flow boiling based on force analysis. Nuclear Engineering and Design **243**: 263-271.

Chen, L., Y. S. Tian and T. G. Karayiannis (2006). The effect of tube diameter on vertical two-phase flow regimes in small tubes. International Journal of Heat and Mass Transfer **49**(21-22): 4220-4230.

Chen, Y., L. Wang, H. Chang and Q. Zhang (2023). A review of drag coefficient models in gas-liquid two-phase flow. ChemBioEng Reviews **10**(3): 311-325.

Chen, Y. J., T. L. Yang, J. J. Yu, C. L. Kao and C. R. Kao (2013). Gold and palladium embrittlement issues in three-dimensional integrated circuit interconnections. Materials Letters **110**: 13-15.

Chung, K.-H., S. Jeong, B.-J. Kim, K.-H. An, Y.-K. Park and S.-C. Jung (2018). Enhancement of photocatalytic hydrogen production by liquid phase plasma irradiation on metal-loaded TiO_2/carbon nanofiber photocatalysts. International Journal of Hydrogen Energy **43**(24): 11422-11429.

Cifani, P., W. R. Michalek, G. J. M. Priems, J. G. M. Kuerten, C. W. M. van der Geld and B. J. Geurts (2016). A comparison between the surface compression method and an interface reconstruction method for the VOF approach. Computers & Fluids **136**: 421-435.

Clift, R. (1978). Bubbles, drops, and particles. New York, Academic Press.

Cossar, E., F. Murphy and E. A. Baranova (2022). Nickel-based anodes in anion exchange membrane water electrolysis: a review. Journal of Chemical Technology & Biotechnology **97**(7): 1611-1624.

Cox, R. G. and S. K. Hsu (1977). The lateral migration of solid particles in a laminar flow near a plane. International Journal of Multiphase Flow **3**(3): 201-222.

David, M., C. Ocampo-Martínez and R. Sánchez-Peña (2019). Advances in alkaline water electrolyzers: A review. Journal of Energy Storage **23**: 392-403.

Davidson, J. F. and B. O. G. Schüler (1997). Bubble formation at an orifice in a viscous liquid. Chemical Engineering Research and Design **75**: S105-S115.

Davis, J. T., J. Qi, X. Fan, J. C. Bui and D. V. Esposito (2018). Floating membraneless PV-electrolyzer based on buoyancy-driven product separation. International Journal of Hydrogen Energy **43**(3): 1224-1238.

Dawood, F., M. Anda and G. M. Shafiullah (2020). Hydrogen production for energy: An overview. International Journal of Hydrogen Energy **45**(7): 3847-3869.

De, B. S., P. Kumar, N. Khare, J.-L. Luo, A. Elias and S. Basu (2021). Microfabrication of the ammonia plasma-activated nickel nitride–nickel thin film for overall water splitting in the microfluidic membraneless electrolyzer. ACS Applied Energy Materials **4**(9): 9639-9652.

De, B. S., A. Singh, A. Elias, N. Khare and S. Basu (2020). An electrochemical neutralization energy-assisted membrane-less microfluidic reactor for water electrolysis. Sustainable Energy & Fuels **4**(12): 6234-6244.

Diogo, M. F. S., A. C. S. César and L. F. José (2013). Hydrogen production by alkaline water electrolysis. Química Nova **36**(8): 1176-1193.

Don, W. G. and H. P. Robert (2008). Perry's Chemical Engineers' Handbook, Eighth Edition. New York, McGraw-Hill Education.

Du, Z., C. Liu, J. Zhai, X. Guo, Y. Xiong, W. Su and G. He (2021). A review of hydrogen purification technologies for fuel cell vehicles. Catalysts **11**(3): 393.

Dubey, P. K., A. S. K. Sinha, S. Talapatra, N. Koratkar, P. M. Ajayan and O. N. Srivastava (2010). Hydrogen generation by water electrolysis using carbon nanotube anode. International Journal of Hydrogen Energy **35**(9): 3945-3950.

Duhar, G. and C. Colin (2006). Dynamics of bubble growth and detachment in a viscous shear flow. Physics of Fluids **18**(7): 077101.

Eigeldinger, J. and H. Vogt (2000). The bubble coverage of gas-evolving electrodes in a flowing electrolyte. Electrochimica Acta **45**(27): 4449-4456.

El-Emam, R. S. and H. Özcan (2019). Comprehensive review on the techno-economics of sustainable large-scale clean hydrogen production. Journal of Cleaner Production **220**: 593-609.

Erdener, B. C., B. Sergi, O. J. Guerra, A. Lazaro Chueca, K. Pambour, C. Brancucci and B.-M. Hodge (2023). A review of technical and regulatory limits for hydrogen blending in natural gas pipelines. International Journal of Hydrogen Energy **48**(14): 5595-5617.

Esposito, D. V. (2017). Membraneless electrolyzers for low-cost hydrogen production in a renewable energy future. Joule **1**(4): 651-658.

Esposito, D. V., S. T. Hunt, Y. C. Kimmel and J. G. Chen (2012). A new class of electrocatalysts for hydrogen production from water electrolysis: metal monolayers supported on low-cost transition metal carbides. Journal of the American Chemical Society **134**(6): 3025.

Evangelio, A., F. Campo-Cortés and J. M. Gordillo (2015). Pressure gradient induced generation of microbubbles. Journal of Fluid Mechanics **778**: 653-668.

Feng, J., H. H. Hu and D. D. Joseph (1994). Direct simulation of initial value problems for the motion of solid bodies in a Newtonian fluid. Part 2. Couette and Poiseuille flows. Journal of Fluid Mechanics **277**: 271-301.

Fernández, D., M. Martine, A. Meagher, M. E. Möbius and J. M. D. Coey (2012). Stabilizing effect of a magnetic field on a gas bubble produced at a microelectrode. Electrochemistry Communications **18**: 28-32.

Fernandez, D., P. Maurer, M. Martine, J. M. Coey and M. E. Mobius (2014). Bubble formation at a gas-evolving microelectrode. Langmuir **30**(43): 13065-13074.

Fiegenbaum, F., E. M. Martini, M. O. de Souza, M. R. Becker and R. F. de Souza (2013). Hydrogen production by water electrolysis using tetra-alkyl-ammonium-sulfonic acid ionic liquid electrolytes. Journal of Power Sources **243**: 822-825.

Funk, J. E. and R. M. Reinstrom (1966). Energy requirements in production of hydrogen from water. Industrial & Engineering Chemistry Process Design and Development **5**(3): 336-342.

Ge, S., L. Xinchun, Q. Weizhong, C. Wei, S. Congyu, S. Yongjun and Y. Xiaoqiu (2012). Recombination of hydrogen and oxygen in fluidized bed reactor with different gas distributors. Energy Procedia **29**: 552-558.

Gillespie, M. I. and R. J. Kriek (2017). Hydrogen production from a rectangular horizontal filter press Divergent Electrode-Flow-Through (DEFT™) alkaline electrolysis stack. Journal of Power Sources **372**: 252-259.

Gillespie, M. I. and R. J. Kriek (2018). Scalable hydrogen production from a mono-circular filter press Divergent Electrode-Flow-Through alkaline electrolysis stack. Journal of Power Sources **397**: 204-213.

Gillespie, M. I., F. van der Merwe and R. J. Kriek (2015). Performance evaluation of a membraneless divergent electrode-flow-through (DEFT) alkaline electrolyser based on optimisation of electrolytic flow and electrode gap. Journal of Power Sources **293**: 228-235.

Gim, B., K. J. Boo and S. M. Cho (2012). A transportation model approach for constructing the cost effective central hydrogen supply system in Korea. International Journal of Hydrogen Energy **37**(2): 1162-1172.

Godula-Jopek, A., D. Stolten and C. Bourasseau (2015). Hydrogen production : by electrolysis. Weinheim, Germany, WILEY-VCH Verlag GmbH & Co. KGaA.

Goldstein, S., J.-M. Borgard and X. Vitart (2005). Upper bound and best estimate of the efficiency of the iodine sulphur cycle. International Journal of Hydrogen Energy **30**(6): 619-626.

Gorensek, M. B., C. Corgnale and W. A. Summers (2017). Development of the hybrid sulfur cycle for use with concentrated solar heat. I. Conceptual design. International Journal of Hydrogen Energy **42**(33): 20939-20954.

H. Hashemi, S. M., P. Karnakov, P. Hadikhani, E. Chinello, S. Litvinov, C. Moser, P. Koumoutsakos and D. Psaltis (2019). A versatile and membrane-less electrochemical reactor for the electrolysis of water and brine. Energy & Environmental Science **12**(5): 1592-1604.

H. Hashemi, S. M., M. A. Modestino and D. Psaltis (2015). A membrane-less electrolyzer for hydrogen production across the pH scale. Energy & Environmental Science **8**(7): 2003-2009.

Hadikhani, P., S. M. H. Hashemi and D. Psaltis (2020). The Impact of surfactants on the inertial separation of bubbles in microfluidic electrolyzers. Journal of The Electrochemical Society **167**(13): 134504.

Hadikhani, P., S. M. H. Hashemi, G. Balestra, L. Zhu, M. A. Modestino, F. Gallaire and D. Psaltis (2018). Inertial manipulation of bubbles in rectangular microfluidic channels. Lab Chip **18**(7): 1035-1046.

Hadikhani, P., S. M. H. Hashemi, S. A. Schenk and D. Psaltis (2021). A membrane-less electrolyzer with porous walls for high throughput and pure hydrogen production. Sustain Energy Fuels **5**(9): 2419-2432.

Haring, M. M. (1936). Principles and applications of electrochemistry. Vol. II. Applications (Koehler, W. A.). Journal of Chemical Education **13**(2): 97.

Haverkort, J. W. and H. Rajaei (2021). Voltage losses in zero-gap alkaline water electrolysis. Journal of Power Sources **497**: 229864.

Hodges, A., A. L. Hoang, G. Tsekouras, K. Wagner, C. Y. Lee, G. F. Swiegers and G. G. Wallace (2022). A high-performance capillary-fed electrolysis cell promises more cost-competitive renewable hydrogen. Nature Communications **13**(1): 1304.

Holmes-Gentle, I., F. Hoffmann, C. A. Mesa and K. Hellgardt (2017). Membrane-less photoelectrochemical cells: product separation by hydrodynamic control. Sustainable Energy & Fuels **1**(5): 1184-1198.

Hreiz, R., L. Abdelouahed, D. Fünfschilling and F. Lapicque (2015). Electrogenerated bubbles induced convection in narrow vertical cells: A review. Chemical Engineering Research and Design **100**: 268-281.

Hreiz, R., L. Abdelouahed, D. Fünfschilling and F. Lapicque (2015). Electrogenerated bubbles induced convection in narrow vertical cells: PIV measurements and Euler–Lagrange CFD simulation. Chemical Engineering Science **134**: 138-152.

Hua, D., J. Huang, E. Fabbri, M. Rafique and B. Song (2022). Development of anion exchange membrane water electrolysis and the associated challenges: a review. ChemElectroChem **10**(1): e202200999.

Hydrogen and Fuel Cell Technologies Office. Hydrogen Storage. Retrieved 3rd Aug, 2023, from https://www.energy.gov/eere/fuelcells/hydrogen-storage.

Hydrogen Council. (2023). Hydrogen Insights 2023. Retrieved 10th Aug, 2023, from https://hydrogencouncil.com/en/hydrogen-insights-2023/.

International Energy Agency. (2022). World Energy Outlook 2022. Retrieved 15th Jul, 2023, from https://www.iea.org/reports/world-energy-outlook-2022.

Jang, J.-Y. and Y.-F. Gan (2018). Numerical simulation of a two-phase flow for the acrylonitrile electrolytic adiponitrile process in a vertical/horizontal electrolysis cell. Energies **11**(10): 2731.

Johnston, C., M. H. Ali Khan, R. Amal, R. Daiyan and I. MacGill (2022). Shipping the sunshine: an open-source model for costing renewable hydrogen transport from Australia. International Journal of Hydrogen Energy **47**(47): 20362-20377.

Jones, S. F., G. M. Evans and K. P. Galvin (1999). Bubble nucleation from gas cavities — a review. Advances in Colloid and Interface Science **80**(1): 27-50.

Kazakis, N. A., A. A. Mouza and S. V. Paras (2008). Experimental study of bubble formation at metal porous spargers: Effect of liquid properties and sparger characteristics on the initial bubble size distribution. Chemical Engineering Journal **137**(2): 265-281.

Kim, G. J., J. H. Shin and S. Chang Hong (2020). Study on the role of Pt and Pd in Pt–Pd/TiO_2 bimetallic catalyst for H_2 oxidation at room temperature. International Journal of Hydrogen Energy **45**(35): 17276-17286.

Kim, T., Y. Song, J. Kang, S. K. Kim and S. Kim (2022). A review of recent advances in hydrogen purification for selective removal of oxygen: Deoxo catalysts and reactor systems. International Journal of Hydrogen Energy **47**(59): 24817-24834.

Kim, Y. C., B. Van Dang, R. Taylor and T. Barber (2021). Controlled generation of single microbubbles. Experiments in Fluids **62**(10): 220.

Klausner, J. F., R. Mei, D. M. Bernhard and L. Z. Zeng (1993). Vapor bubble departure in forced convection boiling. International Journal of Heat and Mass Transfer **36**(3): 651-662.

Kodým, R., V. Fíla, D. Šnita and K. Bouzek (2016). Poisson–Nernst–Planck model of multiple ion transport across an ion-selective membrane under conditions close to chlor-alkali electrolysis. Journal of Applied Electrochemistry **46**(6): 679-694.

Kolev, N. I. (2007). Bubble Departure Diameter. Multiphase Flow Dynamics 2: Thermal and Mechanical Interactions. N. I. Kolev. Berlin, Heidelberg, Springer Berlin Heidelberg**:** 417-438.

Kraglund, M., D. Aili, K. Jankova, E. Christensen, Q. Li and J. Jensen (2016). Zero-gap alkaline water electrolysis using ion-solvating polymer electrolyte membranes at reduced KOH concentrations. Journal Of The Electrochemical Society **163**(11): F3125-F3131.

Krasae-in, S., J. H. Stang and P. Neksa (2010). Development of large-scale hydrogen liquefaction processes from 1898 to 2009. International Journal of Hydrogen Energy **35**(10): 4524-4533.

Kumar, R. and N. K. Kuloor (1970). The formation of bubbles and drops. Advances in Chemical Engineering. T. B. Drew, G. R. Cokelet, J. W. Hoopes and T. Vermeulen, Academic Press. **8:** 255-368.

Lafaurie, B., C. Nardone, R. Scardovelli, S. Zaleski and G. Zanetti (1994). Modelling merging and fragmentation in multiphase flows with SURFER. Journal of Computational Physics **113**(1): 134-147.

Lafmejani, S. S., A. C. Olesen and S. K. Kær (2017). VOF modelling of gas–liquid flow in PEM water electrolysis cell micro-channels. International Journal of Hydrogen Energy **42**(26): 16333-16344.

Lamy, C. (2016). From hydrogen production by water electrolysis to its utilization in a PEM fuel cell or in a SO fuel cell: Some considerations on the energy efficiencies. International Journal of Hydrogen Energy **41**(34): 15415-15425.

Langlois, S. and F. Coeuret (1989). Flow-through and flow-by porous electrodes of nickel foam. I. Material characterization. Journal of Applied Electrochemistry **19**(1): 43-50.

Langlois, S. and F. Coeuret (1989). Flow-through and flow-by porous electrodes of nickel foam. II. Diffusion-convective mass transfer between the electrolyte and the foam. Journal of Applied Electrochemistry **19**(1): 51-60.

Lee, H. and S. Balachandar (2010). Drag and lift forces on a spherical particle moving on a wall in a shear flow at finite Re. Journal of Fluid Mechanics **657**: 89-125.

Lee, J. W., D. K. Sohn and H. S. Ko (2019). Study on bubble visualization of gas-evolving electrolysis in forced convective electrolyte. Experiments in Fluids **60**(10): 156.

Lee, W. and J.-Y. Lee (2020). Experiment and modeling of lift force acting on single high Reynolds number bubbles rising in linear shear flow. Experimental Thermal and Fluid Science **115**: 110085.

Legendre, D. and J. Magnaudet (1997). A note on the lift force on a spherical bubble or drop in a low-Reynolds-number shear flow. Physics of Fluids **9**(11): 3572-3574.

Legendre, D. and J. Magnaudet (1998). The lift force on a spherical bubble in a viscous linear shear flow. Journal of Fluid Mechanics **368**: 81-126.

Leroy, R. L. (1980). The thermodynamics of aqueous water electrolysis. Journal of The Electrochemical Society **127**(9): 1954.

Lesage, F. J. and F. Marois (2013). Experimental and numerical analysis of quasi-static bubble size and shape characteristics at detachment. International Journal of Heat and Mass Transfer **64**: 53-69.

Li, R. (2017). Latest progress in hydrogen production from solar water splitting via photocatalysis, photoelectrochemical, and photovoltaic-photoelectrochemical solutions. Chinese Journal of Catalysis **38**(1): 5-12.

Li, X., F. C. Walsh and D. Pletcher (2011). Nickel based electrocatalysts for oxygen evolution in high current density, alkaline water electrolysers. Phys Chem Chem Phys **13**(3): 1162-1167.

Li, Z., Y. Zhao, X. Song, H. Yu, S. Jiang and M. Ishii (2016). Experimental investigation of single small bubble motion in linear shear flow in water. Nuclear Engineering and Design **305**: 334-346.

Liu, C. L., Z. Sun, G. M. Lu and J. G. Yu (2018). Hydrodynamic characteristics of the two-phase flow field at gas-evolving electrodes: numerical and experimental studies. R Soc Open Sci **5**(5): 171255.

Liu, G., H. Hagelin-Weaver and B. Welt (2023). A concise review of catalytic synthesis of methanol from synthesis gas. Waste **1**(1): 228-248.

Liu, Q. and Z.-H. Luo (2018). CFD-VOF-DPM simulations of bubble rising and coalescence in low hold-up particle-liquid suspension systems. Powder Technology **339**: 459-469.

Lo Faro, M., S. C. Zignani, S. Trocino, V. Antonucci and A. S. Aricò (2019). New insights on the co-electrolysis of CO_2 and H_2O through a solid oxide electrolyser operating at intermediate temperatures. Electrochimica Acta **296**: 458-464.

Loutzenhiser, P. G. and A. P. Muroyama (2017). A review of the state-of-the-art in solar-driven gasification processes with carbonaceous materials. Solar Energy **156**: 93-100.

Lu, P. W. T. and R. L. Ammon (1982). Sulfur dioxide depolarized electrolysis for hydrogen production: Development status. International Journal of Hydrogen Energy **7**(7): 563-575.

Lubetkin, S. (2003). Thermal marangoni effects on gas bubbles are generally accompanied by solutal marangoni effects. Langmuir **19**(26): 10774-10778.

Luberti, M. and H. Ahn (2022). Review of polybed pressure swing adsorption for hydrogen purification. International Journal of Hydrogen Energy **47**(20): 10911-10933.

Lucentini, I., X. Garcia, X. Vendrell and J. Llorca (2021). Review of the decomposition of ammonia to generate hydrogen. Industrial & Engineering Chemistry Research **60**(51): 18560-18611.

Luo, L. and H. S. White (2013). Electrogeneration of single nanobubbles at sub-50-nm-radius platinum nanodisk electrodes. Langmuir **29**(35): 11169-11175.

Maciel, P., T. Nierhaus, S. V. Damme, H. V. Parys, J. Deconinck and A. Hubin (2009). New model for gas evolving electrodes based on supersaturation. Electrochemistry Communications **11**(4): 875-877.

Maeda, K. and K. Domen (2010). Photocatalytic water splitting: recent progress and future challenges. The Journal of Physical Chemistry Letters **1**(18): 2655-2661.

Magnaudet, J., S. H. U. Takagi and D. Legendre (2003). Drag, deformation and lateral migration of a buoyant drop moving near a wall. Journal of Fluid Mechanics **476**: 115-157.

Marini, S., P. Salvi, P. Nelli, R. Pesenti, M. Villa, M. Berrettoni, G. Zangari and Y. Kiros (2012). Advanced alkaline water electrolysis. Electrochimica Acta **82**: 384-391.

Martel, J. M. and M. Toner (2014). Inertial focusing in microfluidics. Annu Rev Biomed Eng **16**: 371-396.

McLaughlin, J. B. (2006). Inertial migration of a small sphere in linear shear flows. Journal of Fluid Mechanics **224**: 261-274.

Mei, R. and J. F. Klausner (1994). Shear lift force on spherical bubbles. International Journal of Heat and Fluid Flow **15**(1): 62-65.

Mei, R., J. F. Klausner and C. J. Lawrence (1994). A note on the history force on a spherical bubble at finite Reynolds number. Physics of Fluids **6**(1): 418-420.

Meulenbroek, A. M., A. W. Vreman and N. G. Deen (2021). Competing Marangoni effects form a stagnant cap on the interface of a hydrogen bubble attached to a microelectrode. Electrochimica Acta **385**.

Modisha, P. M., C. N. M. Ouma, R. Garidzirai, P. Wasserscheid and D. Bessarabov (2019). The prospect of hydrogen storage using liquid organic hydrogen carriers. Energy & Fuels **33**(4): 2778-2796.

Mohamed, N. M., R. Bashiri, F. K. Chong, S. Sufian and S. Kakooei (2015). Photoelectrochemical behavior of bimetallic Cu–Ni and monometallic Cu, Ni doped TiO2 for hydrogen production. International Journal of Hydrogen Energy **40**(40): 14031-14038.

Moradpoor, I., S. Syri and A. Santasalo-Aarnio (2023). Green hydrogen production for oil refining – Finnish case. Renewable and Sustainable Energy Reviews **175**: 113159.

Mortazavi, S. and G. Tryggvason (2000). A numerical study of the motion of drops in Poiseuille flow. Part 1. Lateral migration of one drop. Journal of Fluid Mechanics **411**: 325-350.

Murugan, A. and A. S. Brown (2015). Review of purity analysis methods for performing quality assurance of fuel cell hydrogen. International Journal of Hydrogen Energy **40**(11): 4219-4233.

Nagai, N., M. Takeuchi and T. Furuta (2006). Effects of bubbles between electrodes on alkaline water electrolysis efficiency under forced convection of electrolyte. 16th World Hydrogen Energy Conference 2006, WHEC 2006 **1**: 100-109.

Nagai, N., M. Takeuchi, T. Kimura and T. Oka (2003). Existence of optimum space between electrodes on hydrogen production by water electrolysis. International Journal of Hydrogen Energy **28**(1): 35-41.

Nagai, N., M. Takeuchi and M. Nakao (2003). Influences of bubbles between electrodes onto efficiency of alkaline water electrolysis. Proceedings of PSFVIP-4, Chamonix, France.

Nagy, Z. (1976). Calculations on the effect of gas evolution on the current-overpotential relation and current distribution in electrolytic cells. Journal of Applied Electrochemistry **6**(2): 171-181.

Najafi, A. S., Z. Xu and J. Masliyah (2008). Single micro-bubble generation by pressure pulse technique. Chemical Engineering Science **63**(7): 1779-1787.

Nakamura, T. (1977). Hydrogen production from water utilizing solar heat at high temperatures. Solar Energy **19**(5): 467-475.

Ni, M., M. K. H. Leung, D. Y. C. Leung and K. Sumathy (2007). A review and recent developments in photocatalytic water-splitting using TiO2 for hydrogen production. Renewable and Sustainable Energy Reviews **11**(3): 401-425.

Nikonenko, V. V., K. A. Lebedev and S. S. Suleimanov (2009). Influence of the convective term in the Nernst-Planck equation on properties of ion transport through a layer of solution or membrane. Russian Journal of Electrochemistry **45**(2): 160-169.

Noring, J. E., R. B. Diver and E. A. Fletcher (1981). Hydrogen and oxygen from water—V. the ROC system. Energy **6**(2): 109-121.

O'Neil, G. D., C. D. Christian, D. E. Brown and D. V. Esposito (2016). Hydrogen production with a simple and scalable membraneless electrolyzer. Journal of The Electrochemical Society **163**(11): F3012-F3019.

Obata, K., A. Mokeddem and F. F. Abdi (2021). Multiphase fluid dynamics simulations of product crossover in solar-driven, membrane-less water splitting. Cell Reports Physical Science **2**(3): 100358.

Ohl, C. D. (2001). Generator for single bubbles of controllable size. Review of scientific instruments **72**(1): 252-254.

Ostmann, S. and R. Schwarze (2018). A compact device for the deterministic generation of medium-sized bubbles. Rev Sci Instrum **89**(12): 125108.

Özcan, H. and I. Dincer (2016). Comparative performance assessment of three configurations of magnesium–chlorine cycle. International Journal of Hydrogen Energy **41**(2): 845-856.

Özcan, H. and I. Dincer (2018). Experimental investigation of an improved version of the four-step magnesium-chlorine cycle. International Journal of Hydrogen Energy **43**(11): 5808-5819.

Pacheco Tanaka, D. A., J. A. Medrano, J. L. Viviente Sole and F. Gallucci (2020). 1 - Metallic membranes for hydrogen separation. Current Trends and Future Developments on (Bio-) Membranes. A. Basile and F. Gallucci, Elsevier**:** 1-29.

Pang, X., J. T. Davis, A. D. Harvey and D. V. Esposito (2020). Framework for evaluating the performance limits of membraneless electrolyzers. Energy & Environmental Science **13**(10): 3663-3678.

Parkinson, L., R. Sedev, D. Fornasiero and J. Ralston (2008). The terminal rise velocity of 10-100 microm diameter bubbles in water. J Colloid Interface Sci **322**(1): 168-172.

Pereiro, I., A. Fomitcheva Khartchenko, L. Petrini and G. V. Kaigala (2019). Nip the bubble in the bud: a guide to avoid gas nucleation in microfluidics. Lab Chip **19**(14): 2296-2314.

Ping, Z., W. Laijun, C. Songzhe and X. Jingming (2018). Progress of nuclear hydrogen production through the iodine–sulfur process in China. Renewable and Sustainable Energy Reviews **81**: 1802-1812.

Pistidda, C. (2021). Solid-state hydrogen storage for a decarbonized society. Hydrogen **2**(4): 428-443.

Pistorius, P. C. (2014). Bubbles in process metallurgy. Treatise on Process Metallurgy**:** 179-196.

Raffel, M. (2018). Particle Image Velocimetry: A Practical Guide. Cham, Springer International Publishing.

Rajaei, H., A. Rajora and J. W. Haverkort (2021). Design of membraneless gas-evolving flow-through porous electrodes. Journal of Power Sources **491**.

Rarotra, S., T. K. Mandal and D. Bandyopadhyay (2017). Microfluidic electrolyzers for production and separation of hydrogen from sea water using naturally abundant solar energy. Energy Technology **5**(8): 1208-1217.

Rarotra, S., S. Shahid, M. De, T. K. Mandal and D. Bandyopadhyay (2021). Graphite/RGO coated paper μ-electrolyzers for production and separation of hydrogen and oxygen. Energy **228**.

Renardy, Y. and M. Renardy (2002). PROST: A parabolic reconstruction of surface tension for the Volume-of-Fluid method. Journal of Computational Physics **183**(2): 400-421.

Riegel, H., J. Mitrovic and K. Stephan (1998). Role of mass transfer on hydrogen evolution in aqueous media. Journal of Applied Electrochemistry **28**(1): 10-17.

Rodríguez, J. and E. Amores (2020). CFD modeling and experimental validation of an alkaline water electrolysis cell for hydrogen production. Processes **8**(12): 1634.

Rue, R. E. D. L. and C. W. Tobias (1959). On the conductivity of dispersions. Journal of The Electrochemical Society **106**(9): 827.

Sá, S., H. Silva, L. Brandão, J. M. Sousa and A. Mendes (2010). Catalysts for methanol steam reforming—A review. Applied Catalysis B: Environmental **99**(1-2): 43-57.

Saffman, P. G. (1965). The lift on a small sphere in a slow shear flow. Journal of Fluid Mechanics **22**(2): 385-400.

Salehmin, M. N. I., T. Husaini, J. Goh and A. B. Sulong (2022). High-pressure PEM water electrolyser: A review on challenges and mitigation strategies towards green and low-cost hydrogen production. Energy Conversion and Management **268**: 115985.

Samir De, B., J. Cunningham, N. Khare, J.-L. Luo, A. Elias and S. Basu (2022). Hydrogen generation and utilization in a two-phase flow membraneless microfluidic electrolyzer-fuel cell tandem operation for micropower application. Applied Energy **305**: 117945.

Sanada, T. and K. Abe (2013). Generation of single bubbles of various sizes using a slitting elastic tube. Review of Scientific Instruments 84(8): 085106.

Schiller, L., Naumann, A (1933). Über die grundlegenden Berechnungen bei der Schwerkraftauĩereitung. Zeitschrift des Vereins Deutscher Ingenieure 77: 318-320.

Schmidt, O., A. Gambhir, I. Staffell, A. Hawkes, J. Nelson and S. Few (2017). Future cost and performance of water electrolysis: An expert elicitation study. International Journal of Hydrogen Energy **42**(52): 30470-30492.

Segré, G. and A. Silberberg (1961). Radial particle displacements in poiseuille flow of suspensions. Nature **189**(4760): 209-210.

Shamim, R. O., I. Dincer, G. F. Naterer and C. Zamfirescu (2014). Experimental investigation of a solar tower based photocatalytic hydrogen production system. International Journal of Hydrogen Energy **39**(11): 5546-5556.

Shi, J., N. Wan, L. Li, Z. Li and H. Han (2022). Review on treatment technologies of coal gasification wastewater in China. Journal of Cleaner Production **333**: 130166.

Shi, P. and R. Rzehak (2019). Lift forces on solid spherical particles in unbounded flows. Chemical Engineering Science **208**: 115145.

Shi, P. and R. Rzehak (2020). Lift forces on solid spherical particles in wall-bounded flows. Chemical Engineering Science **211**: 115264.

Shi, P., R. Rzehak, D. Lucas and J. Magnaudet (2020). Hydrodynamic forces on a clean spherical bubble translating in a wall-bounded linear shear flow. Physical Review Fluids **5**(7): 073601.

Sillen, C. W. M. P., E. Barendrecht, L. J. J. Janssen and S. J. D. van Stralen (1982). Gas bubble behaviour during water electrolysis. International Journal of Hydrogen Energy **7**(7): 577-587.

Sim, K.-S., Y.-M. Son and J.-W. Kim (1993). Some thermochemical cycles composed of copper compounds with three-step reactions. International Journal of Hydrogen Energy **18**(4): 287-290.

Simpson, M. F., S. D. Herrmann and B. D. Boyle (2006). A hybrid thermochemical electrolytic process for hydrogen production based on the reverse Deacon reaction. International Journal of Hydrogen Energy **31**(9): 1241-1246.

Solovey, V. V., A. A. Shevchenko, M. M. Zipunnikov, A. L. Kotenko, N. T. Khiem, B. D. Tri and T. T. Hai (2022). Development of high pressure membraneless alkaline electrolyzer. International Journal of Hydrogen Energy **47**(11): 6975-6985.

Struck, B. D., R. Junginger, D. Boltersdorf and J. Gehrmann (1980). The anodic oxidation of sulfur dioxide in the sulfuric acid hybrid cycle. International Journal of Hydrogen Energy **5**(5): 487-497.

Struyven, F., Z. Guo, D. F. Fletcher, M. Kim, R. Inguanta, M. Sellier and P. Mandin (2022). Suitability of the VOF Approach to Model an Electrogenerated Bubble with Marangoni Micro-Convection Flow. Fluids **7**(8).

Sun, Y. and Y. Frank Cheng (2022). Hydrogen-induced degradation of high-strength steel pipeline welds: A critical review. Engineering Failure Analysis **133**: 105985.

Sussman, M. and E. G. Puckett (2000). A Coupled Level Set and Volume-of-Fluid Method for Computing 3D and Axisymmetric Incompressible Two-Phase Flows. Journal of Computational Physics **162**(2): 301-337.

Swiegers, G. F., A. L. Hoang, A. Hodges, G. Tsekouras, C.-Y. Lee, K. Wagner and G. Wallace (2022). Current status of membraneless water electrolysis cells. Current Opinion in Electrochemistry **32**: 100881.

Takemura, F. and J. Magnaudet (2003). The transverse force on clean and contaminated bubbles rising near a vertical wall at moderate Reynolds number. Journal of Fluid Mechanics **495**: 235-253.

Takemura, F. and J. Magnaudet (2009). Lateral migration of a small spherical buoyant particle in a wall-bounded linear shear flow. Physics of Fluids **21**(8): 083303.

Takemura, F., J. Magnaudet and P. Dimitrakopoulos (2009). Migration and deformation of bubbles rising in a wall-bounded shear flow at finite Reynolds number. Journal of Fluid Mechanics **634**: 463.

Takemura, F., S. H. U. Takagi, J. Magnaudet and Y. Matsumoto (2002). Drag and lift forces on a bubble rising near a vertical wall in a viscous liquid. Journal of Fluid Mechanics **461**: 277-300.

Talabi, O. O., A. E. Dorfi, G. D. O'Neil and D. V. Esposito (2017). Membraneless electrolyzers for the simultaneous production of acid and base. Chem Commun (Camb) **53**(57): 8006-8009.

Tanaka, Y., K. Kikuchi, Y. Saihara and Z. Ogumi (2005). Bubble visualization and electrolyte dependency of dissolving hydrogen in electrolyzed water using Solid-Polymer-Electrolyte. Electrochimica Acta **50**(25-26): 5229-5236.

Taqieddin, A., R. Nazari, L. Rajic and A. Alshawabkeh (2017). Review-Physicochemical hydrodynamics of gas bubbles in two phase electrochemical systems. Journal of the Electrochemical Society **164**(13): E448-E459.

Tiwari, P., G. Tsekouras, K. Wagner, G. F. Swiegers and G. G. Wallace (2019). A new class of bubble-free water electrolyzer that is intrinsically highly efficient. International Journal of Hydrogen Energy **44**(42): 23568-23579.

Tjaden, B., S. J. Cooper, D. J. L. Brett, D. Kramer and P. R. Shearing (2016). On the origin and application of the Bruggeman correlation for analysing transport phenomena in electrochemical systems. Current Opinion in Chemical Engineering **12**: 44-51.

Tobias, C. W. (1959). Effect of gas evolution on current distribution and ohmic resistance in electrolyzers. Journal of The Electrochemical Society **106**(9): 833.

Tomiyama, A. (1998). Struggle with computational bubble dynamics. Multiphase Science and Technology **10**(4): 369-405.

Tomiyama, A., H. Tamai, I. Zun and S. Hosokawa (2002). Transverse migration of single bubbles in simple shear flows. Chemical Engineering Science **57**(11): 1849-1858.

Tsekouras, G., R. Terrett, Z. Yu, Z. Cheng, G. F. Swiegers, T. Tsuzuki, R. Stranger and R. J. Pace (2021). Insights into the phenomenon of ‘bubble-free’ electrocatalytic oxygen evolution from water. Sustainable Energy & Fuels **5**(3): 808-819.

Vejrazka, J., M. Fujasová, P. Stanovsky, M. C. Ruzicka and J. Drahoš (2008). Bubbling controlled by needle movement. Fluid Dynamics Research **40**(7-8): 521-533.

Vogt, H. (1983). Frictional pressure drop of pure and contaminated bubble-electrolyte dispersions in electrochemical reactors. Journal of Applied Electrochemistry **13**(6): 705-707.

Vogt, H. (1983). Gas-evolving electrodes. Comprehensive treatise of electrochemistry: Electrodics: Transport. E. Yeager, J. O. M. Bockris, B. E. Conway and S. Sarangapani. Boston, MA, Springer US**:** 445-489.

Vogt, H. (2012). The actual current density of gas-evolving electrodes—Notes on the bubble coverage. Electrochimica Acta **78**: 183-187.

Vogt, H. (2013). Heat transfer in boiling and mass transfer in gas evolution at electrodes – The analogy and its limits. International Journal of Heat and Mass Transfer **59**: 191-197.

Vogt, H. (2016). Single-phase free convective mass transfer in electrochemical reactors. Canadian Journal of Chemical Engineering **94**(2): 368-373.

Vogt, H. (2017). The quantities affecting the bubble coverage of gas-evolving electrodes. Electrochimica Acta **235**: 495-499.

Wan, Z., Y. Tao, J. Shao, Y. Zhang and H. You (2021). Ammonia as an effective hydrogen carrier and a clean fuel for solid oxide fuel cells. Energy Conversion and Management **228**: 113729.

Wang, R. R., Y. Q. Zhao, A. Babich, D. Senk and X. Y. Fan (2021). Hydrogen direct reduction (H-DR) in steel industry—An overview of challenges and opportunities. Journal of Cleaner Production **329**: 129797.

Wang, S., A. Lu and C. J. Zhong (2021). Hydrogen production from water electrolysis: role of catalysts. Nano Converg **8**(1): 4.

Wentorf Jr, R. H. and R. E. Hanneman (1974). Thermochemical hydrogen generation. Science **185**(4148): 311-319.

Xiao, J., L. Fang, P. Bénard and R. Chahine (2018). Parametric study of pressure swing adsorption cycle for hydrogen purification using Cu-BTC. International Journal of Hydrogen Energy **43**(30): 13962-13974.

Xu, W.-t., S.-s. Li, L.-m. Pan and Z.-c. Li (2021). Experimental investigation about the lift force of a single bubble in the water at a linear shear flow. International Journal of Multiphase Flow **145**: 103819.

Xu, Y., C. Wang, Y. Huang and J. Fu (2021). Recent advances in electrocatalysts for neutral and large-current-density water electrolysis. Nano Energy **80**: 105545.

Yahiaoui, S. and F. Feuillebois (2010). Lift on a sphere moving near a wall in a parabolic flow. Journal of Fluid Mechanics **662**: 447-474.

Yang, B., M. Jafarian, N. Freidoonimehr and M. Arjomandi (2022). Trajectory of a spherical bubble rising in a fully developed laminar flow. International Journal of Multiphase Flow **157**: 104250.

Yang, J., Y. Li and H. Tan (2023). Study on performance comparison of two hydrogen liquefaction processes based on the Claude cycle and the Brayton refrigeration cycle. Processes **11**(3): 932.

Yang, X., F. Karnbach, M. Uhlemann, S. Odenbach and K. Eckert (2015). Dynamics of single hydrogen bubbles at a platinum microelectrode. Langmuir **31**(29): 8184-8193.

Yilmaz, C. and M. Kanoglu (2014). Thermodynamic evaluation of geothermal energy powered hydrogen production by PEM water electrolysis. Energy **69**: 592.

Yin, L. and Y. Ju (2020). Process optimization and analysis of a novel hydrogen liquefaction cycle. International Journal of Refrigeration **110**: 219-230.

Yip, H. L., A. Srna, A. C. Y. Yuen, S. Kook, R. A. Taylor, G. H. Yeoh, P. R. Medwell and Q. N. Chan (2019). A review of hydrogen direct injection for internal combustion engines: Towards Carbon-Free Combustion. Applied Sciences **9**(22): 4842.

Yue, M., H. Lambert, E. Pahon, R. Roche, S. Jemei and D. Hissel (2021). Hydrogen energy systems: A critical review of technologies, applications, trends and challenges. Renewable and Sustainable Energy Reviews **146**: 111180.

Yun, B.-J., A. Splawski, S. Lo and C.-H. Song (2012). Prediction of a subcooled boiling flow with advanced two-phase flow models. Nuclear Engineering and Design **253**: 351-359.

Zahedi, S., M. Kronbichler and G. Kreiss (2012). Spurious currents in finite element based level set methods for two-phase flow. International Journal for Numerical Methods in Fluids **69**(9): 1433-1456.

Zarghami, A., N. G. Deen and A. W. Vreman (2020). CFD modeling of multiphase flow in an alkaline water electrolyzer. Chemical Engineering Science **227**: 115926.

Zeng, K. and D. Zhang (2010). Recent progress in alkaline water electrolysis for hydrogen production and applications. Progress in Energy and Combustion Science **36**(3): 307-326.

Zeng, L., S. Balachandar and P. Fischer (2005). Wall-induced forces on a rigid sphere at finite Reynolds number. Journal of Fluid Mechanics **536**: 1-25.

Zeng, L., F. Najjar, S. Balachandar and P. Fischer (2009). Forces on a finite-sized particle located close to a wall in a linear shear flow. Physics of Fluids **21**(3): 033302.

Zhang, D. and K. Zeng (2012). Evaluating the behavior of electrolytic gas bubbles and their effect on the cell voltage in alkaline water electrolysis. Industrial & Engineering Chemistry Research **51**(42): 13825-13832.

Zhang, L. and M. Shoji (2001). Aperiodic bubble formation from a submerged orifice. Chemical Engineering Science **56**(18): 5371-5381.

Zhang, N., P. Bénard, R. Chahine, T. Yang and J. Xiao (2021). Optimization of pressure swing adsorption for hydrogen purification based on Box-Behnken design method. International Journal of Hydrogen Energy **46**(7): 5403-5417.

Zhou, D., P. Li, W. Xu, S. Jawaid, J. Mohammed-Ibrahim, W. Liu, Y. Kuang and X. Sun (2020). Recent Advances in Non-Precious Metal-Based Electrodes for Alkaline Water Electrolysis. ChemNanoMat **6**(3): 336-355.

Zhou, J., B. Qi, Y. Zhang, J. Wei, Y. Yang and Q. Cao (2020). Experimental and theoretical study of bubble coalescence and departure behaviors during nucleate pool boiling on uniform smooth and micro-pin-finned surfaces under different subcoolings and heat fluxes. Experimental Thermal and Fluid Science **112**: 109996.

Ziegenhein, T., A. Tomiyama and D. Lucas (2018). A new measuring concept to determine the lift force for distorted bubbles in low Morton number system: Results for air/water. International Journal of Multiphase Flow **108**: 11-24.

Zohuri, B. a. (2019). Hydrogen energy challenges and solutions for a cleaner future, Springer International Publishing: Imprint: Springer.

Chapter 3

Industrial application of membrane-free water electrolyser

3.1 Chapter overview

This chapter investigates the feasibility of using the membrane-free water electrolyser (MFE) for liquid hydrogen (LH_2) production. Industrial LH_2 production involves the cooling of gaseous H_2 to approximately -253°C under a pressure of 10 bar. Water electrolysers can be employed as the H_2 source for H_2 liquefaction process.

In conventional AWE cells, ion-solvating membranes are used to separate H_2 and O_2 while preserving ionic conductivity. The operating temperature of AWE is typically constrained at 60°C–90°C to protect its membrane, which can degrade rapidly when exposed to higher temperatures. The operating pressure of AWE is usually capped at 30 bar to maintain a high purity level of the product (>99.9%), since higher pressure will cause pronounced gas crossover across the membrane. In contrast, MFE technology offers a lower ohmic resistance and can operate under elevated temperatures and pressures. This can enhance cell efficiency; however, it also results in compromised product purity levels (<99%) as a trade-off.

In this chapter, a mathematical model is developed to simulate hydrogen generation through both AWE and MFE. The H_2 produced from these electrolysers acts as the feedstock for subsequent purification and liquefaction processes, which are simulated using Aspen HYSYS software. A series of sensitivity studies have been conducted to examine the influence of the operating conditions of the electrolyser and the purity of the raw H_2 on the overall power consumption required for LH_2 production.

The findings indicate that the operating conditions of the electrolyser play a crucial role in determining the power consumption of LH_2 production. Specifically, it is found that increasing the operating pressure can contribute to a reduction in energy consumption. This is advantageous because electrolysers operating at elevated pressures experience diminished bubble coverage over the electrodes, resulting in decreased ohmic overpotential. Moreover, a high-pressure H_2 stream can attain a greater temperature drop upon expansion through a Joule-Thomson control valve, subsequently minimising the cooling power required for H_2 liquefaction.

The findings suggest that the optimal operating temperature of electrolyser can significantly affect its performance. While higher temperatures typically lead to a reduction in reaction potential, bubble coverage, and electrolyte resistance, they also result in an increase in activation overpotential. This combination of factors accounts for the rise in cell voltage for MFE at high temperatures (> 120 °C). Raising the operating temperature of electrolyser also introduces a slight increase in the cooling load for H_2 liquefaction.

This chapter demonstrates the potential of using MFE as an alternative H_2 source for LH_2 production. Compared to conventional AWE, operating MFE at elevated temperatures and pressures can reduce power consumption for LH_2 production by up to 10%. Furthermore, when MFE is used as the H_2 source, the O_2 from the raw H_2 feedstock can be efficiently removed during the cryogenic cooling process, yielding high-purity LH_2 (>99.9%). Nonetheless, improving the purity of the raw H_2 is still advantageous as it lowers power consumption and mitigates safety concerns associated with gas crossover.

These findings fulfill the first research objective: they demonstrated the feasibility of using MFE for commercial-scale LH_2 production via cryogenic cooling. This chapter developed knowledge and techniques for efficient and scalable LH_2 production using MFE technology.

3.2 Feasibility of using membrane-free water electrolyser for liquid hydrogen production

This section consists of the following journal article:

> Yang, B., M. Jafarian, N. Freidoonimehr, and M. Arjomandi, Membrane-free water electrolyser for liquid hydrogen production. Submitted to International Journal of Hydrogen Energy.

This article is identical to the submitted version, with the exception of the numbering and positioning of figures, tables, and equations.

Statement of Authorship

Title of Paper	Membrane-free water electrolyser for liquid hydrogen production			
Publication Status	☐	Published	☐	Accepted for Publication
	☒	Submitted for publication	☐	Unpublished and Unsubmitted work written in manuscript style
Publication Details	Yang, B., M. Jafarian, N. Freidoonimehr, and M. Arjomandi, Membrane-free water electrolyser for liquid hydrogen production. Submitted to International Journal of Hydrogen Energy.			

International Journal of Hydrogen Energy

Principal Author

Name of Principal Author (Candidate)	Bo Yang		
Contribution to the Paper	Developed ideas, conducted experiments, performed data analysis, interpreted results, wrote manuscript, and acted as corresponding author.		
Overall percentage (%)	80%		
Certification:	This paper reports on original research I conducted during the period of my Higher Degree by Research candidature and is not subject to any obligations or contractual agreements with a third party that would constrain its inclusion in this thesis. I am the primary author of this paper.		
Signature		Date	25/09/2023

Co-Author Contributions

By signing the Statement of Authorship, each author certifies that:

i. the candidate's stated contribution to the publication is accurate (as detailed above);
ii. permission is granted for the candidate in include the publication in the thesis; and
iii. the sum of all co-author contributions is equal to 100% less the candidate's stated contribution.

Name of Co-Author	Mehdi Jafarian		
Contribution to the Paper	Supervised the development of the research, participated in developing ideas and concept, helped in interpreting results, and assisted in evaluating and editing the manuscript.		
Signature		Date	25/09/2023

Name of Co-Author	Navid Freidoonimehr		
Contribution to the Paper	Supervised the development of the research, participated in developing ideas and concept, helped in interpreting results, and assisted in evaluating and editing the manuscript.		
Signature		Date	25/09/2023

Name of Co-Author	Maziar Arjomandi		
Contribution to the Paper	Supervised the development of the research, participated in developing ideas and concept, helped in interpreting results, and assisted in evaluating and editing the manuscript.		
Signature		Date	25/09/2023

Membrane-Free Water Electrolyser for Liquid Hydrogen Production

Abstract

Transporting hydrogen in a liquid state holds promise as a cost-effective solution for long-distance and large-scale distribution. This paper investigates the feasibility of the application of a membrane-free water electrolyser for liquid hydrogen production. Both alkaline and membrane-free water electrolysers are considered for hydrogen production. The hydrogen produced by these electrolysers is used as the feedstock for subsequent purification and liquefaction processes. Aspen HYSYS is used for systematic investigation of the impact of electrolyser operating conditions and hydrogen purity on the total power consumption for liquid hydrogen production. The findings reveal that membrane-free water electrolysers offer an energy-efficient alternative to alkaline water electrolysers, potentially reducing power consumption by up to 10%.

3.2.1 Introduction

The growing severity of climate change has emphasised the urgent necessity to shift from fossil fuels to clean energy sources (Hydrogen Council 2023). Among the various energy options available, hydrogen stands out due to its wide range of applications and substantial environmental benefits. That is because when H_2 is oxidised as a fuel or reductant, it only emits water vapour, establishing it as a highly sustainable alternative to fossil fuels (Kim *et al.* 2022). Hydrogen has been used as a fuel in fuel cells as an efficient pathway for power generation (Wan *et al.* 2021, Wang *et al.* 2021, Moradpoor *et al.* 2023). Hydrogen can be also used as a reductive agent in mineral processing, significantly reducing greenhouse gas emissions (Wang *et al.* 2021). However, despite the significant potential, the production of H_2 from renewable resources, its storage, and transportation are currently challenging and expensive (Valenti 2016, Zohuri 2019, Shiva Kumar and Lim 2022). Therefore, there is a need to develop technologies to reduce the cost of production, transportation, and storage of H_2.

Hydrogen's low volumetric energy density under atmospheric conditions (11 kJ/L) poses challenges for its storage and transportation (Hydrogen and Fuel Cell Technologies Office, Pistidda 2021). While pressurising hydrogen improves its volumetric energy density, this method is economically viable only for consumers with small-scale demands. In contrast, liquid hydrogen (LH_2) offers a significantly higher volumetric energy density (8.5 MJ/L), making it an attractive option for transportation (Aziz 2021).

The production of LH_2 is typically realised by cooling gaseous H_2 to approximately -253°C at a pressure of 10 bar. The simple Claude cycle is a classic system employed for H_2 liquefaction, as illustrated in Figure 3-1 (Valenti 2016, Yang *et al.* 2023). In this cycle, the H_2 feed gas undergoes three major stages: compression and pre-cooling (1→3), Ortho-to-Para conversion (3→6), and liquefaction (6→7) (Al Ghafri *et al.* 2022). An intermediate extraction (4→e) is utilised to improve overall efficiency. Pre-cooling often involves a liquid N_2 cooling system, while the hydrogen vapour from the LH_2 storage tank serves as the refrigerant for the main cooling processes (g→12).

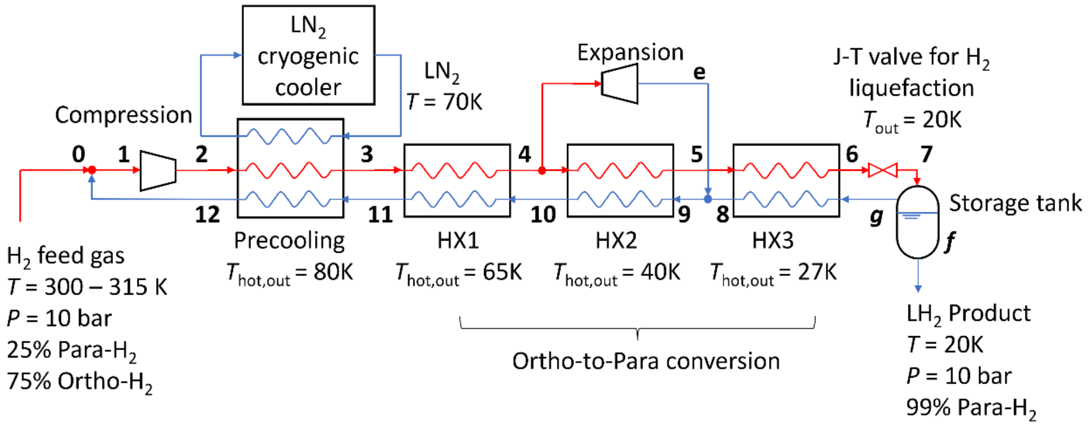

Figure 3-1. Schematic flow diagram of a simple Claude cycle for hydrogen liquefaction (Yang, Li *et al.* 2023).

The theoretical minimum specific energy consumption of LH_2 from a simple Claude cycle is about 22 kWh/kg$_{H_2}$ (Al Ghafri *et al.* 2022). Over the past decades, a few variations based on the simple Claude cycle have been developed to improve system efficiency. The modern state-of-the-art system, incorporating dual compression, improved heat exchangers, liquid nitrogen precooling, helium refrigeration cycle, and dedicated intermediate extraction systems has been reported achieving a specific energy consumption of about 13-18 kWh/kg$_{H2}$ (Krasae-in *et al.* 2010, Yin and Ju 2020).

It is expected that water electrolysers will remain the main technology for hydrogen production into the future as they offer both higher hydrogen purity and fewer greenhouse gas emissions compared to conventional production methods (Brauns and Turek 2020, Du *et al.* 2021). Alkaline water electrolysers (AWE) and proton exchange membrane electrolysers (PEM) are the predominant technologies for generating high-purity hydrogen (>99.9%) from water. According to the Nernst equation, operating electrolysers at elevated temperatures and pressures can significantly reduce the reversible potential for water splitting, and potentially improve their efficiencies (Borsboom-Hanson *et al.* 2022). Figure 3-2 presents the calculated reversible voltage of a water electrolyser cell as a function of temperature for various operating pressures (Haug *et al.* 2017). As shown an increase in temperature reduces the reversible voltage at all pressures studied. In contrast, a higher operating pressure leads to an increase in the reversible voltage, while it can mitigate the work required for the compression of the produced H_2, thereby facilitating storage and transportation.

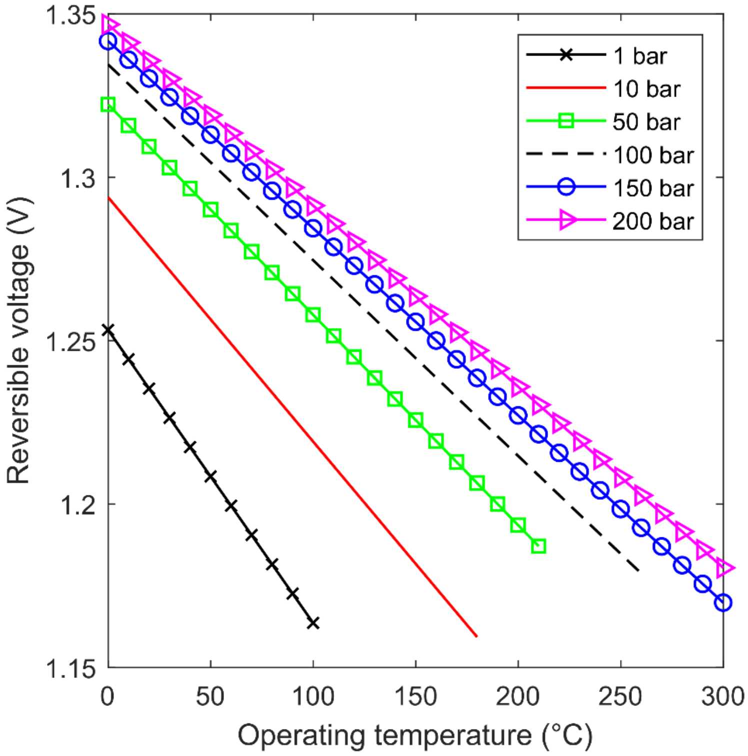

Figure 3-2. Reversible voltage of water electrolysis cell under various operating temperatures and pressures.

Commercial AWE and PEM systems employ membranes to separate hydrogen and oxygen gases. Although membrane technology has seen significant advancements, these membranes still degrade when exposed to temperatures above 90°C (Hua *et al.* 2022). As a result, the operating temperature for commercial AWE and PEM systems is generally limited to 60°C–90°C (Salehmin *et al.* 2022).

The membrane-free water electrolyser (MFE) is an emerging water electrolysis cell technology, which eliminates the need for the membrane and employs alternative methods to separate H_2 and O_2 such as control of hydrodynamics of the produced O_2 and H_2 bubbles to avoid their mixing. Figure 3-3 provides a schematic of an MFE. An MFE electrolyser, similar to an AWE cell, consists of an electrolyte channel, and parallelly positioned anodes and cathodes. In this system, membranes are not used for separation of H_2 and O_2 bubbles. Instead, the gap between the electrodes and fluid movement in between the electrodes are designed such the produced H_2 and O_2 bubbles are separated via the

Segré–Silberberg effect under a laminar flow regime in the channel (Segré and Silberberg 1961, O'Neil *et al.* 2016, De *et al.* 2021). The shear-induced lift force (F_L) tend to push bubbles towards the electrode where they evolve.

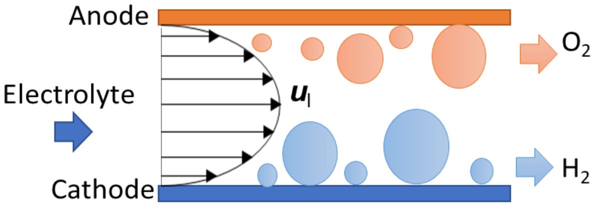

Figure 3-3. Concept of flow-by membrane-free water electrolyser (Swiegers *et al.* 2022). The electrolyte is maintained in laminar flow, facilitating bubble separation via shear-induced lift force.

Membrane-free design provides several advantages. It eliminates both the capital and maintenance costs associated with the membranes, which are typically very sensitive to impurities. In addition, MFE offers the potential to reduce ohmic resistance of the cell via elimination of the ohmic loss of the membrane, thereby increasing cell efficiency. Furthermore, MFE systems can operate at elevated temperatures and pressures, potentially enhancing their overall performance. Nevertheless, MFE suffers from low hydrogen purity (<99%), which increases at higher current densities (>4000 A/m2) (Hashemi *et al.* 2019, Hadikhani *et al.* 2021). Consequently, the raw H_2 produced by an MFE system needs to be purified to increase its utility.

Several techniques have been developed for H_2 purification and separation of O_2 and H_2 at both research and industrial levels, including pressure swing adsorption (PSA), temperature swing adsorption (TSA), membrane separation, catalytic oxidation, metal hydride, and cryogenic cooling (Miura *et al.* 2012, Schorer *et al.* 2019, Ligen *et al.* 2020, Luberti and Ahn 2022). However, if the ultimate objective is to convert gaseous H_2 into LH_2 for transport, cryogenic cooling method is a more logical choice, given it is practically the most effective method to liquefy H_2. Also, the boiling point of O_2 (-183°C at 1 atm) is significantly higher than that of H_2 (-253°C at 1 atm), allowing O_2 to be liquefied and separated in the H_2 liquefaction process.

Compared to AWE technology, MFE offers a trade-off: it provides a higher efficiency but at the cost of lower H_2 purity. Consequently, using MFE for LH_2 production may reduce the electrical power consumption for generating raw H_2, but will likely increase the energy required for O_2 separation in the cryogenic cooling system. If the conserved energy during H_2 production outweighs the additional energy required for O_2 removal, then MFE could emerge as a competitive approach for LH_2 production.

This paper aims to evaluate the feasibility of utilising MFE in LH_2 production. To complete this goal, we assess the overall energy consumption of LH_2 generated through MFE compared to that of conventional AWE, both integrated with cryogenic cooling systems. The electrical power needed for raw H_2 production is calculated for both MFE and conventional AWE under various operating conditions using simplified analytical equations. Aspen HYSYS software is used to simulate the cryogenic cooling system and estimate the energy consumption for LH_2 production in both MFE and AWE scenarios. Various operating parameters are considered in this analysis, including cell efficiency, operating temperature and pressure of the electrolysis cell, the purity of the hydrogen feed gas supplied to the cryogenic cooling system, and the temperatures involved in the cryogenic cooling process.

3.2.2 Methods

3.2.2.1 Mathematical model of water electrolyser

Figure 3-4 provides the schematics for both alkaline water electrolyser (AWE) and membrane-free water electrolyser (MFE). A 30% *wt* KOH solution serves as the electrolyte in each case. In the AWE cell, the cathode and anode are positioned parallel to each other, separated by a distance of $\delta_{el} + \delta_m$. A Zirfon® membrane, with a thickness of δ_m, is employed to separate H_2 and O_2 bubbles in the AWE cell (Vermeiren *et al.* 1998). In the MFE cell, the membrane is removed, and the electrodes are placed δ_{el} apart. In this study, the value of δ_{el} and δ_m are set as 5mm and 0.5mm, respectively (Hu *et al.* 2022).

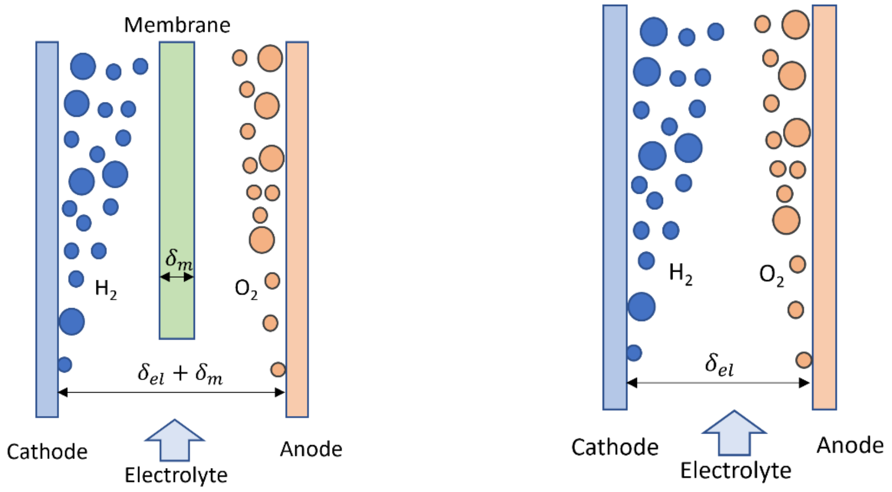

(a)

(b)

Figure 3-4. Schematics of (a) an alkaline water electrolyser with a membrane thickness of δ_m and electrode spacing of $(\delta_{el} + \delta_m)$ and (b) a membrane-free water electrolyser with electrode spacing of δ_{el}.

At steady-state, the molar flow rate (mol/s) of H_2 is calculated according to Faraday's Law (B. Yang *et al.* 2023):

$$\dot{n}_{\mathrm{H}_2} = \frac{I}{2\mathrm{F}} \; . \qquad (3\text{-}1)$$

The cell voltage is represented as the sum of the reaction potential, activation overpotential and ohmic overpotential:

$$V_{cell} = V_{rea} + \underbrace{(V_{ca} + V_{an})}_{V_{activation}} + \underbrace{(V_m + V_{el})}_{V_{ohmic}} \; . \qquad (3\text{-}2)$$

The reaction potential represents the minimum energy required to drive the water splitting reaction (Zeng and Zhang 2010):

$$V_{rea} = {}^{-\Delta G}/_{2F} \text{ ,} \tag{3-3}$$

where ΔG is the Gibbs free energy (kJ/mol) and F is the Faraday constant (96485 c/mol) (Aikens 1983). According to the Nernst equation, the reaction potential can be expressed as (Abdin *et al.* 2017):

$$V_{rea} = V^0 + (T - T^0) \times \frac{\Delta S^0}{2F} + \frac{RT}{2F}\left[\ln\left(\frac{(p - p_{\mathrm{H_2O}})^{1.5}}{a_{\mathrm{H_2O}}}\right)\right]. \tag{3-4}$$

In this equation, the reversible potential is V^0=1.229 V at 25℃ and 1 atm. T stands for temperature (K), and $\frac{\Delta S^0}{2F}$ is the standard state entropy change (-0.9×10^{-3} J/(mol·K)$^{-1}$) at 298K and 1 atm). R is the gas constant (8.314 J/(mol·K)). p and $p_{\mathrm{H_2O}}$ are the operating pressure (bar) and partial pressure of water, respectively (Le Bideau *et al.* 2019). The water pressure in a KOH solution is calculated as (Leroy 1980):

$$p_{\mathrm{H_2O}} = T^{-3.498} \exp\left(37.93 - \frac{6426.32}{T}\right) \exp\,(0.016214 - 0.13802m + 0.19330\sqrt{m}. \tag{3-5}$$

Here, m is the molar concentration of KOH. In Equation 3-4, $a_{\mathrm{H_2O}}$ is the water activity of the electrolyte solution (bar), which is expressed as (Amphlett *et al.* 1995):

$$\log\,(a_{\mathrm{H_2O}}) = -0.08 - \frac{19.19}{T}. \tag{3-6}$$

The activation overpotentials for the cathode and anode reactions can be calculated using the Butler-Volmer equation (Bessarabov and Millet 2018):

$$V_{\mathrm{ca}} = \frac{RT}{\alpha_{\mathrm{ca}}F}\ln\left(\frac{j}{j_{\mathrm{ca}}(1-\theta)}\right), \tag{3-7}$$

$$V_{\mathrm{an}} = \frac{RT}{\alpha_{\mathrm{an}}F}\ln\left(\frac{j}{j_{\mathrm{an}}(1-\theta)}\right). \tag{3-8}$$

Here, α_{ca} and α_{an} stand for the charge transfer coefficient for the cathode and anode, respectively. In this study, α_{ca}= 0.73, and α_{an}= 1.65 (Abdin, Webb *et al.* 2017). j is the current density (A/m^2). The effective exchange current densities for cathode (j_{ca}) and anode (j_{an}) are assumed to be 0.43 A/m^2 and 0.37 A/m^2, respectively (An *et al.* 2014, Bessarabov and Millet 2018). The term $(1-\theta)$ accounts for the bubble coverage (θ) over the electrode, which is empirically determined as (Vogt and Balzer 2005, Vogt 2012):

$$\theta = \left(\frac{j}{j_{\mathrm{lim}}}\right)^{0.3}\left(\frac{Tp^0}{T^0p}\right)^{\frac{2}{3}}. \tag{3-9}$$

Here, j_{lim} is the limiting current density (300 kA/m^2) (Vogt 2012).

The ohmic overpotential is proportional to the current in the circuit (I):

$$V_{ohmic} = I(\, r_m \, + \, r_{el}\,)\ , \tag{3-10}$$

In this equation, the resistance of the membrane r_m is calculated as:

$$r_m \, = \frac{\delta_m}{k_m A}, \tag{3-11}$$

where A and k_{m} are the area (1 m^2) and the electrical conductivity (20 S/m) of the membrane, respectively (Vermeiren *et al.* 1998, Rodriguez *et al.* 2019).

Bubbles in the electrolyte can result in a reduced electric conductivity. Consequently, Bruggeman's equation is adopted to calculate the electrolyte resistance (r_{el}) (Rue and Tobias 1959, Tjaden *et al.* 2016):

$$r_{el} = \frac{\delta_{el}}{(1-\varphi)^{1.5} k_{el} A}. \tag{3-12}$$

Here, φ is the void fraction, which is equivalent to the bubble coverage (θ), as suggested by Abdin *et al.* (2017). k_{el} denotes the conductivity of the electrolyte (S/m), which can be correlated as (Gilliam *et al.* 2007, Allebrod *et al.* 2012):

$$k_{el} = 1.357\,T - 340.98. \tag{3-13}$$

3.2.2.2 Cryogenic cooling system

A cryogenic cooling system designed for hydrogen purification and liquefaction is simulated using Aspen HYSYS V11 software. Figure 5 shows the simulation model that comprises four primary components including precooling, hydrogen purification, hydrogen liquefaction, and cold recovery units. The Peng-Robinson equation of state is chosen as the thermodynamic property package to estimate the thermo-physical properties of the materials in the developed HYSYS models (Yin and Ju 2020). For simplicity, pressure losses in the electrolysers, pipes, heat exchangers and flash tank are omitted.

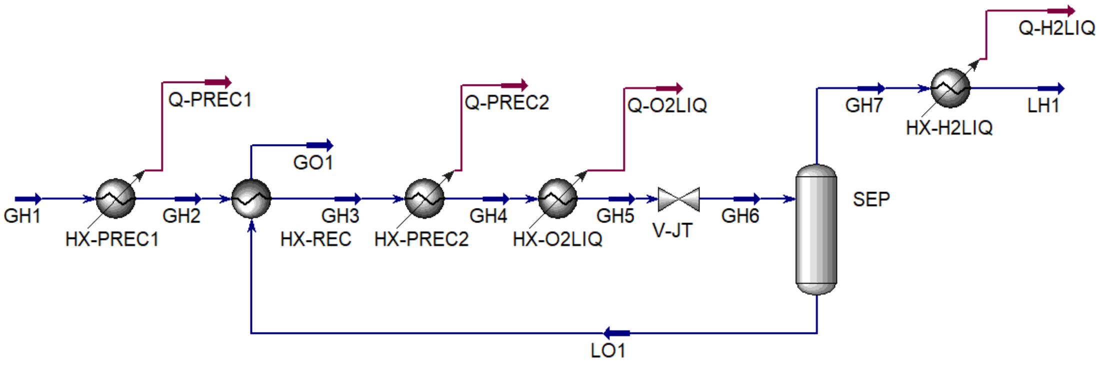

Figure 3-5. The process diagram of cryogenic cooling system for hydrogen purification and liquefaction.

The H_2 from both AWE and MFE is considered as feed (GH-1) for this liquefaction process in different cases. The AWE-derived H_2 is assumed to have a high purity of 99.9%, and a temperature and pressure range of 60–90°C and 10–30 bar, respectively (Brauns and Turek 2020, Hu *et al.* 2022). In contrast, the MFE-derived H_2 is assumed to have a purity ranging from 66.7% to 99%, with temperature and pressure ranges of 60–300°C and 10–200 bar, respectively (Esposito 2017, Manzotti *et al.* 2023).

To reduce the cooling load on cryogenic coolers, the H_2 feed gas is directed to a precooler (HX-PREC1) to bring its temperature down to 45°C (GH2). Subsequently, this cooled H_2 stream passes through a cold recovery heat exchanger (HX-REC) before being further cooled in a liquid nitrogen (LN_2) precooler (HX-PREC2) to a temperature of -190°C. In this precooler, nitrogen enters at -195°C and exits at 20 °C. The power consumption of LN_2 production is assumed to be 0.36kWh/kg_{N2} (Aneke and Wang 2015, Rizvi *et al.* 2021).

The H_2 purification unit comprises an O_2 liquefier (HX-O2LIQ), a Joule-Thomson control valve (V-JT), and a gas-liquid separator (SEP). These blocks cool the incoming raw H_2 to temperatures below -215°C. This process facilitates the removal of liquefied O_2, ultimately yielding purified H_2 with a purity level of over 99.9%. The collected liquid O_2 is routed back to a cold recovery heat exchanger (HX-REC) before being vented to the atmosphere at 30 °C.

The purified H_2 is then channelled to an H_2 liquefier (HX-H2LIQ) where it undergoes the phase transition to form LH_2 at -253°C. The conversion of orthohydrogen to parahydrogen takes place as (Woolley *et al.* 1948, McIntosh 2015):

$$ortho - H_2 \xrightarrow{\Delta H = -1.455 kJ/mol \ \ at\ 20K} para - H_2, \tag{3-14}$$

The rate constant of the catalytic ortho-para H_2 conversion is 1.2 s^{-1} (Cardella *et al.* 2017, Yin and Ju 2020). While the ortho-para conversion is not explicitly modelled in the HYSYS simulations, its associated cooling load is incorporated when calculating the cooling load required for LH_2 liquefaction.

Table 3-1 summarises the parameters used in the case study. The independent variables under consideration are the temperature, pressure, and purity of raw H_2 gas (stream GH1). For simplification purposes, pressure drops within the electrolyser, piping, heat exchangers, and separator are ignored in this study. The coefficient of performances (COP) of precooling and cryogenic cooling is assumed based on values reported in the literature (Radenbaugh 2004, Radebaugh 2009, Bustamante *et al.* 2016, Li *et al.* 2018). The electric power consumptions (W) for the coolers are calculated as follows:

$$W = \frac{Q(T_h - T_c)}{T_c} \frac{1}{\%COP_{carnot}}. \tag{3-15}$$

Table 3-1. Specified conditions for cryogenic cooling process for case study.

Parameter	Stream/Block	Value	
		AWE	MFE
Raw H_2 temperature	GH1	60°C–90°C	60°C–300°C
Raw H_2 pressure	GH1	10–30 bar	10–200 bar
H_2 purity	GH1	99.9%	66.7%–99%
Air-precooled raw H_2 temperature	GH2	45°C	
LN_2-precooled raw H_2 temperature	GH4	-190°C	
O_2 liquefier outlet temperature	GH5	-210°C	
J-T valve outlet pressure	GH6	10 bar	
H_2 liquefier outlet temperature	LH1	-253°C	
Catalytic reaction constant of ortho-para H_2 conversion	-	1.2 s^{-1}	
Precooler COP	HX-PREC	3 at 289K (Bustamante *et al.* 2016, Li *et al.* 2018)	
O_2 liquefier COP	HX-O2LIQ	15% Carnot at 50K (Radenbaugh 2004, Radebaugh 2009)	
H_2 liquefier COP	HX-H2LIQ	5% Carnot at 10K (Radenbaugh 2004, Radebaugh 2009)	

The reliability of the model has been verified through comparison of the calculated boiling point of O_2 and H_2 with the experimental data (Don and Robert 2008). Moreover, the developed models were checked to ensure that the calculations were run with no ‘error’ or ‘warning’ messages, which implies that the energy and mass balances were within acceptable limits.

3.2.3 Results

3.2.3.1 Electrolyser performance

Figure 3-6 illustrates various performance metrics—including cell voltage, reaction potential, activation overpotentials, and ohmic overpotentials—for an alkaline water electrolyser (AWE) operating at 80 °C and 10 bar across a range of current densities. The results show that the overpotentials increase with rising current density. At lower current densities (j<2000 A/m2), both ohmic and activation overpotentials show rapid growth, with the activation overpotential serving as the primary contributor. As the current density rises, the rate of increase for the activation overpotential becomes less pronounced. On the other hand, the ohmic overpotential demonstrates a consistent linear increase with growing current density, and it becomes the dominant factor at high current densities (j>4000 A/m2). Notably, the membrane accounts for about one-third of the ohmic overpotential.

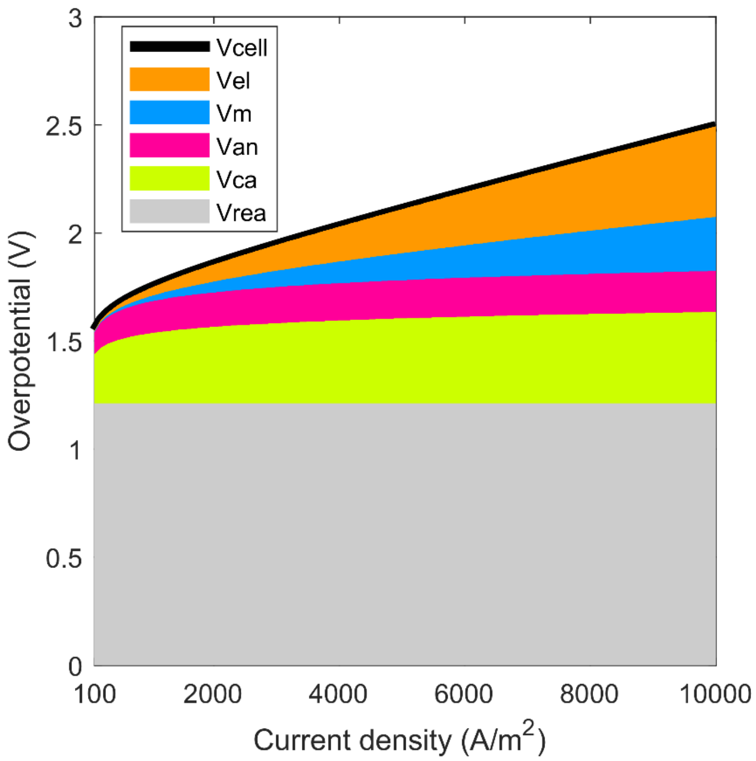

Figure 3-6. Dependence of overpotentials on current density for an alkaline water electrolyser under 80 °C and 30 bar.

Figure 3-7 shows the impact of varying operating pressure on the cell voltage for both AWE and membrane-free water electrolysers (MFE). The absence of membranes allows MFE to operate at a considerably lower cell voltage compared to AWE at the same current density. Moreover, for both types of electrolysers, an increase in operating pressure leads to a slight elevation in cell voltage when operating at low to moderate current densities (j<8000 A/m^2). This is likely due to the increase in reaction potential as the operating pressure rises. However, at high current densities (j>8000 A/m^2), both AWE and MFE exhibit a reduced cell voltage at elevated pressures. This reduction can be attributed to the decrease in bubble coverage on the electrodes, which consequently results in a lower ohmic overpotential (as per Equation 2-8).

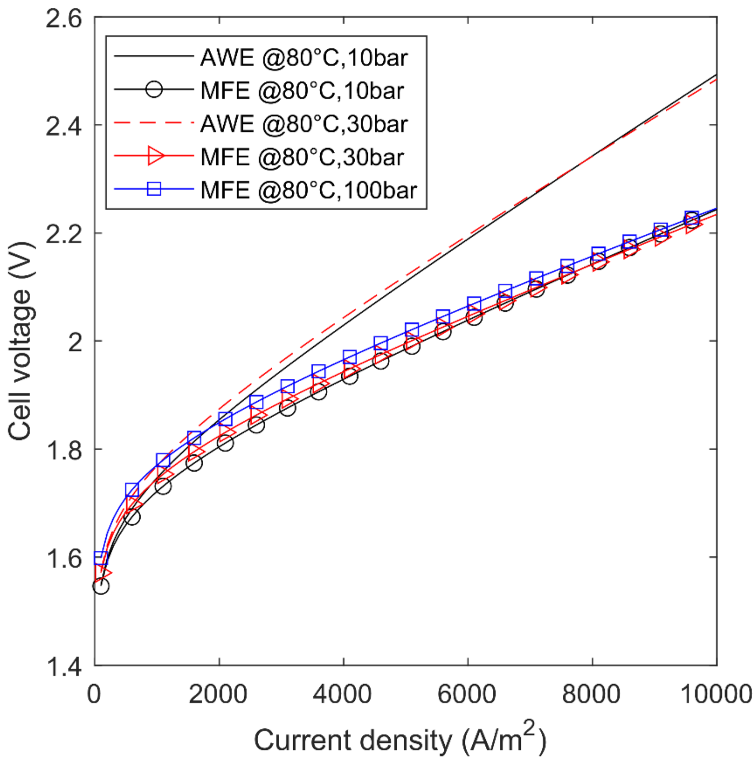

Figure 3-7. Effect of current density on cell voltage of alkaline and membrane-free water electrolysers under 80 °C and various operating pressures.

Figure 3-8 presents the dependence of cell voltages on current density for AWE and MFE under 50 bar and various operating temperatures. Generally, it can be observed that cell voltage decreases as operating temperature increases. For instance, at a current density of j=4000 A/m^2, the cell voltage of AWE is reduced from 2.2 V to 2.1 V when the temperature rises from 20 °C to 80 °C. However, MFE exhibits an increase in cell voltage when the operating temperature reaches 200 °C. While elevated temperatures generally lead to a reduction in reaction potential, bubble coverage, and electrolyte resistance, they also result in an increase in activation overpotential. This interplay of factors accounts for the observed rise in cell voltage for MFE at higher temperatures.

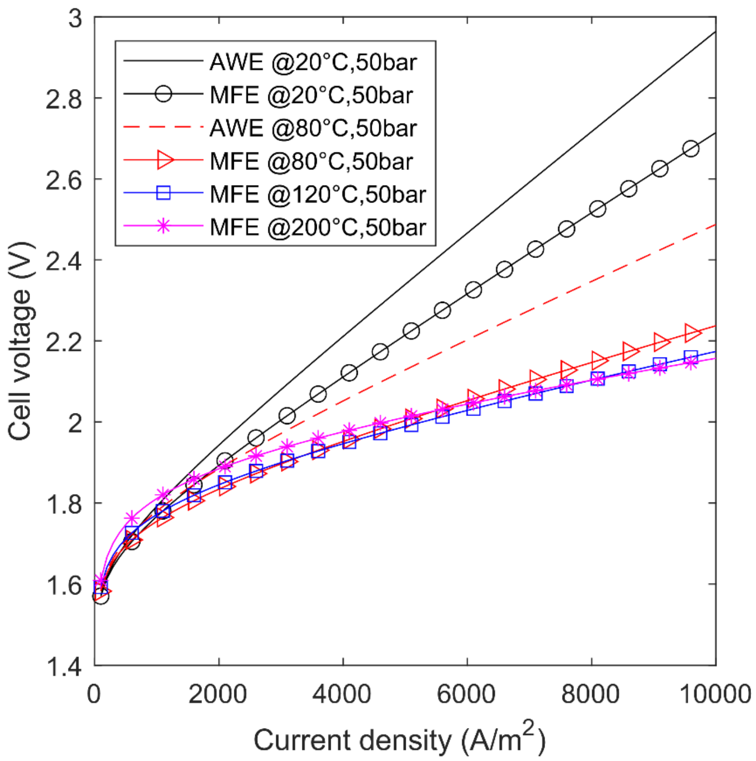

Figure 3-8. Effect of current density on cell voltage of alkaline and membrane-free water electrolysers under various operating temperatures and 50 bar.

3.2.3.2 Hydrogen purification and liquefaction

Figure 3-9 illustrates the impact of H_2 purification temperature and pressure on the purity of liquefied hydrogen (LH2). The graph reveals that LH_2 purity improves as the hydrogen purification temperature decreases. In the low-pressure regime (below 10 bar), LH_2 purity increases with rising pressure. However, this trend reverses when the pressure exceeds 40 bar, resulting in decreased LH_2 purity. The optimal pressure range for efficient O_2 removal appears to be approximately 10–40 bar, within which the vapor concentration of O_2 in H_2 reaches its minimum.

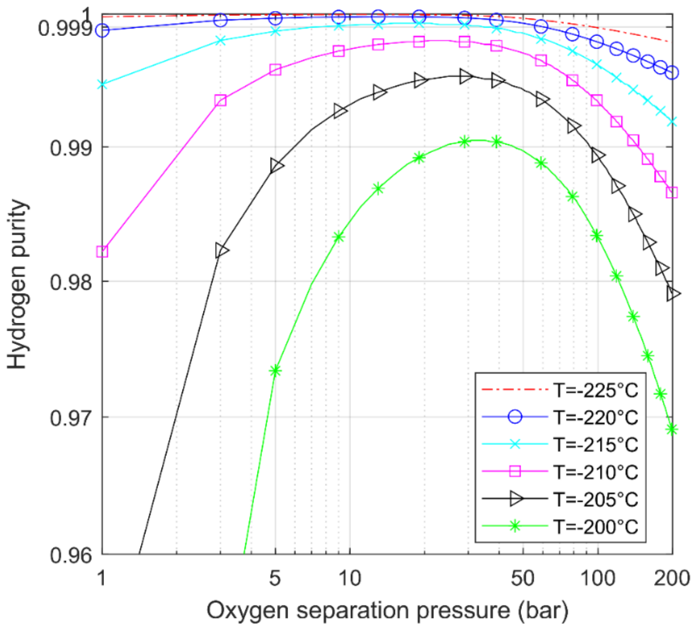

Figure 3-9. Effect of H_2 purification temperature and pressure on product hydrogen purity.

Figure 3-10 depicts the dependence of power consumption of cryogenic cooling system on the feed H_2 purity. Raw H_2 is fed into the system at 80 °C and 100 bar. Figure 3-10 reveals that the liquid nitrogen (LN_2) precooler and H_2 liquefier are the primary consumers of power, while the contributions of the air precooler and the O2 liquefier to overall power consumption are negligible. Also, improving the purity of feed H_2 can significantly reduce the energy required for the cryogenic cooling process. This reduction is largely due to decreased energy consumption in the H_2 liquefier, as more heat is rejected by the LN_2 precooler. Figure 3-10 also indicates that improving the purity of feed H_2 can lower the H_2/O_2 separation temperature, leading to higher LH_2 purity.

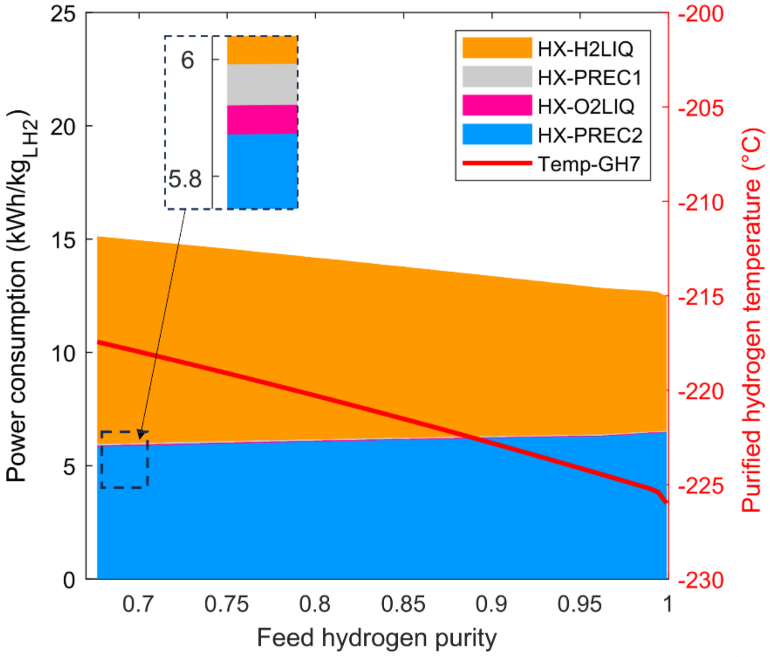

Figure 3-10. Effect of purity of feed hydrogen on power consumption and hydrogen purification temperature. The hydrogen is fed at 80 °C and 100 bar.

Figure 3-11 illustrates the power consumption of the cryogenic cooling process, with raw H_2 feed at 80 °C, with a purity of 96% and under various pressures. It shows that increasing raw H_2 pressure can significantly reduce the overall power consumption of the cryogenic process. This is achieved primarily by reducing the temperature of the purified H_2, which in turn reduces the cooling load at extremely low cryogenic temperatures. The mechanism behind this reduction lies in the behaviour of H_2 gas as it passes through the Joule-Thomson control valve. A higher-pressure H_2 stream can achieve a larger temperature decrease upon expansion through this valve. For instance, when the pressure of the feed hydrogen is increased from 50 bar to 100 bar, the temperature of the purified hydrogen drops from -218 °C to -224 °C, which can significantly improve LH_2 purity.

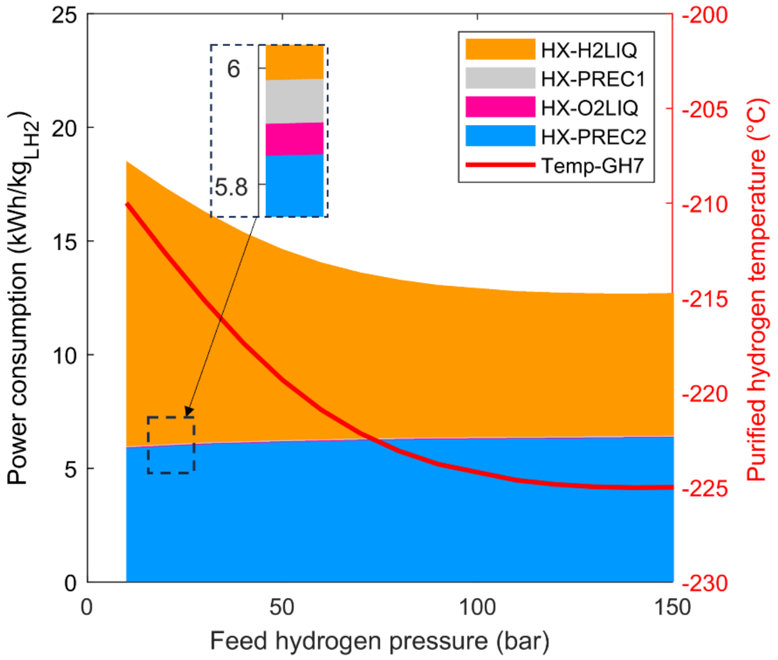

Figure 3-11. Effect of feed hydrogen pressure on power consumption and hydrogen purification temperature for feed hydrogen with a purity of 96% and at 80 °C.

Figure 3-12 illustrates the power consumption of the cryogenic cooling process, with raw H_2 feed with a purity of 96%, under 100 bar and at different temperatures. The result shows that the temperature of the raw H_2 has a limited impact on the overall power consumption of the cryogenic cooling system. The increase in power consumption at higher raw H_2 temperatures is primarily attributed to the higher heating load imposed on the air precooler. On the other hand, the feed H_2 temperature has a negligible effect on the cooling load of cryogenic coolers.

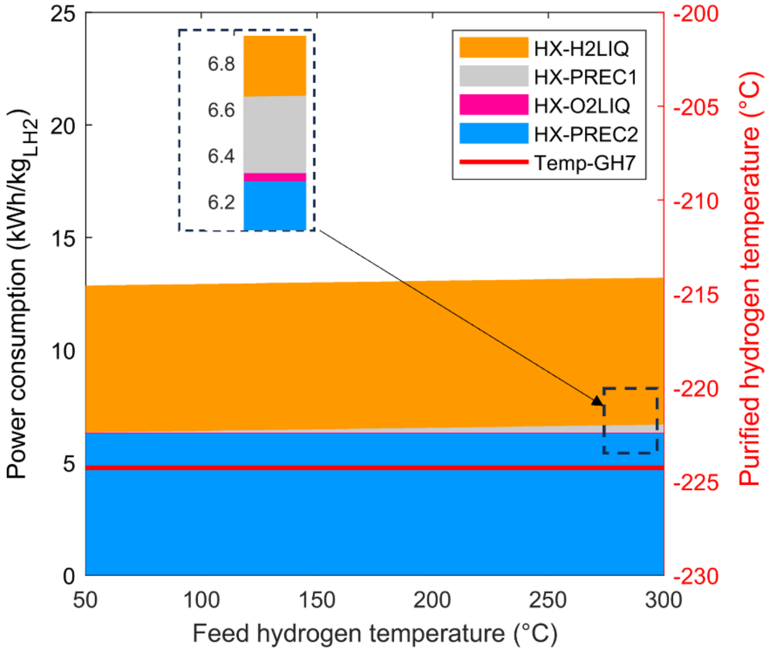

Figure 3-12. Influence of feed hydrogen temperature on hydrogen purification temperature and power consumption for feed hydrogen with a purity of 96% and under 100 bar.

3.2.3.3 Overall power consumption of liquid hydrogen

The overall power consumption of LH_2 considers the energy required for both the water electrolyser and cryogenic cooling process. Figure 3-13 shows the overall power consumption for LH_2 production using both AWE and MFE, integrated with a cryogenic cooling system. The electrolysers are operated at 80 °C and 30 bar, which is the typical operating condition for industrial AWE cells. The raw H_2 purity produced from AWE is 99.9%, whereas MFE generates H_2 with a purity range of 96%-99%. MFE offers a lower power consumption for LH_2 production compared to AWE. For example, at a current density of 4000 A/m2, MFE with an H_2 purity of 97.5% consumes 70.9 kWh/kg$_{LH2}$. In comparison, using AWE as the hydrogen production method results in an energy consumption of 73.5 kWh/kg$_{LH2}$. It's worth noting that enhancing the H_2 purity in MFE can significantly reduce its energy requirements.

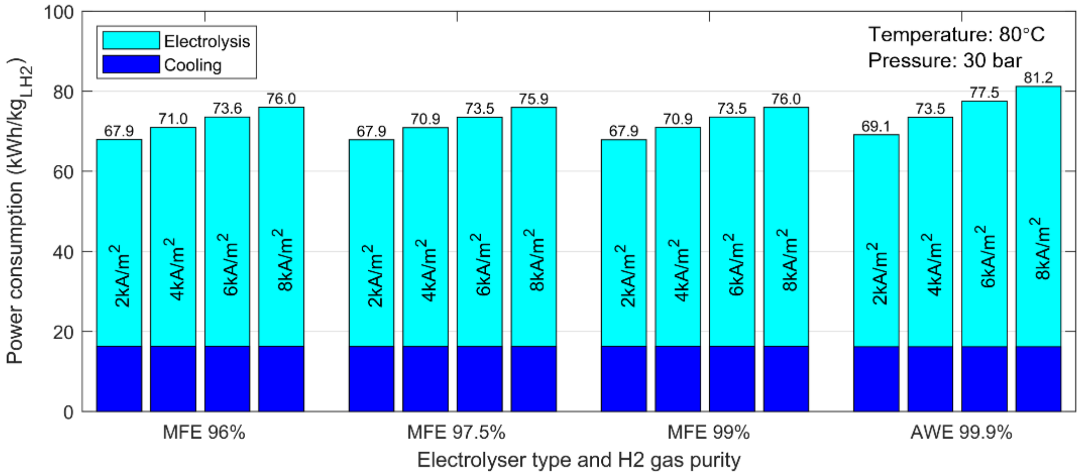

Figure 3-13. Power consumption for liquid hydrogen production using alkaline water electrolysers and membrane-free water electrolysers with different hydrogen purities.

Figure 3-14 shows the power consumption associated with LH_2 production via MFE and AWE under various operating pressures and at 80 °C. Generally, the results show that elevating the operating pressure can lead to a decrease in energy consumption. Specifically, at a current density of 4000 A/m2, raising the operating pressure of MFE from 10 bar to 150 bar reduces energy consumption from 72.6kWh/kg$_{LH2}$ to 68.2kWh/kg$_{LH2}$. However, the benefits diminish beyond a certain point; for example, when the operating pressure climbs to 190 bar, energy consumption slightly increases to 68.5kWh/kg$_{LH2}$. Compared to the baseline, where AWE operated at 80 °C and 30 bar, utilising high-pressure MFE as the H_2 source for LH_2 production can result in energy savings ranging from approximately 4% to 10%.

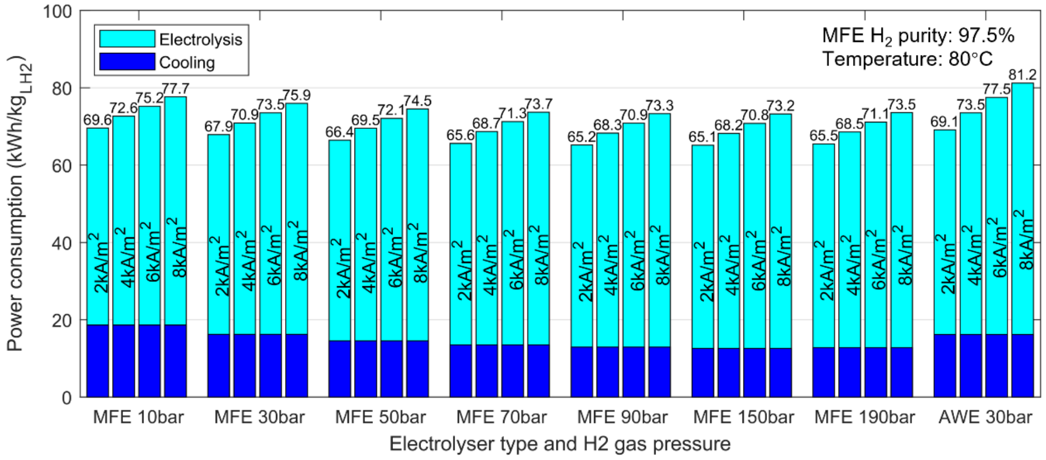

Figure 3-14. Power consumption for liquid hydrogen production using membrane-free water electrolysers operated at various pressures and 80 °C, with alkaline water electrolysers operated at 80 °C and 30 bar as a reference.

Figure 3-15 demonstrates the impact of varying operating temperatures on the energy consumption of LH_2 production when using MFE. The MFE system operates under 100 bar and at various temperatures, delivering H_2 with a purity of 97.5%. The data shows that as the temperature rises, energy consumption generally declines, reaching a minimum when operated at 120 °C. However, beyond this optimal point, an increase in temperature leads to a rise in energy consumption. This phenomenon can be attributed to two primary factors: first, elevated temperatures lead to an increase in activation overpotential, thereby increasing the energy requirements for water electrolysis; second, higher temperatures also increase the cooling load required during the precooling of raw H_2.

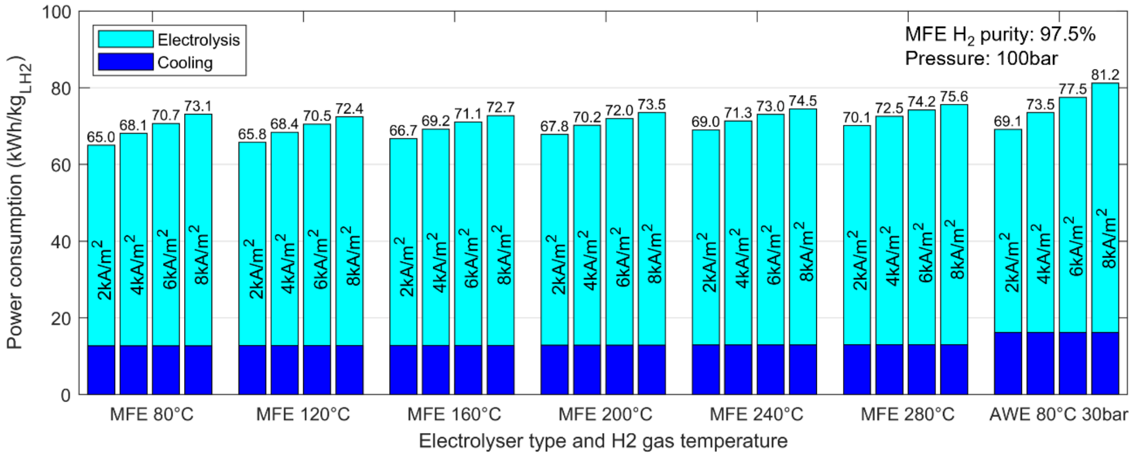

Figure 3-15. Comparison of power consumption for liquid hydrogen production between alkaline water electrolysers operated at 80 °C and 30 bar and membrane-free water electrolysers operated at various temperatures and 100 bar.

3.2.4 Discussion

The MFE modelled in this study maintains the same interelectrode distance as conventional AWE. Reducing this distance to approximately 1 mm could result in even greater energy efficiency, however, the H_2 purity can be remarkably decreased. While our study demonstrates that MFE is more energy-efficient in producing LH_2 compared to AWE, there remains an imperative to incorporate adequate safety measures. Despite various techniques being proposed, ranging from inertial bubble separation (Hadikhani *et al.* 2018) and innovative cell design (Hadikhani *et al.* 2021), to the enhancement of bubble distribution control (Yang *et al.* 2024), the gas crossover in an industrial-scale MFE remains a safety concern.

The modelling for water electrolysers in this study relies on empirical formulas derived from existing literature. Owing to the absence of experimental data, potential inaccuracies may arise in calculating parameters such as bubble coverage and activation overpotential—especially when the electrolyser operates under elevated temperatures and pressures. Due to the simplifications used in empirical equations, this paper only offers a rough estimation of cooling power consumption, which is higher than the energy consumption of the state-of-art hydrogen liquefaction process (13–18 kWh/kg_{LH2}) (Krasae-in *et al.* 2010, Yin and Ju 2020). Optimisation of the cryogenic cooling process, however, falls outside the scope of this study.

3.2.5 Conclusion

This paper explores the integration of alkaline and membrane-free water electrolysers (MFE) with a cryogenic cooling system for liquid H_2 (LH_2) production. The results indicate that the cryogenic cooling process effectively eliminates O_2 from the raw H_2 feedstock of MFE, yielding a final product with over 99.9% purity. Moreover, it is found that MFE, when operated at elevated temperatures and pressures, can reduce power consumption for LH_2 production by up to 10% compared to alkaline water electrolysers. The study thereby establishes the potential of MFE as a viable alternative for more energy-efficient LH_2 production.

References

Abdin, Z., C. J. Webb and E. M. Gray (2017). Modelling and simulation of an alkaline electrolyser cell. Energy **138**: 316-331.

Aikens, D. A. (1983). Electrochemical methods, fundamentals and applications. Journal of Chemical Education **60**(1): A25.

Al Ghafri, S. Z. S., S. Munro, U. Cardella, T. Funke, W. Notardonato, J. P. M. Trusler, J. Leachman, R. Span, S. Kamiya, G. Pearce, A. Swanger, E. D. Rodriguez, P. Bajada, F. Jiao, K. Peng, A. Siahvashi, M. L. Johns and E. F. May (2022). Hydrogen liquefaction: a review of the fundamental physics, engineering practice and future opportunities. Energy & Environmental Science **15**(7): 2690-2731.

Allebrod, F., C. Chatzichristodoulou, P. Mollerup and M. Mogensen (2012). Electrical conductivity measurements of aqueous and immobilized potassium hydroxide. International Journal of Hydrogen Energy **37**: 16505–16514.

Amphlett, J. C., R. M. Baumert, R. F. Mann, B. A. Peppley, P. R. Roberge and T. J. Harris (1995). Performance modeling of the Ballard Mark IV solid polymer electrolyte fuel cell: II. Empirical Model Development. Journal of The Electrochemical Society **142**(1): 9.

An, L., T. S. Zhao, Z. H. Chai, P. Tan and L. Zeng (2014). Mathematical modeling of an anion-exchange membrane water electrolyzer for hydrogen production. International Journal of Hydrogen Energy **39**(35): 19869-19876.

Aneke, M. and M. Wang (2015). Potential for improving the energy efficiency of cryogenic air separation unit (ASU) using binary heat recovery cycles. Applied Thermal Engineering **81**: 223-231.

Aziz, M. (2021). Liquid Hydrogen: A review on liquefaction, storage, transportation, and safety. Energies **14**(18): 5917.

Bessarabov, D. and P. Millet (2018). Chapter 3 - Fundamentals of Water Electrolysis. PEM Water Electrolysis. Academic Press**:** 43-73.

Borsboom-Hanson, T., T. Holm and W. Mérida (2022). A high temperature and pressure framework for supercritical water electrolysis. International Journal of Hydrogen Energy **47**(48): 20705-20717.

Brauns, J. and T. Turek (2020). Alkaline water electrolysis powered by renewable energy: a review. Processes **8**(2): 248.

Bustamante, J. G., A. S. Rattner and S. Garimella (2016). Achieving near-water-cooled power plant performance with air-cooled condensers. Applied Thermal Engineering **105**: 362-371.

Cardella, U., L. Decker, J. Sundberg and H. Klein (2017). Process optimization for large-scale hydrogen liquefaction. International Journal of Hydrogen Energy **42**(17): 12339-12354.

De, B. S., P. Kumar, N. Khare, J.-L. Luo, A. Elias and S. Basu (2021). Microfabrication of the ammonia plasma-activated nickel nitride–nickel thin Film for overall water splitting in the microfluidic membraneless electrolyzer. ACS Applied Energy Materials **4**(9): 9639-9652.

Du, Z., C. Liu, J. Zhai, X. Guo, Y. Xiong, W. Su and G. He (2021). A Review of hydrogen purification technologies for fuel cell vehicles. Catalysts **11**(3): 393.

Gilliam, R. J., J. W. Graydon, D. W. Kirk and S. J. Thorpe (2007). A review of specific conductivities of potassium hydroxide solutions for various concentrations and temperatures. International Journal of Hydrogen Energy **32**(3): 359-364.

H. Hashemi, S. M., P. Karnakov, P. Hadikhani, E. Chinello, S. Litvinov, C. Moser, P. Koumoutsakos and D. Psaltis (2019). A versatile and membrane-less electrochemical reactor for the electrolysis of water and brine. Energy & Environmental Science **12**(5): 1592-1604.

H. Hashemi, S. M., M. A. Modestino and D. Psaltis (2015). A membrane-less electrolyzer for hydrogen production across the pH scale. Energy & Environmental Science **8**(7): 2003-2009.

Hadikhani, P., S. M. H. Hashemi and D. Psaltis (2020). The Impact of surfactants on the inertial separation of bubbles in microfluidic electrolyzers. Journal of The Electrochemical Society **167**(13): 134504.

Hadikhani, P., S. M. H. Hashemi, G. Balestra, L. Zhu, M. A. Modestino, F. Gallaire and D. Psaltis (2018). Inertial manipulation of bubbles in rectangular microfluidic channels. Lab Chip **18**(7): 1035-1046.

Hadikhani, P., S. M. H. Hashemi, S. A. Schenk and D. Psaltis (2021). A membrane-less electrolyzer with porous walls for high throughput and pure hydrogen production. Sustain Energy Fuels **5**(9): 2419-2432.

Hu, S., B. Guo, S. Ding, F. Yang, J. Dang, B. Liu, J. Gu, J. Ma and M. Ouyang (2022). A comprehensive review of alkaline water electrolysis mathematical modeling. Applied Energy **327**: 120099.

Hua, D., J. Huang, E. Fabbri, M. Rafique and B. Song (2022). Development of anion exchange membrane waterelectrolysis and the associated challenges: A Review. ChemElectroChem **10**(1): e202200999.

Hydrogen and Fuel Cell Technologies Office. Hydrogen Storage. Retrieved 3rd Auguest, 2023, from https://www.energy.gov/eere/fuelcells/hydrogen-storage.

Hydrogen Council. (2023). Hydrogen Insights 2023. Retrieved 10th Aug, 2023, from https://hydrogencouncil.com/en/hydrogen-insights-2023/.

Kim, T., Y. Song, J. Kang, S. K. Kim and S. Kim (2022). A review of recent advances in hydrogen purification for selective removal of oxygen: Deoxo catalysts and reactor systems. International Journal of Hydrogen Energy **47**(59): 24817-24834.

Krasae-in, S., J. H. Stang and P. Neksa (2010). Development of large-scale hydrogen liquefaction processes from 1898 to 2009. International Journal of Hydrogen Energy **35**(10): 4524-4533.

Le Bideau, D., P. Mandin, M. Benbouzid, M. Kim and M. Sellier (2019). Review of necessary thermophysical properties and their sensivities with temperature and electrolyte mass fractions for alkaline water electrolysis multiphysics modelling. International Journal of Hydrogen Energy **44**(10): 4553-4569.

Leroy, R. L. (1980). The thermodynamics of aqueous water electrolysis. Journal of The Electrochemical Society **127**(9): 1954.

Li, X., N. Wang, L. Wang, Y. Yang and F. Maréchal (2018). Identification of optimal operating strategy of direct air-cooling condenser for Rankine cycle based power plants. Applied Energy **209**: 153-166.

Ligen, Y., H. Vrubel and H. Girault (2020). Energy efficient hydrogen drying and purification for fuel cell vehicles. International Journal of Hydrogen Energy **45**(18): 10639-10647.

Luberti, M. and H. Ahn (2022). Review of Polybed pressure swing adsorption for hydrogen purification. International Journal of Hydrogen Energy **47**(20): 10911-10933.

McIntosh, G. E. (2015). Applications of ortho-para hydrogen catalyst. IOP Conference Series: Materials Science and Engineering **101**: 021079.

Miura, S., A. Fujisawa and M. Ishida (2012). A hydrogen purification and storage system using metal hydride. International Journal of Hydrogen Energy **37**(3): 2794-2799.

Moradpoor, I., S. Syri and A. Santasalo-Aarnio (2023). Green hydrogen production for oil refining – Finnish case. Renewable and Sustainable Energy Reviews **175**: 113159.

O'Neil, G. D., C. D. Christian, D. E. Brown and D. V. Esposito (2016). Hydrogen production with a simple and scalable membraneless electrolyzer. Journal of The Electrochemical Society **163**(11): F3012-F3019.

Pistidda, C. (2021). Solid-state hydrogen storage for a decarbonized society. Hydrogen **2**(4): 428-443.

Radebaugh, R. (2009). Cryocoolers: the state of the art and recent developments. J Phys Condens Matter **21**(16): 164219.

Radenbaugh, R. (2004). Refrigeration for superconductors. Proceedings of the IEEE **92**(10): 1719-1734.

Rizvi, S. F. J., S. Miran, M. Azam, W. Arif, M. Wasif and H. P. Garcia (2021). Numerical analysis of a liquid nitrogen (LN(2)) engine for efficient energy conversion. ACS Omega **6**(24): 15663-15673.

Rodriguez, J., S. Palmas, M. Sanchez-Molina, E. Amores, L. Mais and R. Campana (2019). Simple and precise approach for determination of ohmic contribution of diaphragms in alkaline water electrolysis. Membranes (Basel) **9**(10): 129.

Rue, R. E. D. L. and C. W. Tobias (1959). On the conductivity of dispersions. Journal of The Electrochemical Society **106**(9): 827.

Salehmin, M. N. I., T. Husaini, J. Goh and A. B. Sulong (2022). High-pressure PEM water electrolyser: A review on challenges and mitigation strategies towards green and low-cost hydrogen production. Energy Conversion and Management **268**.

Schorer, L., S. Schmitz and A. Weber (2019). Membrane based purification of hydrogen system (MEMPHYS). International Journal of Hydrogen Energy **44**(25): 12708-12714.

Segré, G. and A. Silberberg (1961). Radial particle displacements in poiseuille flow of suspensions. Nature **189**(4760): 209-210.

Swiegers, G. F., A. L. Hoang, A. Hodges, G. Tsekouras, C.-Y. Lee, K. Wagner and G. Wallace (2022). Current status of membraneless water electrolysis cells. Current Opinion in Electrochemistry **32**: 100881.

Tjaden, B., S. J. Cooper, D. J. L. Brett, D. Kramer and P. R. Shearing (2016). On the origin and application of the Bruggeman correlation for analysing transport phenomena in electrochemical systems. Current Opinion in Chemical Engineering **12**: 44-51.

Valenti, G. (2016). Hydrogen liquefaction and liquid hydrogen storage. Compendium of Hydrogen Energy**:** 27-51.

Vermeiren, P., W. Adriansens, J. P. Moreels and R. Leysen (1998). Evaluation of the Zirfon® separator for use in alkaline water electrolysis and Ni-H2 batteries. International Journal of Hydrogen Energy **23**(5): 321-324.

Vogt, H. (2012). The actual current density of gas-evolving electrodes—Notes on the bubble coverage. Electrochimica Acta **78**: 183-187.

Vogt, H. and R. J. Balzer (2005). The bubble coverage of gas-evolving electrodes in stagnant electrolytes. Electrochimica Acta **50**(10): 2073-2079.

Wan, Z., Y. Tao, J. Shao, Y. Zhang and H. You (2021). Ammonia as an effective hydrogen carrier and a clean fuel for solid oxide fuel cells. Energy Conversion and Management **228** :113729.

Wang, R. R., Y. Q. Zhao, A. Babich, D. Senk and X. Y. Fan (2021). Hydrogen direct reduction (H-DR) in steel industry—An overview of challenges and opportunities. Journal of Cleaner Production **329**: 129797.

Woolley, H. W., R. B. Scott and F. G. Brickwedde (1948). Compilation of thermal properties of hydrogen in its various isotopic and ortho-para modifications. J Res Natl Bur Stand (1934) **41**(5): 379-475.

Yang, B., M. Jafarian, N. Freidoonimehr and M. Arjomandi (2023). Controlled bubble formation from a microelectrode single bubble generator. Journal of Fluids Engineering **145**(11): 111401.

Yang, J., Y. Li and H. Tan (2023). Study on performance comparison of two hydrogen liquefaction processes based on the Claude cycle and the Brayton refrigeration cycle. Processes **11**(3): 932.

Yin, L. and Y. Ju (2020). Process optimization and analysis of a novel hydrogen liquefaction cycle. International Journal of Refrigeration **110**: 219-230.

Zeng, K. and D. Zhang (2010). Recent progress in alkaline water electrolysis for hydrogen production and applications. Progress in Energy and Combustion Science **36**(3): 307-326.

Chapter 4

Bubble formation from a microelectrode

4.1 Chapter overview

This chapter presents the development of a microbubble generator, which can introduce microbubbles into an electrolyte with precise control over size and frequency. As discussed in Section 2.4, bubble size is a critical factor of rising behaviour in an electrolyser. In modern electrolysers, bubble diameters span from several micrometres to the millimetre scale. Notably, bubbles with diameters smaller than 0.1 mm exhibit low Stokes numbers (<0.1). As a result, their rising trajectories` can be predicted by the electrolyte flow field as these bubbles closely follow the streamline of the flow. Conversely, bubbles with diameters exceeding 0.3 mm exhibit Stokes numbers above 1. Therefore, the behaviour of these large microbubbles within an electrolyser significantly deviates from their smaller counterparts.

Conventional bubble-generation techniques predominantly employ the injection of gases into a liquid through a submerged nozzle. To prevent continuous bubbles, this approach relies on the precision controlling of the gas flow supplied to the nozzle, which involves sophisticated fabrication of flow controlling and monitoring systems. In contrast, the microelectrode single bubble generator introduced in this chapter presents a straightforward and potentially economical alternative. The developed bubble generator is fabricated by embedding a microelectrode within a small nozzle. The size and frequency of the bubbles are controlled by varying the applied current and the geometrical parameters of the bubble generator.

This study investigates the formation and detachment of bubbles on a microelectrode. Specifically, when the microelectrode is entirely exposed to electrolyte, it exclusively generates continuous bubbles with diameters below 0.2mm. On the other hand, when housed within a nozzle, the microelectrode tends to form single bubbles. The dimension of the microelectrode also plays a crucial role, with continuous bubbles prevailing when the microelectrode diameter exceeds 0.25mm. Importantly, a concealed microelectrode under minimal current tends to produce continuous bubbles. As the current is elevated, bubble coalescence intensifies, creating a single, expanding bubble sitting on the nozzle, which detaches upon reaching its critical diameter.

Moreover, it is found that a microelectrode thinly concealed within the nozzle can successfully produce bubbles with diameters spanning 0.3–1.4 mm at an approximate frequency of 1 Hz. The development of the novel bubble-producing technique achieves the second research objective, facilitating the subsequent investigation of bubble rising behaviour in an electrolyser channel.

4.2 Single bubble formation from microelectrode

This section consists of the following journal article:

> Yang, B., M. Jafarian, N. Freidoonimehr, and M. Arjomandi, Controlled bubble formation from a microelectrode single bubble generator. Journal of Fluids Engineering, 2023. 145(11). DOI: 10.1115/1.4062962.

This article is identical to the submitted version, with the exception of the numbering and positioning of figures, tables, and equations. Additionally, all American spellings have been revised to their British equivalents.

Statement of Authorship

Title of Paper	Controlled bubble formation from a microelectrode single bubble generator
Publication Status	☒ Published ☐ Accepted for Publication ☐ Submitted for publication ☐ Unpublished and Unsubmitted work written in manuscript style
Publication Details	Yang, B., M. Jafarian, N. Freidoonimehr, and M. Arjomandi, Controlled bubble formation from a microelectrode single bubble generator. Journal of Fluids Engineering, 2023. 145(11). DOI: 10.1115/1.4062962.

Principal Author

Name of Principal Author (Candidate)	Bo Yang		
Contribution to the Paper	Developed ideas, conducted experiments, performed data analysis, interpreted results, wrote manuscript, and acted as corresponding author.		
Overall percentage (%)	80%		
Certification:	This paper reports on original research I conducted during the period of my Higher Degree by Research candidature and is not subject to any obligations or contractual agreements with a third party that would constrain its inclusion in this thesis. I am the primary author of this paper.		
Signature		Date	25/07/2022

Co-Author Contributions

By signing the Statement of Authorship, each author certifies that:

i. the candidate's stated contribution to the publication is accurate (as detailed above);
ii. permission is granted for the candidate in include the publication in the thesis; and
iii. the sum of all co-author contributions is equal to 100% less the candidate's stated contribution.

Name of Co-Author	Mehdi Jafarian		
Contribution to the Paper	Supervised the development of the research, participated in developing ideas and concept, helped in interpreting results, and assisted in evaluating and editing the manuscript.		
Signature		Date	25/07/2022

Name of Co-Author	Navid Freidoonimehr		
Contribution to the Paper	Supervised the development of the research, participated in developing ideas and concept, helped in interpreting results, and assisted in evaluating and editing the manuscript.		
Signature		Date	25/07/2022

Name of Co-Author	Maziar Arjomandi		
Contribution to the Paper	Supervised the development of the research, participated in developing ideas and concept, helped in interpreting results, and assisted in evaluating and editing the manuscript.		
Signature		Date	25/07/2022

Controlled bubble formation from a microelectrode single bubble generator

Bo Yang, Mehdi Jafarian, Navid Freidoonimehr and Maziar Arjomandi

Abstract

In this work, a new microelectrode bubble generator is presented that employs a microelectrode installed inside a small nozzle enabling the production of bubbles with controllable size and frequency. This bubble generator can be employed as a simple and potentially cheap method for the generation of single bubbles in a liquid, as long as it enables ion exchange, as an alternative to more complicated methods such as timely injection of a gas through a nozzle, which requires sophisticated nozzle design, manufacturing and monitoring of the injected gas flow rate. A systematic investigation was conducted to assess the effect of the bubble generator dimensions, applied voltage and electrolyte flow conditions on the size and frequency of the generated bubbles. It was shown that when the microelectrode is thinly concealed within the nozzle, this bubble generator can successfully produce bubbles covering a wide range of diameters from 0.4-1.4 mm with a size distribution standard deviation of about 25%. The mechanism of single and continuous bubbles formation from the proposed bubble generator is also discussed. While this paper introduces this new microelectrode bubble generator, further work is required to optimise it, enabling more accurate control over bubble size and frequency.

Nomenclature

A	Area [m^2]
D	Diameter [m]
E	Voltage [V]

F	Force [N]
g	Gravitational acceleration [m/s^2]
$\mathcal{F}$	Faraday constant, 96485 [c/mol]

4.2.1 Introduction

Generation of bubbles with controlled size and frequency is of significant importance in several industries and research fields. For example, bubbles are used as a tool to deliver drugs across the blood–brain barrier (Unger *et al.* 2002, Unger *et al.* 2004), as contrast agents in ultrasonic imaging (Stride and Saffari 2003), and for therapeutics through sonoporation (van Wamel *et al.* 2006) and sonothrombolysis (Unger 2005). Other examples include the manufacturing of foams and hollow structures (Schroers *et al.* 2004, Zhang *et al.* 2018), delivery of free radicals in the water treatment industry for oxidation/detoxification of contaminated water (Agarwal *et al.* 2011) and improvement of appearance, texture, and digestibility of foods (Xu *et al.* 2008). Bubble generation mechanisms and hydrodynamics have also been found to significantly affect the performance of low to mid-temperature electrolyses, in particular emerging membrane-less type (Davis *et al.* 2019, Swiegers *et al.* 2022), in which the product hydrogen and oxygen bubbles on electrodes are to be separated mainly through their hydrodynamics of the bubbles (Gillespie *et al.* 2015, Esposito 2017).

Typically, in experiments where bubbles are needed, they are generated by supplying gas through a submerged nozzle (or a needle) (Kumar and Kuloor 1970, Sanada and Abe 2013). When the bubble is formed from a submerged nozzle in a quiescent liquid, the primary force that contributes to the detachment of the bubble from the orifice is generally the buoyancy force, while the surface tension force acting along the edge of the nozzle contributes to restraining the bubble from departure. If the inertia of gas is neglected, the bubble detaching radius (r_d) can be estimated when the buoyancy and surface tension forces on the bubble are in equilibrium (Kumar and Kuloor 1970, Kolev 2007):

$$r_d = \left(\frac{3\sigma D_o}{4\rho_l g}\right)^{\frac{1}{3}}. \tag{4-1}$$

Here σ and ρ_l are the surface tension and density of the liquid, respectively; D_o is the diameter of the nozzle, and g is the gravitational acceleration. Equation 4-1 shows that the bubble radius varies proportionally to $D_0^{\frac{1}{3}}$. This means that one can use a nozzle with a certain diameter to achieve the desired bubble size. However, the production of bubbles with a diameter of less than 1 mm (D_b < 1 mm) requires a nozzle diameter smaller than 50μm, which is technically challenging. Otherwise, drag force needs to be employed to control bubble departure from the nozzle, either by directly applying liquid co-flow over the growing bubble (Evangelio *et al.* 2015, Kim *et al.* 2021) or utilizing orifice movement to enhance bubble departure (Vejrazka *et al.* 2008). Moreover, injecting gas into the nozzle without control is likely to produce a continuous bubble plume because the nozzle has limited control over the gas flow rate (Davidson and Schüler 1997, Bari and Robinson 2013). As to produce single bubbles, it is crucial to frequently stop the gas flow once the bubble at the nozzle is released. This is why the timed gas injection technique has become a popular method to generate single bubbles from a nozzle (Najafi *et al.* 2008, Parkinson *et al.* 2008, Kim *et al.* 2021). The timed gas injection system includes a group of precision gas valves together with a precise control system, which induces pressure pulses in the gas fed to the nozzle to prevent the formation of bubble plume. Hence, the effectiveness of this gas-injection type bubble generator significantly relies on the response time of the valves and the accuracy of their control system.

Electrolysis can also be used as an alternative method to generate bubbles in water with no mass added to the system. Depending on the surface characteristics of the electrode and operating conditions, the diameters of electrolytic hydrogen and oxygen bubbles range from dozens of micrometers to hundreds of micrometers (Zeng and Zhang 2010, Zhang and Zeng 2012). Water electrolysis tends to produce a dense bubble plume at the surface of a regular-sized electrode. However, it is found that when the electrode size is sufficiently small, single bubbles can be formed on the electrode surface (Li *et al.* 2011, Fernandez *et al.* 2014, Yang *et al.* 2015). In an experimental work by Fernández *et al.* (Fernandez *et al.* 2014), a platinum microelectrode with a diameter of 125 μm was fabricated and coated with an optical resin to investigate the formation of hydrogen bubbles. In their work, single bubbles with a diameter of 500-800 μm were successfully generated at a frequency of 1.5-3.5 Hz. Yang *et al.* (Yang *et al.* 2015) studied the growth and detachment of single hydrogen bubbles from a microelectrode in a water electrolyser. Single H_2 bubbles with a diameter of 100-300 μm were generated using a microelectrode fabricated by embedding a 100μm diameter platinum wire into an epoxy resin. Others have found that the bubble diameter decreases when the size of the electrode is reduced (Fernández *et al.* 2012, Luo and White 2013, Bashkatov *et al.* 2019). The recent works pertaining to the generation of single bubbles are included in Table 4-1.

Table 4-1. A summary of techniques used for generating single bubbles in water.

Bubble generation method	Bubble size	Bubble frequency	Control technique/instrument	Ref.
Gas and water injection through a 4 mm nozzle.	0.5-2.5 mm	-	Control the opening duration for gas and water supply valves	(Ohl 2001)
Gas injection through a 0.5 mm diameter orifice using a piston-cylinder	2-4 mm	up to 70 Hz depending on gas injection rate.	Precision valves and pressure sensors	(Ostmann and Schwarze 2018)
Gas injection through a 0.3 mm inner diameter capillary tube using pressurised air	1-3 mm	1-18 Hz depending on gas injection rate.	Regulating valve sets and pressure gauge	(Duhar and Colin 2006)

Gas injection through a 2 mm inner diameter capillary tube using pressurised air	>5 mm	20-50 Hz depending on gas injection rate.	Regulating valve sets with flow meter	(Zhang and Shoji 2001)
Gas injection through a slit on an elastic tube with an inner diameter of 5 mm and an acoustic pressure wave to generate gas pulse.	about 0.5 mm	Controllable, up to 500 Hz	Slit opens by acoustic wave generated by a loudspeaker.	(Abe and Sanada 2015)
Gas injection through syringe needles with an inner diameter of 0.5-1.2 mm	about 3mm	-	Gas injection rate controlled by fine tuning syringe displacement with a cordless drill and a rotary motion sensor.	(Lesage and Marois 2013)
Gas injection through nozzles with inner diameter of 0.292-3.025 mm	0.9-7.35 mm	-	Gas injection controlled by a pressure controller, a flowmeter and valves.	(Bolaños-Jiménez *et al.* 2008)
Gas bubble injection through a nozzle near the outlet of a pressurised chamber to generate external flow around the needle.	0.05-0.8 mm	0.1-8Hz depending on bubble size.	External flow is controlled by the pressure in a chamber.	(Evangelio *et al.* 2015)
Gas injection through a micropipette with an inner diameter of less than 1μm.	less than 0.2 mm	One bubble per cycle.	Gas controlled by pressure sensors to generate a pressure pulse.	(Kim *et al.* 2021)
Gas injection through needles (20-450 μm) with rapid movements to accelerate	0.2-2.5 mm	40-160Hz depending on needle size.	Specially designed needle.	(Vejrazka, *et al.* 2008)

bubble departure.				
Electrolytic bubble generated from a 125 μm diameter platinum wire.	0.2-0.8 mm	1-8 Hz depending on bubble size.	Bubble diameter controlled by applied voltage.	(Fernandez *et al.* 2014)
Electrolytic bubble generated from a 100 μm diameter platinum wire.	about 1 mm	60-180 Hz depending on bubble size.	Bubble diameter controlled by applied voltage.	(Bashkatov *et al.* 2019)
Electrolytic bubble generated from a 100 μm diameter platinum wire.	0.05-0.25 mm	1-1000 Hz depending on bubble size.	-	(Yang *et al.* 2015)

Compared to gas-injection type bubble generators, a significant advantage of electrolytic bubble generators is the simplicity, which only needs a pair of electrodes together with a DC power supply. Gas cylinders, piping, precision valves and controlling system are not required since hydrogen and oxygen gases can be obtained from the electrolysis of water, with their flow rate determined by the applied voltage over the electrodes. Commensurate with this, in the majority of the previous works, the microelectrodes were made of a thin metal wire embedded in a non-conductive material, with only the tip of the wire exposed to the electrolyte. They have also focused on the dependence of the applied current on the size distribution of produced bubbles. However, the effect of electrode geometry on the size and frequencies of bubbles has not been studied in detail.

In taking advantage of both the submerged nozzle and electrode-based bubble generators mentioned above, a new type of single bubble generator is introduced in this paper. The proposed bubble generator produces single electrolytic bubbles using a microelectrode installed inside a small nozzle. A systematic study has also been conducted to investigate the effect of bubble generator geometry, applied voltage and flow parameters on the size and frequency of the generated bubbles.

4.1.2 Methodology

4.1.2.1 Experimental setup

The proposed bubble generator (shown in Figure 4-1) comprises a microelectrode sitting inside a tube with an opening on its top. The liquid penetrates through the opening toward electrode surface, where bubbles are formed and merged to get to a certain size before they leave the tube. In this work, enamel copper wire was chosen as the microelectrode, whose insulation layer ensures that bubbles are formed only at the tip of the wire. A 50mm-long quartz tube was also used as the nozzle. The bubble generator is made by installing the enamel copper wire inside the quartz tube. The retraction distance (h) is defined as the gap between the tip of the microelectrode and the opening of the nozzle, which can be adjusted during the experiments to provide additional control over the bubble formation and departure. To systematically investigate the effect of the geometry on the bubble formation using this type of bubble generator, ten sets of microelectrodes and nozzles were tested in this work, as listed in Table 4-2.

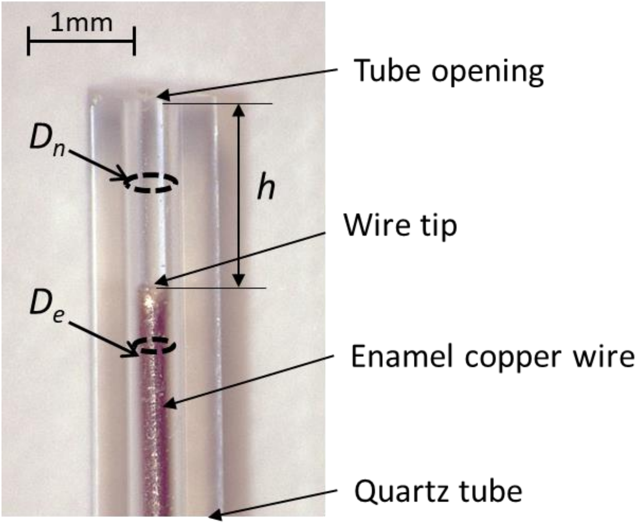

Figure 4-1. A photo of the proposed bubble generator.

Table 4-2. Size of microelectrodes and nozzles for bubble generator used in this work. The wall thickness of the nozzles varies from 0.2 mm-1.2 mm.

No.	Diameter of microelectrode, D_e (mm)	Inner diameter of nozzle, D_n (mm)	D_n/D_e
1	0.2	0.3	1.5
2	0.2	0.4	2
3	0.2	0.6	3
4	0.25	0.3	1.2
5	0.25	0.4	1.6
6	0.25	0.5	2
7	0.25	0.6	2.4
8	0.25	1.0	4
9	0.5	0.6	1.2
10	0.5	1.0	2

The proposed microelectrode bubble generator was tested in a vertical water channel shown in Figure 4-2. The channel was fabricated from acrylic with a height of 1700 mm and a square cross-section of 16 mm × 16 mm. The bubble generator was located at the channel centre at a distance of 1200 mm from the channel inlet, where the flow was fully developed under the experimental condition of this work ($0 \leq Re_l \leq 1000$) (Yang *et al.* 2022). To facilitate the installation of the bubble generator, a 60mm long, 2mm wide hole was added to the acrylic channel at a distance of 1200 mm from its inlet. Two sets of 0.5 mm-diameter holders were used to support the bubble generator. The holders were installed onto a rubber plug, which was used to seal the rectangular hole during the experiments. The cathode (1 mm × 10 mm nickel electrode) was installed close to the channel outlet. A pump (4 L/min) was used to circulate the electrolyte (0.1 wt% NaOH aqueous solution) in the channel. The electrolyte and instrumentation properties are shown in Table 4-3.

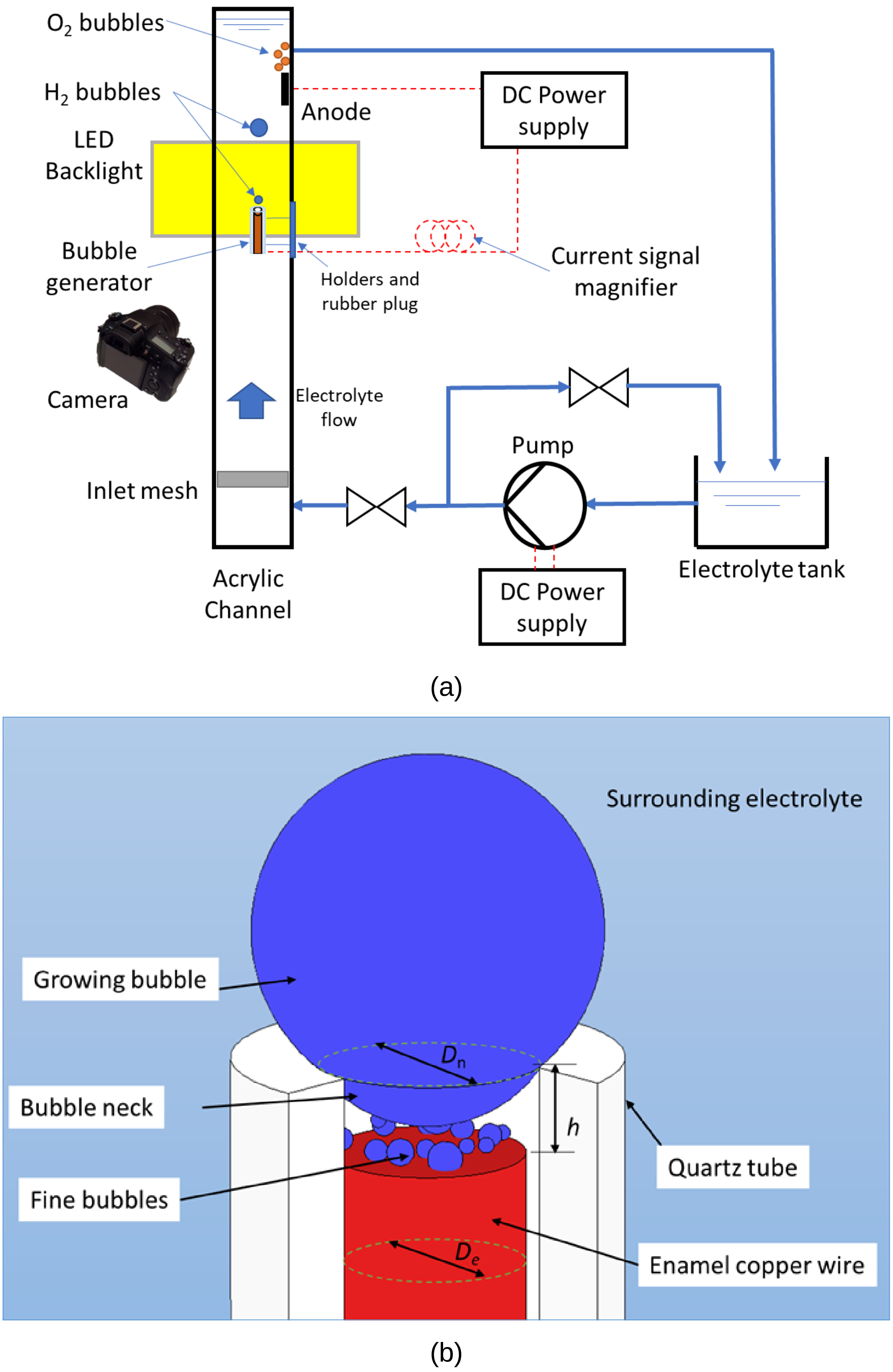

Figure 4-2. (a) The experimental setup of this work. (b) A schematic of the bubbles formed from the bubble generator.

Table 4-3. Electrolyte properties and equipment used in this work.

Item	**Parameters**
Power supply	0-30 V
Current probe	Fluke i310s current clamp, resolution: 50 mA
datalogger	USB1408fs, sample rate 1 kHz
Pump	4L/min
Camera	SONY RX10IV
Backlight	DC 5V LED
Tank	10L
Channel	1700 mm length with a 16mmx16mm cross-section made from acrylic
Temperature	20 ℃±2 ℃
Electrolyte	σ=0.07 N/m, μ=1.02 mPa/s, ρ=999 kg/m^3 [40]

A DC power supply was used to provide the required voltage for the generation of hydrogen bubbles at the bubble generator. The voltage output of the power supply controls the current supplied to the microelectrode. According to Faraday's Law, the volumetric flow rate (m^3/s) of H_2 can be calculated by (Zhou *et al.* 2020):

$$\dot{V}_{\mathrm{H2}} = \frac{\mathrm{R}T}{P}\dot{n}_{\mathrm{H2}} = \frac{\mathrm{R}T}{P}\frac{I}{2\mathcal{F}}, \tag{4-2}$$

where P, T and I are the pressure (Pa), temperature (K) and current (A/m^2), respectively. R and $\mathcal{F}$ are the gas constant (8.3145 J/mol·K) and the Faraday constant (96485 c/mol), respectively. A current signal magnifier containing 500 coils of wire was employed in the circuit. The current probe (Fluke i310s current clamp) was clamped on the coils. This increased the measured current by 500 times compared to the actual value. Therefore, the resolution of the current probe was improved from 50 mA to 0.1 mA. During the experiments, the current data were recorded by a datalogger connected to a PC at a sampling frequency of is 1kHz.

4.2.2.2 Bubble visualisation and data acquisition

A high-speed camera equipped with a macro lens (Raynox m250) was used to record the generation of H_2 bubbles illuminated by a LED backlight. The depth of field and the field of view are approximately 0.5 mm and 5.4 mm× 3.2 mm, respectively. The camera was set to high frame rate mode (500fps) and focused on the tip of the bubble generator. The videos of bubble generation from the bubble were recorded with a pixel size of about 3μm. For each group of experiments, at least 500 generated bubbles were recorded. A MATLAB code was developed to identify the bubbles from the video frames using Circular Hough Transform (CHT) based algorithm (Yuen *et al.* 1990, Atherton and Kerbyson 1999, Davies 2005).

Figure 4-3 shows raw images of produced hydrogen bubble using the No.1 bubble generator in the vertical channel with no electrolyte flow (Re_l=0) under an applied voltage of 15 V. The retraction distance is set to zero (h=0). The presented images show the growth and departure of a hydrogen bubble.

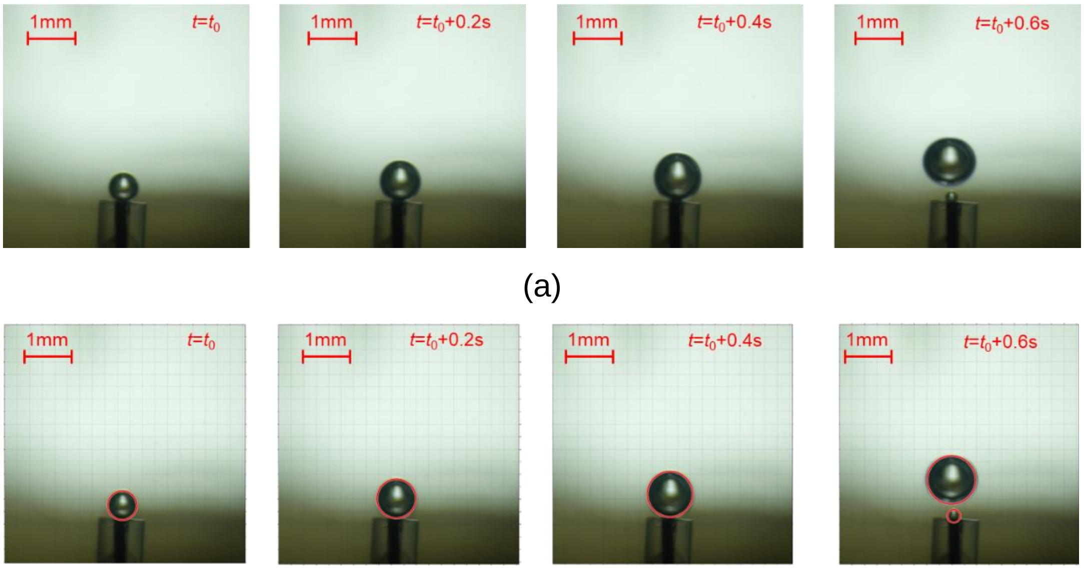

(a)

(b)

Figure 4-3. Example images of (a) generated bubbles using one of the proposed bubble generators (D_e=0.2mm, D_o=0.3 mm) in stagnant electrolyte under the applied voltage of 15 V, and (b) bubbles identified using developed MATLAB code from the same images. The grid size is 10 pixels.

Figure 4-4 shows an example of the measured current in the circuit in 60 s during the generation of H_2 bubbles. As can be seen, the current fluctuates in the circuit. That is because the surface of the bubble is fully exposed to the electrolyte at the beginning of the phenomenon. However, the growth of bubble at the electrode surface results in a reduction in the surface area of the electrode in contact with the electrolyte, leading to a reduced current in the circuit (for example, from about 12 mA to 7 mA in this case). The surface of the electrode is fully exposed to the electrolyte when the bubble detaches. The consecutive occurrence of this phenomenon leads to variations in the current reading.

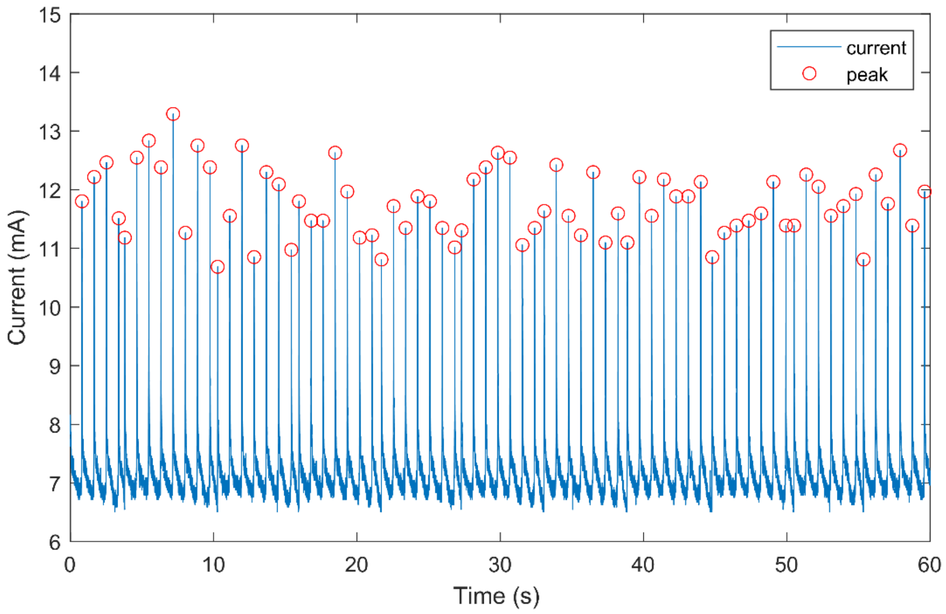

(a)

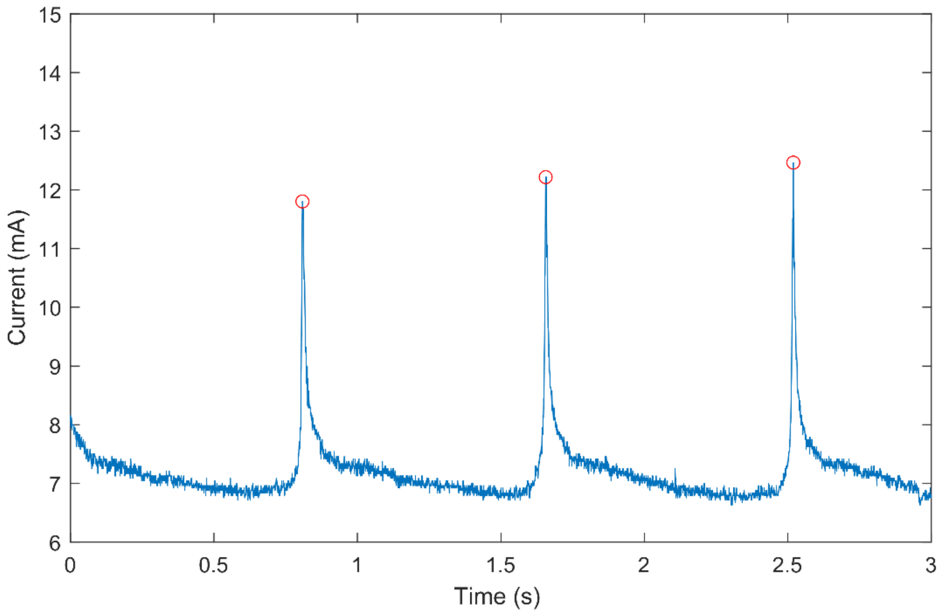

(b)

Figure 4-4. Example of (a) current readings during the generation of H_2 bubbles using one of the proposed bubble generators (D_e=0.2 mm, D_o=0.3 mm) in stagnant electrolyte at an applied voltage of 15 V, and (b) the first 3s of the measured current.

4.2.2.3 Uncertainty analysis

Table 4-4 summarises the uncertainties of the parameters used in this work. The error for each parameter ($\delta R/R$) was calculated using the technique proposed by Moffat *et al.* (1985):

$$\frac{\delta R}{R} = \sqrt{\left(a\frac{\delta x_1}{x_1}\right)^2 + \left(b\frac{\delta x_2}{x_2}\right)^2 + \cdots + \left(N\frac{\delta x_n}{x_n}\right)^2},$$

$$R = {x_1}^a {x_2}^b \ldots {x_n}^N \ . \tag{4-3}$$

Table 4-4. Summary of uncertainties of this work.

Parameter	Maximum uncertainty
Temperature, K	±0.7%
Fluid viscosity, Pa·s	±5.1%
Fluid surface tension, N/m	±3.2%
Fluid Density, kg/m^3	Negligible
Hydrogen density, kg/m^3	Negligible
Current, A	±3.3%
Channel width, m	±3.1%
Cross-section area of the channel, m^2	±4.2%
Bubble diameter, m	±8.0%
Fluid velocity, m/s	±4.0%

4.2.3 Results

4.2.3.1 Generation of hydrogen bubbles with zero retraction distance

To achieve zero retraction distance (h=0), the microelectrode was set at the same height as the opening of the nozzle. All bubble generators were tested in a stagnant electrolyte under various applied voltages. It is observed that only No.1 and No.4 bubble generators were able to produce single bubbles, while continuous bubbles were generated by other bubble generators. The dependence of the applied current on the average bubble diameter is plotted in Figure 4-5. As can be seen, the dominating size of the produced bubbles increases with the increase of the applied voltage, which agrees with the work by Fernandez *et al.* and Zhang *et al.* (Zhang and Zeng 2012, Fernandez *et al.* 2014). Also, the increase in microelectrode diameter results in a larger bubble diameter.

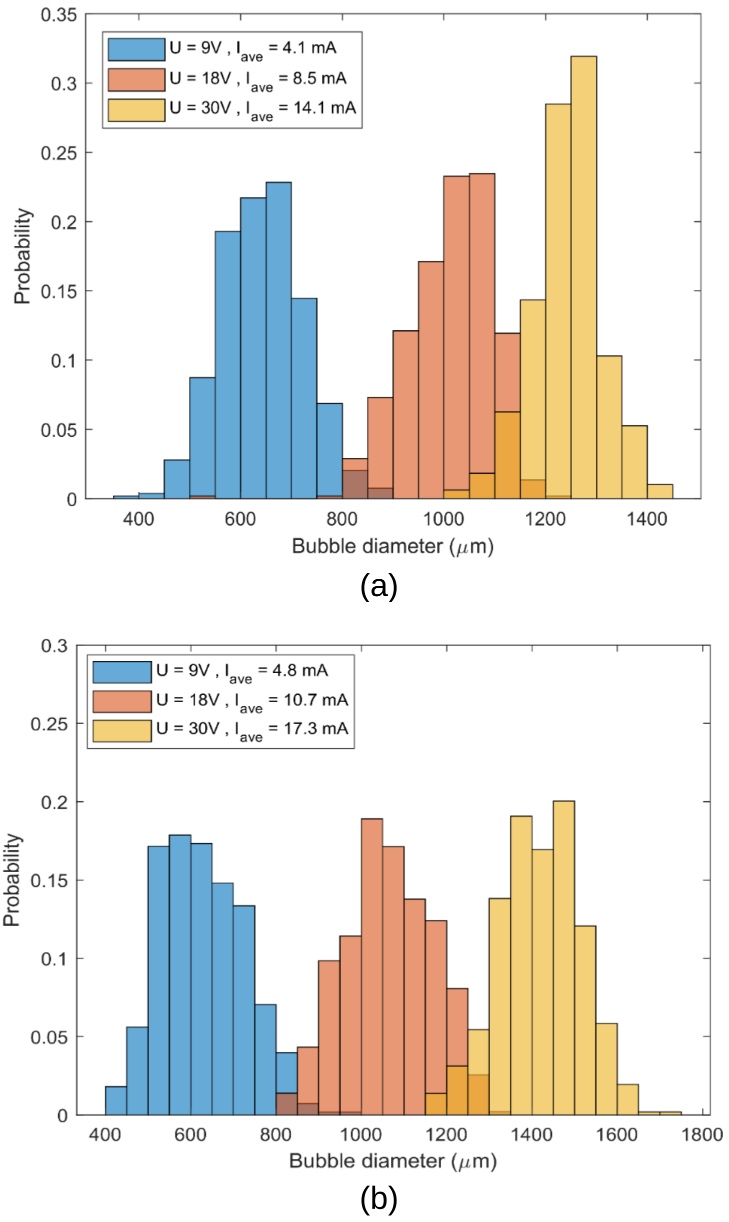

(a)

(b)

Figure 4-5. Probability distribution of bubble diameters produced by a) No.1 and b) No.4 bubble generator under different applied voltages in a stagnant electrolyte.

The average diameter of the bubbles produced by No.1 and No.4 bubble generators are shown in Figure 4-6. It can be seen that for both No.1 and No.4 bubble generators, the average bubble diameter has increased with the applied current. This is because with a higher applied current, the rate of gas generation at the electrode surface increases, which results in larger bubbles being formed before it leaves the electrode (Vogt 1989). Moreover, under the same applied current, No. 4 bubble generator produced slightly larger bubbles than the ones of No.1 bubble generator. This indicates that using a larger electrode can provide a greater circular contact area for the bubble to grow, which leads to an increase in bubble diameter (Zhang and Zeng 2012).

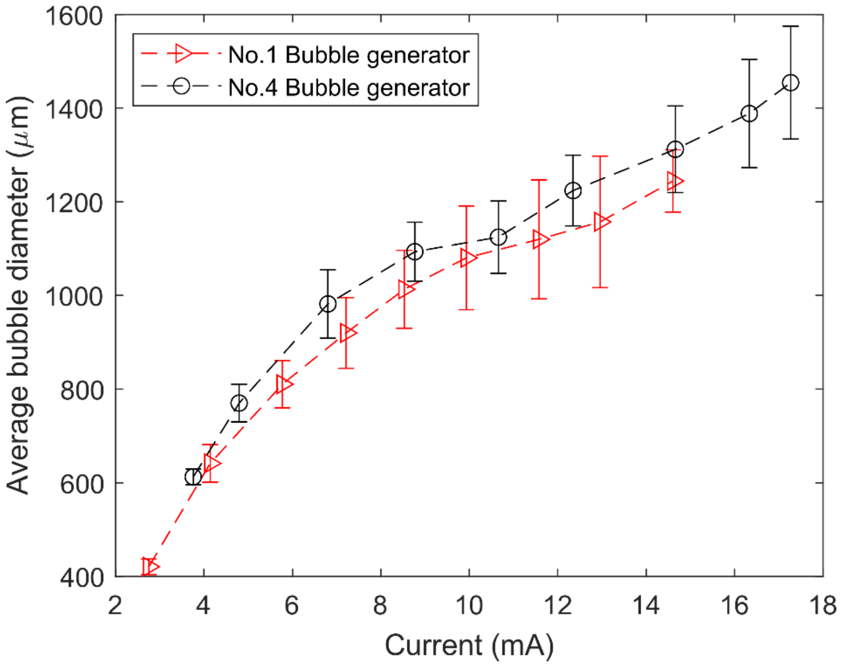

Figure 4-6. Average diameter of produced bubble versus applied current to the bubble generator by a) No.1 and b) No.4 bubble generator in a stagnant electrolyte. The error bars show the standard deviation.

The frequencies of produced bubbles using No.1 and No.4 bubble generators under different applied voltages are plotted in Figure 4-7. It was found that with an increase in the applied current, the intervals between generated bubbles also increase, and a larger microelectrode will produce bubbles at a higher frequency. For example, at an applied current of 10 mA, the average interval between the generated bubbles for No.1 bubble generator is about 1050ms. However, the average interval is decreased to 760 ms for No.4 bubble generator with the same applied current. This is because when a lower current is applied, smaller bubbles are formed at the electrode surface, which can quickly detach from the electrode surface, allowing the formed single bubble to escape from the electrode surface more frequently.

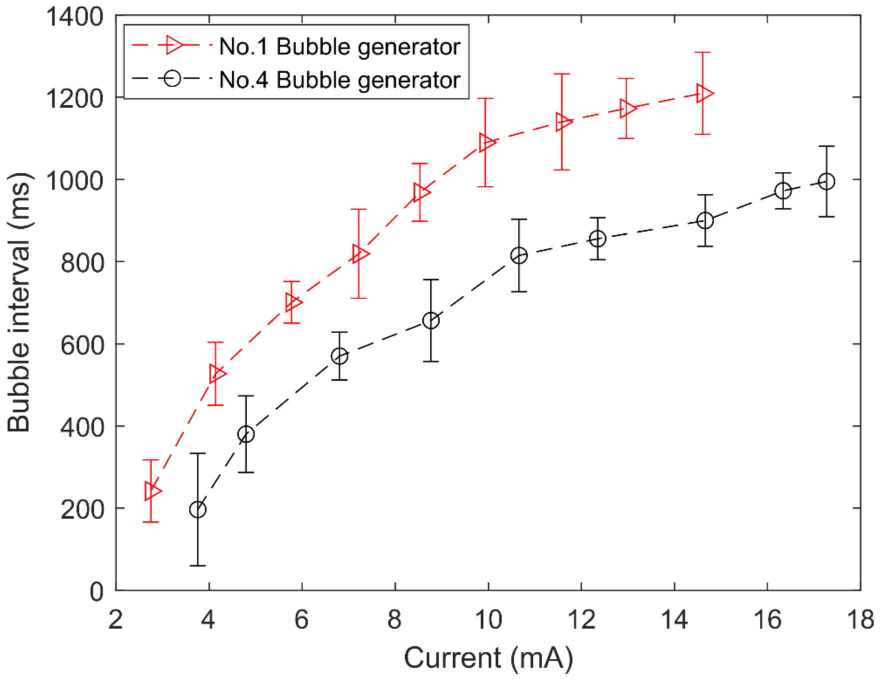

Figure 4-7. Effect of applied current to the bubble generator on the intervals of generated bubbles produced by a) No.1 and b) No.4 bubble generator in a stagnant electrolyte. The error bars show the standard deviation.

4.2.3.2 Effect of retraction distance on bubble generation

In this section, all bubble generators were tested at different applied voltages with various retraction distances in a stagnant electrolyte. It was found that the retraction distance has a significant effect on the bubble production performance. No.1 and No.4 bubble generators show the best performance in producing single bubbles with a wide range of diameters of choice at reasonable frequencies, whereas a minimum retraction distance of 600 μm is required for other bubble generators to produce single bubbles. Figure 4-8 shows the effect of retraction distance on average current under different applied voltages for No.1 and No.4 bubble generators. It was found that with the increase of retraction distance, the average current in the circuit reduces significantly. This is because when the microelectrode is retracted, the single bubble will form a “neck” inside the nozzle (as illustrated in Figure 4-15, Section 4). Since the bubble neck is full of non-conductive gas, it will block the electrode from contacting the electrolyte outside of the nozzle. Consequently, this blockage will lead to high electrical resistance inside the nozzle. The resistance increases with the increase of the neck length, i.e., the retraction distance. At zero retraction distance, the bubble neck is disappeared so that the extra electrical resistance due to the bubble neck vanishes. When the microelectrode is further retracted to 300 μm, the applied current to the bubble generator decreases drastically.

Figure 4-9 shows the dependence of average bubble diameter on the retraction distance for No.1 and No.4 bubble generators under various applied voltages in a stagnant electrolyte. It is found that the average bubble diameter reduces with an increase in retraction distance. Also, the deviation in bubble size increases with the increase of the retraction distance. Furthermore, the average bubble diameter increases with the applied voltage. The detailed discussion about the effect of retraction distance on the bubble diameter can be found in Section 4 of this paper.

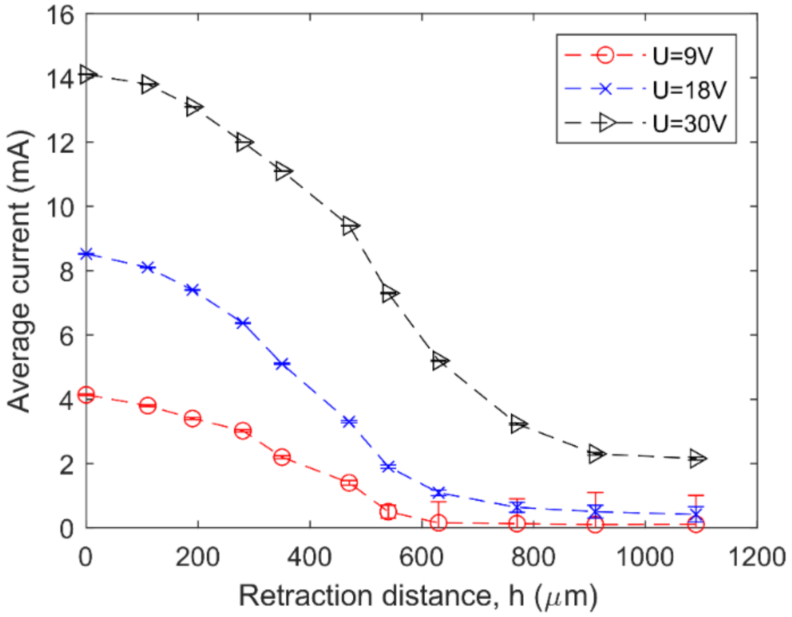

(a)

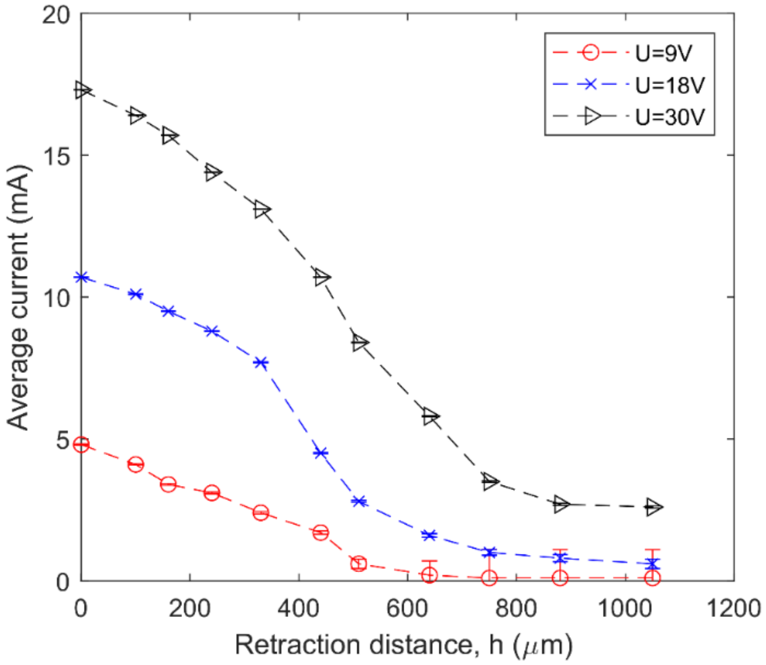

(b)

Figure 4-8. Effect of retraction distance on the average current applied to a) No.1 and b) No.4 bubble generators in a stagnant electrolyte. The error bars show the standard deviation.

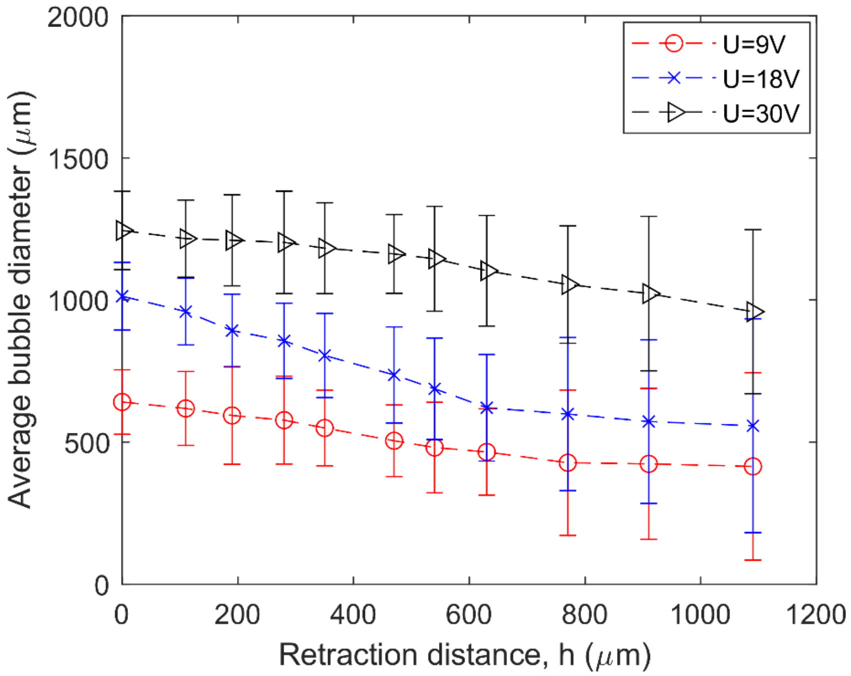

(a)

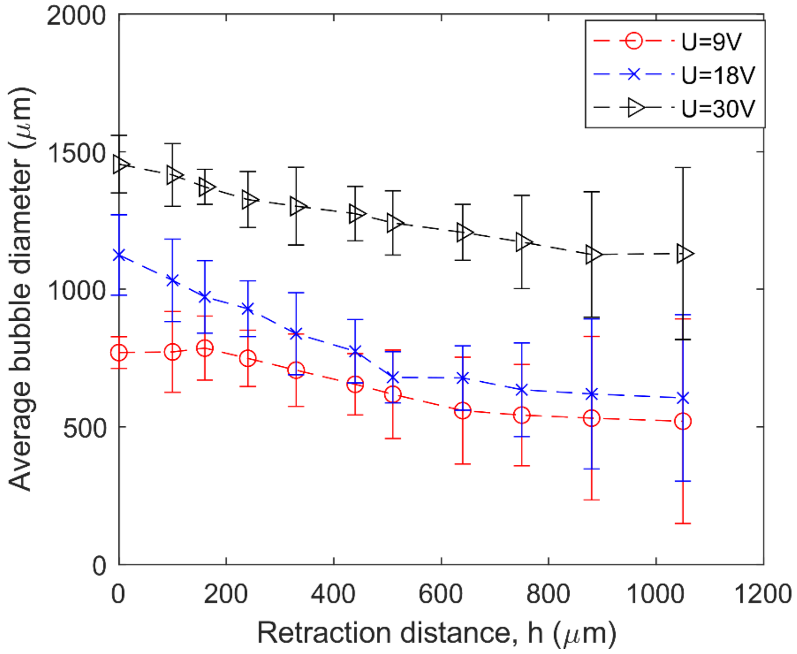

(b)

Figure 4-9. Dependence of the average bubble diameter on the retraction distance for a) No.1 and b) No.4 bubble generators at various applied voltages in a stagnant electrolyte. The error bars show the standard deviation.

Figure 4-10 shows the dependence of the average intervals of produced bubbles on the applied current for No.1 and No.4 bubble generators. For small retraction distances (h<300 μm), the average bubble interval increases slightly with the retraction distance. This is because with the increase of retraction distance, the current applied to the electrode reduces dramatically, which increases the duration for the bubble to grow to its departure diameter. Also, the small standard deviation indicates that bubble production is steady. However, with a further increase in the retraction distance, the bubbles' interval and their standard deviation increase significantly. Therefore, a small retraction distance shall be selected to achieve more consistent diameters and frequencies of produced bubbles, and only No.1 and No.4 bubble generators satisfy this requirement since others need h>600 μm to produce single bubbles.

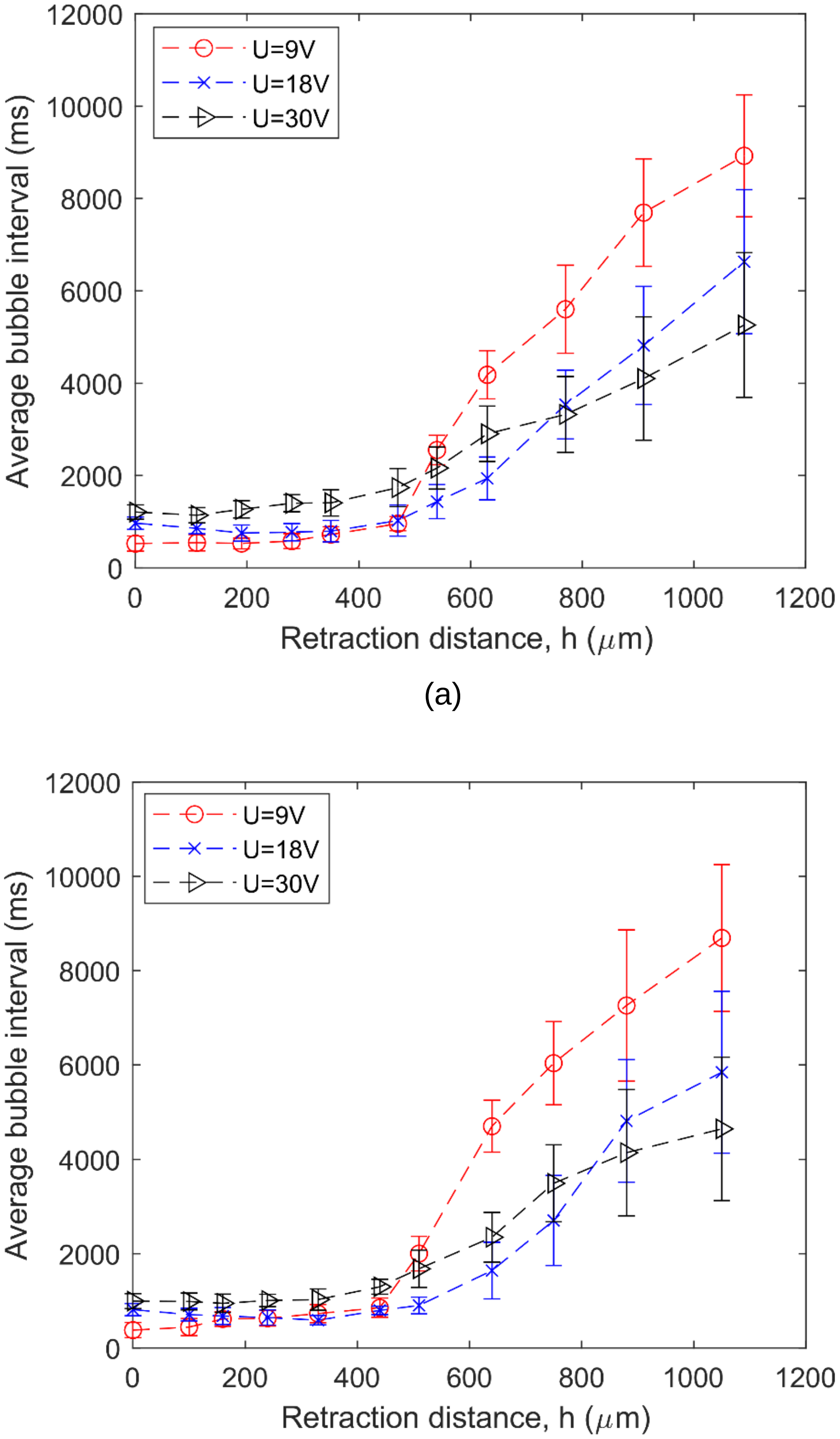

(a)

(b)

Figure 4-10. Dependence of the average intervals of the produced bubbles on applied current for a) No.1 and b) No.4 bubble generators. The error bars show the standard deviation.

4.2.3.3 Effect of external flow on bubble generation

To examine the effect of the external flow on bubble formation, bubble generators were tested in the centre of the vertical channel, where the bubbles are exposed to hydrodynamic forces generated by the circulation of electrolyte flow. The average diameter and interval of generated bubbles under different electrolyte Reynolds numbers for bubble generators No.1 and No.4 with zero retraction distance are plotted in Figures 4-11 and 4-12, respectively. As can be seen, both the bubble diameter and the intervals between the bubble formation reduce with the increase of the electrolyte velocity. This is because the departure of H_2 bubbles from the bubble generator is accelerated due to the induced drag force on the bubbles by the electrolyte flow around the nozzle.

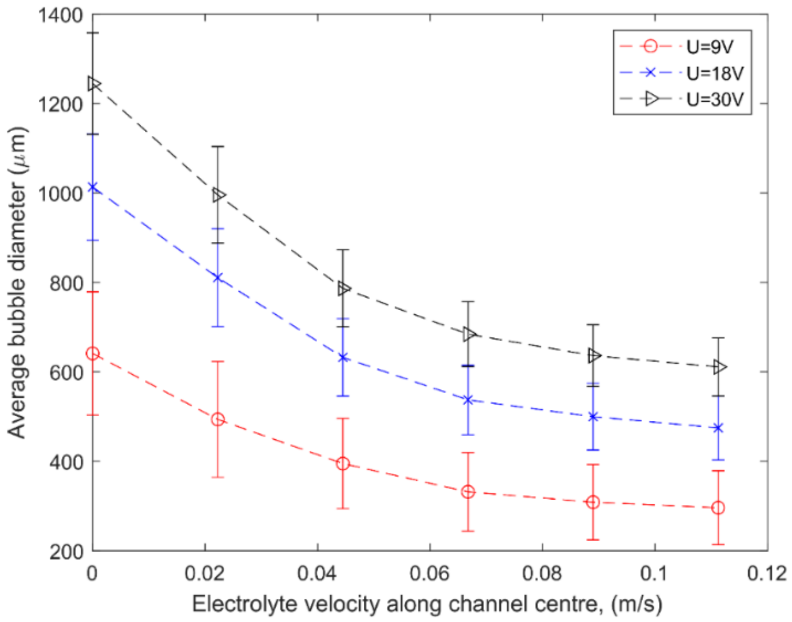

(a)

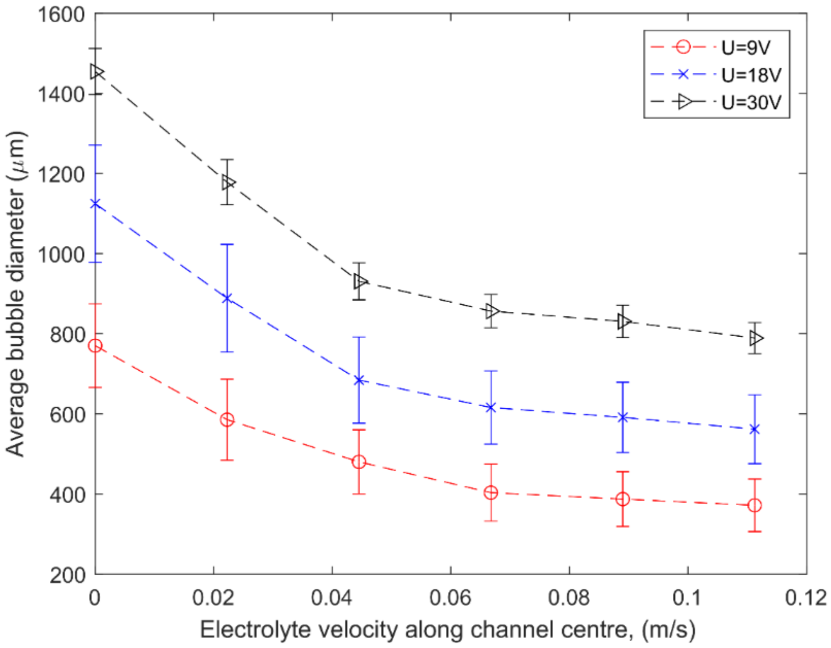

(b)

Figure 4-11. Average diameter of generated bubbles under different electrolyte flow velocities and applied voltages for a) No.1 and b) No.4 bubble generators with zero retraction distance.

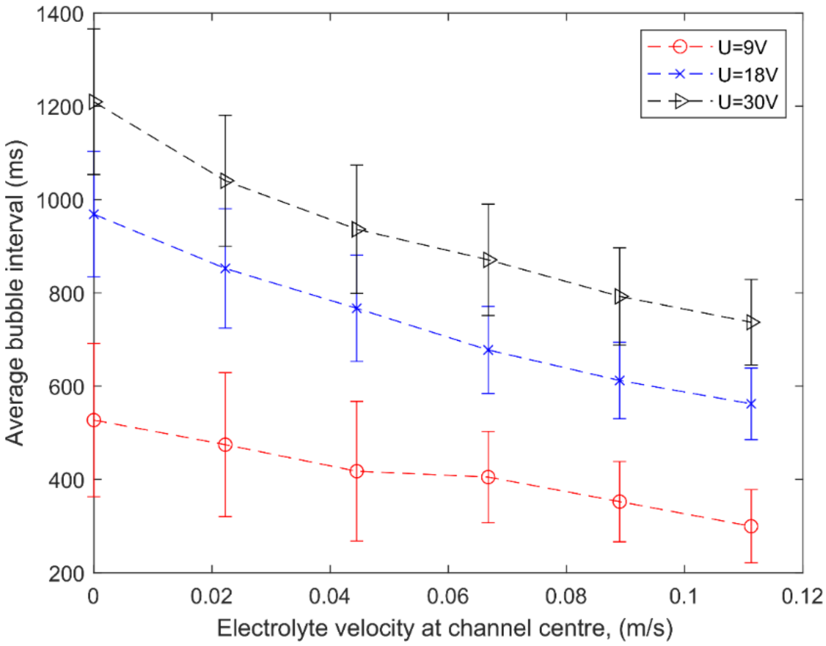

(a)

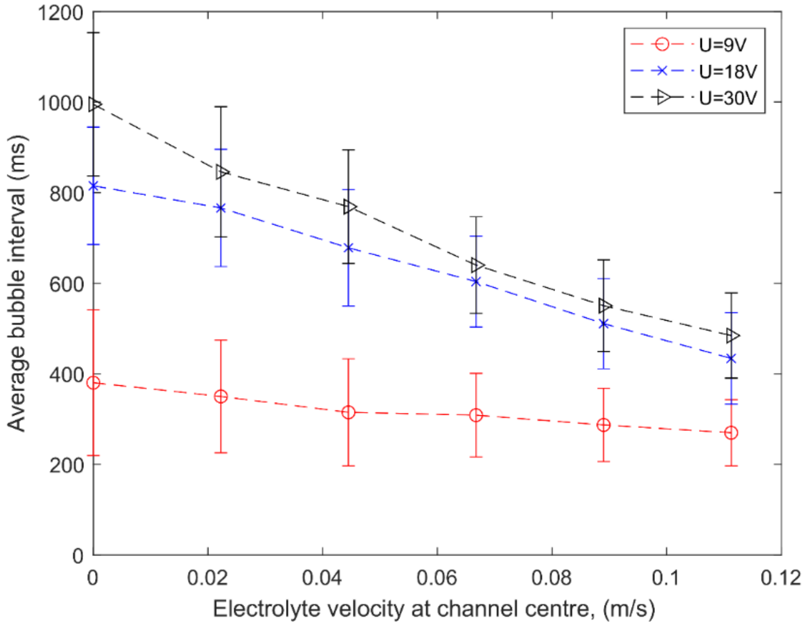

(b)

Figure 4-12. Average diameter of generated bubbles under different electrolyte flow velocities and applied voltages for a) No.1 and b) No.4 bubble generators with zero retraction distance.

4.2.4 Discussion

The bubble formation is significantly influenced by the geometries of the bubble generators. When the microelectrode is pulled out from the nozzle, a continuous stream of electrolytic bubbles is formed at the microelectrode surface, as shown in Figure 4-13. That is, the mechanism of the formation of continuous electrolytic bubbles in the proposed bubble generator relies on the coalescence of fine bubbles in the vicinity of the electrode, which has been extensively discussed in the literature (Vogt 1989, Yang *et al.* 2015, Vogt 2017, Bashkatov *et al.* 2019). By retracting the microelectrode back into the nozzle, continuous bubbles are still produced until the top of the microelectrode is aligned with the opening of the nozzle, i.e., the retraction distance equals zero.

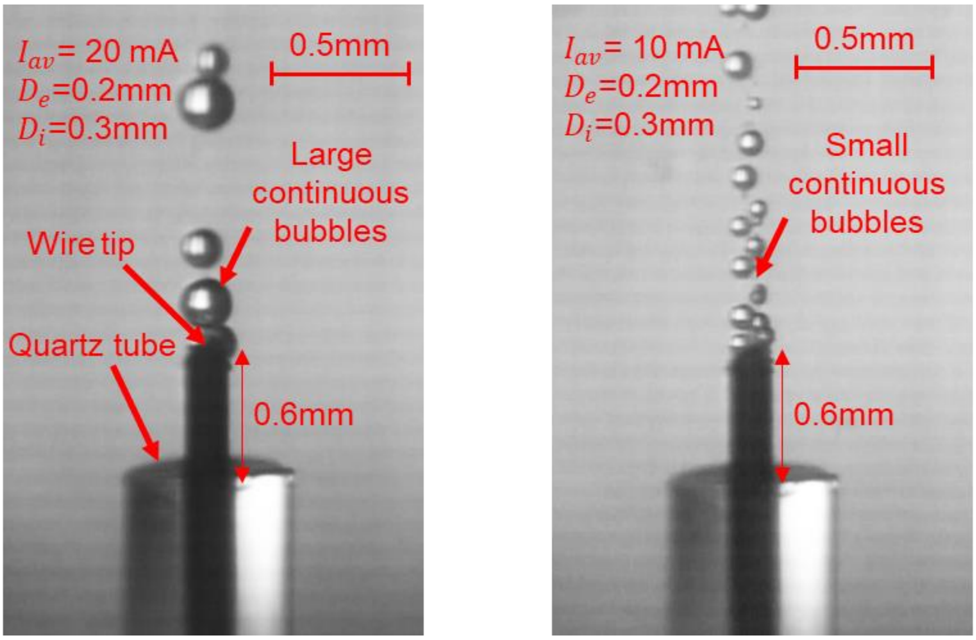

(a) (b)

Figure 4-13. Photos of continuous stream of bubbles formed at the top of the microelectrode which were pulled out from the nozzle under an average current of (a) 20 mA and (b) 10 mA in a stagnant electrolyte.

At zero retraction distance, bubble generators No.1 and No. 4 produce single bubbles when a minimum current is applied, while continuous bubbles are generated by other bubble generators regardless of the applied current. This is because the ratios of nozzle diameter to electrode diameter (D_n/D_e) for bubble generators No.1 and No. 4 are relatively small (1.5 and 1.2, respectively). Also, the gaps between the microelectrode and the inner nozzle wall are smaller than those of other bubble generators. With a high applied current, large bubbles tend to form at the microelectrode surface. When the neck of a large bubble is in contact with the nozzle, the surface tension force will resist its departure. Then the bubble will sit on the tip of the nozzle and gradually grow until it reaches a large departure diameter (Figure 4-14a). However, with the decrease of applied current, the size of bubbles at the microelectrode reduces until the bubbles are too small to stay in contact with the nozzle; hence they depart immaturely. Consequently, a continuous stream of bubbles is produced (Figure 4-14b). It is worth mentioning that bubble generators No.2, 3, 5-8 have D_n/D_e of 2, 3, 1.6, 4, respectively. This contributes to large gaps between the microelectrode and the inner nozzle wall. This gap prevents the contact between the growing bubbles and the nozzle so that the continuous bubbles are formed regardless of applied current (Figure 4-14c). Furthermore, only bubble generators using a thin microelectrode can produce single bubbles under experimental conditions. Bubble generators no. 9 and 10 have microelectrode with a diameter of 0.5 mm, which can only produce continuous large bubbles at h=0 (Figure 4-14d).

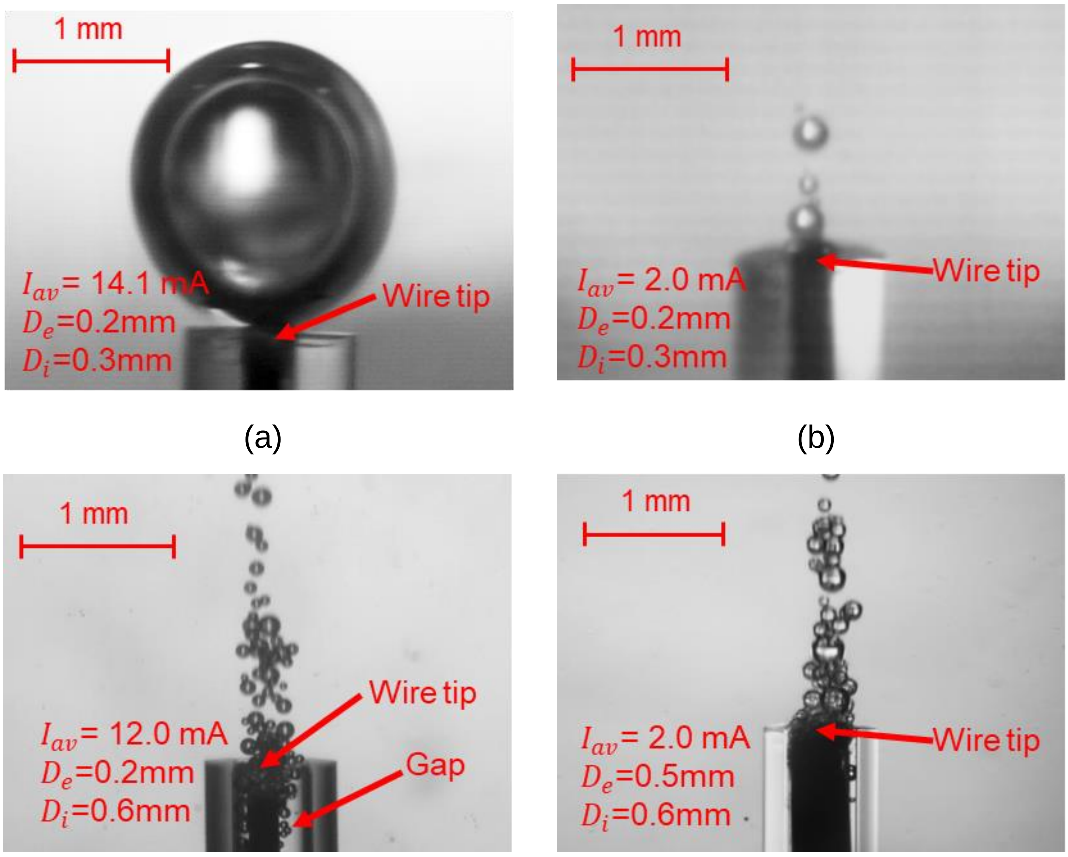

(a) (b)

(c) (d)

Figure 4-14. Photos of (a) single bubble and (b) continuous bubbles formed from the tip No.1 bubble generator, continuous bubbles produced by (c) No.3 and (d) No.9 bubble generators under different currents in a stagnant electrolyte.

With a further increase in the retraction distance, a very small recess is formed between the microelectrode and the nozzle. This geometry controls the process of bubble growth, as schematically shown in Figure 4-15. If the retraction distance is small, a bubble can grow inside the nozzle without being deformed (Figure 4-15a), and hence, there is no pressure force on the bubble from the wall (F_W=0). The surface tension force F_T can be calculated as:

$$F_T = D_b \pi \sigma \, . \tag{4-4}$$

where σ is the surface tension of the electrolyte.

With an increase in the retraction distance, the bubble is slightly deformed (Figure 4-15b). Due to the surface tension forces, the wall applies a pressure force (F_W) to the bubble at its neck. The Y-component of the pressure force can be presented as:

$$F_{wY} = -F_T(cos\alpha - sin\beta)\,. \tag{4-5}$$

The contact angle β is determined by the surface characteristics of the nozzle. In addition to the nozzle surface, the contact angle α is also affected by the retraction distance. Since the bottom surface of the bubble adheres to the top of the microelectrode (or the microbubble carpet (Bashkatov *et al.* 2019)), α reduces with the increase of h until $h < 0.5\,D_n$ (Figure 4-15c). Hence, F_{wY} increases with the increase of h, which promotes bubble departure, resulting in a decrease in the average bubble diameter (Figure 4-9). Further increasing of h leads to the reduction of α and the formation of a Taylor bubble inside the nozzle (Figure 4-15d and 15e). This could be the reason for the plateau of the average bubble diameter in Figure 4-9 at large h values. Further investigation is needed to better understand the mechanism of bubble formation in the proposed bubble generator.

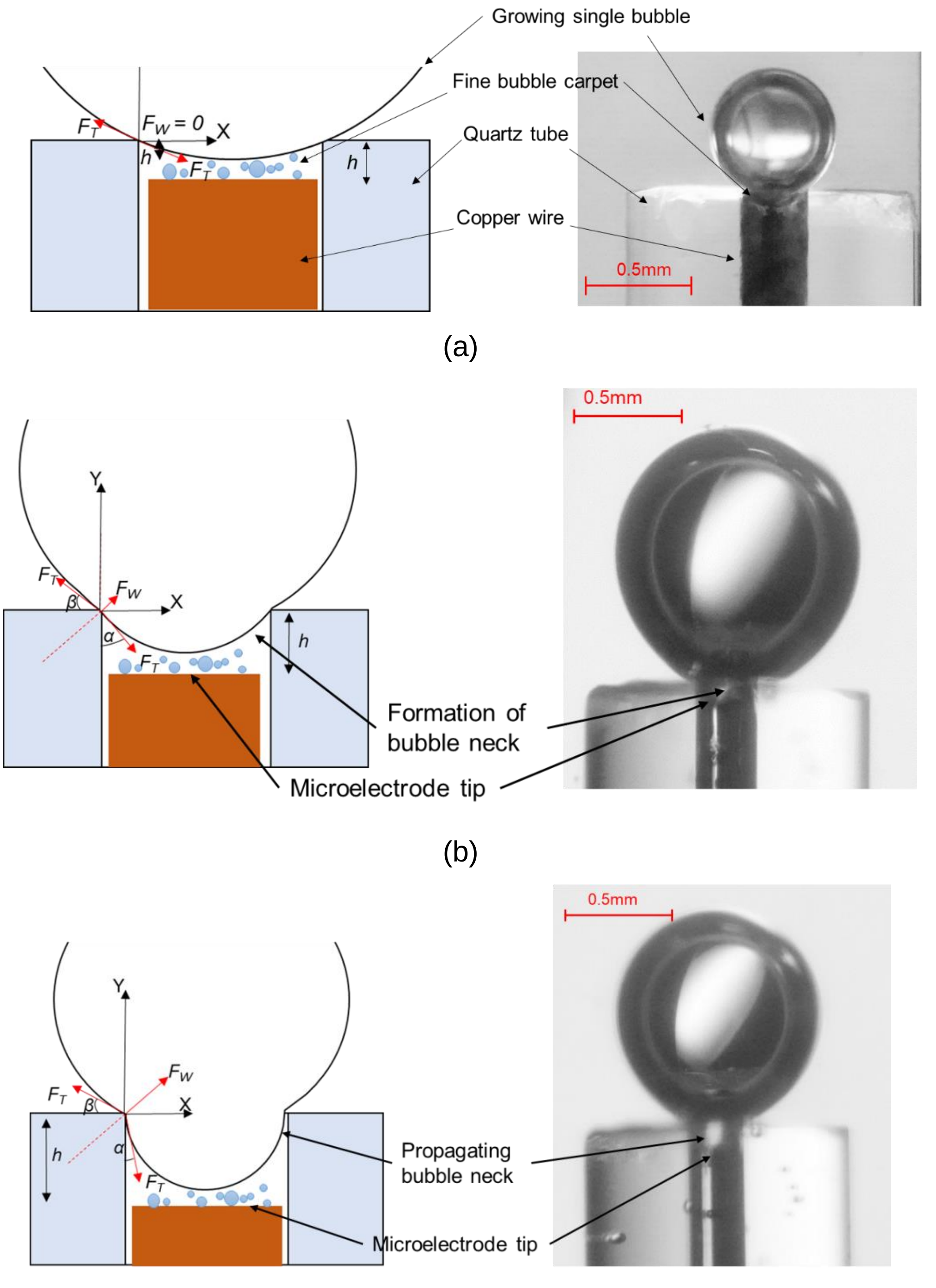
Growing single bubble
Fine bubble carpet
Quartz tube
Copper wire
F_T
F_W = 0
X
h
0.5mm
(a)
Y
F_W
β
α
Formation of bubble neck
Microelectrode tip
(b)
Propagating bubble neck
(c)

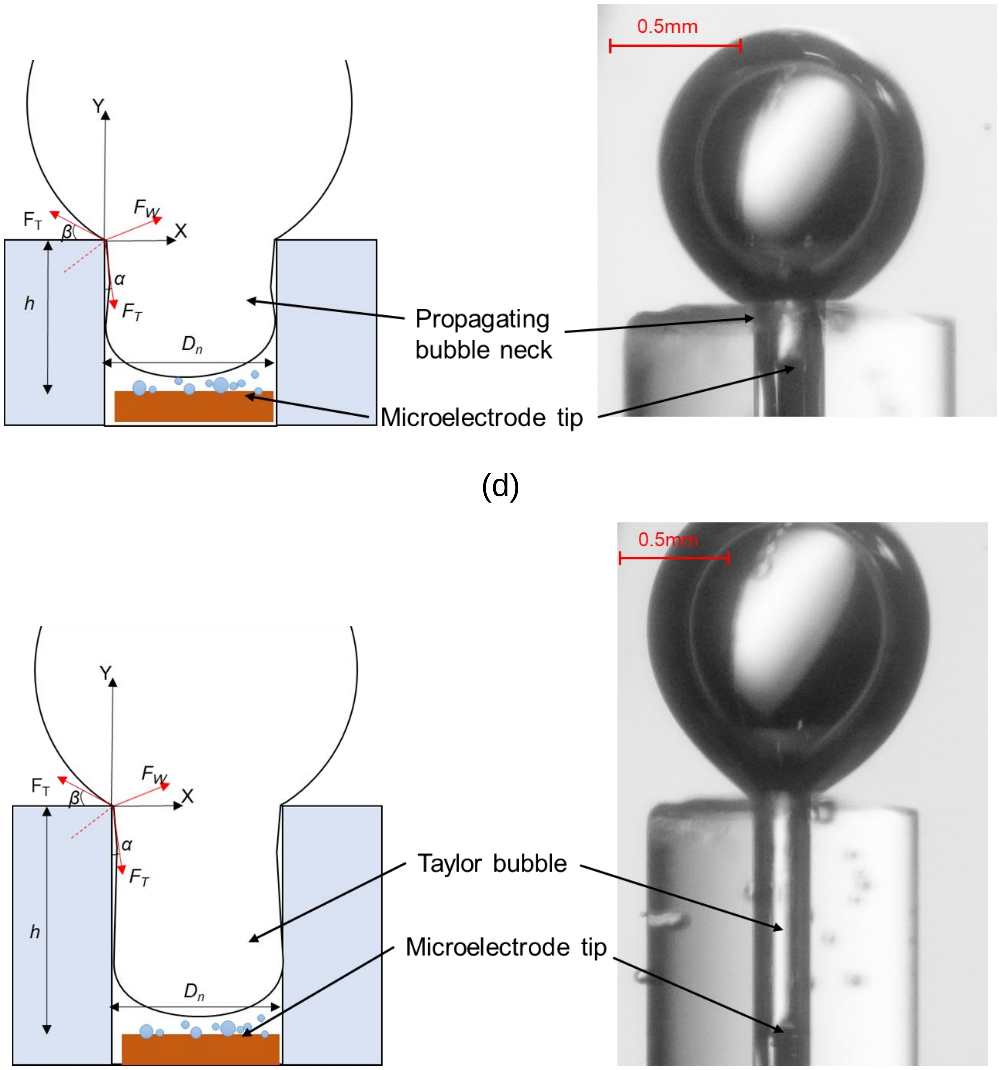

(d)

(e)

Figure 4-15. Schematics and images of different scenarios of pressure force applied to a growing bubble by the nozzle wall with various retraction distances (h): (a) Bubble deformation is negligible for h ~ 0.1D_n; (b) A slightly deformed bubble for h~0.3D_n; (c) Half of the bubble is formed inside the nozzle where h =0.5D_n ; (d) Taylor bubble formed inside the nozzle with a further increase of h; (e) Long Taylor bubble formed inside the nozzle with h greater than 2D_n.

The electrolytic bubble generator relies on the coalescence of small fine bubbles and can only produce single bubbles at certain diameter conditions and applied voltages. The coalescence of the fine bubbles can bring randomness in bubble growth so that a relatively large deviation in bubble departure diameter is observed for certain diameter conditions and applied voltages. Based on the discussions above, the conditions for an electrolytic bubble generator to produce single bubbles with controllable sizes and frequencies are summarized:

The microelectrode should be sufficiently small (D_e ≤ 0.25 mm) to ensure only single bubble is formed. The microelectrode surface that is in contact with the electrolyte should be electrolytically insulated except its tip.

The nozzle diameter (D_n) should satisfy $\frac{D_n}{D_e} \leq 1.5$ to minimise the gap between the electrode and the nozzle. This prevents the fine bubbles from leaving the nozzle without coalescence.

The retraction distance (h) should be less than 0.3 D_n. A larger retraction distance can lead to more significant deviations in the sizes and frequencies of the produced bubbles.

Once the geometric parameters are determined, the sizes and frequencies of the bubbles should be adjusted by the voltage applied to the bubble generator.

It should be noted that the proposed bubble generator utilizes water electrolysis to generate hydrogen or oxygen bubbles, which may limit the application of this method where air or other gas bubbles are required. Also, the performance of the proposed bubble generator can be further improved. Some areas for improvement include introducing programmed control over the current applied to the microelectrode to manipulate the bubble frequency, increasing the hydrophobicity of the nozzle to enhance bubble departure, reducing the size of microelectrode and nozzles to further decrease the bubble size, and improving the manufacturing quality of the microelectrode and nozzle, especially for their tips.

4.2.5 Conclusion

An electrolytic bubble generator, consisting of a microelectrode installed inside a tube, is presented in this paper. The concept of this simple bubble generator is to combine the advantages of both the gas-injection and microelectrode bubble generators with the aim to control the growth and departure of the generated bubble with a nozzle, providing a low-cost method for bubble generation with controlled size and frequency.

The proposed bubble generator is easy to fabricate and able to produce single bubbles without any dedicated control system, which may have a potential application in the fundamental research on bubble behaviour. While the paper introduces this concept and analyses it, further work is needed to improve the performance of the proposed bubble generator.

This work also expanded the understanding of the effect of the geometry of embedded microelectrode on the formation of electrolytic bubbles. By increasing the retraction distance of the microelectrode, smaller bubbles were formed at lower frequencies. The mechanism of single and continuous bubbles formation from an electrolytic bubble generator with different geometric parameters was also discussed.

Acknowledgements

The first author acknowledges the support from Adelaide Graduate Research Scholarship.

Funding

This research received no specific grant from any funding agency in the public, commercial, or not-for-profit sectors.

References

Agarwal, A., W. J. Ng and Y. Liu (2011). Principle and applications of microbubble and nanobubble technology for water treatment. Chemosphere **84**(9): 1175-1180.

Atherton, T. J. and D. J. Kerbyson (1999). Size invariant circle detection. Image and vision computing **17**(11): 795-803.

Bari, S. D. and A. J. Robinson (2013). Experimental study of gas injected bubble growth from submerged orifices. Experimental Thermal and Fluid Science **44**: 124-137.

Bashkatov, A., S. S. Hossain, X. Yang, G. Mutschke and K. Eckert (2019). Oscillating hydrogen bubbles at Pt microelectrodes. Physical Review Letters **123**(21): 214503.

Davidson, J. F. and B. O. G. Schüler (1997). Bubble formation at an orifice in a viscous liquid. Chemical Engineering Research and Design **75**: S105-S115.

Davies, E. R. (2005). Machine Vision: Theory, Algorithms, Practicalities. Burlington, Elsevier Science & Technology.

Davis, J. T., D. E. Brown, X. Pang and D. V. Esposito (2019). High speed video investigation of bubble dynamics and current density distributions in membraneless electrolyzers. Journal of The Electrochemical Society **166**(4): F312-F321.

Don, W. G. and H. P. Robert (2008). Perry's Chemical Engineers' Handbook, Eighth Edition. New York, McGraw-Hill Education.

Esposito, D. V. (2017). Membraneless electrolyzers for low-cost hydrogen production in a renewable energy future. Joule **1**(4): 651-658.

Evangelio, A., F. Campo-Cortés and J. M. Gordillo (2015). Pressure gradient induced generation of microbubbles. Journal of Fluid Mechanics **778**: 653-668.

Fernández, D., M. Martine, A. Meagher, M. E. Möbius and J. M. D. Coey (2012). Stabilizing effect of a magnetic field on a gas bubble produced at a microelectrode. Electrochemistry Communications **18**: 28-32.

Fernandez, D., P. Maurer, M. Martine, J. M. Coey and M. E. Mobius (2014). Bubble formation at a gas-evolving microelectrode. Langmuir **30**(43): 13065-13074.

Gillespie, M. I., F. van der Merwe and R. J. Kriek (2015). Performance evaluation of a membraneless divergent electrode-flow-through (DEFT) alkaline electrolyser based on optimisation of electrolytic flow and electrode gap. Journal of Power Sources **293**: 228-235.

Kim, Y. C., B. Van Dang, R. Taylor and T. Barber (2021). Controlled generation of single microbubbles. Experiments in Fluids **62**(10): 220.

Kolev, N. I. (2007). Bubble departure diameter. Multiphase Flow Dynamics 2: Thermal and Mechanical Interactions. N. I. Kolev. Berlin, Heidelberg, Springer Berlin Heidelberg**:** 417-438.

Kumar, R. and N. K. Kuloor (1970). The formation of bubbles and drops. Advances in Chemical Engineering. T. B. Drew, G. R. Cokelet, J. W. Hoopes and T. Vermeulen, Academic Press. **8**: 255-368.

Li, X., F. C. Walsh and D. Pletcher (2011). Nickel based electrocatalysts for oxygen evolution in high current density, alkaline water electrolysers. Phys Chem Chem Phys **13**(3): 1162-1167.

Luo, L. and H. S. White (2013). Electrogeneration of single nanobubbles at sub-50-nm-radius platinum nanodisk electrodes. Langmuir **29**(35): 11169-11175.

Moffat, R. J. (1985). Using uncertainty analysis in the planning of an experiment. Journal of Fluids Engineering **107**(2): 173-178.

Najafi, A. S., Z. Xu and J. Masliyah (2008). Single micro-bubble generation by pressure pulse technique. Chemical Engineering Science **63**(7): 1779-1787.

Parkinson, L., R. Sedev, D. Fornasiero and J. Ralston (2008). The terminal rise velocity of 10-100 microm diameter bubbles in water. Journal of Colloid and Interface Science **322**(1): 168-172.

Sanada, T. and K. Abe (2013). Generation of single bubbles of various sizes using a slitting elastic tube. Review of Scientific Instruments **84**(8): 085106.

Schroers, J., C. Veazey, M. D. Demetriou and W. L. Johnson (2004). Synthesis method for amorphous metallic foam. Journal of Applied Physics **96**(12): 7723-7730.

Stride, E. and N. Saffari (2003). Microbubble ultrasound contrast agents: A review. Proceedings of the Institution of Mechanical Engineers, Part H: Journal of Engineering in Medicine **217**(6): 429-447.

Swiegers, G. F., A. L. Hoang, A. Hodges, G. Tsekouras, C.-Y. Lee, K. Wagner and G. Wallace (2022). Current status of membraneless water electrolysis cells. Current Opinion in Electrochemistry **32**: 100881.

Unger, E. (2005). Sonothrombolysis with Phospholipid-Coated Perfluoropropane Microbubbles. AIP Conference Proceedings**:** 58-61.

Unger, E. C., T. O. Matsunaga, T. McCreery, P. Schumann, R. Sweitzer and R. Quigley (2002). Therapeutic applications of microbubbles. European Journal of Radiology **42**(2): 160-168.

Unger, E. C., T. Porter, W. Culp, R. Labell, T. Matsunaga and R. Zutshi (2004). Therapeutic applications of lipid-coated microbubbles. Advanced Drug Delivery Reviews **56**(9): 1291-1314.

van Wamel, W. J., S. H. Rooijakkers, M. Ruyken, K. P. van Kessel and J. A. van Strijp (2006). The innate immune modulators staphylococcal complement inhibitor and chemotaxis inhibitory protein of Staphylococcus aureus are located on beta-hemolysin-converting bacteriophages. Journal of Bacteriology **188**(4): 1310-1315.

Vejrazka, J., M. Fujasová, P. Stanovsky, M. C. Ruzicka and J. Drahoš (2008). Bubbling controlled by needle movement. Fluid Dynamics Research **40**(7-8): 521-533.

Vogt, H. (1989). The problem of the departure diameter of bubbles at gas-evolving electrodes. Electrochimica Acta **34**(10): 1429-1432.

Vogt, H. (2017). The quantities affecting the bubble coverage of gas-evolving electrodes. Electrochimica Acta **235**: 495-499.

Xu, Q., M. Nakajima, S. Ichikawa, N. Nakamura and T. Shiina (2008). A comparative study of microbubble generation by mechanical agitation and sonication. Innovative Food Science & Emerging Technologies **9**(4): 489-494.

Yang, B., M. Jafarian, N. Freidoonimehr and M. Arjomandi (2022). Trajectory of a spherical bubble rising in a fully developed laminar flow. International Journal of Multiphase Flow 157: 104250.

Yang, X., F. Karnbach, M. Uhlemann, S. Odenbach and K. Eckert (2015). Dynamics of single hydrogen bubbles at a platinum microelectrode. Langmuir **31**(29): 8184-8193.

Yuen, H. K., J. Princen, J. Illingworth and J. Kittler (1990). Comparative study of Hough Transform methods for circle finding. Image and vision computing **8**(1): 71-77.

Zeng, K. and D. Zhang (2010). Recent progress in alkaline water electrolysis for hydrogen production and applications. Progress in Energy and Combustion Science **36**(3): 307-326.

Zhang, D. and K. Zeng (2012). Evaluating the behavior of electrolytic gas bubbles and their effect on the cell voltage in alkaline water electrolysis. Industrial & Engineering Chemistry Research **51**(42): 13825-13832.

Zhang, R., R. Hu, X. Li, Z. Zhen, Z. Xu, N. Li, L. He and H. Zhu (2018). A bubble-derived strategy to prepare multiple graphene-based porous materials. Advanced Functional Materials **28**(23): 1705879.

Zhou, D., P. Li, W. Xu, S. Jawaid, J. Mohammed‐Ibrahim, W. Liu, Y. Kuang and X. Sun (2020). Recent advances in non‐precious metal‐based electrodes for alkaline water electrolysis. ChemNanoMat **6**(3): 336-355.

Chapter 5

Bubble rising behaviour in an electrolyser channel

5.1 Chapter overview

This chapter investigates the forces acting on rising bubbles in a vertical electrolyser channel. In a membrane-free water electrolyser (MFE), the rising H_2 and O_2 bubbles are subjected to three dominant forces: buoyancy, lift and drag. The buoyancy and drag forces determine the rising velocity of the bubbles, while the lift force primarily dictate their transverse motion, thus playing a vital role in the separation of H_2 and O_2 bubbles in an MFE.

Existing literature extensively explores lift forces on solid particles and large bubbles (D_b>1 mm) in simple shear flow. However, there exists a notable lack of experimental data regarding the lift force on a spherical microbubble rising in parabolic flow. The research undertaken in this chapter aims to address this gap.

In this chapter, an experimental study on electrolytic H_2 bubbles rising in a vertical electrolyser channel with fully developed laminar flow is conducted. Utilising the microbubble generator developed in Chapter 4, H_2 bubbles with diameters of 0.3 mm-1.0 mm are introduced into the electrolyser channel. A bubble visualisation technique is employed to track the bubbles within the channel and acquire their rising trajectories. The lift and drag forces on the rising bubbles are subsequently assessed.

The results reveal that the lift force, induced by the flow's velocity gradient, directs the bubbles toward the wall region. As a bubble approaches this region, its transverse velocity increases, while its vertical velocity decreases. Moreover, by positioning the bubble release point closer to the wall, increasing the bubble diameter, and applying a higher flow Reynolds number, the bubbles can reach the wall region more swiftly. Based on the experimental data, a new correlation is proposed to calculate the shear-induced lift force on a microbubble rising in a vertical channel with a parabolic flow, bridging a gap in the existing studies. This chapter advances the knowledge of lift force on a microbubble rising in a wall bounded flow with a parabolic velocity profile, which fulfills the third research objective.

5.2 Microbubble rising in an electrolyser channel

This section consists of the following journal article:

Yang, B., M. Jafarian, N. Freidoonimehr, and M. Arjomandi, Trajectory of a spherical bubble rising in a fully developed laminar flow. International Journal of Multiphase Flow, 2022. 157. DOI: 10.1016/j.ijmultiphaseflow.2022.104250.

This article is identical to the submitted version, with the exception of the numbering and positioning of figures, tables, and equations.

Statement of Authorship

Title of Paper	Trajectory of a spherical bubble rising in a fully developed laminar flow
Publication Status	☒ Published ☐ Accepted for Publication ☐ Submitted for publication ☐ Unpublished and Unsubmitted work written in manuscript style
Publication Details	Yang, B., M. Jafarian, N. Freidoonimehr, and M. Arjomandi, Trajectory of a spherical bubble rising in a fully developed laminar flow. International Journal of Multiphase Flow, 2022. 157. DOI: 10.1016/j.ijmultiphaseflow.2022.104250.

Principal Author

Name of Principal Author (Candidate)	Bo Yang		
Contribution to the Paper	Developed ideas, conducted experiments, performed data analysis, interpreted results, wrote manuscript, and acted as corresponding author.		
Overall percentage (%)	80%		
Certification:	This paper reports on original research I conducted during the period of my Higher Degree by Research candidature and is not subject to any obligations or contractual agreements with a third party that would constrain its inclusion in this thesis. I am the primary author of this paper.		
Signature		Date	15/09/2023

Co-Author Contributions

By signing the Statement of Authorship, each author certifies that:

i. the candidate's stated contribution to the publication is accurate (as detailed above);
ii. permission is granted for the candidate in include the publication in the thesis; and
iii. the sum of all co-author contributions is equal to 100% less the candidate's stated contribution.

Name of Co-Author	Mehdi Jafarian		
Contribution to the Paper	Supervised the development of the research, participated in developing ideas and concept, helped in interpreting results, and assisted in evaluating and editing the manuscript.		
Signature		Date	15/09/2023

Name of Co-Author	Navid Freidoonimehr		
Contribution to the Paper	Supervised the development of the research, participated in developing ideas and concept, helped in interpreting results, and assisted in evaluating and editing the manuscript.		
Signature		Date	15/09/2023

Name of Co-Author	Maziar Arjomandi		
Contribution to the Paper	Supervised the development of the research, participated in developing ideas and concept, helped in interpreting results, and assisted in evaluating and editing the manuscript.		
Signature		Date	15/09/2023

Trajectory of a spherical bubble rising in a fully developed laminar flow

Bo Yang, Mehdi Jafarian, Navid Freidoonimehr and Maziar Arjomandi

Abstract

The rising trajectory of bubbles subjected to shear-induced lift force in a vertical channel is of great interest for designing and optimising a variety of electrochemical equipment. In this work, the rising trajectory of a spherical microbubble with a diameter of 0.3-1.0 mm in a vertical channel with a fully developed laminar flow is investigated experimentally. Subsequently, the lift and drag forces on the bubble are assessed. Due to the limitation of the existing correlations for lift force coefficient, a new correlation is developed, which can be used to estimate the trajectory of a bubble in a vertical channel. The effect of flow velocity gradient and bubble diameter on the bubble motion is discussed to control bubble rising trajectory. It is concluded that the lift coefficient for a spherical microbubble in vertical channels with a fully developed laminar flow is slightly higher than the reported shear lift coefficient for larger bubbles rising in a highly viscous liquid.

Keywords

Lift coefficient; Bubble trajectory; Bubble hydrodynamics; Shear-induced lift force; Bubble image velocimetry

Nomenclature

A	Area, m^2
a	Half of channel width, m
C_L	Lift coefficient
C_D	Drag coefficient
D	Diameter, m
E	Voltage, V
F	Force, N
g	Gravitational acceleration, 9.8 m/s^2

h	The gap between copper wire tip and quartz tube opening, m
I	Current, A
J	Current density, A/m^2
n	Amount of substance, mol
P	Pressure, Pa
R	Gas constant, 8.3145 J/mol·K
T	Temperature, K
t	Time, s
U	Velocity, m/s
V	Volume, m^3
w	Velocity gradient, s^{-1}
Dimensionless numbers	
$Ar = \frac{gD_b{}^3\rho_f{}^2}{\mu^2}$	Archimedes number
$Eo = \frac{(\rho_f - \rho_g)gD_\mathrm{b}{}^2}{\sigma}$	Eotvos number
$Mo = \frac{(\rho_f - \rho_g)g\mu_f{}^4}{\rho_f{}^2\sigma^3}$	Morton number
$Re = \frac{\rho_f UD}{\mu_f}$	Reynolds number
$Sr = \frac{wD_b}{\left\lvert U_f - U_b \right\rvert}$	Shear rate
Subscripts	
av	Average
B	Buoyancy
b	Bubble
D	Drag
L	Lift
f	Liquid flow
s	Slip velocity
stk	Stokes

t	Terminal
w	Wall
x	Axial
y	Translational

Greek letters

α	Virtual mass coefficient, 0.5 for spherical bubbles
φ	Gas holdup
σ	Surface tension, N/m
μ	Dynamic viscosity, kg/m·s
ω	Velocity gradient, s^{-1}
θ	The angle between drag force and x-axis
χ	Aspect ratio

5.2.1 Introduction

Gas flow regimes exist widely in electrochemical, physical, petrochemical and biochemical industries (Mudde 2005). In these systems, bubbles typically move in a restrained liquid with solid boundaries. The bubbles are either injected into the liquid through nozzles or evolved from physical or chemical reactions, or even generated at the surface of a submerged electrode within the liquid. Examples of this include the air-lift reactors (Upham *et al.* 2017), heat exchangers (Basatakoti *et al.* 2019), bubble columns (Kantarci *et al.* 2005, Jafarian *et al.* 2017), liquid chemical looping combustion/gasification (Sarafraz, Jafarian *et al.* 2018) and electrolysers (Brauns and Turek 2020). In these applications, the diameter of the bubbles can range from a few micrometres to centimetres. Depending on bubble diameter and liquid properties, the shape of the bubbles can be spherical, oblate, or skirted (Clift 1978, Fernandez *et al.* 2014, Zhou *et al.* 2020). The presence of bubbles in the liquid induces momentum, augments turbulence and mixing, and consequently enhances the rate of heat and mass transfer. In general, in any system where bubbles are involved, the characteristics of the bubbles, e.g. their size distribution, shape and density, together with their motion greatly influence the system efficiency. Therefore, understanding the bubbles' movement and trajectory within the liquids under different flow regimes is vital for design and optimisation of systems that involves gas flow regimes. Since the bubble trajectory in liquids is dominated by the forces acting on the bubbles, there is a need to understand and characterise the significance and impact of these forces. The overall objective of this paper is to meet this need.

Figure 5-1 shows a schematic of a gas bubble rising in a vertical channel with a fully developed laminar flow and the forces acting on it. The velocity of the flow in the channel is represented as $U_f(y)$, and the bubble is subjected to buoyancy (F_B), drag (F_D), and lift (F_L) forces. The bubble centre is located at a distance of S from the wall, such that S is significantly greater than the bubble diameter (D_b). Therefore, the lubrication effect is neglected (Takemura *et al.* 2002). The bubble motion can be described by Newton's second law as follows (Tomiyama *et al.* 2002, Mehdi and Kim 2015):

$$\underbrace{(\rho_g + \alpha\rho_f)V_b\frac{dU_b}{dt}}_{mass\ and\ acceleration} = \underbrace{(\rho_l - \rho_g)gV_b\boldsymbol{e}_x}_{F_B} - \underbrace{C_L\rho_f V_b(U_b - U_f) \times \frac{\partial U_f}{\partial y}}_{F_L} - \underbrace{\frac{\pi}{8}C_D\rho_f {D_b}^2(U_b - U_f)|U_b - U_f|}_{F_D}. \qquad (5\text{-}1)$$

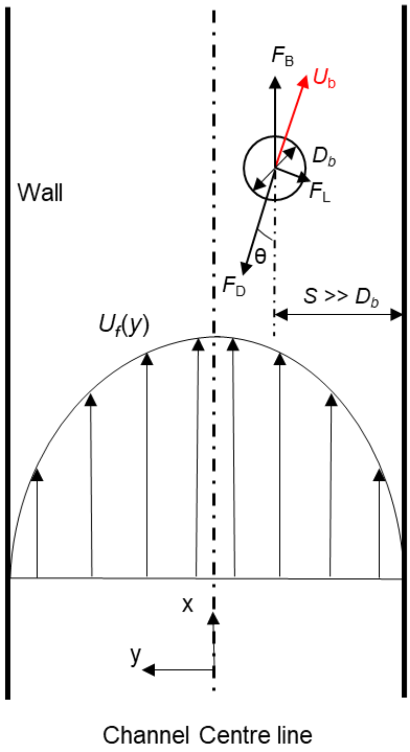

Figure 5-1. Schematic representation of a bubble in a fully developed laminar flow in a vertical channel. The bubble is rising through the flow and far from the channel wall. The buoyancy, drag and lift forces are shown in the figure.

Where U_b, U_f, ρ_g, ρ_f are the bubble velocity, liquid velocity, gas density and liquid density, respectively, V_b is the bubble volume, and $\boldsymbol{e}_x$ is the unit vector in x-direction. Moreover, C_D and C_L represent the drag and lift coefficients, respectively. The virtual mass coefficient, α, is assumed as 0.5 for spherical bubbles (Kolev 2007).

The drag coefficient for bubbles in a bubbly flow regime has been intensively studied. Various correlations for estimating the drag force on bubbles with different diameters have been proposed (Schiller and Naumann 1933, Mei and Klausner 1994, Tomiyama *et al.* 2002). One of the widely used models was presented by Tomiyama *et al.* (2002):

$$C_D = max\left[min\left\{\frac{16}{Re}(1+0.15Re^{0.687}), \frac{48}{Re}\right\}, \frac{8}{3}\frac{Eo}{Eo+4}\right]. \tag{5-2}$$

Evaluating the lift force term in Equation 5-1 is more complicated than the drag force term mainly because the lift force can be generated by both the flow distribution referred to as shear-induced and the wall-induced force. The shear-induced force is in the direction of dominant relative velocity, pushing the bubble towards the wall in particular where (S/D_b <1) (Saffman 1965, McLaughlin 2006, Shi *et al.* 2020). On the other hand, the wall-induced force on a bubble is more complex: it always pushes a contaminated bubble away from wall (Zeng *et al.* 2005, Amini *et al.* 2014), and for clean bubbles with Re_b <35 were found to be repelled by the wall, whereas a clean bubble with Re_b ≥35 is attracted (Takemura and Magnaudet 2003). More recent studies show that the motion of rising bubbles in the wall region (S/D_b <1) is dominated by the wall effect (Takemura and Magnaudet 2009, Takemura *et al.* 2009, Zeng *et al.* 2009). However, the wall-induced forces reduce significantly when the bubble is outside the wall region (Shi and Rzehak 2020, Shi *et al.* 2020).

The transverse motion of bubble under the wall- and shear-induced lift forces have been the focus of a large number of studies. Cox and Hsu (1977), Asmolov (1999) and Yahiaoui and Feuillebois (2010) developed theoretical models for the lateral inertial migration of a solid spherical particle suspended in laminar flow. Legendre and Magnaudet (1997) studied the shear-induced lift force on a spherical bubble in a low-Reynolds-number shear flow and derived an analytical expression for C_L. Direct numerical simulation (DNS) of the motion of particle or drop in laminar flow have also been conducted. In the work of Feng *et al.* (1994), it is found that the motion of a circular particle in a Poiseuille flow is affected by wall lubrication, shear slip, particle rotation and velocity profile curvature. Mortazavi and Tryggvason (2000) found that the motion of a deformable drop in a Hagen Poiseuille flow depends on the Reynolds number, viscosity ratio and the deformability of the drop. Also, drops undergo oscillatory motion with the increase of flow Reynolds number. Later, Legendre and Magnaudet (1998) studied the lift force on a spherical bubble in a shear flow with 0.1<Re_b<500 using direct numerical simulation. They found that with the increase of Re_b, the lift force coefficient reaches the minimum value of 0.3 at Re_b=5, then gradually increases to 0.5. More recently, Shi *et al.* (2020) numerically studied the effect of bubble Reynolds number, slip velocity, shear rate, and wall distance on the lift forces experienced by spherical bubble, with the mechanisms of the wall- and shear-induced lift forces discussed in detail.

High-fidelity experimental data pertained to the lift force on bubbles is limited in the literature, as summarised in Table 5-1. Tomiyama *et al.* (2002) studied the trajectories of air bubbles rising in a simple shear flow generated by a rolling belt. In their work, bubbles were generated by injecting air into a submerged nozzle. The trajectories of air bubbles with a diameter of 2.8mm to 5.7mm rising in highly viscous liquid (water-glycerol solution of various concentrations) were obtained under a range of Morton (Mo) and Eötvös numbers (Eo) ($-5.5 < \log_{10} Mo < -2.8$ and $1.39 < Eo < 5.74$) and a velocity gradient of less than 8.3 s^{-1}. A force-balance model describing the motion of a rising bubble was proposed, and the lift force coefficient was derived by fitting the estimated bubble trajectories with the experimental data. They proposed three possible regions for the lateral migration of the bubbles depending on the bubble diameter including (1) wall-focusing (0.4 mm < D_b < 5 mm), (2) core-focusing (D_b > 5 mm) and (3) neutral (5 mm< D_b <6 mm and D_b <0.4 mm). Tomiyama *et al.*'s experimental database was later expanded to $-6.6 < \log_{10} Mo < -3.2$ and $0.022 < Eo < 5.0$ by Aoyama *et al.* (2017) using a similar experimental setup.

Li *et al.* (2016) and Xu *et al.* (2021) investigated the motion of oblate bubbles in a downward simple shear water flow generated by a curved screen. Bubbles with a diameter of 1-20 mm were generated by injecting air through a nozzle. The drag and lift forces were calculated based on the trajectories of bubbles. However, the study lacks the investigation of lift force on microbubbles (D_b<1.0 mm). In addition, more recent studies on the lift force on gas bubbles rising in water have implicated that most of the available existing lift models for bubbles in high-viscosity fluids may not apply to the prediction of lift force in low-viscosity liquids (Ziegenhein *et al.* 2018, Lee and Lee 2020).

To the best of author's knowledge, experimental data for the shear-induced lift forces on microbubbles (D_b < 1.0 mm) rising in low viscous liquid is not studied in the literature. The challenges associated with the investigation of the lift force on microbubbles include both the generation of single microbubbles with controllable size and accurate measurement of the trajectory microbubbles within the channel (Kim *et al.* 2021). To investigate the shear-induced lift force on microbubbles, a novel technique is introduced to generate single microbubbles in a vertical channel with a fully developed laminar flow. The current research establishes a model for the shear-induced lift force on microbubbles under the following conditions: 280<Re_f <1000, 4.5<Re_b <112.4, 0.005 < Eo <0.134,0< Sr <0.22 and $\log_{10} Mo$=-11.

Table 5-1. Empirical correlations for shear-induced lift force on a rising bubble in a simple shear flow.

Author	Correlation	Conditions	Velocity gradient generation	Bubble generation	Bubble shape and diameter
Tomiyama *et al.* (2002)	$C_L = \begin{cases} min[0.288\tanh(0.121Re), f(Eo)], & Eo < 4 \\ f(Eo), & 4 \le Eo \le 10.7 \end{cases}$ $f(Eo) = 0.00105\, Eo^3 - 0.0159Eo^2 - 0.0204Eo + 0.474$	$-5.5 < \log_{10} Mo < -2.8$, $1.39 < Eo < 5.74$, $0 < w < 8.3$ s^{-1}	Moving belt	Gas injected through a nozzle	Oblate, 2.8-5.7 mm
Aoyama *et al.* (2017)	-	$-6.6 < \log_{10} Mo < -3.2$, $0.022 < Eo < 5.0$, $0 < w < 7.9$ s^{-1}	Moving belt	Gas injected through a nozzle	Spherical to Oblate, 0.34-5.7 mm
Li *et al.* (2016)	-	$\log_{10} Mo = -11$, $0.82 < Eo < 1.5$, $0.4 < w < 0.57$ s^{-1}, counterflow	Curved screen	Gas injected through a nozzle	Oblate, 2.24-3.04 mm
Xu *et al.* (2021)	$C_L = \max(-6.3(1 - 2.1\,\varepsilon^{0.2})\tanh(2.8(Eo - 1.3\varepsilon_1), -3.65exp(-0.05\varepsilon^{0.2}Eo - 0.2\varepsilon_1))$	$\log_{10} Mo = -11$, $1 < Eo < 55$, $0.28 < w < 0.51$ s^{-1}, counterflow	Curved screen	Gas injected through a nozzle	Oblate, 1-20 mm

	$\varepsilon = (\frac{Sr}{Re})^{0.5}, \varepsilon_1 = (SrRe)^{0.5}$				
Ziegenhein *et al.* (2018)	-	$\log_{10} Mo = -10.6$, $0.62 < Eo < 3.83$	Bubble induced circulation in a tank	Gas injected through a nozzle	Oblate, 2.45-6.4 mm
Legendre and Magnaudet (1998)	$C_L = \sqrt{\left(\frac{6}{\pi^2}\frac{2.255}{\sqrt{SrRe}(1+0.2Re/Sr)^{1.5}}\right)^2 + \left(\frac{1}{2}\frac{Re+16}{Re+29}\right)^2}$	$0.1 < Re_b < 500$, $0 < Sr < 1$	Numerical method	-	Solid spherical particle or spherical bubble
Lee (2020)	$C_L = 0.5 - 2.8\chi^{2.2}Oh$ $Oh = \mu/(\rho u d)^{0.5}$	$\log_{10} Mo = -10.6$ $0.63 < Eo < 54.8$	Sharp 90°bend with uniformly distributed vanes	Gas injected through a nozzle	Oblate, 2-12 mm

5.2.2 Methodology

5.2.2.1 Experimental setup

Figure 5-2 shows a schematic of the experimental setup used in this study for the investigation of the lift force on a microbubble rising in a vertical channel with a fully developed laminar flow. The vertical channel of the experimental rig was fabricated from a 1.7 m long acrylic channel with a square cross-section of 16 mm × 16 mm. In this work, hydrogen bubbles are generated using an electrolysis method (Rocha *et al.* 2021). The cathode was used as a hydrogen bubble generator, which was fabricated from a 0.25 mm enamel copper wire inserted into a 20mm long quartz tube with an inner diameter of 0.3 mm (Figure. 5-2 (b)). The gap between the quartz tube opening and the copper wire tip (h) was fine-tuned to enable the generation of single bubbles with controllable size. The bubble generator was installed in the channel at a distance of 1.2 m from the channel inlet, where the flow was fully developed under the experimental condition of this work (Re_f ≤1000). The initial location of the bubbles in the channel is determined by the y-coordinate of the bubble generator. The anode (1 mm × 10 mm nickel plate) was installed close to the channel outlet, enabling the product oxygen bubbles, over the anode electrode, to leave the channel directly. This avoids any interference of oxygen and hydrogen bubbles, and the latter are used in our observations and measurements. The flow circulation system consists of a 12V DC pump (4 L/min), a 10 L tank, valves and pipes. Dilute NaOH aqueous solution (0.1 wt%) is stored in the tank as the electrolyte. This solution provides better electrical conductivity and maintains similar density, viscosity and surface tension compared with water. The electrolyte properties and instrumentation features are summarised in Table 5-2.

Table 5-2. Summary of electrolyte properties and parameters of the main instruments used in this work.

Item	**Properties / Instrument parameter**
Temperature	20±2℃
Electrolyte	0.1 wt%s NaOH solution, ρ=999 kg/m^3, μ=1.02 mPa/s, σ=0.07 N/m (Don and Robert 2008)
Power supply DC1	PS-3005, 0-30 V
Power supply DC2	Manson 3402, 0-30 V
Digital multimeter	Klein mm400
Pump	4L/min, 0-12V
Camera	SONY RX10IV
Lens	Raynox m250
Backlight	DC 5 V LED
Tank	10 L
Channel	16 mmx16 mm cross-section acrylic channel

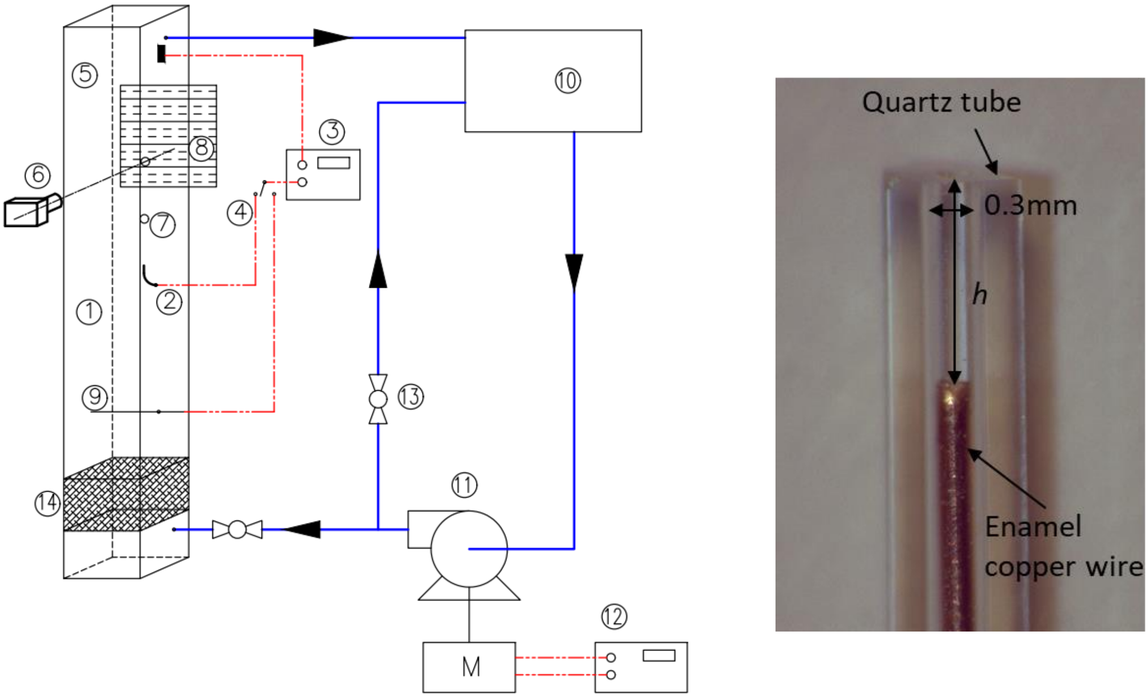

(a) (b)

Figure 5-2. A schematic of (a) the experimental setup used in this study, which includes: 1- Channel, 2- Bubble generator, 3- Power supply DC1, 4- Switch, 5- Anode plate, 6- Camera, 7- Rising bubble, 8- Backlight, 9- “Mirco-wire”, 10- Tank, 11- Pump, 12- Power supply DC2, 13- Valve, 14- Inlet mesh. (b) A detailed view of the bubble generator.

The power supply (DC 1, PS-3005, 0-30 V) provided the required potential to form hydrogen bubbles at the copper wire tip of the bubble generator, as shown in Figure 5-2. The frequencies and sizes of the H_2 bubbles were determined by the current, which is controlled by the voltage output of the power supply (Vogt 1989, Vogt 2017). During the experiment, the current was measured using a digital multimeter. According to Faraday's Law, the volumetric flow rate (m^3/s) of H_2 is calculated as (Zhou *et al.* 2020):

$$\dot{V_{\mathrm{H2}}} = \frac{\mathrm{R}T}{P}\dot{n_{\mathrm{H_2}}} = \frac{\mathrm{R}T}{P}\frac{JA}{2\mathrm{F}}, \tag{5-3}$$

where R is the gas constant (8.3145 J/mol·K), P and T are the operating pressure (Pa) and temperature (K), respectively, F is the Faraday constant (96485 c/mol), J is the current density (A/m^2), and A is the surface area of the electrode (m^2). The H_2 gas holdup, φ_b, can be calculated as:

$$\varphi_b = \frac{\dot{V_{\mathrm{H_2}}}}{\dot{V_{\mathrm{H_2}}} + \dot{V_f}}, \tag{5-4}$$

where $\dot{V_f}$ is the volumetric flow rate of the electrolyte in the channel. The flow rate in the channel was controlled by adjusting the two valves as well as the power supply of the pump (DC 2).

5.2.2.2 Flow velocity profile in the channel

The velocity field of the electrolyte in the channel was measured using a Bubble image Velocimetry (BIV) setup (Ryu *et al.* 2005). A nickel micro-wire (d =0.02 mm) was installed at the inlet of the channel to generate seeding bubbles. During the experiment, the power supply (DC 1) and the micro-wire were turned on, and the seeding H_2 bubbles ($D_{b,av}$=0.083 mm) were released into the channel. In addition, the output of the power supply was adjusted to ensure a similar size distribution of the bubbles was achieved for different flow rates in the channel.

A camera (SONY RX10IV) was used to record the motions of bubbles in the channel 100 mm above the level of the bubble generator tip (1.3m above the channel inlet). A macro lens (Raynox m250) was equipped to the camera to achieve a narrow depth of field and a field of view of approximately 0.5 mm and 20 mm×13.2 mm, respectively. The camera was set to focus on the plane of the symmetry of the channel (z =0). The motion of the bubbles illuminated by a LED backlight was recorded at 500fps (Figure 5-3). The resolution of the videos was approximately 200 pixels/mm. The videos were processed with PIVLab software to calculate the velocity distribution of the flow (Raffel 2018, Thielicke and Sonntag 2021). An example of the calculated mean velocity field of 1000 frames is presented in Figure 5-4.

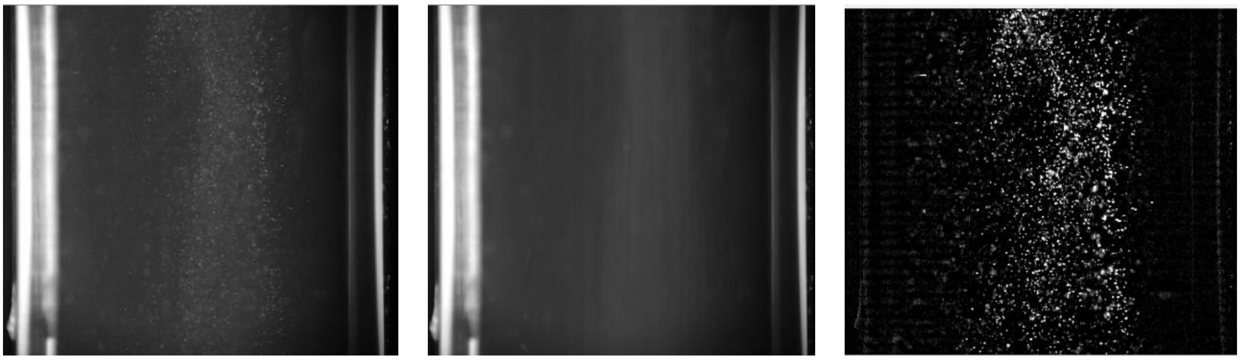

(a) (b) (c)

Figure 5-3. Raw video frame (a), background frame (b) and the filtered frame of seeding bubbles in the channel (c), which was calculated by subtracting the background frame from the raw frame. The bubbles were recorded at 500 fps with a LED backlight source at Re_f=800.

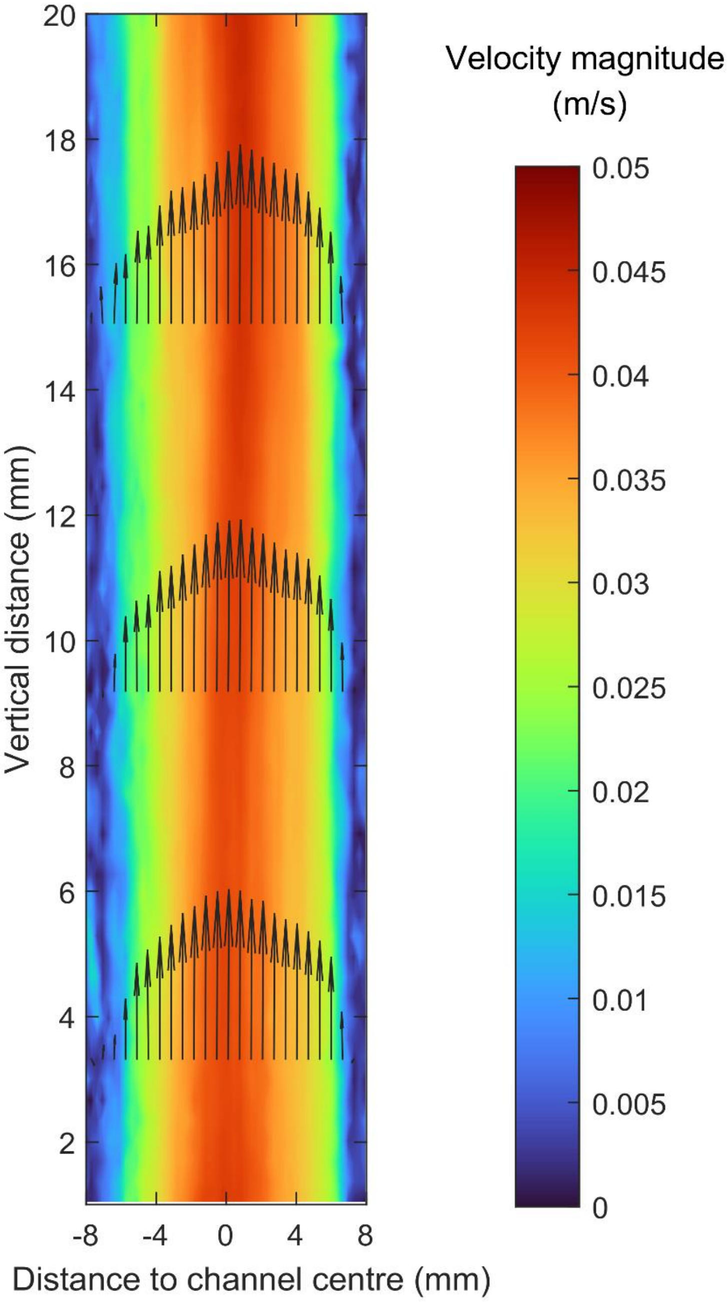

Figure 5-4. Hydrogen bubble flow visualisation results for the mean flow velocity field in the vertical channel at Re_f=800.

Since the seeding H_2 bubbles are buoyant, the actual flow velocity (U_f) of the electrolyte was derived using the following correlation (Holland and Bragg 1995):

$$U_s = U_b - U_f = U_t(1 - \varphi_b)^{n-1}. \tag{5-5}$$

where U_s is the slip velocity, U_b is the bubble rising velocity derived from hydrogen bubble flow visualisation, and φ_b is the gas holdup, which can be estimated using Equation 5-3 and 5-4, U_t is the terminal velocity of gas bubbles in the stagnant water. In this work, U_t was calculated according to Nguyen *et al.* (1997) and Nguyen (1998) based on the average diameter of the seeding bubbles:

$$U_t = U_{stk}\left\{1 + \frac{Ar/_{96}}{(1 + 0.079Ar^{0.749})^{0.755}}\right\}^{-1}. \tag{5-6}$$

In equation 5-6, $U_{stk} = \frac{\rho_f g {D_b}^2}{18\mu_f}$, and Ar is the bubble Archimedes number:

$$Ar = \frac{g{D_b}^3{\rho_f}^2}{{\mu_f}^2}. \tag{5-7}$$

The value of n in Equation 5-5 is 4.2, as suggested by Holland *et al.* (Holland and Bragg 1995). Nevertheless, the maximum $\varphi_b$was less than 0.1% under all experimental conditions so that the gas holdup in Equation 5-5 can be neglected.

To obtain the diameter distribution of the seeding H_2 bubbles, the camera was set to slow continuous shooting mode (4Hz) with a shutter speed of 1/4000s. The images were taken at 50 mm above the level of the bubble generator. For each flowrate, 50 images of the seeding bubbles were obtained with a pixel size of 1.8 μm. The images were then processed using an in-house MATLAB code to obtain the diameters of the bubbles. The bubbles were identified using Circular Hough Transform (CHT) based algorithm (Yuen *et al.* 1990, Atherton and Kerbyson 1999, Davies 2005), as shown in Figure 5-5.

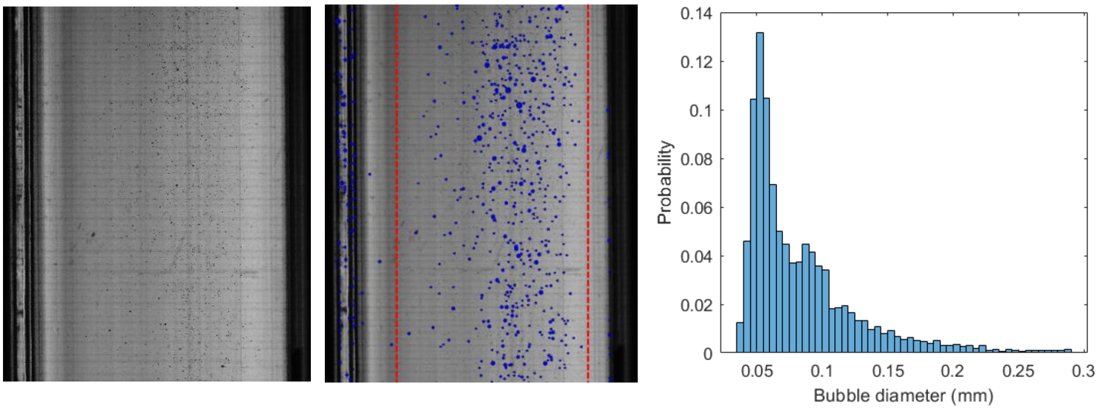

(a) (b) (c)

Figure 5-5. (a) Image of seeding bubbles in the vertical channel used as tracers at Re_f = 800 and J=2 A/cm^2 (b) Bubbles identified by MATLAB code. The detected “bubbles” outside the dashed lines were not included. (c) Probability distribution of bubble diameter.

Figure 5-6 shows the measured velocity profile inside the channel for various values of Re_f using the BIV method. For comparison, velocity profiles of a fully developed laminar flow for various values of Re_f were also calculated using the following Equation:

$$U_x = U_{max}\left(1 - \left({}^{y}/_{a}\right)^2\right). \tag{5-8}$$

It can be seen that the measured velocity profiles in this work provide a good agreement with the calculated profiles for $Re_f \leq$ 1000 with an error of less than 10%. However, as shown in Figure 5-6, the measured velocity profiles for $Re_f >$ 1000 significantly deviate from the ones determined using Equation 5-6, which is not in the range of Reynolds number used in this study.

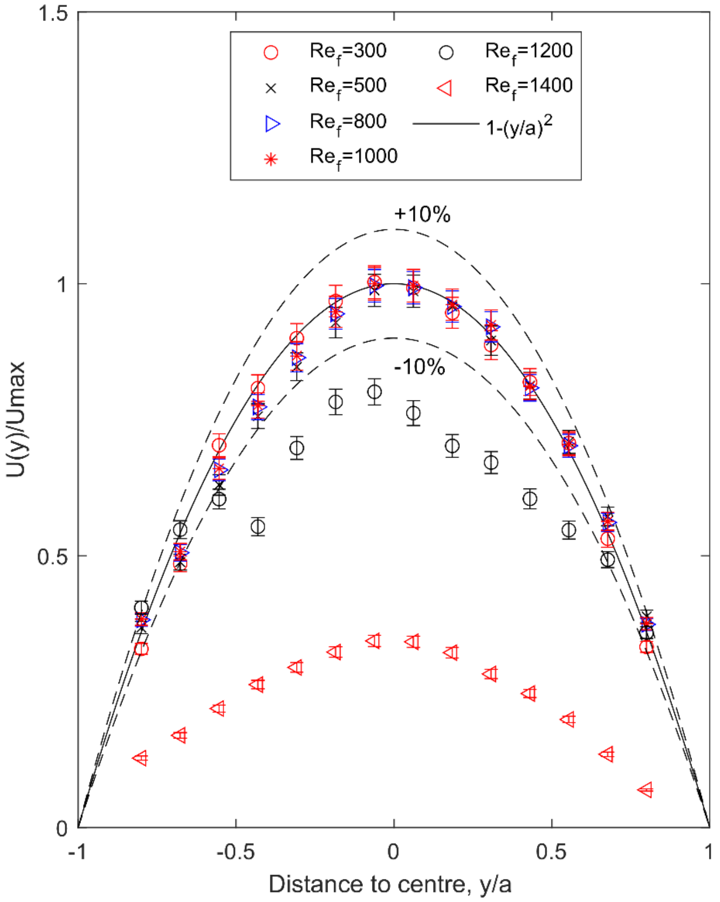

Figure 5-6. Flow velocity profiles obtained at 1.25 m above the inlet of the channel under various Re_f.

5.2.2.3 Visualisation of bubble trajectory

After the validation of the flow profile in the channel and its comparison against the fully developed laminar flow, the micro-wire was disconnected, whereas the bubble generator was switched on. For visualisation of the generated H_2 bubbles in the channel, the same camera and backlight were used. To validate the experimental data, the measured slip velocities of bubbles with different diameters were compared against the correlation proposed by Gaudin (Gaudin 1957) and Nguyen (Nguyen 1998). To ensure the vertical movement of bubble is stable, the bubble generator is placed at the centre of the channel, and the camera is positioned 100 mm above the bubble generator to capture the videos of rising bubbles. The videos were taken at 500 fps with a pixel size of 5μm.

The bubble rising velocity was calculated based on the vertical distance that a bubble rose in a certain number of frames divided by the total time interval of the frames. Since the velocity profile of the channel flow is known, the bubble slip velocity can be subsequently calculated based on Equation 5-5.

The measured dependence of the slip velocities of bubbles on their diameter for various bubble diameters is shown in Figure 5-7. It can be seen that the slip velocity of the microbubbles increases almost linearly with their diameter, and the experimental measurements of this work are in agreement with Gaudin (Gaudin 1957) and Nguyen (Nguyen 1998) with a deviation of ± 10%.

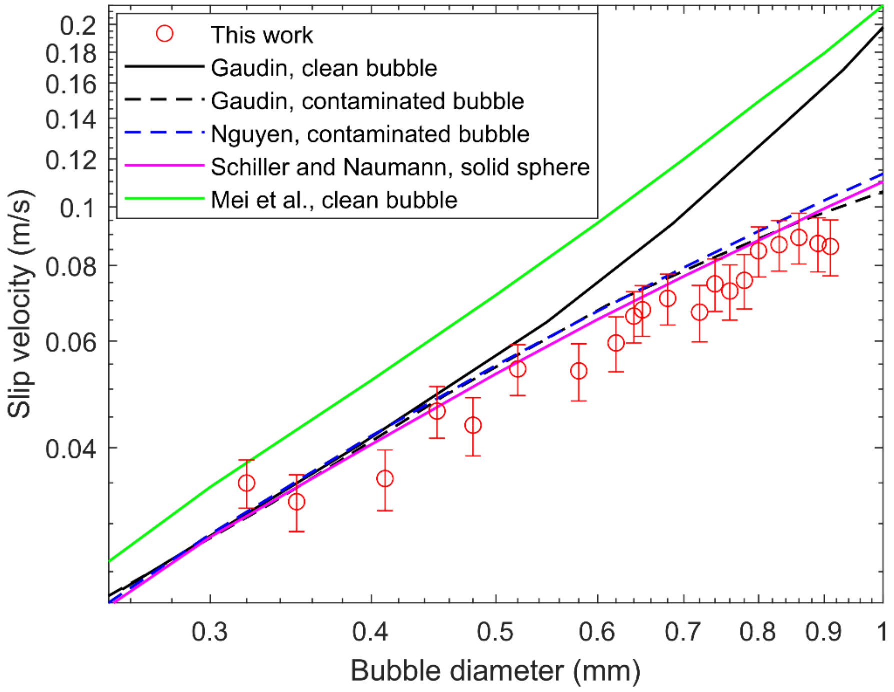

Figure 5-7. Dependence of slip velocity of bubbles on bubble diameter (Clift 1978). Correlations for slip velocity given by Gaudin (1957), Nguyen (1998), Schiller and Naumann (1933) and Mei *et al.* (1994) was provided as a comparison.

Experimental works studying wall-induced lift force on bubbles commonly focus on large bubbles rising in a highly viscous liquid (Takemura and Magnaudet 2003, Takemura *et al.* 2009). This can reduce bubble rising velocity, making it possible for a camera to track one particular bubble. However, using the same technique is quite challenging when studying microbubbles in water, where the magnification of camera becomes the priority to visualise microbubbles. Meanwhile, the camera should still retain a reasonably wide field of view. Otherwise, the fast-rising bubbles could not be successfully recorded. Therefore, to study the trajectory of the hydrogen bubbles in the channel, images of bubbles were taken at every 50 mm in the vertical direction above the level of the bubble generator, as shown in Figure 5-8. The camera was set to slow continuous shooting mode (4Hz) with a shutter speed of 1/4000s. For each location, 600 images were taken. The pixel size of the images was 1.8 μm.

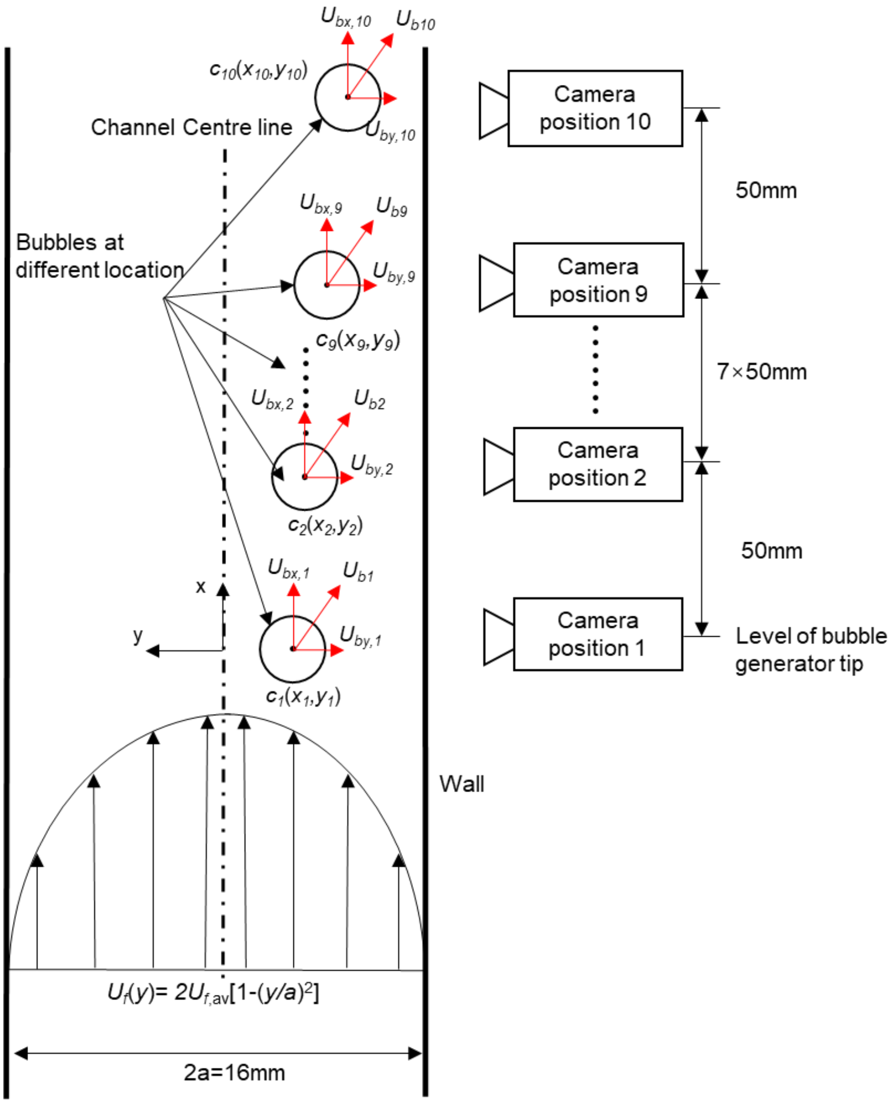

Figure 5-8. Bubble rising trajectory obtained from bubble visualisation method.

Using the same image processing technique as explained in section 5.2.2.2, the coordinates and diameters for all the bubbles were recorded. The data were then categorised into different groups based on bubble diameter, with a bin size of 20 μm. For example, the group "D_b= 400 mm" include bubbles with 390 mm<D_b<410 mm. The averaged coordinate and diameter in each group were used to calculate the forces acting on the bubbles. Considering $\rho_f \gg \rho_g$ and $V_b = \frac{\pi {D_b}^3}{6}$, Equation 5-1, which describes the forces acting on a bubble rising in a vertical channel, can be decomposed into x and y directions in the simplified form (Aoyama, Hayashi *et al.* 2017):

$$\frac{dU_{bx}}{dt} = \frac{3C_D}{2D_b}\left(U_b - U_f\right)\left|U_b - U_f\right| \cos\theta + 2C_L\left(U_b - U_f\right)\frac{\partial U_{ly}}{\partial y}\sin\theta + 2g, \qquad (5\text{-}9)$$

$$\frac{dU_{by}}{dt} = \frac{3C_D}{2D_b}\left(U_b - U_f\right)\left|U_b - U_f\right| \sin\theta + 2C_L\left(U_b - U_f\right)\frac{\partial U_{ly}}{\partial y}\cos\theta, \qquad (5\text{-}10)$$

where $\tan\theta = \frac{F_L}{F_D}$. To solve for the unknown C_L and θ, first assume $\sin\theta = 0$ so the bubble is rising in x-direction at its terminal velocity, $U_{b,x} = U_f + U_t$. Then Equation 5-9 can be solved for C_D. The time interval ($t_{m+1} - t_m$) for a bubble travel from $c_m(x_m, y_m)$ to $c_{m+1}(x_{m+1}, y_{m+1})$can be calculated by:

$$t_{m+1} - t_m = \frac{x_{m+1} - x_m}{U_{bx,m}}, \qquad (5\text{-}11)$$

where 1≤ m ≤9. The transverse velocities of the bubbles at different locations can be estimated by:

$$U_{by,m+1} = \frac{2(y_{m+1} - y_m)}{t_{m+1} - t_m} - U_{b,y,m}\,. \qquad (5\text{-}12)$$

Note that $U_{by,1} = 0$. After obtaining the transverse velocities, one can solve for C_L using Equation 5-10. Then the obtained C_L can be used to calculate θ using Equation 5-9 so that the accurate values for C_L and θ can be derived iteratively until the residuals for C_L and θ are less than 0.1%.

5.2.2.4 Uncertainty analysis

An uncertainty analysis was conducted to identify the reliability of the experimental data, as summarised in Table 5-3. The error for each parameter was calculated using the technique proposed by Moffat *et al.* (Moffat 1985):

$$\frac{\delta R}{R} = \sqrt{\left(a\frac{\delta x_1}{x_1}\right)^2 + \left(b\frac{\delta x_2}{x_2}\right)^2 + \cdots + \left(N\frac{\delta x_n}{x_n}\right)^2}, R = {x_1}^a {x_2}^b \ldots {x_n}^N. \tag{5-13}$$

Table 5-3. Summary of uncertainties of this work.

Parameter	**Maximum uncertainty**
Temperature	±1.0%
Viscosity, fluid	±4.5%
Surface tension, fluid	±3.2%
Density, fluid	Negligible
Density, H_2 bubble	Negligible
Channel width	±3.1%
Channel cross-section area	±6.3%
Bubble diameter	±8.0%
Bubble displacement	±4.0%
Velocity, H_2 bubble	±4.0%
Velocity, fluid	±4.0%
Acceleration, H_2 bubble	±5.6%
Drag coefficient	±8.9%
Lift coefficient	±8.9%

5.2.3 Results

5.2.3.1 Bubble size

Figure 5-9 shows the dependence of average bubble diameter on current density applied to the bubble generator under flow Reynolds numbers of 300, 500, 800 and 1000. It was found that the average bubble diameter increases linearly with the increase of applied current density. At a higher current density, a higher volumetric flow rate of H_2 is achieved at the electrode tip so that a larger bubble can be formed before it leaves the tip of the bubble generator (Zhang and Zeng 2012). A higher flow Reynolds number can result in a reduced average bubble diameter. For example, at a current density of 2.4 A/cm^2, an average bubble diameter of 0.86mm is achieved at a flow Reynolds number of 300. However, the average bubble diameter is decreased to 0.68 mm when the flow Reynolds number is increased to 1000. This is because, at the higher flow Reynolds numbers, the velocity of the flow surrounding the bubble increases, leading to higher drag force which promotes bubble departure (Raj *et al.* 2017, Mazzocco *et al.* 2018).

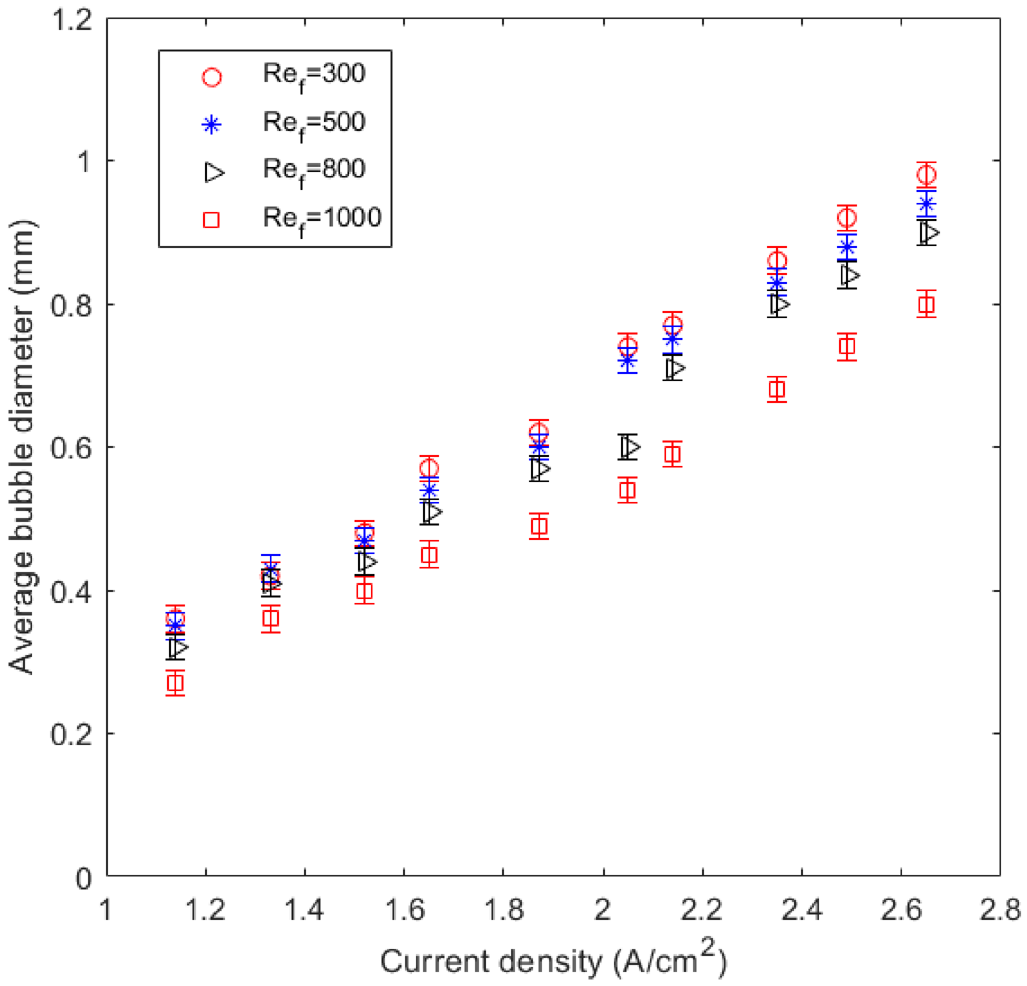

Figure 5-9. Dependence of average bubble diameter on the applied current density over the bubble generator under various flow Reynolds numbers.

Figure 5-10 shows the size distribution of H_2 bubbles in the channel at a flow Reynolds number of 500 for current densities of 2.3, 1.7 and 1.3 A/cm^2, respectively. It can be seen that the probability of the formation of H_2 bubbles with a larger diameter is increased with the increase of current density at the copper wire tip of the bubble generator. Also, the average diameter of H_2 increases with the increase of current density. Examples of images for bubbles with various diameters just separating from the tip of the bubble generator are shown in Figure 5-11.

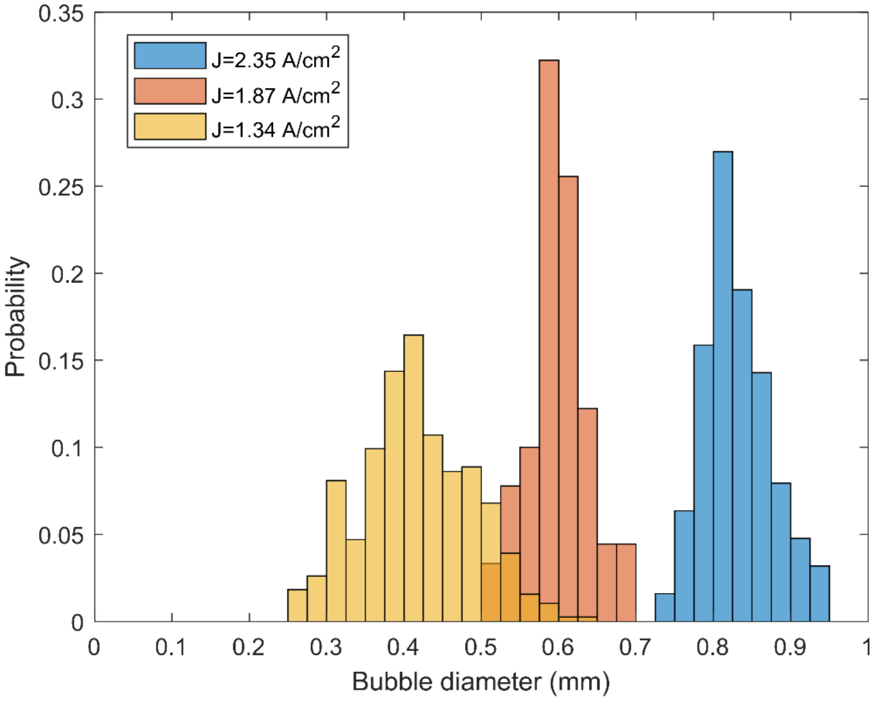

Figure 5-10. Bubble size distribution under different current densities at a flow Reynolds number of 500.

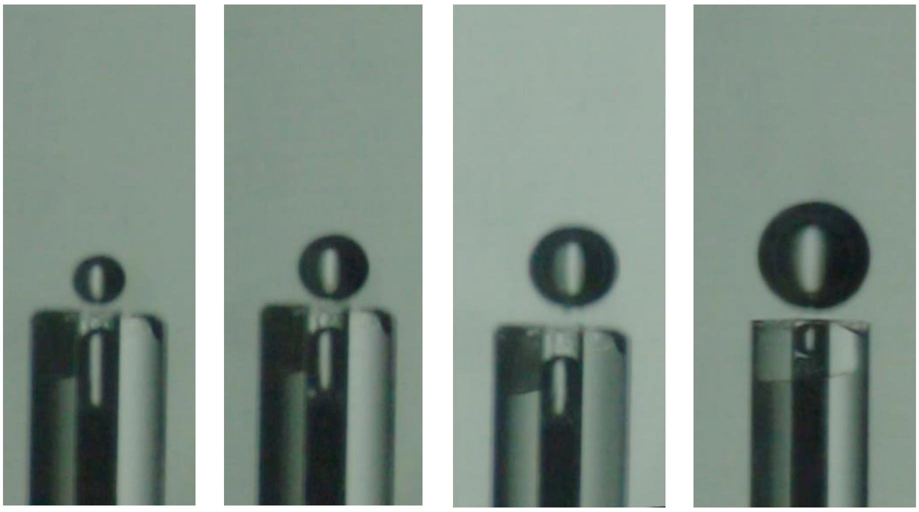

(a) D_b =0.41 mm J =1.3 A/cm^2 h = 0.9 mm

(b) D_b =0.60 mm J =1.7 A/cm^2 h = 0.9 mm

(c) D_b =0.82 mm J =2.3 A/cm^2 h = 0.9 mm

(d) D_b =0.95 mm J =2.3 A/cm^2 h = 0.7 mm

Figure 5-11. Images of bubbles with various diameters 2ms after jump-off from the tip of bubble generator under different current densities and with different gaps between the tip of enamel copper wire and quartz tube opening.

5.2.3.2 Bubble rising trajectory

Figure 5-12 shows the measured trajectory of bubbles at different sizes of 0.4 mm, 0.6 mm and 0.8 mm, released from various locations i.e. y/a = 0.2, 0.4, 0.6 and 0.8 in the channel at Re_f = 500. Consider the size of bubbles in the system, y/a ≥0.875 was defined as the wall region (Shi and Rzehak 2020, Shi, Rzehak *et al.* 2020). As can be seen, in all assessed cases, the bubbles move towards the wall. In addition, the vertical distance that a bubble travels in the channel before it reaches the wall region is related to the initial position of the bubble. For example, a bubble with a diameter of 0.8 mm released at y/a = 0.8 reaches the wall region at H = 0.1 m, whereas the H is increased to 0.31 m when the bubble is released at y/a = 0.4. This is because, compared to the latter, bubble released near the channel centreline has not only a higher rising velocity but also a longer distance for it to migrates into the wall region. Commensurate with this, it is also found that when released at the same position in the channel, even with higher rising velocities, the larger bubbles reach the wall faster than the smaller ones. For example, a D_b=0.8 mm bubble reaches the wall at H =0.3 m when released from y/a =0.6, whereas a D_b=0.4 mm bubble released from the same position reaches the wall at H=0.34 m. This indicates that larger bubbles experience much stronger lift force than the smaller ones. In addition, once bubbles enter the wall region, they slide at the wall surface and never leave the wall region.

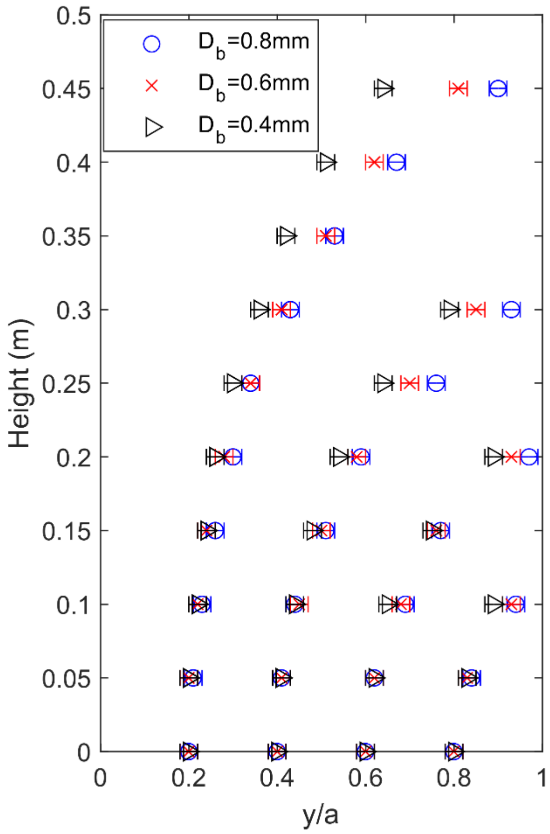

Figure 5-12. Rising trajectories of bubbles with diameters of 0.4 mm, 0.6 mm and 0.8 mm, released from y/a =0.2, y/a =0.4, y/a =0.6 and y/a =0.8 in the channel at a Re_f = 500.

The measured transverse velocities (U_{by}) for bubbles released at y/a =0.2 and y/a =0.6 at the same Re_f=500 as a function of their distance from the channel wall are plotted in Figure 5-13. It can be seen that U_{by} increases as the bubbles move towards the wall region, which indicates the shear-induced lift force dominates the transverse motion of bubbles. Furthermore, larger bubbles have a higher transverse velocity than small ones. For example, bubbles with D_b = 0.8 mm have a transverse velocity of approximately 0.0053 m/s at y/a =0.6. However, the measured U_{by} for bubbles with D_b = 0.4 mm is 0.0031 m/s. This is possibly because a larger bubble has a higher slip velocity (U_b-U_f), resulting in a greater lift force. In addition, a higher U_{by} is achieved when bubbles are released closer to the channel centreline, which indicates the lift force on bubbles is always directed to the wall side.

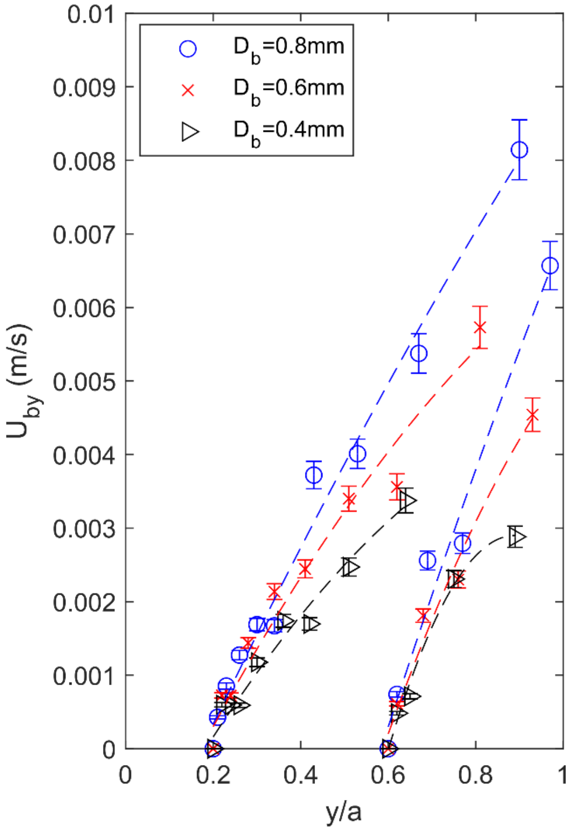

Figure 5-13. Measured dependence on the transverse velocities of bubbles with diameters of 0.4 mm, 0.6 mm and 0.8 mm when released from y/a =0.2 and y/a =0.6 in the channel at Re_f= 500.

The dependence of the ratio of the transverse velocity (U_{by}) to the vertical velocity (U_{bx}) on the distance from the channel wall (y/a) for bubbles released from y/a = 0.2 and y/a = 0.6 and for Re_f=500 is plotted in Figure 5-14. The values of U_{by}/U_{bx} increase as bubbles move towards the wall region (y/a >

0.875), which is caused by both the increase of U_{by}due to the dominating shear-induced lift force and the decrease of U_{bx} due to the reduced local flow velocity. Compared to bubbles released near the wall, bubbles released closer to the channel centreline will experience a stronger impulse due to the shear-induced lift force, leading to a higher value of U_{by}/U_{bx}. Importantly, the bubble diameter has no prominent effect on U_{by}/U_{bx}.

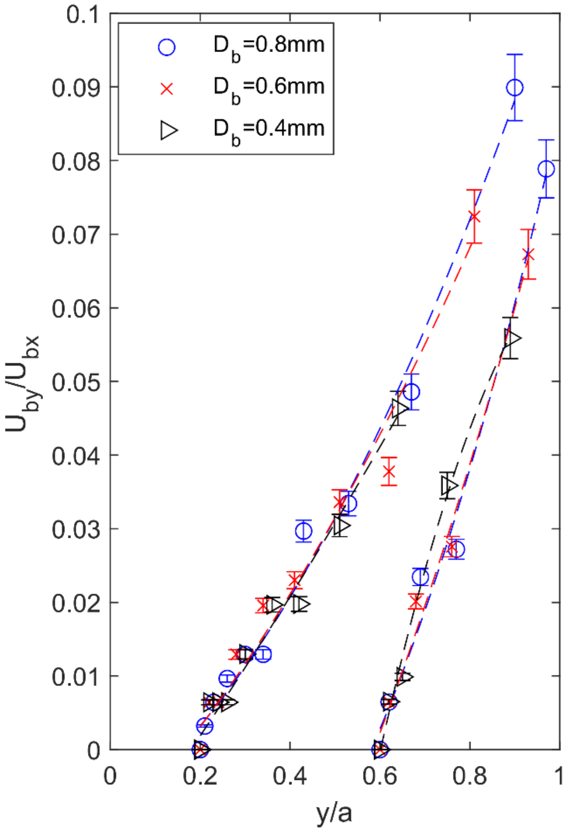

Figure 5-14. Measured dependence of the ratio of the transverse velocity and vertical velocity of bubbles with diameters of 0.4 mm, 0.6 mm and 0.8 mm on the normalised distance from the channel wall, when released from y/a =0.2 and y/a =0.6 in the channel at a Re_f = 500.

Figure 5-15 shows the trajectory of 0.6 mm bubbles (in x-direction) as a function of normalised distance from the channel wall and for four releasing points of y/a = 0.2, 0.4, 0.6 and 0.8 and various values of Re_f = 300, 500 and 800. It is found that the locations at which the bubbles enter the wall region (y/a > 0.875) are significantly dependent on the Re_f. For example, when a bubble is released at y/a =0.4, the bubble enters the wall region at H = 0.28 m when Re_f is 800, while it enters the wall region at H = 0.36 m when Re_f is 300. This is because bubbles rising in the channel with a higher flow Reynolds number are subjected to a stronger shear-induced lift force due to the increased shear rate, regardless of their initial position.

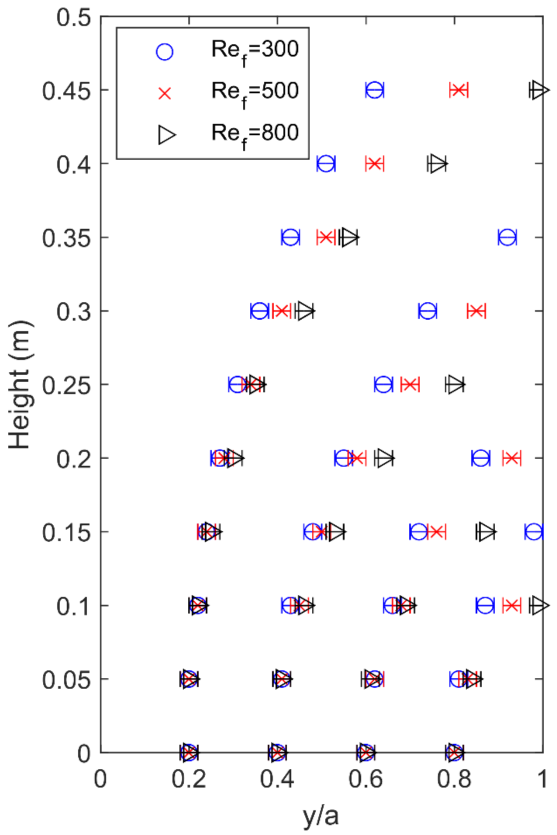

Figure 5-15. Measured rising trajectory of a single bubble with a diameter of 0.6 mm versus its normalised distance from the channel centre for the normalised release locations of y/a =0.2, 0.4, 0.6 and 0.8 in the channel with Re_f= 300, 500 and 800.

The measured transverse velocity (U_{by}) of bubbles with a diameter of 0.6 mm versus their normalised distance from the channel centre (y/a) for bubbles released from y/a =0.2 and y/a =0.6 and for the flow Reynolds numbers (Re_f) of 300, 500 and 800 is shown in Figure 5-16. It can be seen that the transverse velocity increases with Re_f. For instance, a bubble primarily released at y/a =0.2 achieves an U_{by} ≈0.0023m/s at y/a = 0.4 for Re_f= 300, while it achieves a U_{by} ≈ 0.004 m/s for Re_f = 800. This is because as Re_f is increased, the velocity gradient ($\frac{\partial U_f}{\partial y}$) at the same y/a also increases, which leads to a greater shear-induced lift force on the bubble.

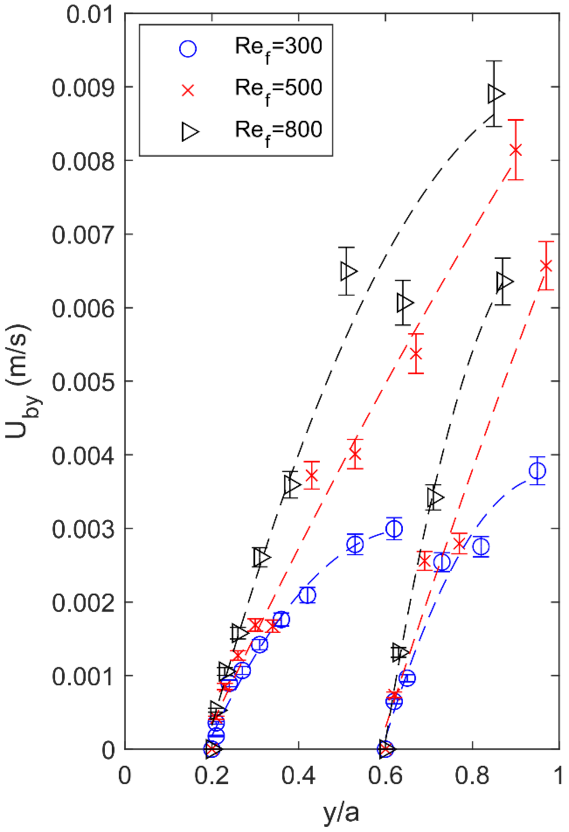

Figure 5-16. Measured variations of the transverse velocity of a single bubble with a diameter of 0.6 mm versus its normalised distance from the channel centre for bubbles released from y/a =0.2 and y/a =0.6 and for Re_f = 300, 500 and 800.

The ratio of transverse velocities (U_{by}) to vertical velocities (U_{bx}) for bubbles with D_b=0.6 mm released from y/a =0.2 and y/a =0.6 under Re_f of 300, 500 and 800 is plotted in Figure 5-17. It can be seen, U_{by}/U_{bx} slightly increases as bubble Re_f increases. For instance, bubble released from y/a =0.6 at Re_f=300 reaches U_{by}/U_{bx}=0.03 when it moves to y/a =0.8. However, U_{by}/U_{bx} increases to approximately 0.06 when Re_f is increased to 800. Also, at Re_f = 500 and Re_f = 800, a greater value of U_{by}/U_{bx} can be achieved by releasing bubbles nearer to the channel centreline. However, for a lower Re_f, a greater U_{by}/U_{bx} is found when a bubble is released nearer to the wall.

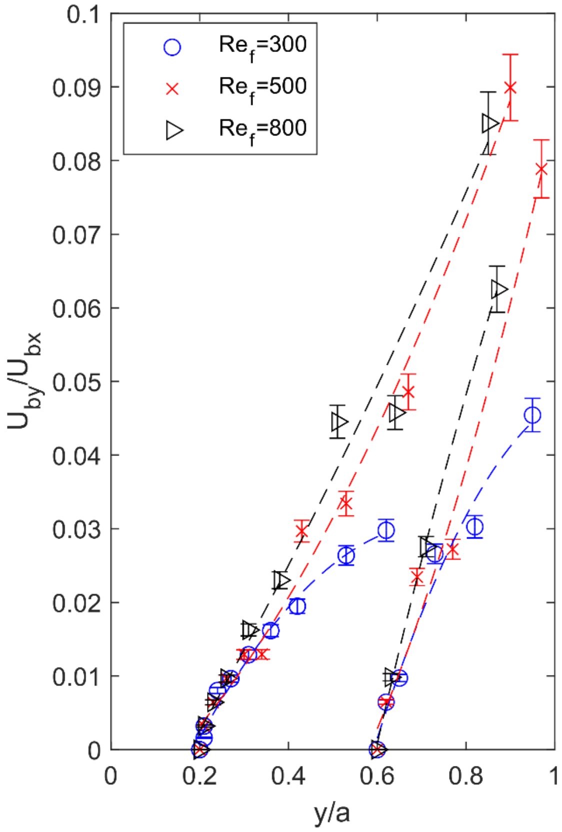

Figure 5-17. The ratio between transverse velocity and vertical velocity of bubbles with a diameter of 0.6 mm when released from y/a =0.2 and y/a =0.6 in the channel at Re_f of 300, 500, and 800.

5.2.3.3 Lift coefficient

Figure 5-18 presents the calculated C_L for bubbles with various diameters under different curvatures of the flow velocity profile. The value of C_L increases with the increase of the flow Reynolds number and the decrease of bubble Reynolds number. The calculated C_L in this work is slightly higher than that proposed by Tomiyama *et al.* (Tomiyama *et al.* 2002) and Aoyama *et al.* (Aoyama *et al.* 2017), where the C_L is derived experimentally from larger bubbles rising in a highly viscous liquid with a simple shear flow. Based on the calculated data, the following correlation is provided for C_L for microbubbles (D_b<1.0 mm) rising in a vertical channel with a fully developed laminar flow and a dimensionless shear rate of 0< Sr <0.22:

$$C_L = 0.04 {Re_b}^{-0.17} {Re_f}^{0.5} , \tag{5-14}$$

where Re_b and Re_f are the bubble Reynolds number and flow Reynolds number, respectively.

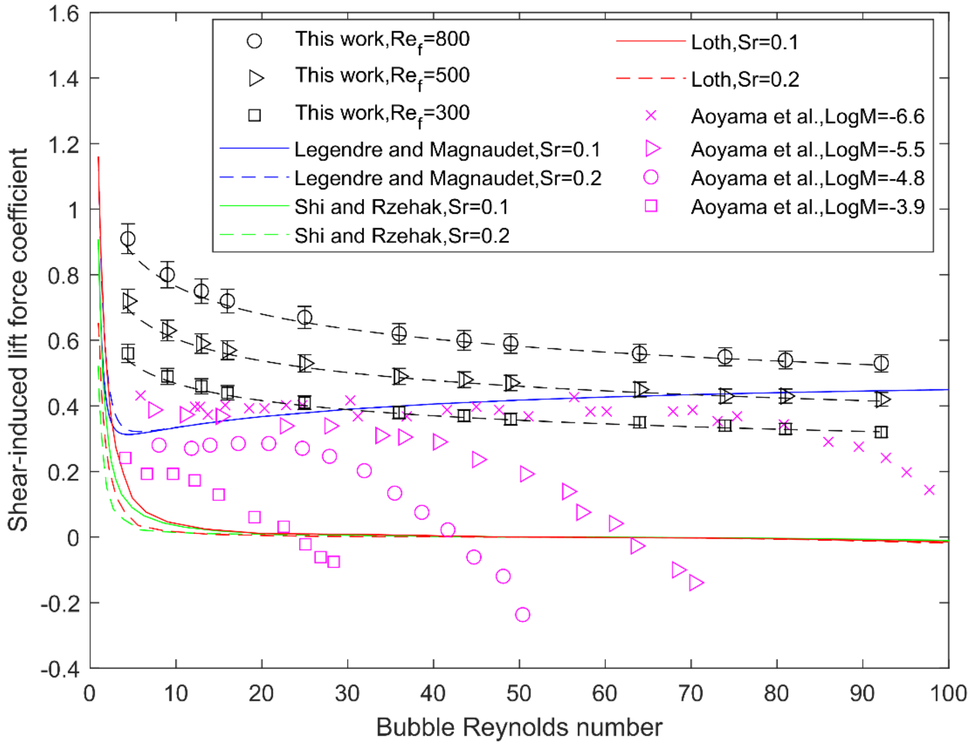

Figure 5-18. Lift force coefficient (C_L) for spheric microbubbles derived from experimental data. Experimental results by Aoyama *et al.* (2017), correlations proposed by Legendre and Magnaudet (1998), Shi and Rzehak (2019) and Loth (2008) are presented.

The trajectory for a bubble rising in a vertical channel can be estimated using the proposed correlation for C_L. Figure 5-19 shows the estimated trajectories for bubbles with diameters of 0.4-0.9 mm released from various locations in the channel under different Re_f. The results show that the proposed correlation for C_L can provide a good prediction for the rising trajectory of a bubble in a vertical channel with a deviation of ± 10%.

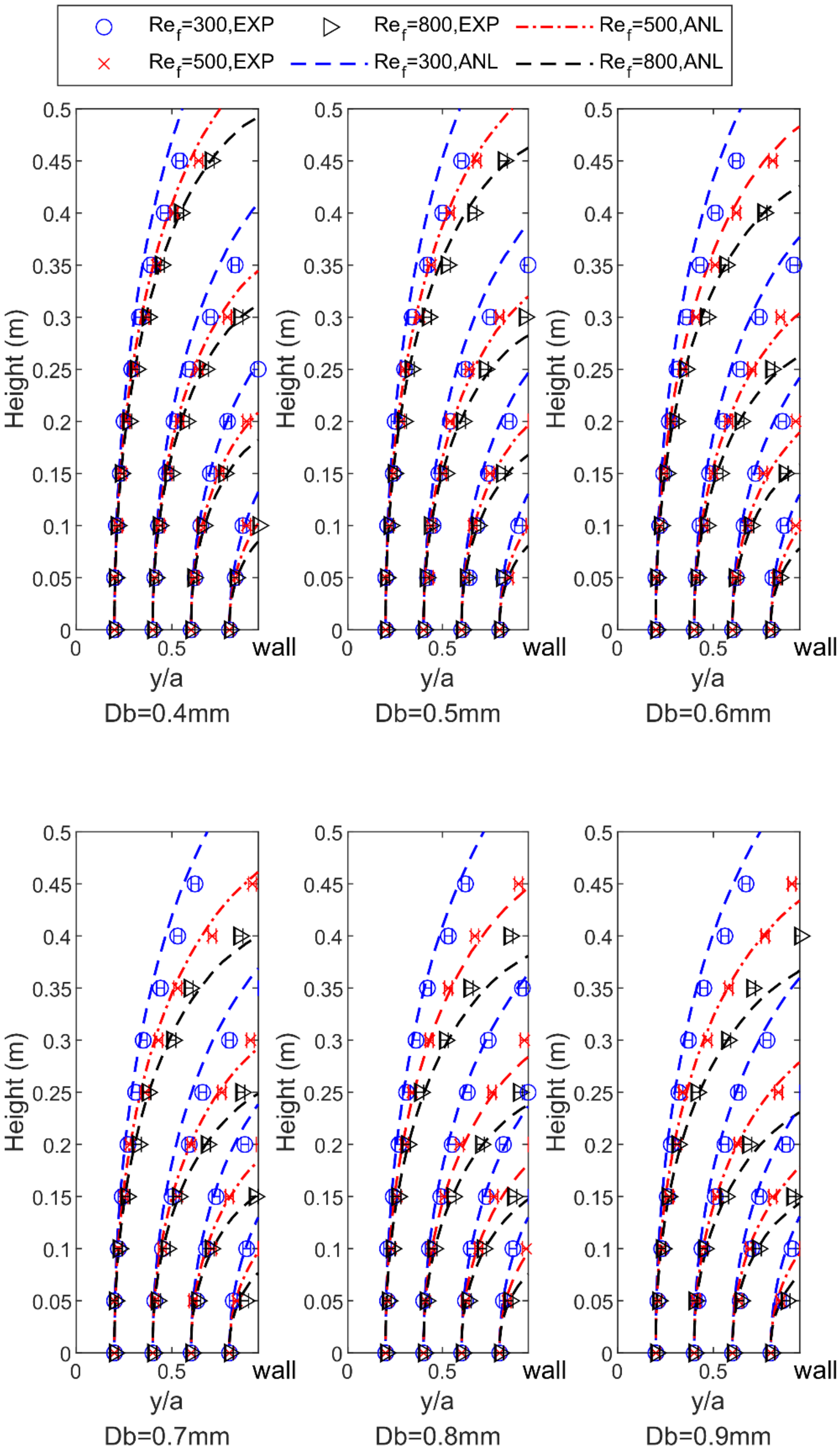

Figure 5-19. Comparison between experimentally derived bubble rising trajectories and estimated trajectory based on the proposed correlation for C_L.

5.2.4 Discussion

The experimental data suggests that the trajectory of a rising bubble in a vertical channel is determined by the bubble diameter, the location of the releasing point as well as the flow Reynolds number. It is also found that the shear-induced lift force has a more significant effect on bubbles of larger diameters. The behaviour of the rising bubbles can be characterised by their Stokes numbers:

$$Stk = \frac{t_b U_s}{D_b}, \tag{5-15}$$

where the relaxation time of bubble (t_b) is calculated as (Schiller and Naumann 1933):

$$t_b = \frac{(\rho_b + \alpha\rho_f){D_b}^2}{18\mu_f}\frac{24}{Re_b C_D}. \tag{5-16}$$

Using the correlation for drag coefficient (C_D) in Equation 5-2 (Tomiyama *et al.* 2002), the calculated Stokes numbers for microbubbles rising in the vertical channel at their terminal velocities are plotted in Figure 5-20. It can be seen that Stokes number increases approximately linearly with the increase of bubble diameter. Bubbles with diameters of less than 0.1 mm have Stk<0.1, which closely follow the streamline of the flow in the channel. However, with the increase of bubble diameter, the effect of shear-induced lift force becomes more dominant, and the transverse motion of bubbles are more significant. Bubbles investigated in this work have 0.1< Stk < 2. Hence, with the decrease of bubble diameter, bubble's response to the velocity gradient in the channel is gradually reduced.

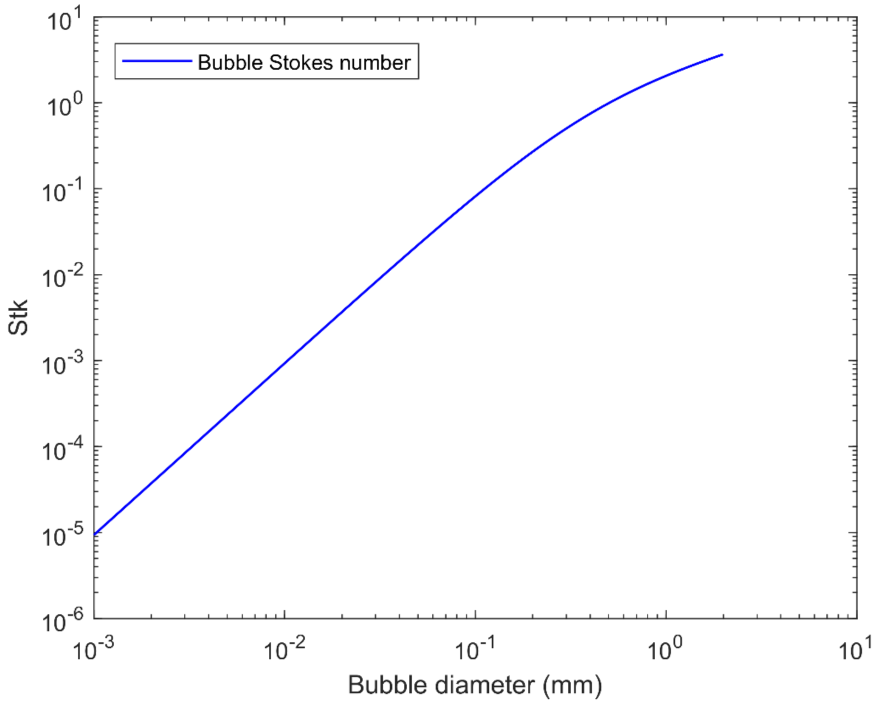

Figure 5-20. Stokes number of microbubbles (D_b <1 mm) rising in 20℃ water in a vertical channel at their terminal velocities.

Due to wall- and shear-induced lift forces, bubbles rising in a vertical channel with a fully developed laminar flow reach their equilibrium position in y-direction, if the channel is long enough. The results of experiments in this work show that for 280<Re_f <1000 and 4.5< Re_b <112.4, once bubbles enter the wall region (y/a ≥ 0.875), they start sliding against the wall and never leave this region until they reach to the end of the channel. Oscillation of bubbles (Mortazavi and Tryggvason 2000) in the channel are not detected. Nevertheless, to be able to accurately investigate the wall effect and also the oscillating of the bubbles in this region the length of the channel needs to be further extended (Asmolov 1999, Shi *et al.* 2020).

5.2.5 Conclusion and recommendation

The trajectory of microbubbles rising in a vertical channel with a fully developed laminar flow was evaluated, and the lift force coefficient for microbubbles was investigated. The experiments were conducted under the conditions of 280<Re_f <1000, 4.5<Re_b <112.4, 0.005 < Eo <0.134, 0< Sr <0.22 and $\log_{10} Mo$=-11.

The velocity profile of the flow in the channel was investigated using a BIV setup with a micro-wire installed at the channel inlet to generate seeding bubbles. The following conclusions were obtained:

- Bubbles rising in the vertical channel moves to the wall region under the lift force induced by the velocity gradient of the flow. The bubble transverse velocity increases as the distance between the rising bubble and the electrode increases, whereas the bubble vertical velocity decreases as the bubble moves towards the wall.
- Bubbles rising in a vertical channel move to the wall region faster by means of a) moving the bubble releasing position nearer to the wall, b) increasing bubble diameter, and c) increasing flow Reynolds number.
- A new correlation for the lift coefficient for microbubbles was proposed based on the results of flow visualisation experiments. This correlation can be used to predict the trajectory of a microbubble rising in a vertical channel with a fully developed laminar flow.

This work revealed the trajectory of a buoyant object in a vertical channel can be customised by controlling the velocity profile of the flow in the channel. This technique can be applied to various applications such as: the isolation and separation of cells with different sizes in pharmaceutical industries; boiling heat exchangers and conventional water electrolysers, where bubbles are preferred to be separated from the wall; novel membrane-less electrolysers, where bubble trajectory management is critical.

References

Aoyama, S., K. Hayashi, S. Hosokawa, D. Lucas and A. Tomiyama (2017). Lift force acting on single bubbles in linear shear flows. International Journal of Multiphase Flow **96**: 113-122.

Asmolov, E. S. (1999). The inertial lift on a spherical particle in a plane Poiseuille flow at large channel Reynolds number. Journal of Fluid Mechanics **381**: 63-87.

Atherton, T. J. and D. J. Kerbyson (1999). Size invariant circle detection. Image and vision computing **17**(11): 795-803.

Clift, R. (1978). Bubbles, drops, and particles. New York, Academic Press.

Davies, E. R. (2005). Machine vision: theory, algorithms, practicalities. Burlington, Elsevier Science & Technology.

Don, W. G. and H. P. Robert (2008). Perry's Chemical Engineers' Handbook, Eighth Edition. New York, McGraw-Hill Education.

Gaudin, A. M. (1957). Flotation. New York, McGraw-Hill.

Holland, F. A. and R. Bragg (1995). 7 **-** Gas–liquid two-phase flow. Fluid Flow for Chemical Engineers (Second Edition). F. A. Holland and R. Bragg. Oxford, Butterworth-Heinemann**:** 219-267.

Kolev, N. I. (2007). Bubble departure diameter. Multiphase Flow Dynamics 2: Thermal and Mechanical Interactions. N. I. Kolev. Berlin, Heidelberg, Springer Berlin Heidelberg**:** 417-438.

Legendre, D. and J. Magnaudet (1998). The lift force on a spherical bubble in a viscous linear shear flow. Journal of Fluid Mechanics **368**: 81-126.

Loth, E. (2008). Lift of a spherical particle subject to vorticity and/or spin. AIAA Journal **46**(4): 801-809.

Mazzocco, T., W. Ambrosini, R. Kommajosyula and E. Baglietto (2018). A reassessed model for mechanistic prediction of bubble departure and lift off diameters. International Journal of Heat and Mass Transfer **117**: 119-124.

Mei, R., J. F. Klausner and C. J. Lawrence (1994). A note on the history force on a spherical bubble at finite Reynolds number. Physics of Fluids **6**(1): 418-420.

Moffat, R. J. (1985). Using Uncertainty Analysis in the Planning of an Experiment. Journal of Fluids Engineering **107**(2): 173-178.

Mortazavi, S. and G. Tryggvason (2000). A numerical study of the motion of drops in Poiseuille flow. Part 1. Lateral migration of one drop. Journal of Fluid Mechanics **411**: 325-350.

Nguyen, A. V. (1998). Prediction of bubble terminal velocities in contaminated water. AIChE journal **44**(1): 226-230.

Nguyen, A. V., H. Stechemesser, G. Zobel and H. J. Schulze (1997). An improved formula for terminal velocity of rigid spheres. International journal of mineral processing **50**(1): 53-61.

Raffel, M. (2018). Particle Image Velocimetry: A Practical Guide. Cham, Springer International Publishing.

Raj, S., M. Pathak and M. K. Khan (2017). An analytical model for predicting growth rate and departure diameter of a bubble in subcooled flow boiling. International Journal of Heat and Mass Transfer **109**: 470-481.

Rocha, F., Q. de Radiguès, G. Thunis and J. Proost (2021). Pulsed water electrolysis: A review. Electrochimica Acta **377**.

Ryu, Y., K.-A. Chang and H.-J. Lim (2005). Use of bubble image velocimetry for measurement of plunging wave impinging on structure and associated greenwater. Measurement Science and Technology **16**(10): 1945-1953.

Schiller, L., Naumann, A (1933). Über die grundlegenden Berechnungen bei der Schwerkraftauĩereitung. Zeitschrift des Vereins Deutscher Ingenieure 77: 318-320.

Shi, P. and R. Rzehak (2019). Lift forces on solid spherical particles in unbounded flows. Chemical Engineering Science **208**: 115145.

Shi, P. and R. Rzehak (2020). Lift forces on solid spherical particles in wall-bounded flows. Chemical Engineering Science **211**: 115264.

Shi, P., R. Rzehak, D. Lucas and J. Magnaudet (2020). Hydrodynamic forces on a clean spherical bubble translating in a wall-bounded linear shear flow. Physical Review Fluids **5**(7): 073601.

Takemura, F. and J. Magnaudet (2003). The transverse force on clean and contaminated bubbles rising near a vertical wall at moderate Reynolds number. Journal of Fluid Mechanics **495**: 235-253.

Takemura, F., J. Magnaudet and P. Dimitrakopoulos (2009). Migration and deformation of bubbles rising in a wall-bounded shear flow at finite Reynolds number. Journal of Fluid Mechanics **634**: 463.

Thielicke., W. and R. Sonntag. (2021). Particle image velocimetry for MATLAB: accuracy and enhanced algorithms in PIVlab. Journal of Open Research Software **9**(1): 12.

Tomiyama, A., H. Tamai, I. Zun and S. Hosokawa (2002). Transverse migration of single bubbles in simple shear flows. Chemical Engineering Science **57**(11): 1849-1858.

Vogt, H. (1989). The problem of the departure diameter of bubbles at gas-evolving electrodes. Electrochimica Acta **34**(10): 1429-1432.

Vogt, H. (2017). The quantities affecting the bubble coverage of gas-evolving electrodes. Electrochimica Acta **235**: 495-499.

Yuen, H. K., J. Princen, J. Illingworth and J. Kittler (1990). Comparative study of Hough Transform methods for circle finding. Image and vision computing **8**(1): 71-77.

Zhang, D. and K. Zeng (2012). Evaluating the behavior of electrolytic gas bubbles and their effect on the cell voltage in alkaline water electrolysis. Industrial & Engineering Chemistry Research **51**(42): 13825-13832.

Zhou, D., P. Li, W. Xu, S. Jawaid, J. Mohammed‐Ibrahim, W. Liu, Y. Kuang and X. Sun (2020). Recent advances in non‐precious metal‐based electrodes for alkaline water electrolysis. ChemNanoMat **6**(3): 336-355.

Chapter 6

Flow control for bubble management

6.1 Chapter overview

This chapter explores the application of flow control to manage bubble distribution in a membrane-free water electrolyser (MFE). In the previous Chapter, the critical role of the electrolyte velocity field in controlling the distribution of bubbles within an MFE is highlighted. When the electrolyte maintains a parabolic velocity profile, H_2 and O_2 bubbles will rise near the electrode due to the shear-induced lift force. However, this can only occur when the void fraction is relatively low so that the bubble-induced velocity is negligible. As the void fraction increases, bubbles near the electrode induce a high local velocity, disrupting the velocity field in the electrolyte. This high velocity near the electrode generates a lift force that propels bubbles towards the channel centre, leading to gas crossover. This implies that relying solely on electrolyte flow is inadequate for the effective separation of H_2 and O_2 gases in an MFE. The research conducted in this chapter aims to address this challenge.

In this chapter, a novel flow controller is developed to control the flow field within the MFE. This flow controller consists of two sets of thin, porous plates positioned between the anode and cathode. A three-dimensional computational fluid dynamics (CFD) model of an MFE is developed using Ansys Fluent software. This CFD model is validated by comparing the simulated distribution of bubble curtain thickness against experimental results. Based on the CFD model, the impact of flow controller geometry and its position in the channel on the electrolyte flow field, and the distribution of gases in the electrolyser channel is numerically investigated. Furthermore, a prototype of the flow controller is fabricated via 3D-printing from ABS plastic with a wall thickness of 0.4 mm. The flow controller is tested within an MFE channel with a 6 mm×6 mm cross-section and a height of 134 mm at various flow Reynolds numbers and applied current densities.

The results show that the flow controller can significantly mitigate gas crossover in the MFE by maintaining a W-shaped velocity field within the channel. This tailored velocity field ensures that the shear-induced lift forces consistently direct H_2 and O_2 towards the electrodes where they evolve. The optimal position of the flow controller was found to be at approximately $0.25w$ from the channel wall (where w represents the channel width). The experimental result of the prototype flow controller demonstrated its capability to significantly reduce gas crossover in an MFE without compromising cell efficiency. The findings of this chapter reveal that flow controllers can generate an optimal velocity field in an MFE, which effectively mitigates gas crossover. Consequently, this accomplishes the fourth research objective.

6.2 Flow control in membrane-free water electrolyser

This section consists of the following journal article:

Yang, B., Jafarian, M., Freidoonimehr, N., & Arjomandi, M. (2024). Flow control for bubble management in a membrane-free electrolyser. International Journal of Multiphase Flow, 174, 104770.

This article is identical to the submitted version, with the exception of the numbering and positioning of figures, tables, and equations.

Statement of Authorship

Title of Paper	Bubble management in flow-by membrane-free water electrolyser by flow control
Publication Status	☒ Published ☐ Accepted for Publication ☐ Submitted for publication ☐ Unpublished and Unsubmitted work written in manuscript style
Publication Details	Yang, B., Jafarian, M., Freidoonimehr, N., & Arjomandi, M. (2024). Flow control for bubble management in a membrane-free electrolyser. International Journal of Multiphase Flow, 174, 104770.

Principal Author

Name of Principal Author (Candidate)	Bo Yang		
Contribution to the Paper	Developed ideas, conducted experiments, performed data analysis, interpreted results, wrote manuscript, and acted as corresponding author.		
Overall percentage (%)	80%		
Certification:	This paper reports on original research I conducted during the period of my Higher Degree by Research candidature and is not subject to any obligations or contractual agreements with a third party that would constrain its inclusion in this thesis. I am the primary author of this paper.		
Signature		Date	25/11/2023

Co-Author Contributions

By signing the Statement of Authorship, each author certifies that:

i. the candidate's stated contribution to the publication is accurate (as detailed above);

ii. permission is granted for the candidate in include the publication in the thesis; and

iii. the sum of all co-author contributions is equal to 100% less the candidate's stated contribution.

Name of Co-Author	Mehdi Jafarian		
Contribution to the Paper	Supervised the development of the research, participated in developing ideas and concept, helped in interpreting results, and assisted in evaluating and editing the manuscript.		
Signature		Date	25/11/2023

Name of Co-Author	Navid Freidoonimehr		
Contribution to the Paper	Supervised the development of the research, participated in developing ideas and concept, helped in interpreting results, and assisted in evaluating and editing the manuscript.		
Signature		Date	25/11/2023

Name of Co-Author	Maziar Arjomandi		
Contribution to the Paper	Supervised the development of the research, participated in developing ideas and concept, helped in interpreting results, and assisted in evaluating and editing the manuscript.		
Signature		Date	25/11/2023

Flow control for bubble management in a membrane-free electrolyser

Bo Yang, Mehdi Jafarian, Navid Freidoonimehr and Maziar Arjomandi

Abstract

Gas crossover is an important feature affecting the overall performance of membrane-free water electrolysers, as it may lead to compromised product quality and safety risks. In this paper, the concept of using flow control device for reduction of gas crossover in membrane-free water electrolysers is introduced. A numerical study is conducted to investigate the influence of flow controller on the H_2 bubble curtain thickness in a vertical flow-by membrane-free electrolyser under various operating conditions, and the effect of flow controller geometry on the H_2 bubbles is systematically studied. An experimental rig is developed to validate the numerical model and to test the performance of a flow controller prototype. The results show that the proposed flow controller can effectively alleviate the crossover of gases in the electrolyser cell without compromising the cell efficiency.

Keywords

Water electrolysis; Shear-induced lift force; Bubble behaviour

Nomenclature

C_L	Lift coefficient
C_D	Drag coefficient
D	Diameter, m
F	Force, N
g	Gravity acceleration, 9.8 m/s^2
I	Current, A
J	Current density, A/m^2
M	Molar weight, g/mol
m	mass, kg
P	Pressure, Pa
R	Gas constant, 8.3145 J/mol·K

T	Temperature, K
t	Time, s
u	Velocity, m/s
V	Volume, m^3

Dimensionless numbers

$Re = \dfrac{\rho_f U D}{\mu_f}$	Reynolds number
$Sr = \dfrac{w D_b}{\lvert U_f - U_b \rvert}$	Shear rate

Subscriptions

B	Buoyancy
b	Bubble
D	Drag
L	Lift
f	Liquid flow

Greek letters

α	Volume fraction
ρ	Density, kg/m^3
σ	Surface tension, N/m
μ	Dynamic viscosity, kg/m·s

6.2.1 Introduction

Hydrogen generated from renewable resources is a versatile energy carrier with non-toxic emissions and a high heating value (120 MJ/kg) (Zohuri 2019). It also has various applications in chemical industry, hydrocarbon and metallurgical processes, fuel cell technology and transportation sectors (Abbasi *et al.* 2019). Although currently, most of the global H_2 production is from either steam reforming or coal gasification, water electrolysis powered by renewables is gaining increasing support since it is a more sustainable alternative (Manzotti *et al.* 2022). Alkaline and proton exchange membrane water electrolysers are the main commercially available technologies. In a modern alkaline electrolyser cell, a membrane is installed between the anode and cathode to isolate the O_2 and H_2 gases (Paidar *et al.* 2016). Although the membrane plays a crucial role in separating the produced gases, it introduces resistance in the electrolyser cell which reduces the cell efficiency. Also, the membrane can be susceptible to degradation over time especially at high temperatures (>70 ℃), which limits the operating temperature of the water electrolyser and increases the maintenance cost (Vincent and Bessarabov 2018).

To eliminate the membrane to reduce capital and maintenance costs of the electrolysis cell, there has been a growing interest in developing membrane-free water electrolyser (MFE) (Manzotti *et al.* 2022, Swiegers *et al.* 2022). However, due to the lack of a physical barrier to separate the produced H_2 and O_2, the gas crossover has been found as a substantial technical challenge that affects the product purity and operating safety of membrane-free water electrolysers (Esposito 2017). Therefore, there is a need to develop methods for mitigating gas crossover in an MFE.

Tabe 6-1 presents a few representative concepts of MFE in the literature, with flow-through and flow-by emerging as the predominant cell designs. Figure 1(a) shows a schematic of the flow-through MFE, in which the porous anode and cathode are located at the exit of the electrolyte so that the product H_2 and O_2 are directed to different exits. Additionally, in this concept, a minimum electrolyte flow is required to effectively remove bubbles from the electrodes, which results in considerable energy consumption by the pump *et al.* 2015, O'Neil, Christian *et al.* 2016).

Table 6-1. The concepts of MFE from recent works.

Type	Cell specification	Re	Gas cross over	Performance	Reference
Flow-through	30mm-diameter porous electrodes placed 2.5 mm apart	-	>0.17%	η=73% at 500 mA/cm^2; Can operate at high current density up to 4 A/cm^2	Gillespie *et al.* (2015)
Flow-through	5 mmx6 mm channel	0-50	>2.8%	η=72.5% at 100m A/cm^2	O'Neil *et al.* (2016)
Flow-by	horizontal 1 mmx1 mm electrolyser channel	78-312	~1% at high Re (>150)	η=78% at 500 mA/cm^2	Hashemi *et al.* (2015)
Buoyancy	Electrolyte: NaOH(aq) with 3D printed electrode	-	~5% at 50cm^2/mA	η=65% at 50 cm^2/mA	Bui *et al.* (2020)

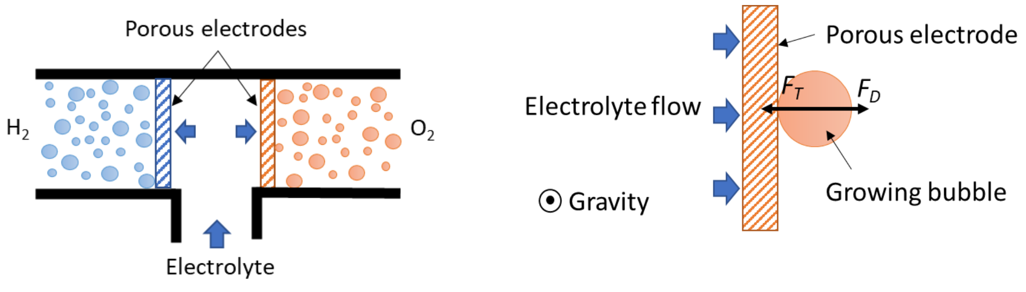

(a) (b)

Figure 6-1. (a) A schematic of a flow-through MFE, where the O_2 and H_2 are collected from separate channels. (b) Surface tension force and drag force acting on a growing bubble at the surface of the porous electrode.

In a flow-by MFE (Figure 6-2), the anode and cathode are positioned parallel to each other, while the electrolyte passes over their surfaces. As a result, the produced H_2 and O_2 bubbles are carried by the electrolyte along the surface of electrodes, as shown in Figure 6-2(a). This type of electrolyser can only operate when the flow is laminar. It is crucial to maintain a parabolic velocity field in the channel such that the shear-induced lift forces (F_{SL}) on the bubbles can force them to stay adjacent to the electrode where they evolve (Segré and Silberberg 1961, Esposito 2017).

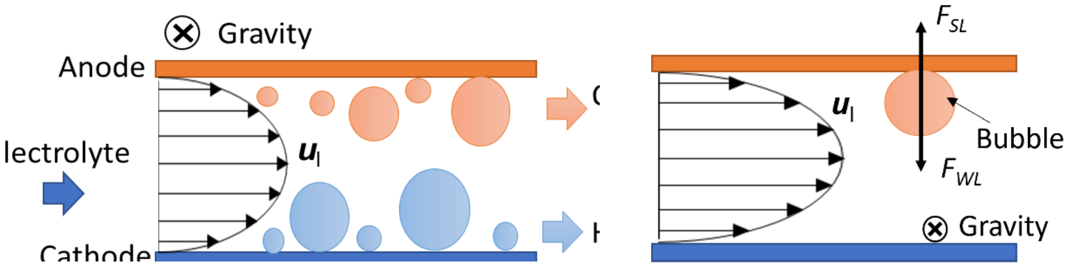

(a) (b)

Figure 6-2. (a) A schematic of a flow-by membrane-free water electrolyser cell design where the anode and cathode are placed in parallel. (b) The shear-induced lift force (F_{SL}) and wall-induced lift force (F_{WL}) on a bubble in a horizontal flow-by membrane-free water electrolyser.

In general, the shear-induced force is proportional to the velocity gradient of the electrolyte flow (Legendre and Magnaudet 1998, Aoyama *et al.* 2017, Shi and Rzehak 2019). Since the working principle of a flow-by MFE is based on the shear-induced forces for separation of the H_2 and O_2 gases, the magnitude of the velocity gradient of the electrolyte is critical to the separation effectiveness (Hashemi *et al.* 2015, Shi *et al.* 2020). In a horizontal flow-by MFE, the gas bubbles tend to accumulate at the top section of the electrolyser channel, where only a diminishing velocity gradient exists. In this case, the shear-induced lift force may become too weak to prevent the crossover of H_2 and O_2 bubbles (Legendre *et al.* 2008). Therefore, the width of the electrode of the horizontal flow-by MFE is restricted to a few millimetres (Hashemi *et al.* 2015, Hashemi *et al.* 2019), which limits its scaling-up.

Figure 6-3 shows a schematic of a vertical MFE. Compared to its horizontal counterpart, the vertical MFE overcomes the electrode width limitation, as it allows bubbles to exit the electrolyser freely. In a vertical MFE, when a parabolic flow profile is applied at the channel inlet, the bubbles near the inlet tend to move to the wall under the shear-induced lift force (No.1 bubble in Figure 6-3), which is favourable for an MFE. With the increase of channel length, as the H_2 and O_2 bubbles lead the flow, they induce flow velocity and eventually create a W-shaped velocity profile, as shown in Figure 6-3 (Hreiz *et al.* 2015) .

Since bubbles rise at their terminal velocities, the directions of the transverse motions of bubbles under the shear-induced lift forces depend on the sign of the velocity gradient ($\frac{\partial u}{\partial z}$): bubbles experiencing a positive velocity gradient move toward the wall (No. 2 and 4 bubbles in Figure 6-3), and bubbles in the zone with a negative velocity gradient move toward the channel centre (No.3 bubble in Figure 6-3) (Yang *et al.* 2022). Consequently, the W-shaped velocity profile can also prevent gas crossover.

Nevertheless, the W-shaped velocity profile cannot be self-maintained. With a further increase in channel length, the bubble-induced velocity increases, and the position of the maximum bubble-induced electrolyte velocity moves towards to the channel centre, forming a V-shaped velocity profile in the electrolyte bulk. As a result, the bubbles subjected to a positive velocity gradient stay in the near wall region (No.6 bubble in Figure 6-3), while bubbles experiencing a negative velocity gradient move towards the channel centre, leading to the gas crossover (No.5 bubble in Figure 6-3). In other words, increasing the channel length can escalate the crossover of H_2 and O_2 gases.

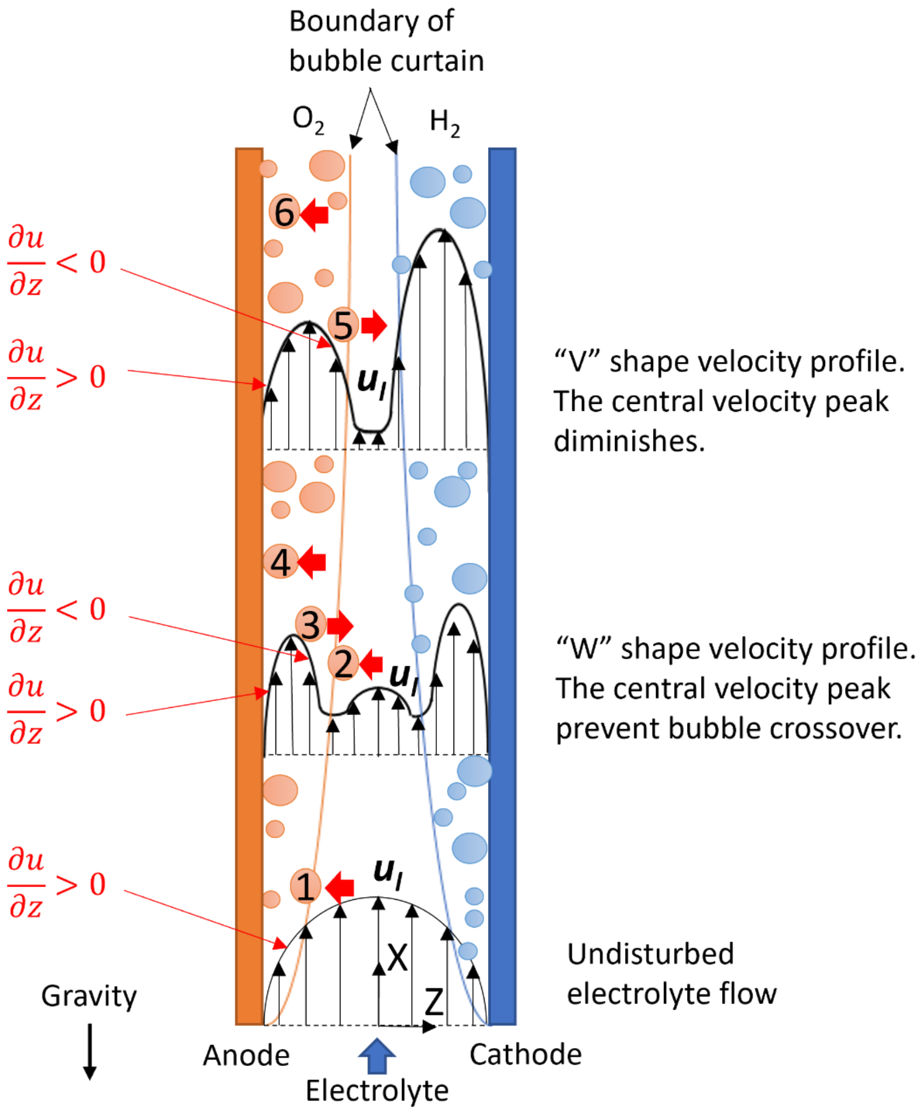

Figure 6-3. A schematic of a vertical flow-by membrane-free water electrolyser with a fully developed laminar flow at the channel inlet. Due to bubble-induced velocity, "W" shape and "V" shape electrolyte velocity profiles are formed at the middle and top sections of the electrolyser channel, respectively, resulting in crossover of H_2 and O_2 bubbles.

As discussed above, the transverse motion of bubbles, as well as the accumulation of bubbles on the surface of the electrodes, contribute to the thickening of the H_2 and O_2 bubble curtains and promoting gas crossover in MFE. In this paper, we propose to use flow controllers to maintain the W-shaped velocity profile in the electrolyser channel to minimise the gas crossover, as shown in Figure 6-4. The flow controllers are placed between the anode and cathode and divide the channel into three subchannels. In this paper, the effect of flow controller geometry and its position in the channel on the distribution of gases in the electrolyser channel is numerically and experimentally studied.

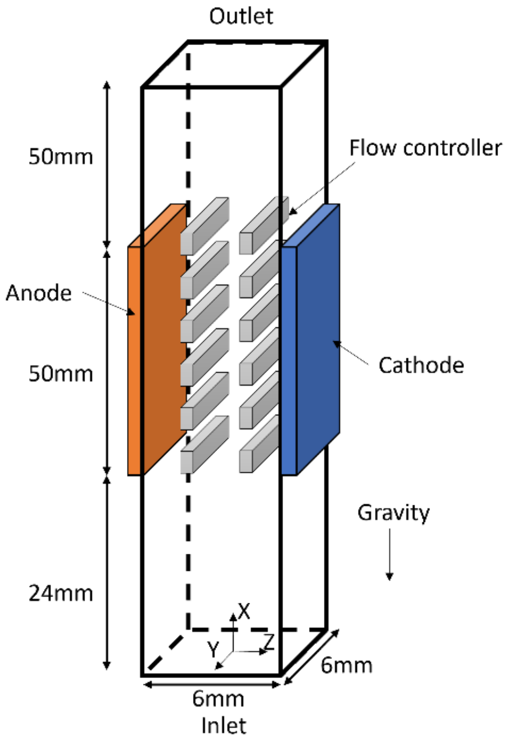

Figure 6-4. A membrane-free water electrolyser equipped with flow controllers.

6.2.2 Methodology

6.2.2.1 Numerical model

Figure 6-5 presents the key components of the proposed membrane-free electrolyser (MFE), which consists of a square channel with a cross-section of 6 mm×6 mm and a height of 124 mm. The anode and cathode are located 24mm above the channel inlet. These dimensions are chosen according to the experimental rig described in Section 6.2.2.2 of this paper. Ansys Fluent 2022 R2 software is used to simulate the gas-liquid two-phase flow in the channel.

In the CFD model, bubbles were introduced as volumetric mass sources in the two regions adjacent to the anode and cathode, respectively (Rodríguez and Amores 2020). The thickness of the regions equal to the bubble diameter defined in the model. In actual electrolysers, H_2 and O_2 bubble diameters can vary from a few millimetres to hundreds of millimetres. This variation depends on factors such as electrode surface characteristics, applied current density, electrolyte properties, and flow field (Vogt 1989, Zhang and Zeng 2012). However, for simplicity, this study assumes a constant bubble diameter of 0.15mm, which is within the range of values frequently utilised in similar research contexts (Abdelouahed *et al.* 2014, Hreiz *et al.* 2015, Zarghami *et al.* 2020). Two sets of flow controllers were placed in the channel between the anode and cathode to generate a W-shaped electrolyte velocity profile. The flow controller has a fixed thickness of 0.2mm. The control parameters in the numerical study are the length (L), spacing (P) and the non-dimensional distance of flow controller to the wall (h), where $h = s/w$ and s represents the distance of the flow controller to the wall, while w denotes the channel width (Figure 5). Note that although the quantity of flow controller pieces varied for different combination of the spacing, the flow controlling length shall cover the entire electrode section. The origin of the coordinate system is at the symmetry axis of the channel, with gravity acting in the negative x-direction. Two groups of different CFD models were simulated in this work: the baseline where the electrolyser was not equipped with flow controller, and the variants where flow controllers were present.

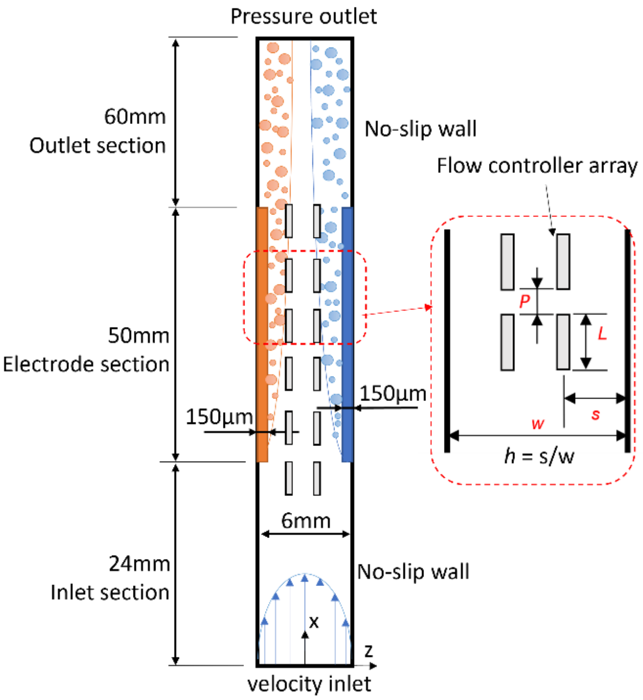

Figure 6-5. A cross-section view of the 3D model on the symmetry plane (y=0).

The system was assumed to be operated at 20 ℃ and 1 atm. A 0.1 wt% NaOH solution was used as the electrolyte. The density, viscosity and surface tension of the electrolyte were assumed ρ_l=1000 kg/m^3, μ_l=1.02 mPa/s and σ_l=0.07 N/m, respectively (Don and Robert 2008). The density of H_2 and O_2 were ρ_{H_2}= 0.07 kg/m^3 and ρ_{O_2}= 1.30 kg/m^3, respectively. Steady, laminar and three-dimensional Eulerian-Eulerian multiphase model was used to study the effect of the flow controller in the electrolyser channel. Three phases were defined for the electrolyte, H_2 and O_2.

The governing continuity equations for the i-*th* phase can be written as:

$$\nabla \cdot (\alpha_i \rho_i \boldsymbol{v}_i) = S_i, \tag{6-1}$$

where α, ρ and $\boldsymbol{v}$ are the volume fraction, density and velocity vector, respectively. The sum of the volume fractions for all phases equals one, i.e., $\sum \alpha_i = 1$. S is the volumetric source term for the mass added into the system. The H_2 and O_2 were added into the system as volumetric mass sources at the thin layer adjacent to the electrode surface. This ensures the initial velocity of these bubbles is zero. Conversely, applying conventional boundary conditions, such as fixed gas superficial velocity, can potentially interfere the propagation of bubble curtain (Hreiz *et al.* 2015, Abdin *et al.* 2017). The flow rate (kg/s) of H_2 and O_2 were calculated according to Faraday's Law (Zhou *et al.* 2020):

$$\dot{m}_{\mathrm{H_2}} = M_{\mathrm{H_2}}\dot{n}_{\mathrm{H_2}} = \frac{IM_{\mathrm{H_2}}}{2\mathrm{F}}, \tag{6-2}$$

$$\dot{m}_{\mathrm{O_2}} = M_{\mathrm{O_2}}\dot{n}_{\mathrm{O_2}} = \frac{IM_{\mathrm{O_2}}}{4\mathrm{F}}, \tag{6-3}$$

where $M_{\mathrm{H_2}}$and $M_{\mathrm{O_2}}$are the molar weight (kg/mol) of H_2 and O_2, respectively. Also I is the current (A), and F is the Faraday constant (96485 c/mol). For the sake of simplicity, it is assumed that both H_2 and O_2 exist solely in the gas phase. Furthermore, the coalescence and breakup of bubbles were not observed in the bubble curtains; therefore, these phenomena were not considered in the scope of this paper. Since the volume fraction of gas phase in the channel was very small (< 1%), the effect of bubbles on the current distribution along the electrodes was neglected (Zarghami *et al.* 2020). Therefore, H_2 and O_2 were assumed to be uniformly released into the channel from the electrodes.

The momentum e for the i-*th* phase is:

$$\nabla\cdot(\alpha_i\rho_i\boldsymbol{u}_i\boldsymbol{u}_i) = -\alpha_i\nabla p + \nabla\cdot\boldsymbol{\tau}_i + \alpha_i\rho_i\boldsymbol{g} + \left(\boldsymbol{F}_{D,i} + \boldsymbol{F}_{SL,i} + \boldsymbol{F}_{td} + \boldsymbol{F}_{VM,i}\right), \tag{6-4}$$

The stress-strain tenor ($\boldsymbol{\tau}$) is defined as:

$$\boldsymbol{\tau}_i = \alpha_i\mu_{m,i}(\nabla\boldsymbol{u}_i + \nabla\boldsymbol{u}_i^T) + \mu_{t,i}(\nabla\boldsymbol{u}_i + \nabla\boldsymbol{u}_i^T) - \frac{2}{3}\rho_i k\mathbf{I}, \tag{6-5}$$

where μ_m is the molecular dynamic viscosity. The dispersed gas phases are assumed to be laminar (Liao *et al.* 2020). The turbulent viscosity (μ_t) and turbulent kinetic energy (k) for the liquid phase are solved by the following turbulent transport equations:

$$\nabla\cdot(\rho_l\boldsymbol{u}_l k_l) = P_l - \beta^*\rho_l k_l\omega_l + \nabla\cdot\left[\left(\mu_{m,l} + \sigma_k\mu_{t,l}\right)\nabla k_l\right], \tag{6-6}$$

$$\nabla \cdot (\rho_l \boldsymbol{u}_l \omega_l) = \frac{\gamma}{\mu_{t,l}} P_k - \beta \rho_l k_l {\omega_l}^2 + \nabla \cdot \left[\left(\mu_{m,l} + \sigma_\omega \mu_{t,l} \right) \nabla \omega_l \right] + (1 - F_l) \frac{2 \rho_l \sigma_{\omega 2}}{\omega_l} \nabla k_l : \nabla \omega_l, \tag{6-7}$$

and the turbulent viscosity ($\mu_{t,l}$) and the production rate of turbulence (P_k) are given as:

$$\mu_{t,l} = \frac{\alpha_1 \rho_l k_l}{\max\left(\alpha_1 \omega_l, S F_2\right)}, \tag{6-8}$$

$$P_k = \min\left(S^2 \mu_{t,l}, 10 \rho_l \beta^* k_l \omega_l\right). \tag{6-9}$$

Here, α_1, β, β^*, γ, σ_k and σ_ω are the standard model constant (ANSYS 2022). F_1 and F_2 are the blending functions, and S is the magnitude of shear strain (Menter 1994).

The forces considered in the model include drag force ($\boldsymbol{F}_D$), shear-induced lift force ($\boldsymbol{F}_L$), turbulent dispersion force ($\boldsymbol{F}_{td}$) and virtual mass force ($\boldsymbol{F}_{VM}$). The drag force due to the electrolyte flow over gas bubbles is expressed as:

$$F_D = \frac{\pi {d_p}^2}{8} \rho_l C_D \left(u_l - u_g\right) \left|u_l - u_g\right|, \tag{6-10}$$

Since the bubbles in the electrolyser were mostly spherical due to their small size and low Ëotvos numbers (Shi *et al.* 2020), Schiller and Naumann (1933) 's relation for the drag coefficient C_D was adopted:

$$C_D = \frac{24}{Re_b} \left(1 + 0.15 Re_b^{0.687}\right), \tag{6-11}$$

where Re_b is the bubble Reynolds number. The shear-induced lift force is calculated based on the Legendre-Magnaudet model (Legendre and Magnaudet 1998):

$$F_L = C_L \rho_l \frac{\pi {d_b}^3}{6} \left(u_l - u_g\right) \times \left(\nabla \times u_l\right), \tag{6-12}$$

where the lift force coefficient is determined by both the Reynolds number of the bubble and the non-dimensional shear rate (Sr) (Legendre and Magnaudet 1998):

$$C_L = \sqrt{\left(\frac{6}{\pi^2}\frac{2.255}{\sqrt{SrRe_b}(1+0.2Re_b/Sr)^{1.5}}\right)^2 + \left(\frac{1}{2}\frac{Re_b+16}{Re_b+29}\right)^2}\ , \tag{6-13}$$

The turbulent dispersion force is calculated according to Burns *et al.* (Burns *et al.* 2004):

$$F_{td} = -\alpha_g \frac{3C_D}{4D_b}\frac{\mu_{t,l}}{Sc}\left|u_l - u_g\right|\left(\frac{1}{\alpha_g}+\frac{1}{\alpha_l}\right)\nabla\alpha_g, \tag{6-14}$$

where the turbulent Schmit number (Sc) is set to 0.9.

The virtual mass force is given by:

$$F_{VM} = \frac{\pi {d_p}^3}{6}\rho_l C_{VM}\left(\frac{d\boldsymbol{u}_l}{dt} - \frac{d\boldsymbol{u}_g}{dt}\right), \tag{6-15}$$

and the virtual mass coefficient (C_{VM}) is set to 0.5 for spherical bubbles (Abdelouahed *et al.* 2014).

The equations above were solved implicitly using pseudo transient method. The Coupled scheme was selected for the pressure-velocity coupling. The momentum and volume fraction are discretised using the QUICK scheme, and the Second-Order scheme was used to discretise the pressure gradient.

A fully developed laminar flow profile was applied to the channel inlet, and a constant pressure was set to the channel outlet. The other boundaries of the channel were set as no-slip walls. The ranges of the Reynolds numbers of the electrolyte and the current density used in this study were 45 – 510 and 0.1-0.58 A/cm^2, respectively.

The electrolyser channel was meshed with hexahedral structured cells created by Ansys meshing. In the channel stream wise direction (x-direction), mesh sizes of 0.5mm and 0.2mm were applied at the inlet and outlet section, and electrode section, respectively. For the channel span wise direction (y-direction), a 0.125 mm of mesh size was applied to the entire domain. The mesh size for the volumetric mass source cells was set to 0.03 mm in the channel transverse direction (z-direction).

A mesh dependency study was carried out by choosing different refinement for three subchannels in the electrode section in the channel width direction (z-direction). Figure 6-6a shows the dependence of the average liquid phase volume fraction at the outlet of electrode section (x=74 mm) to the number of nodes in the x-direction within the sub-channel (N_i) for a current density (i) of 0.1 A/cm^2 and an electrolyte flow Reynolds number (Re) of =360. As can be seen, the deviations in the volume fraction for N_i larger than 18 is less than 1%. For the sake of computational efficiency, N_i=18 is adopted for this study. It is also found that the refinement for the leading edge of the flow controller has little effect on the overall flow field. Therefore, a mesh size of 0.04 mm was set to the leading edge of the flow controller. A detailed slice view of the numerical mesh at Y=0 plane is shown in Figure 6-6b.

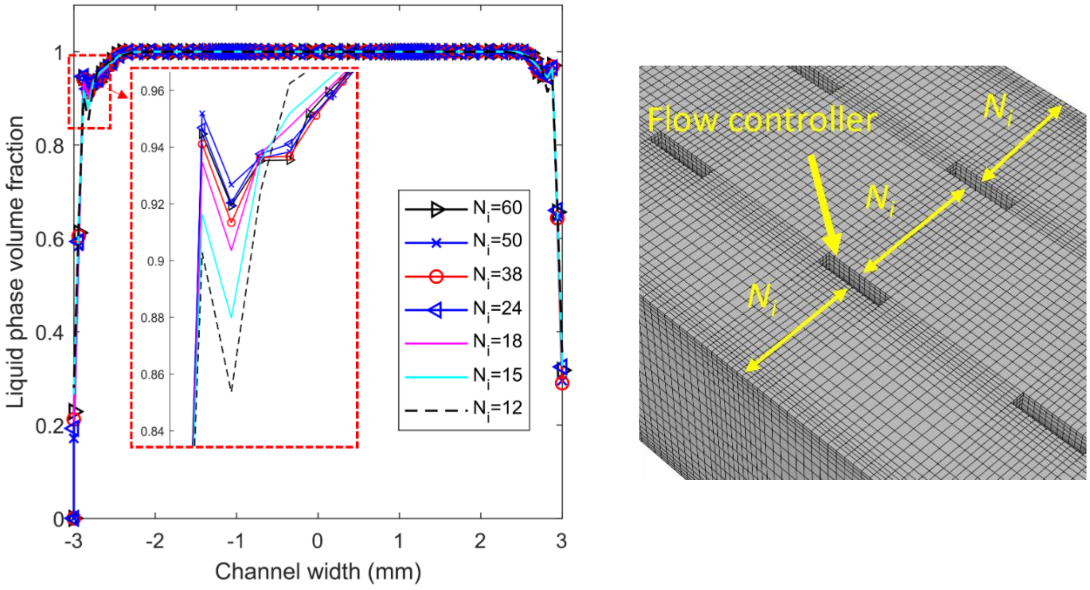

(a) (b)

Figure 6-6. (a) Average fluid phase volume fraction at x=74 mm for i=0.1 A/cm^2 and Re=360 for various number of nodes in the x-direction within the sub-channel. (b) Detailed slice view of the numerical mesh at Y=0 plane.

6.2.2.2 Experimental setup

A test rig was developed in this work, as shown in Figure 6-7. The experiment setup includes the proposed MFE, an electrolyte tank, a pump, valves, piping and two sets of DC power supplies, as shown in Figure 6-7a. A 0.1 wt% NaOH solution is used as the electrolyte. A lab-scale MFE with a 6 mm×6 mm×220 mm square channel was fabricated from clear acrylic to allow the optical access for flow visualisation purposes, as shown in Figure 6-7b. The two nickel electrodes were installed 6mm apart in parallel. The electrodes are located 150mm upstream from the inlet of MFE channel. During the experiment, the electrolyser cell was positioned vertically. The voltage applied to the electrolyser was controlled by a power supply (DC1), and the current was measured using a digital multimeter. The volumetric flow rate (m^3/s) of H_2 was calculated according to Faraday's Law (Zhou *et al.* 2020). The flow rate in the channel was controlled by the valves as well as the power supply of the pump

(DC2). The maximum Reynolds number of the electrolyte was set at 400 to ensure the flow was fully developed at the entrance of electrode section.

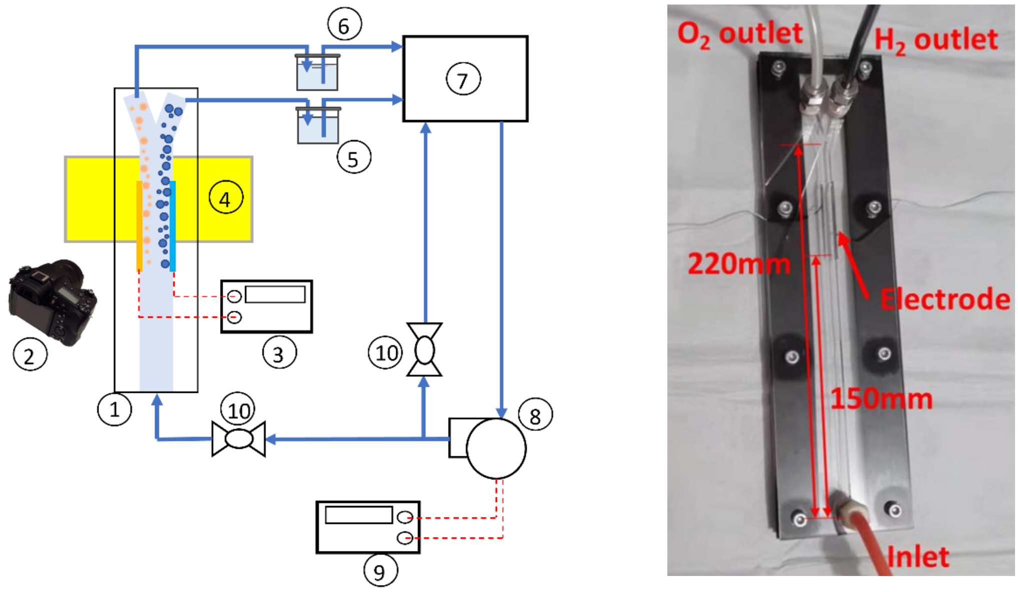

(a) (b)

Figure 6-7. (a) A block diagram of the experimental setup used in this study: 1- Membrane-free water electrolyser, 2- Camera, 3- Power supply DC1, 4- LED backlight, 5- Gas/liquid separator (H_2), 6- Gas/liquid separator (O_2), 7- Electrolyte tank, 8- Pump, 9- Power supply DC2, 10- Valves, and (b) Photo of the membrane-free water electrolyser.

6.2.2.3 Validation

The MFE without flow controller was used for validation of the numerical model. For flow visualisation, a camera (SONY RX10IV) was set such it is focused on the centreline of the channel. The camera is equipped with a macro lens (Raynox m250) to achieve a field of view of approximately 0.5mm depth and 15mm×9.8mm area. Since the electrolyte velocity and the bubble velocity were different in the electrolyser channel, the velocity fields of the electrolyte and the bubbles in the channel were measured using Particle Shadow Velocimetry (PSV) (Khodaparast *et al.* 2013, Pang *et al.* 2020). Hollow glass microspheres (10 μm) were added to the electrolyte as the tracers, and a continuous LED backlight was used to illuminate the particles and bubbles. The tracers and bubbles were recorded by the camera at 500 fps with a pixel size of approximately 10 µm (Figure 6-8). The videos were taken at three locations: at the inlet, middle and outlet of the electrode section.

PIVLab software was used to calculate the velocity distribution of the two-phase flow from the video frames using cross-correlation techniques (Raffel 2018, Thielicke. and Sonntag. 2021). For each operating condition, over 1000 video frames were collected. A representative snapshot from these frames is provided in Figure 8a. To get the velocity of the electrolyte, a small interrogation window (IW) (32×32 pixels) was used. The small window size ensures that the bubbles are not captured so their effect on the calculated velocity field are minimised. On the other hand, large IW (128×128 pixels) was chosen to calculate the velocity of bubbles near the electrodes. The video frames were also processed using an in-house developed code in MATLAB to identify the bubbles using Circular Hough Transform (CHT) based algorithm (Yuen, Princen *et al.* 1990, Atherton and Kerbyson 1999, Davies 2005), as shown in Figure 6-8b. The bubble size distribution is shown in Figure 9. As can be seen, the average bubble diameter is about 0.15 mm.

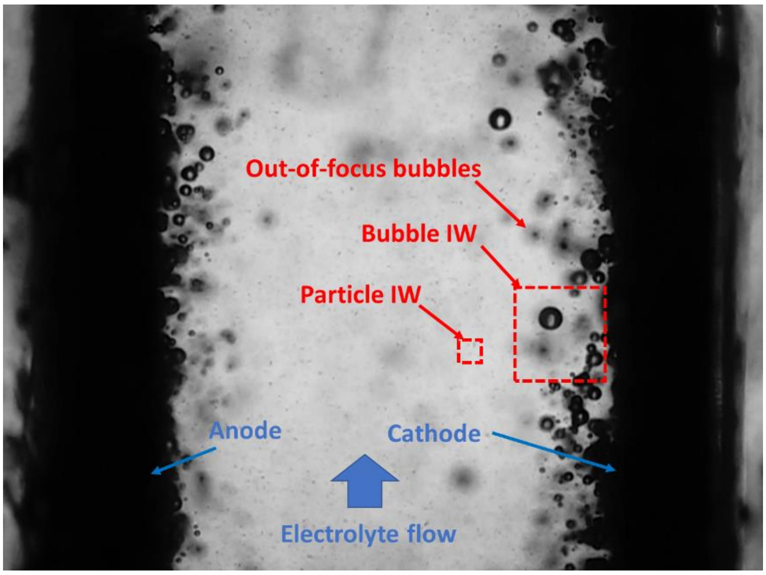

(a)

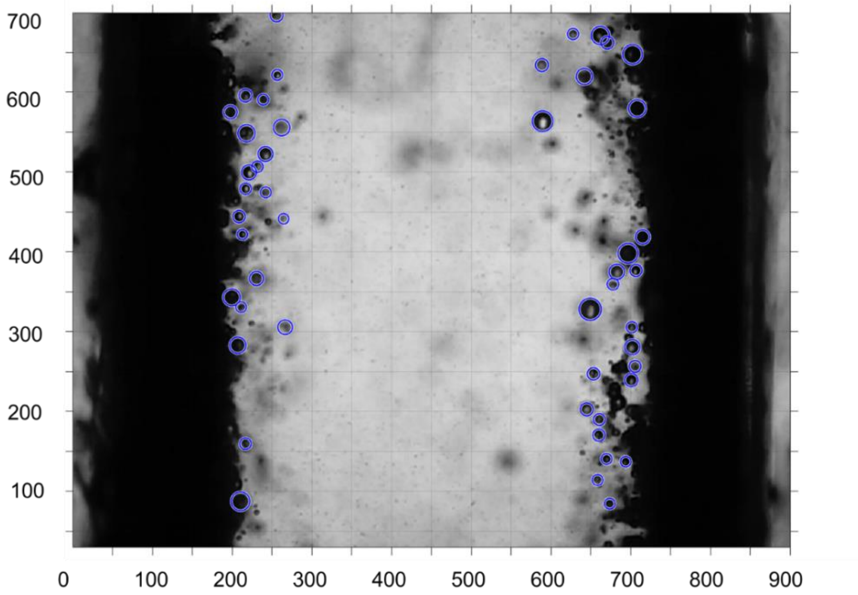

(b)

Figure 6-8. Examples of (a) shadow image of MFE for calculating velocity field using cross-correlation technique and (b) identified bubbles using CHT method. The images were obtained at 0.2 A/cm^2 and Re = 200.

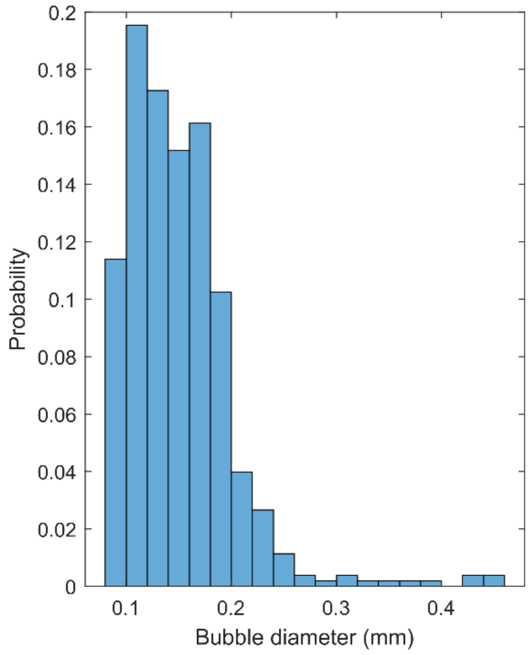

Figure 6-9. Probability density distribution of diameter of bubbles generated from the experimental rig in this work.

The bubble detection algorithm also calculated the distribution of bubbles in the MFE channel, which were subsequently used to determine the bubble curtain thickness. Figure 6-10 shows the thickness of bubble curtain and electrolyte velocity derived from both the CFD simulation and the experimental results at j=0.4 A/cm^2 and various flow Reynolds numbers. Analysis reveals that 98% of the fluid phase volume fraction, as determined by the CFD simulations, aligns with the bubble curtain thickness observed in experiments (as shown in Figure 6-10a). Also, the velocity profile of the electrolyte near the electrode matches the experimental data, showing a maximum deviation of less than 15% (Figure 6-10b).

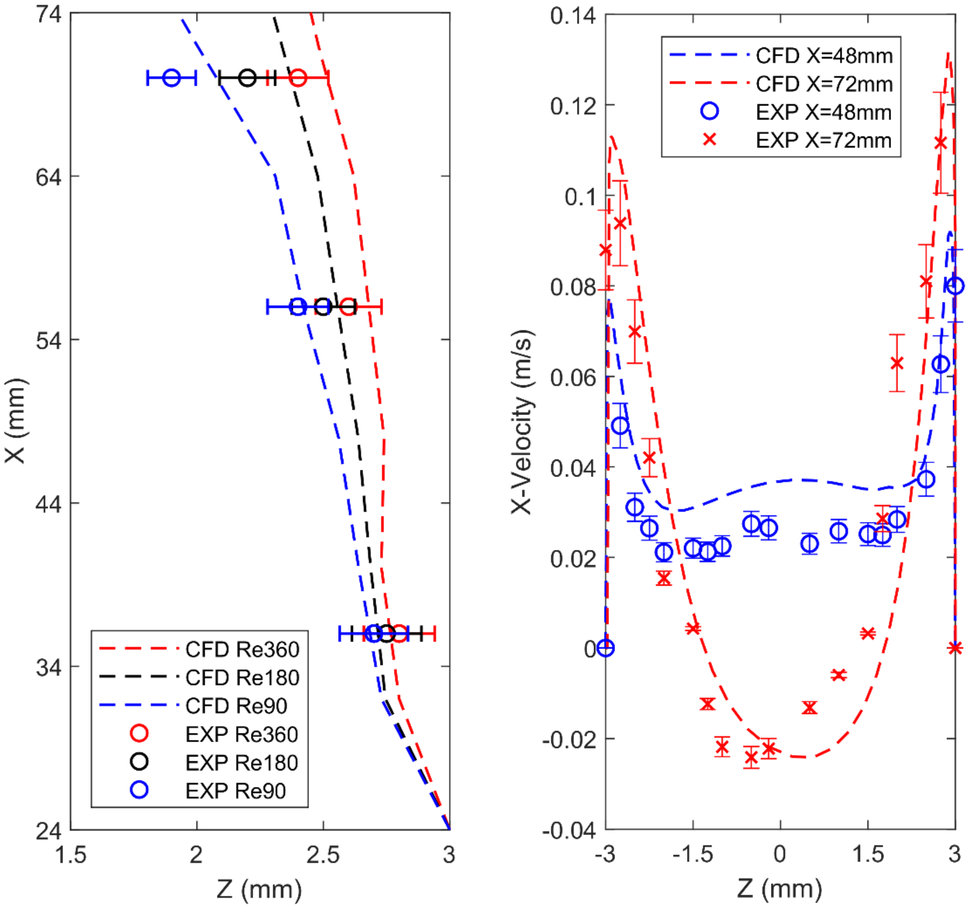

(a) (b)

Figure 6-10. Comparison between CFD and experimental result for (a) the effect of Reynolds number on H_2 bubble curtain thickness under *j*=0.4 A/cm^2, and (b) the electrolyte velocity profiles at X=48 mm and X=72 mm under Re=180 and *j*=0.4 A/cm^2.

In vertical flow-by MFE, H_2 is produced about twice as much as O_2. Therefore, managing H_2 bubble curtain thickness is the key to prevent gas crossover (Lee *et al.* 2019, Zarghami *et al.* 2020).

6.2.3 Numerical results

6.2.3.1 Effect of flow Reynolds number

Figure 6-11a and 6-11b show the estimated thickness of O_2 and H_2 bubble curtains, respectively. The MFE is operated at *j*=0.4 A/cm^2 and various flow

Reynolds numbers (Re) for the variants, where the 1 mm-long flow controllers are set at h=0.15 and spaced 4mm apart. The results show that with the increase of Re, the thickness of both O_2 and H_2 bubble curtains reduce. The reasons are not only because bubbles leave the channel faster due to an increased rising velocity, but also a stronger shear-induced lift force generated at higher Re that restrict bubble transverse movement. The result for the baseline with no flow controller is also provided for comparison. It is clear that the presence of flow controller effectively limits the thickening of the bubble curtain. For example, at Re =180, the H_2 bubble curtain grows to a thickness of about 0.85 mm at the outlet of the electrode section (X=74 mm) when the flow controllers are absent. While it is reduced to 0.47 mm with flow controllers in place under the same operating conditions.

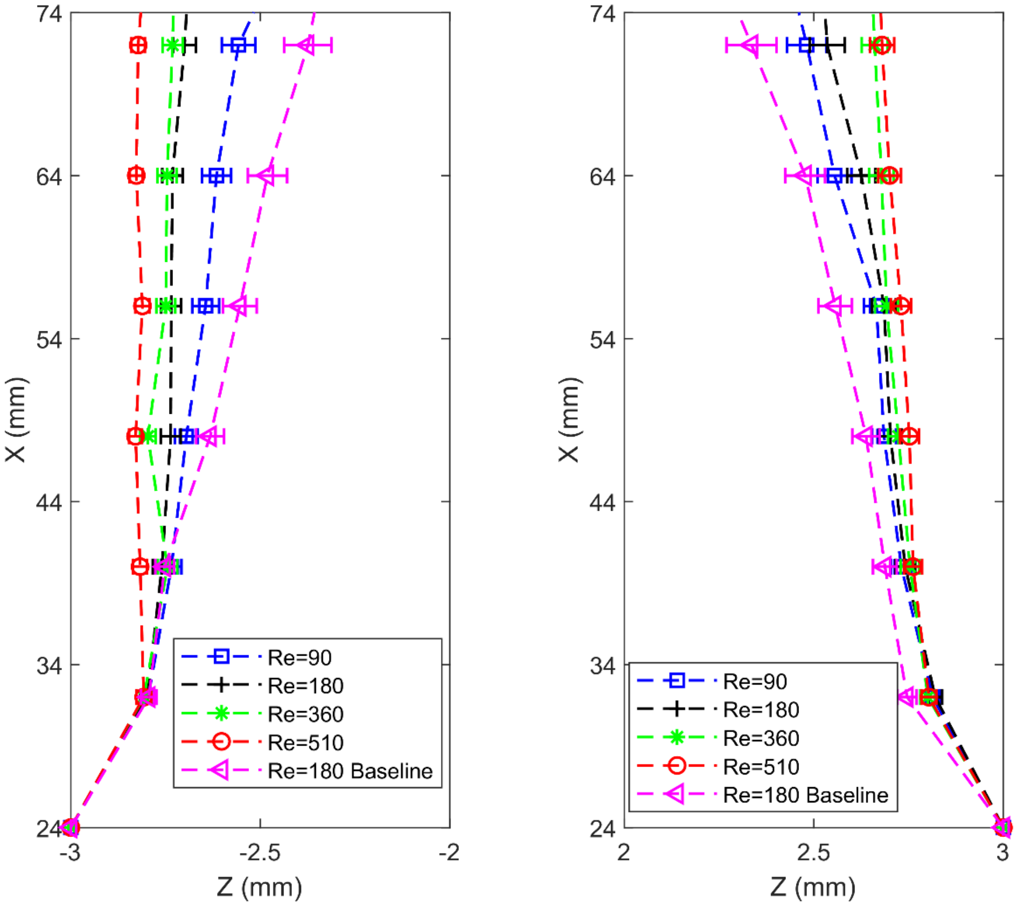

(a) (b)

Figure 6-11. CFD results of bubble curtain thickness for (a) O_2 and (b) H_2. The MFE was operated at j=0.4 A/cm^2 and various flow Reynolds numbers. The parameters for the flow controller are: L=1 mm, P=4 mm and h=0.15.

6.2.3.2 Effect of current density

Figure 6-12 shows the dependence of calculated O_2 and H_2 bubble curtain thickness for the baseline and the variants equipped with 1 mm-long flow controllers set at h=0.15 with spaced at 4 mm apart. The simulation is conducted under a flow Reynolds number of 180 and at various current densities. The results show that with the increase of current density, the thickness of bubble curtain increases. Also, H_2 bubble curtain presents a higher growth rate than that of O_2 bubble curtain. Specifically, as current density increases from 0.1 A/cm^2 to 0.4 A/cm^2, the thickness of O_2 bubble curtain increases from 0.24 mm to 0.32 mm, whereas the thickness of H_2 bubble curtain exhibit a more pronounced growth, expanding from 0.26 mm to 0.47 mm.

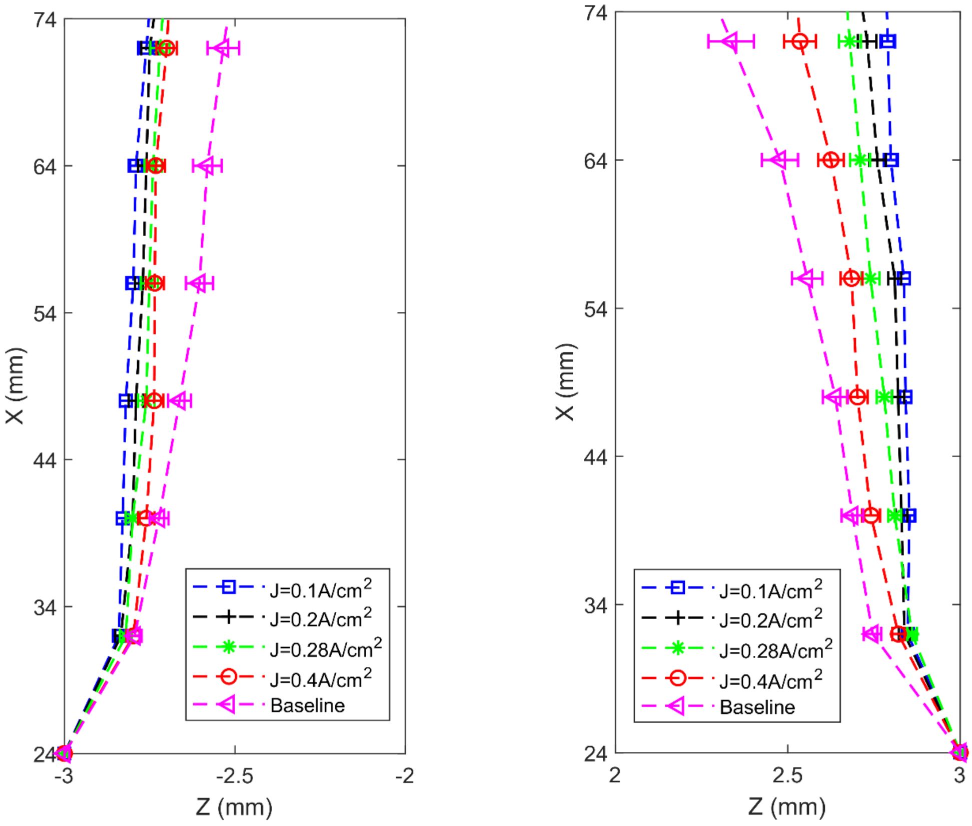

(a) (b)

Figure 6-12. Calculated thickness for (a) O_2 and (b) H_2 bubble curtains. The MFE was operated at Re=180 and various current densities. The parameters for the flow controller are: L=1 mm, P=4 mm and h=0.15.

6.2.3.3 Effect of flow controller geometry

6.2.3.3.1 Positioning of flow controller

Figure 6-13 shows the thickness of bubble curtains for the MFE operated at j=0.4 A/cm^2 and under a flow Reynolds number of 180. In these variants, the 1 mm-long flow controllers are spaced 4mm apart, with different values of h. The results show that when h is reduced from 0.28 to 0.15, there is a corresponding decrease in bubble curtain thickness. This is because moving the flow controller towards the wall can direct more flow towards the channel centre. This results in a more pronounced velocity gradient, facilitating enhanced bubble separation. The optimum h is about 0.15, where the bubble curtain is at its thinnest. However, further reducing h causes an increase in the bubble curtain thickness. For instance, when h is reduced from 0.15 to 0.1, the H_2 bubble curtain thickness is increased from 0.32 mm to 0.56 mm at X=72 mm. This phenomenon can also be observed from the contour plots of the liquid phase at the top of electrode section, as shown in Figure 6-14. The results indicate that the flow controller should be located at a specific distance from the wall, preventing bubbles from escaping towards the channel centre.

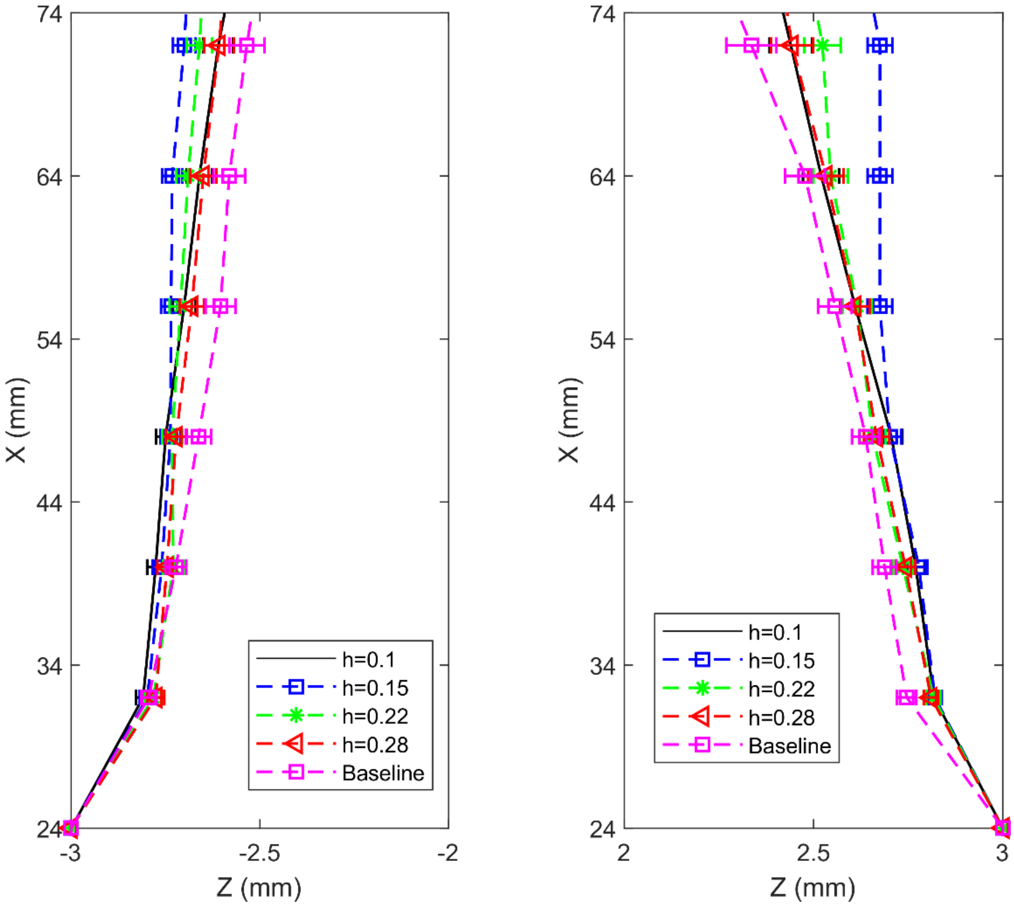

(a) (b)

Figure 6-13. Bubble curtain propagation along the electrode for (a) O_2 and (b) H_2. The MFE is operated at j=0.4 A/cm^2 and Re=180, with 1 mm-long flow controllers installed at 4 mm apart and various h values.

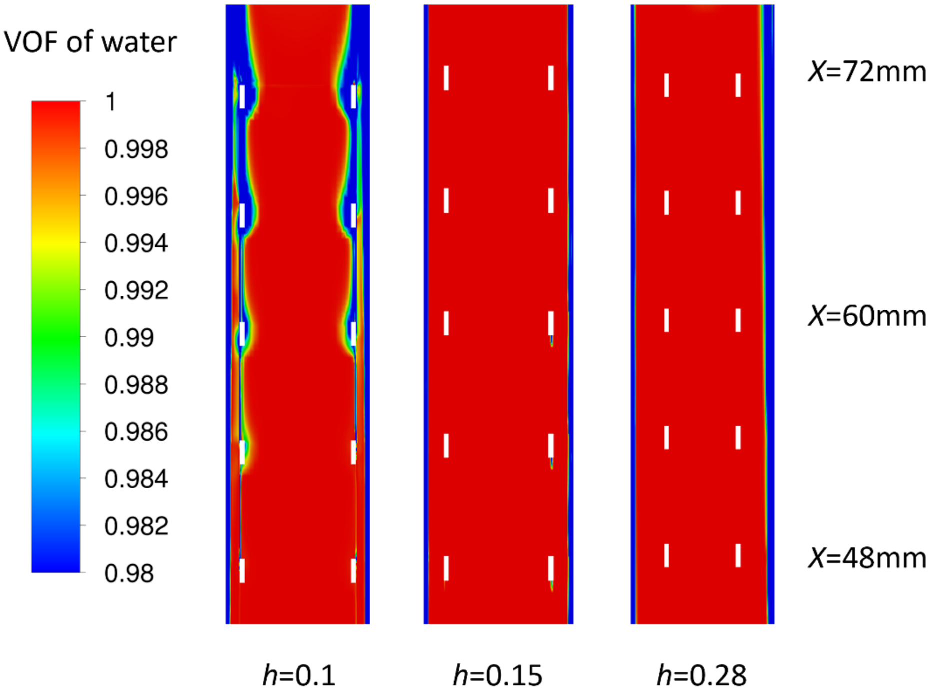

Figure 6-14. Effect of h on the liquid phase volume fraction at the top of electrode section.

6.2.3.3.2 Spacing

Figure 6-15 shows the dependence of the propagation of bubble curtain thickness along the electrode on the spacing of flow controllers (P). The results reveal that the bubble curtain thickness grows with the increase of flow controller spacing. This occurs because wider spacing between flow controllers results in less effective flow regulation, thereby diminishing the efficacy of the flow controllers. Furthermore, when the flow controllers are spaced at intervals of 8mm apart, they lose their effectiveness in controlling bubble distribution within the MFE. The contour plots of the liquid phase at the top of electrode section are shown in Figure 6-16.

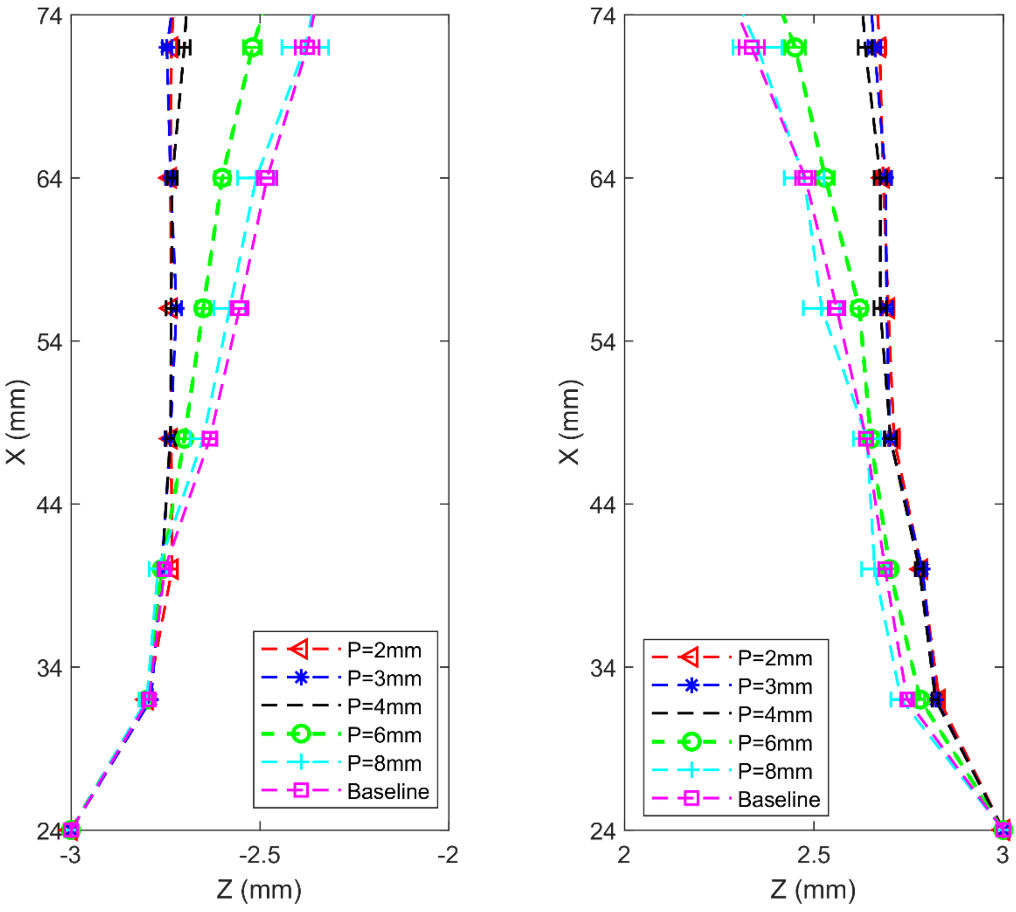

(a) (b)

Figure 6-15. Numerical results for the (a) O_2 and (b) H_2 bubble curtain thickness along the electrode with different flow controllers spacing and h=0.15. The electrolyser cell is operated at j =0.4 A/cm^2 and Re =180.

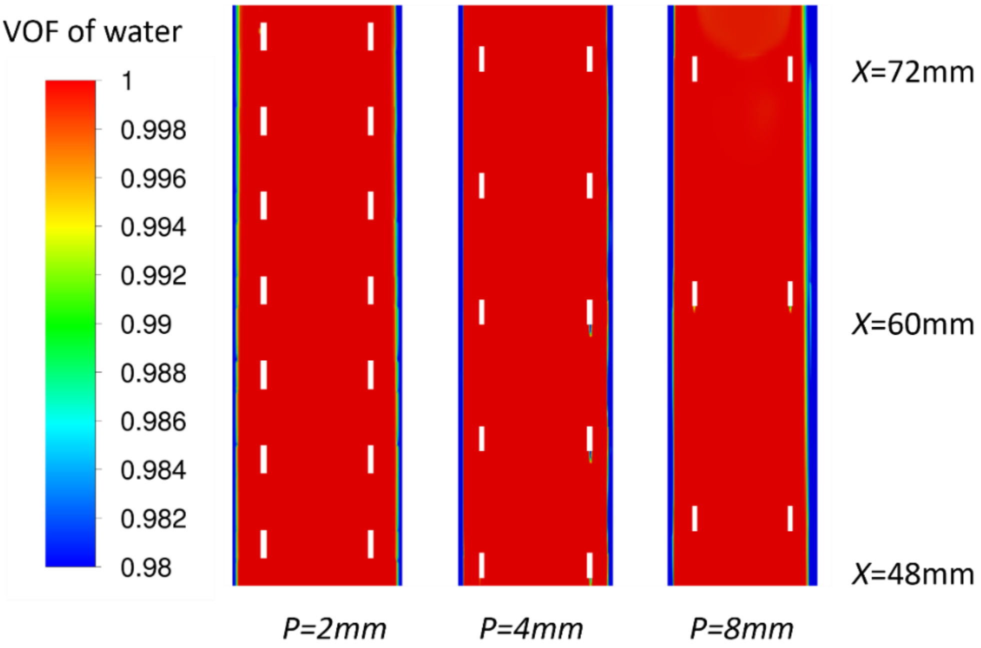

Figure 6-16. Impact of flow controller spacing (P) on the liquid phase volume fraction at the top of electrode section.

6.2.3.3.3 Length

Figure 6-17 presents the thickness of O_2 and H_2 bubble curtains for the MFE operated at j =0.4 A/cm^2 and Re =180. Flow controllers, with a length (L) varying from 1 mm to 4 mm, were positioned at h=0.15 with a spacing of 4mm. The results indicate that increasing L leads to a reduction in the thickness of both O_2 and H_2 bubble curtains. However, the rate of reduction of the thickness of both curtains appears to plateau as L approaches 2 mm. This suggests that increasing L beyond this point may inadvertently increase ohmic overpotential without substantial benefits in reducing bubble crossover. Consequently, it is crucial to fine-tune the length of the flow controller to achieve compromise between minimising bubble crossover and preserving high cell efficiency.

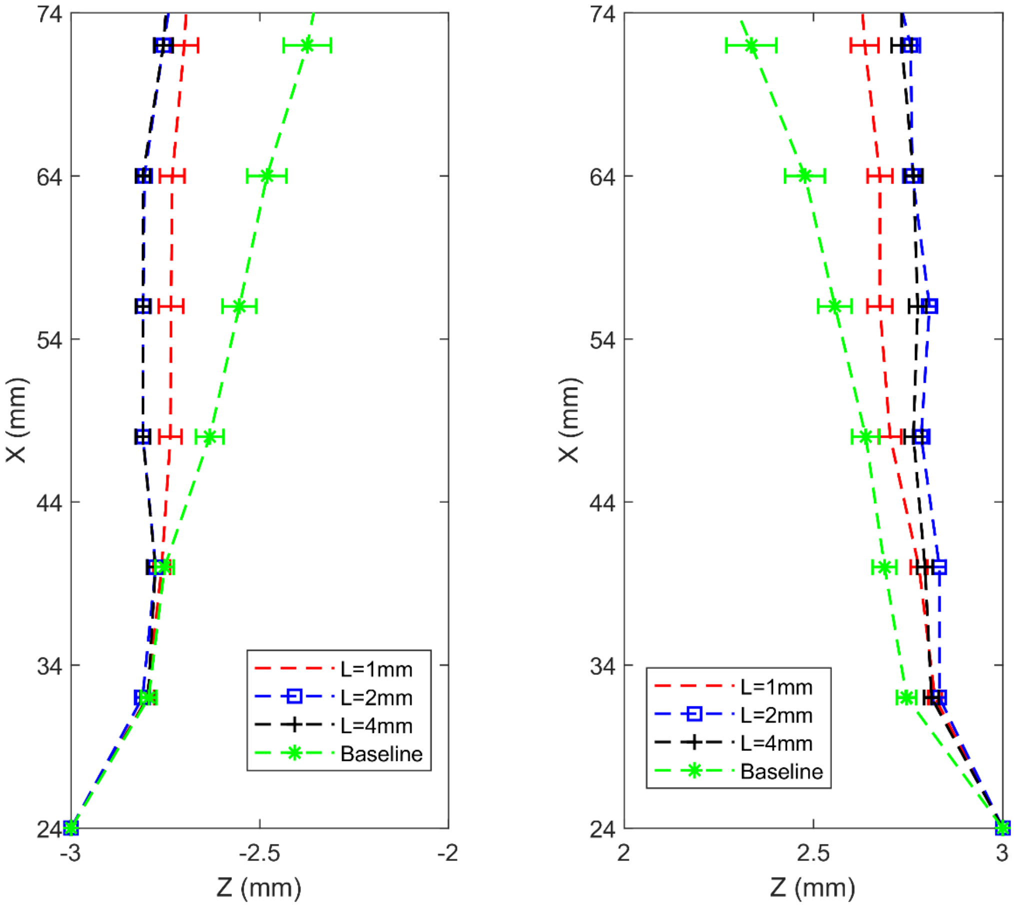

(a) (b)

Figure 6-17. Calculated thickness of (a) O_2 and (b) H_2 bubble curtains in the MFE operated at j =0.4 A/cm^2 and Re =180. The flow controllers have a spacing of 4 mm and h=0.15.

6.2.4 Discussion

6.2.4.1 Flow velocity profile

The primary objective of the flow controllers in the vertical flow-by membrane-free water electrolyser (MFE) is to sustain the W-shaped electrolyte velocity profile. This design leverages the positive velocity gradient at the channel centre to produce the shear-induced lift force on bubbles in the wall direction. Figure 6-18 provides a comparison of the electrolyte velocity profiles for the electrolyser with (dashed line) and without (solid line) flow controllers across varying X values. The simulation is conducted for j =0.05 A/cm^2 and under a flow Reynolds number of 180. The parameters for the flow controller were set at P=4 mm and h=0.36. From the results, it's evident that in the absence of a flow controller, the electrolyte velocity at the channel's centre diminishes significantly as X increases. The positive velocity gradient vanishes past X=59 mm, which results in the electrolyte losing its ability to control the bubble's transverse movement towards the channel centre. However, with the introduction of flow controllers, the W-shaped velocity profile at the channel centre is retained, which is crucial to prevent bubble crossover.

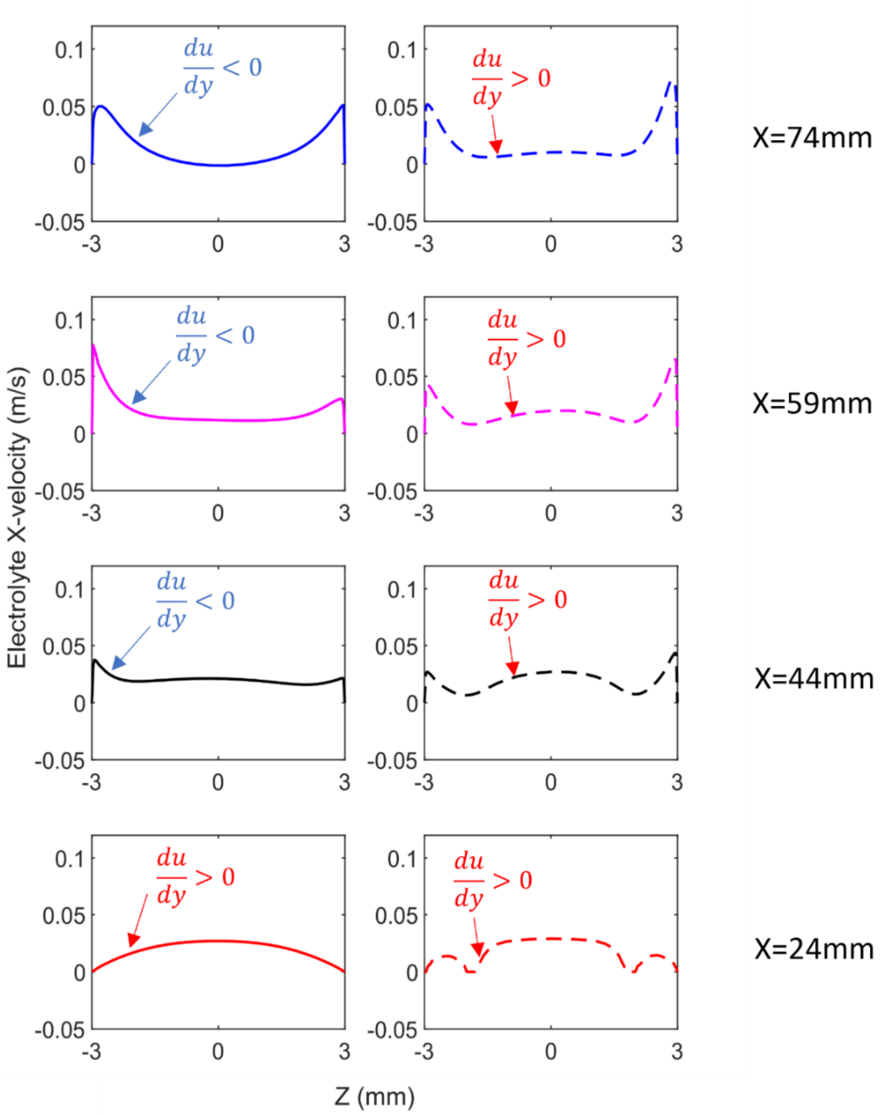

Figure 6-18. Numerical result for the electrolyte X-velocity at different electrode length (H) for the electrolyser with (dashed line) and without (solid line) flow controller.

6.2.4.2 Experiment of prototype flow controller

The CFD simulation demonstrates that the flow controlling technique can effectively mitigate gas crossover in an MFE. To assess the influence of the flow controller on cell efficiency, prototypes were 3D-printed from ABS plastic with a wall thickness of 0.4 mm. To facilitate installation, additional parts have been added to the flow controllers to join them as one single piece, as depicted in Figure 6-19a. Subsequently, the flow controller was integrated into the electrolyser rig, as detailed in section 6.2.2.3 (Figure 6-19b).

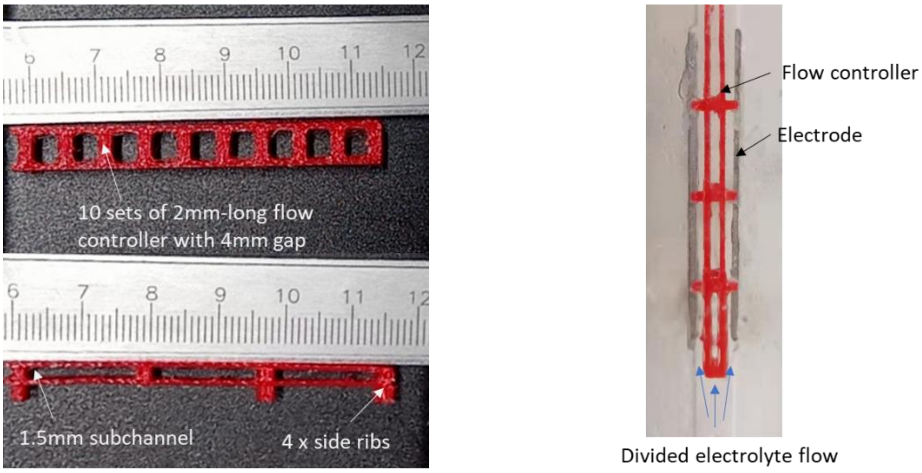

(a) (b)

Figure 6-19. (a) Structure of the prototype flow controller and (b) the MFE installed with a flow controller.

The electrolyser rig was tested at Reynolds numbers of 100, 200 and 400 and at various applied current densities. Figure 6-20 shows the distribution of electrolytic bubbles at the exit of electrode section of the MFE. It was found that, without flow controller, gas crossover can occur at low Reynolds numbers (Re <120) and elevated current densities (j > 0.2 A/cm^2). However, with the installation of flow controller, no gas crossover was observed.

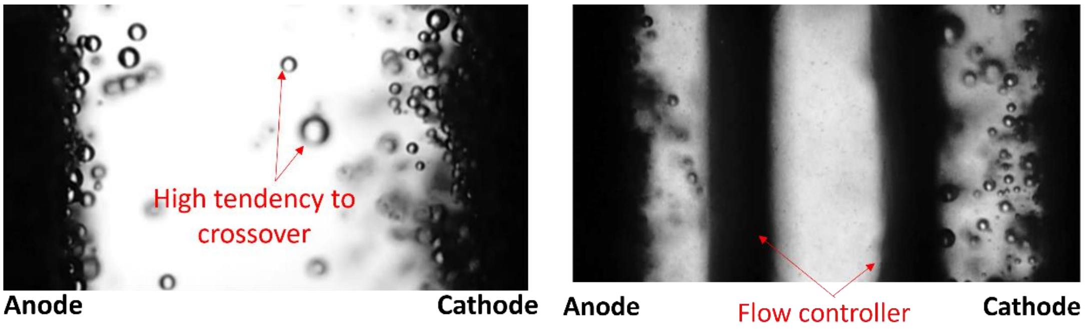

(a) (b)

Figure 6-20. Comparison of bubble distribution at the exit of electrode section of the MFE for the (a) baseline and (b) MFE equipped with flow controllers. The MFE was operated at Re =100 and j = 0.2 A/cm^2.

Figure 6-21 shows the polarisation curve for both the baseline — the electrolyser without a flow controller — and the variants, which include the flow controllers. Although the non-conductive flow controller introduced certain electrical resistance between the electrodes, the cell voltage for the test case was marginally lower than the base case. This indicates that the flow controller has limited impact on the performance of the MFE. Possible reasons for this include: the flow controller increasing the flow velocity in the subchannels and, as a result, facilitating bubble departure due to the amplified drag force; the textured surface of the flow controller generating local turbulence in the electrolyte, which boosts ionic mass transport.

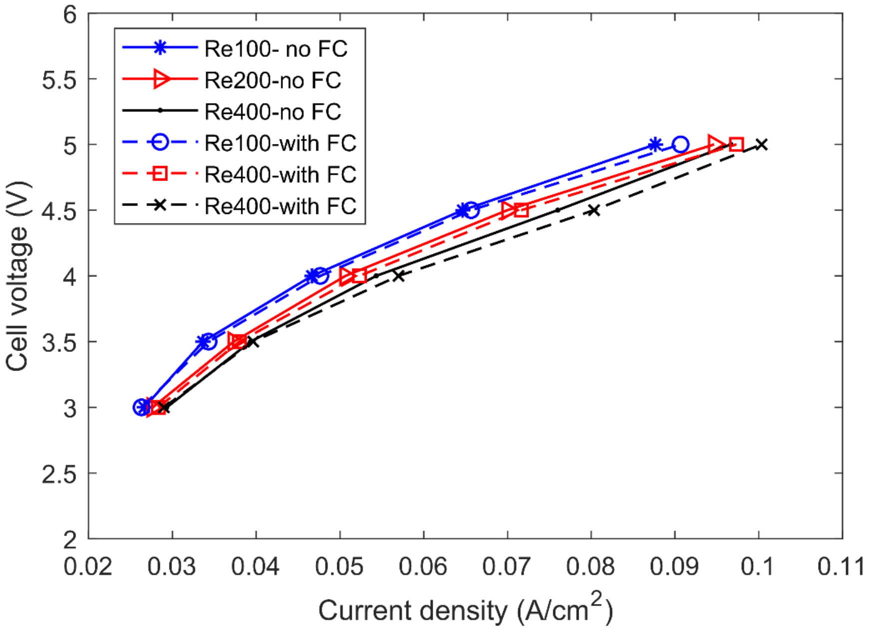

Figure 6-21. Polarisation curve for the MFE operated under various flow Reynolds numbers with and without flow controller.

The proposed flow controller has the potential to alleviate crossover in an MFE by generating a tailored flow field. This ensures that the shear-induced lift force on the bubbles directs them toward the electrode where they evolve. It is conceivable that enhancements in fabrication quality and installation accuracy could significantly improve the performance of the flow controller. However, such optimisation falls beyond the scope of this work.

While implementing flow controllers can potentially improve the purity of product H_2, it is crucial to acknowledge a key consideration for an optimised MFE – the reduction of the gap between electrodes. As the electrode gap decreases, the influence of flow controllers on pumping power and overall cell performance becomes a critical factor that demands careful consideration.

6.2.5 Conclusion

This paper proposed a new concept to reduce gas crossover in an MFE. This is achieved through the implementation of a flow controller, comprising an array of thin plates. Numerical study found that the flow controller can preserve the W-shaped velocity profile of the electrolyte, which is essential in harnessing the shear-induced lift force to effectively manage bubble distribution in an MFE. The simulation results show that properly positioned flow controllers can remarkably supress the propagation of both O_2 and H_2 bubble curtains. This indicates the application of flow control technique can potentially increase the electrode length for the same gap in a vertical MFE, facilitating its scaling up.

Preliminary testing on a prototype flow controller shows that the proposed design can successfully mitigate gas crossover in a vertical flow-by membrane-free electrolyser without compromising the cell efficiency. Enhancing the fabrication and installation quality of the flow controller could offer potential for better performance.

References

Abbasi, R., B. P. Setzler, S. Lin, J. Wang, Y. Zhao, H. Xu, B. Pivovar, B. Tian, X. Chen, G. Wu and Y. Yan (2019). A roadmap to low-cost hydrogen with hydroxide exchange membrane electrolyzers. Advanced Materials **31**(31): e1805876.

Abdelouahed, L., R. Hreiz, S. Poncin, G. Valentin and F. Lapicque (2014). Hydrodynamics of gas bubbles in the gap of lantern blade electrodes without forced flow of electrolyte: Experiments and CFD modelling. Chemical Engineering Science **111**: 255-265.

Abdin, Z., C. J. Webb and E. M. Gray (2017). Modelling and simulation of an alkaline electrolyser cell. Energy **138**: 316-331.

Aoyama, S., K. Hayashi, S. Hosokawa, D. Lucas and A. Tomiyama (2017). Lift force acting on single bubbles in linear shear flows. International Journal of Multiphase Flow **96**: 113-122.

Atherton, T. J. and D. J. Kerbyson (1999). Size invariant circle detection. Image and vision computing **17**(11): 795-803.

Bui, J. C., J. T. Davis and D. V. Esposito (2020). 3D-Printed electrodes for membraneless water electrolysis. Sustainable Energy & Fuels **4**(1): 213-225.

Davies, E. R. (2005). Machine Vision: Theory, Algorithms, Practicalities. Burlington, Elsevier Science & Technology.

Don, W. G. and H. P. Robert (2008). Perry's Chemical Engineers' Handbook, Eighth Edition. New York, McGraw-Hill Education.

Esposito, D. V. (2017). Membraneless electrolyzers for low-cost hydrogen production in a renewable energy future. Joule **1**(4): 651-658.

Gillespie, M. I., F. van der Merwe and R. J. Kriek (2015). Performance evaluation of a membraneless divergent electrode-flow-through (DEFT) alkaline electrolyser based on optimisation of electrolytic flow and electrode gap. Journal of Power Sources **293**: 228-235.

H. Hashemi, S. M., P. Karnakov, P. Hadikhani, E. Chinello, S. Litvinov, C. Moser, P. Koumoutsakos and D. Psaltis (2019). A versatile and membrane-less electrochemical reactor for the electrolysis of water and brine. Energy & Environmental Science **12**(5): 1592-1604.

H. Hashemi, S. M., M. A. Modestino and D. Psaltis (2015). A membrane-less electrolyzer for hydrogen production across the pH scale. Energy & Environmental Science **8**(7): 2003-2009.

Hreiz, R., L. Abdelouahed, D. Fünfschilling and F. Lapicque (2015). Electrogenerated bubbles induced convection in narrow vertical cells: A review. Chemical Engineering Research and Design **100**: 268-281.

Hreiz, R., L. Abdelouahed, D. Fünfschilling and F. Lapicque (2015). Electrogenerated bubbles induced convection in narrow vertical cells: PIV measurements and Euler–Lagrange CFD simulation. Chemical Engineering Science **134**: 138-152.

Khodaparast, S., N. Borhani, G. Tagliabue and J. R. Thome (2013). A micro particle shadow velocimetry (μPSV) technique to measure flows in microchannels. Experiments in Fluids **54**(2): 1474.

Lee, J. W., D. K. Sohn and H. S. Ko (2019). Study on bubble visualization of gas-evolving electrolysis in forced convective electrolyte. Experiments in Fluids **60**(10): 156.

Legendre, D., C. Colin and T. Coquard (2008). Lift, drag and added mass of a hemispherical bubble sliding and growing on a wall in a viscous linear shear flow. Philos Trans A Math Phys Eng Sci **366**(1873): 2233-2248.

Legendre, D. and J. Magnaudet (1998). The lift force on a spherical bubble in a viscous linear shear flow. Journal of Fluid Mechanics **368**: 81-126.

Manzotti, A., E. Quattrocchi, A. Curcio, S. C. T. Kwok, M. Santarelli and F. Ciucci (2022). Membraneless electrolyzers for the production of low-cost, high-purity green hydrogen: A techno-economic analysis. Energy Conversion and Management **254**: 115156.

O'Neil, G. D., C. D. Christian, D. E. Brown and D. V. Esposito (2016). Hydrogen production with a simple and scalable membraneless electrolyzer. Journal of The Electrochemical Society **163**(11): F3012-F3019.

Paidar, M., V. Fateev and K. Bouzek (2016). Membrane electrolysis—History, current status and perspective. Electrochimica Acta **209**: 737-756.

Raffel, M. (2018). Particle Image Velocimetry: A Practical Guide. Cham, Springer International Publishing.

Rodríguez, J. and E. Amores (2020). CFD modeling and experimental validation of an alkaline water electrolysis cell for hydrogen production. Processes **8**(12): 1634.

Segré, G. and A. Silberberg (1961). Radial particle displacements in poiseuille flow of suspensions. Nature **189**(4760): 209-210.

Shi, P. and R. Rzehak (2019). Lift forces on solid spherical particles in unbounded flows. Chemical Engineering Science **208**: 115145.

Shi, P., R. Rzehak, D. Lucas and J. Magnaudet (2020). Hydrodynamic forces on a clean spherical bubble translating in a wall-bounded linear shear flow. Physical Review Fluids **5**(7): 073601.

Swiegers, G. F., A. L. Hoang, A. Hodges, G. Tsekouras, C.-Y. Lee, K. Wagner and G. Wallace (2022). Current status of membraneless water electrolysis cells. Current Opinion in Electrochemistry **32**: 100881.

Thielicke., W. and R. Sonntag. (2021). Particle image velocimetry for MATLAB: accuracy and enhanced algorithms in PIVlab. Journal of Open Research Software **9**(1): 12.

Vincent, I. and D. Bessarabov (2018). Low cost hydrogen production by anion exchange membrane electrolysis: A review. Renewable and Sustainable Energy Reviews **81**: 1690-1704.

Yang, B., M. Jafarian, N. Freidoonimehr and M. Arjomandi (2022). Trajectory of a spherical bubble rising in a fully developed laminar flow. International Journal of Multiphase Flow **157**: 104250.

Yuen, H. K., J. Princen, J. Illingworth and J. Kittler (1990). Comparative study of Hough Transform methods for circle finding. Image and vision computing **8**(1): 71-77.

Zarghami, A., N. G. Deen and A. W. Vreman (2020). CFD modeling of multiphase flow in an alkaline water electrolyzer. Chemical Engineering Science **227**: 115926.

Zhou, D., P. Li, W. Xu, S. Jawaid, J. Mohammed‐Ibrahim, W. Liu, Y. Kuang and X. Sun (2020). Recent advances in non‐precious metal‐based electrodes for alkaline water electrolysis. ChemNanoMat **6**(3): 336-355.

Zohuri, B. a. (2019). Hydrogen energy challenges and solutions for a cleaner future, Springer International Publishing : Imprint: Springer.

Chapter 7

Conclusion and future work

This thesis aims to develop knowledge about bubble behaviour in a membrane-free water electrolysers (MFE) and the technique of using flow control to mitigate gas crossover in an MFE. The thesis started by reviewing the recent developments in H_2 energy, water electrolysers, and bubble behaviour in an MFE. It then demonstrated the feasibility of using MFE for industrial-scale liquid H_2 production. The thesis also investigated bubble formation and departure from a microelectrode bubble generator, the forces acting on a free rising bubble in an electrolyser channel, and the effect of bubble diameter and flow field on the distribution of bubbles in an MFE. Finally, the technique of using a flow controller for bubble management in an MFE was developed.

7.1 Industrial application for membrane-free water electrolyser

Membrane-free water electrolyser (MFE) is a novel electrolyser cell design with the advantages of low cost, improved efficiency and capability to operate at elevated temperatures and pressures. The disadvantage of MFE, compared to the conventional alkaline water electrolyser (AWE), is its low H_2 purity levels due to the lack of a membrane to physically separate O_2 and H_2.

As detailed in Chapter 3, this research demonstrates that MFE is a promising alternative H_2 source for liquid H_2 (LH_2) production. This chapter develops mathematical and simulation models to study H_2 generation through AWE and MFE. It particularly focuses on the impact of electrolyser operating conditions and raw H_2 purity on power consumption for LH_2 production. Findings reveal that the operating conditions, particularly pressure, significantly influence power consumption, with higher pressures leading to improved overall efficiency due to reduced bubble coverage over the electrodes. Higher operating temperatures, while reducing reaction potential, bubble coverage, and electrolyte resistance, simultaneously lead to an increase in activation overpotential and cell voltage, particularly at temperatures over 120 °C.

This chapter shows that MFE is a viable alternative H_2 source for H_2 liquefaction plants as cryogenic cooling enables efficient removal of O_2, yielding high-purity LH_2 (>99.9%). Compared to AWE, MFE can reduce power consumption for LH_2 production by up to 10% when operated at elevated temperatures and pressures. The findings of this chapter contribute to the industrial application of MFE technology.

Furthermore, this chapter has demonstrated that improving the purity of raw H_2 can remarkably reduce the energy consumption in the production of LH_2, while simultaneously addressing safety concerns. Therefore, effectively mitigating gas crossover is essential for the performance and safety of MFE. This goal can be achieved by developing a comprehensive understanding of bubble behaviour and innovating novel techniques for bubble management in an MFE.

7.2 Bubble formation and departure from a microelectrode bubble generator

Generating bubbles with controllable size and frequency is critical for the fundamental study of bubble behaviour. Traditional bubble-generation methods predominantly rely on submerged nozzle gas injection, requiring precise control and sophisticated systems for gas flow. In contrast, the microelectrode single bubble generator presented in Chapter 4 offers a simple and economical solution. The proposed bubble generator is fabricated by embedding a microelectrode within a small nozzle to regulate bubble size and frequency through applied current and its geometrical parameters.

The formation and departure of H_2 bubbles from the microelectrode bubble generator are systematically investigated. It is denoted that a microelectrode, when fully submerged in an electrolyte, predominantly produces continuous, small bubbles (<0.2 mm). However, when placed within a nozzle, the same microelectrode tends to form single bubbles. The dimension of the microelectrode is critical, as larger diameters (>0.25 mm) favour continuous bubble formation. Moreover, concealed microelectrodes tend to produce continuous bubbles under low currents. As the current increases, these bubbles coalesce and form a large, expanding bubble, which eventually detaches from the nozzle upon reaching a critical diameter. Notably, a thinly concealed microelectrode can produce bubbles ranging between 0.3–1.4 mm at a frequency of approximately 1 Hz. This innovation serves as a fundamental step for subsequent studies on bubble behaviour within an electrolyser channel.

7.3 Effect of flow field on bubble rising trajectory

Membrane-free water electrolyser (MFE) utilises shear-induced lift force to separate H_2 and O_2 bubbles. The understanding of the effect of bubble diameter and flow field on the shear-induced lift force holds the key to enhancing bubble management in an MFE. Chapter 5 includes an experimental study on the trajectories of microbubbles rising in a vertical electrolyser channel with a fully developed laminar flow. The primary forces, including buoyancy, lift, and drag, on the behaviour of bubbles with diameters ranging from 0.3 mm to 1.0 mm are assessed.

It is concluded that bubbles, under the influence of lift force induced by the flow’s velocity gradient, move towards the wall region despite their diameters. Releasing bubbles closer to the wall, increasing bubble diameter, and elevating flow Reynolds number can accelerate this movement. As a bubble moves towards the wall, its transverse velocity increases, and its vertical velocity decreases. Furthermore, the effect of wall-induced lift force is negligible on the bubble rising trajectory outside the wall region.

Based on the experiment results, a new correlation was proposed for evaluating the lift coefficient for microbubbles subjected to a fully developed laminar flow. This relationship highlights the dependencies of shear-induced lift force on bubble Reynolds number and flow Reynolds number. Specifically, the lift coefficient is inversely proportional to the bubble Reynolds number, with a negative exponent of -0.17. In contrast, the lift coefficient is directly proportional to the flow Reynolds number, with a positive exponent of 0.5.

The insights gained from the work signify that the trajectory of buoyant objects in vertical channels can be managed by controlling the flow's velocity profile, with potential applications in various fields, especially for managing bubble distribution in an MFE.

7.4 Mitigating gas crossover in membrane-free water electrolyser

The distribution of H_2 and O_2 bubbles is critical to the performance and safety of a membrane-free water electrolyser (MFE). Literature suggests employing a fully developed laminar flow at the electrolyte entrance of an MFE, which generates a lift force that separates H_2 and O_2 bubbles. However, as MFE scaling up, solely on electrolyte flow is inadequate for the effective separation of H_2 and O_2 gases. In Chapter 6 of this thesis, a flow controller is developed to enhance the separation of H_2 and O_2 in an MFE.

The flow controller used in this work consists of two groups of thin, porous plates positioned between the anode and cathode. The results show that the flow controller can successfully maintain a W-shaped velocity field within the channel, which ensures the shear-induced lift forces consistently direct H_2 and O_2 towards the electrodes where they evolve. This reduces the bubble layer thickness and consequently mitigates bubble crossover. It is found that the bubble layer thickness is highly related to the geometrical parameters of the flow controller. As the gap of the flow controller reduces, the thickness of bubble layer decreases. Also, the optimal position of the flow controller is at approximately $0.25\,w$ from the channel wall (where w represents the channel width). Elevated flow Reynolds number can also mitigate gas crossover, as bubble layer thickness reduces with the increase of flow Reynolds number.

An experimental study on an MFE equipped with a flow controller is conducted. The flow controller prototype is fabricated via 3D printing from ABS plastic with a wall thickness of 0.4 mm. The results show that the flow controller can significantly reduce gas crossover in an MFE without compromising cell efficiency.

7.5 Recommendations for future work

The research presented in this thesis contributes to the understanding of bubble behaviour in a membrane-free water electrolyser (MFE) and the industrial application of MFE technology. The following possible directions are recommended for future study:

- Process optimisation of H_2 liquefaction process with MFE as H_2 source

  Chapter 3 of this thesis introduced an H_2 liquefaction process using Aspen HYSYS software. This existing model, based on a series of simplifications and assumptions, employs single-stage heat exchangers for O_2 and H_2 liquefaction and fixed coefficient of performance (COP) values for cryogenic coolers, resulting in elevated projections for energy consumption. For enhanced accuracy and reliability, subsequent research should consider incorporating a helium refrigeration cycle as the cold stream for H_2 liquefaction (Krasae-in *et al.* 2010, Yin and Ju 2020). To improve system efficiency, the process optimisation should focus on the integration of multi-stage heat exchangers throughout the precooling, O_2 liquefaction and H_2 liquefaction stages. The refined model can provide a more accurate evaluation of an industrial LH_2 liquefaction plant with MFE as the H_2 source.

- Development of high-pressure MFE operating at elevated temperatures

  As discussed in Chapter 3, operating an electrolyser at elevated pressure can lower its power consumption for both raw H_2 and LH_2 production. By pressurising the electrolyser, it becomes possible to raise the operating temperature to an optimal level, thereby maximising cell efficiency. Consequently, it is suggested that future research focus on developing a high-pressure MFE. It is also important to note that bubble behaviour can vary significantly at high pressures compared to atmospheric pressure. Therefore, an in-depth understanding of bubble behaviour in a high-pressure MFE is crucial for improving both cell performance and H_2 purity.

- Bubble swarm behaviour in a water electrolyser

  Chapters 4 and 5 detailed experimental studies focusing on the evolution, departure, and rising of single microbubbles within an electrolyte. However, within water electrolysers, bubbles usually exist in swarms, where the interactions between bubbles can significantly influence their behaviour. This is especially important for MFE cells, where controlling bubble distribution is crucial for mitigating gas crossover. Developing a technique capable of capturing the three-dimensional flow field within an electrolyser and tracking bubble distribution within this flow field can facilitate the further investigation of bubble swarm behaviour in a water electrolyser.

- Experimental study on flow controller in a scaled-up MFE

  Chapter 6 of the thesis introduces the concept of employing a flow controller for bubble management in an MFE. Although a prototype flow controller has been developed, there is still room for improvement, including improving fabrication and installation quality. Consequently, further studies are needed to conduct comprehensive evaluations of the flow controller's performance. Such studies should aim to not only assess its performance in lab-scale MFE but also validate its effectiveness in mitigating gas crossover in a scaled-up MFE.

- Enhancement of bubble departure from electrodes

  As mentioned in section 2.4, bubble coverage over the electrode surface can reduce the active area of the electrode and decrease cell efficiency. Therefore, developing an effective and economical technique to remove bubbles from the electrode surface is both crucial and presents a significant challenge. Several studies have explored techniques to expedite bubble departure utilising external fields, which include strategies like rotating electrodes, supergravity, magnetic force, and ultrasonics (Wang *et al.* 2014, Granados Mendoza *et al.* 2017, Scott 2018). Employing higher flow velocities can also be advantageous as it can enhance bubble departure by leveraging drag force (Mazzocco *et al.* 2018, Zhou *et al.* 2020).

Artificially inducing the formation of large bubbles at the bottom of the electrode can be particularly effective; as these larger bubbles rise, they may collide with adhering bubbles, dislodging them from the electrode surface. Additionally, the presence of large bubbles can induce high local velocity near the electrode, swiftly sweeping off the adhering bubbles. To the author’s knowledge, such a technique has yet to be investigated in existing literature.

References

Granados Mendoza, P., S. Moshtarikhah, A. S. Langenhan, M. T. de Groot, J. T. F. Keurentjes, J. C. Schouten and J. van der Schaaf (2017). Intensification of the chlor-alkali process by using a spinning disc membrane electrolyzer. Chemical Engineering Research and Design **128**: 120-129.

Krasae-in, S., J. H. Stang and P. Neksa (2010). Development of large-scale hydrogen liquefaction processes from 1898 to 2009. International Journal of Hydrogen Energy **35**(10): 4524-4533.

Mazzocco, T., W. Ambrosini, R. Kommajosyula and E. Baglietto (2018). A reassessed model for mechanistic prediction of bubble departure and lift off diameters. International Journal of Heat and Mass Transfer **117**: 119-124.

Scott, K. (2018). Process intensification: An electrochemical perspective. Renewable and Sustainable Energy Reviews **81**: 1406-1426.

Wang, M., Z. Wang, X. Gong and Z. Guo (2014). The intensification technologies to water electrolysis for hydrogen production – A review. Renewable and Sustainable Energy Reviews **29**: 573-588.

Yin, L. and Y. Ju (2020). Process optimization and analysis of a novel hydrogen liquefaction cycle. International Journal of Refrigeration **110**: 219-230.

Zhou, J., B. Qi, Y. Zhang, J. Wei, Y. Yang and Q. Cao (2020). Experimental and theoretical study of bubble coalescence and departure behaviors during nucleate pool boiling on uniform smooth and micro-pin-finned surfaces under different subcoolings and heat fluxes. Experimental Thermal and Fluid Science **112**: 109996.